A THEORY FOR HOW AQUAPORIN-1 AND TRANSMURAL PRESSURE INFLUENCE THE MECHANICS OF AND THE TRANSPORT THROUGH THE ARTERY WALL

by

SHRIPAD D. JOSHI

A dissertation submitted to the Graduate Faculty in Chemical Engineering in fulfillment of the requirements for the degree of Doctor of Philosophy, The City University of New York

2012

This manuscript has been read and accepted by the Graduate Faculty in Engineering in satisfaction of the dissertation requirement for the degree of Doctor of Philosophy.

Date	Professor David S. Rumschitzki Chair of Examining Committee
Date	Professor Ardie D. Walser Executive Officer

Professor Morton Denn

Professor Sheldon Weinbaum

Professor John Tarbell

Dr. Kung-Ming Jan, M.D.

Supervisory Comittee

THE CITY UNIVERSITY OF NEW YORK

Abstract

A THEORY FOR HOW AQUAPORIN-1 AND TRANSMURAL PRESSURE INFLUENCE THE MECHANICS OF AND THE TRANSPORT THROUGH THE ARTERY WALL

By

Shripad D. Joshi

Advisor: Professor David Rumschitzki

Macromolecular transport across the vessel wall, the earliest pre-lesion event in atherosclerosis, is known to occur due to advection by transmural pressure-driven plasma (water and small solutes) transport. The wall's hydraulic conductivity, (L_P), the ratio of water flux to the transmural pressure difference, characterize this flow. In the first part of Chapter 2, we improve on Huang et al.'s (36) intimal compression theory by implementing the exact fenestral boundary conditions in a finite difference method, rather than the approximate ones used previously due to computational restrictions, and use it to explain the experimentally observed variations (100, 2, 78, 62) in hydraulic conductivities of intact rabbit and rat artery wall with transmural pressure. Our model results explain the hydraulic conductivity data very well. It confirms that, as the transmural pressure increases, the degree of intimal compression increases and the resulting fenestral blockage significantly lowers L_P of the intact artery wall.

The discovery of the presence of Aquaporin-1 (AQP1) in rat aortic endothelial cells suggests a new possibility: that transmural water transport occurs through (transcellularly) as well as around (paracellularly) the endothelial cell. The second part of Chapter 2 proposes a new theory to explain the pressure-dependent effect, observed experimentally by Nguyen et al. (62), of AQP1-blocking on the L_P of rat aorta. Our hypothesis is that chemical blocking of AQP1s leads to a decrease in the average pressure in the intima, resulting in a higher force/area on the endothelium. This force compresses the intima and induces fenestra blockage at much lower overall transmural pressures. To assess this new theory, we extend Huang et al.'s (36) filtration model to include

transcellular water flow through AQP1s. The results agree well with Nguyen et al.'s (62) experimental data and suggest that the L_P of the intact artery wall indeed decreases with AQP1 blocking (i.e., by decreasing transcellular water transport). This agreement corroborates the significance of AQP1s in the overall water transport across the vessel wall. The model predicts that AQPs contribute at least 30% to the phenomenological endothelial L_P at low transmural pressures and to the intrinsic endothelial L_P. Further, we found that the force acting on the endothelium with functioning AQP1s at 60 mmHg, which gives a partially decompressed intima, is same as that acting on endothelium at 43 mmHg with blocked AQPs. Predictions are also presented to show how the increase in endothelial expression of AQP1s can increase the overall hydraulic conductivity of the vessel wall and shift the dynamic range over which the L_P drops significantly with pressure to higher transmural pressures. These findings suggest that AQP1 up-regulation, leading to higher wall L_P, can increase low density lipoprotein's (LDL) drainage from the sub-endothelial intima (SI) and thus might be beneficial in inhibiting pre-atherosclerotic LDL binding to SI matrix.

However, given the isotonic lumen, this selective AQP1-mediated pure water inflow into the arterial subendothelial intima (SI) should set up an oncotic pressure difference $(\Delta\pi)$ that opposes the ΔP- driven transmural water flow. How then could trans-AQP1 flow persist for many hours, as indicated by experiments that chemically block AQP1? To resolve this paradox, we have extended our filtration theory to include the mass transfer of oncotically active small solutes like albumin in Chapter 3. This addition nonlinearly couples the mass transfer, the fluid flow and the wall mechanics. We employ finite difference methods to simultaneously solve the steady filtration and mass-transfer problem as a long-time solution of a fictitious unsteady problem. The model reveals the surprising finding that, due to media filtration, the steady albumin concentration in the SI is in fact higher than in the glycocalyx (GX). This results in higher oncotic pressure in the SI that sucks water from the lumen into, rather than pushing it out of the SI. We find that endothelial AQP1 up-regulation increases the overall driving force across the EC and the total L_P of the vessel wall than that predicted by our filtration based model. Surprisingly, the model predicts that GX degrading enzymes cause a significant decrease in the overall driving force across the EC that

ultimately reduces the water flux across the vessel wall.

As noted earlier, the transmural flow plays an important role in determining LDL's concentration inside the vessel wall. We hypothesize that an increase in transmural water flux can lower the concentration of such macromolecules in the SI and flush them out of the wall by virtue of increased advection. Chapter 4 investigates the effects of endothelial aquaporin-1 (AQP1) up-regulation, and the resulting increase in transcellular and thus overall transmural water flux, on the tracer concentration inside the arterial wall at various transmural pressures. We combine the predictions from our earlier local filtration model with Zeng et al.'s (131) 2-D macromolecular transport model and include the changes in macromolecular transport properties like the retardation coefficient (f), the available volume fraction (γ) and the diffusion coefficient (D) with pressure induced intimal deformation. Our findings suggest a pressure-dependent decrease in intimal tracer concentration with increasing endothelial AQP1 expression, with the greatest effect observed at higher transmural pressures. These predictions are amenable to experimental verification and suggest AQP1 up-regulation as a potential route for mitigating pre-atherosclerotic lesion formation.

Acknowledgements

I would like to sincerely thank my advisor, Prof. David Rumschitzki, for all the guidance, support and encouragement he has provided during this research. I would also like to thank my thesis committee members - Prof. Morton Denn, Prof. Sheldon Weinbaum, Prof. John Tarbell and Dr. Kung-Ming Jan - for their guidance.

To all the support staff - Junjun Mao (PhD), Andy Eng and Zeng Xu - thank you for your help. I am also thankful to my fellow lab members - Chirag Raval (PhD), Jinyong Bao (PhD), Lin Zeng (PhD) for their help, especially to my good friend Chirag whose presence has made this journey much easier. I would like to specially thank all of my friends (both former and current graduate students in Chemical Engineering Department) for their help and support during my stay at the City College.

I would like to sincerely thank my mother, father, brother and all other family members for their blessings and the support they have provided throughout my PhD. Special thanks to my grandparents as I may not have reached this position without their blessings.

Finally to my wife - Manali - thank you very much for being patient with me. Your sincerity and hard-working nature has always been a great motivation for me. Thanks for helping me achieve this very important goal of my life.

To Shridhar kaka and my family

Contents

List of Figures

List of Tables

Chapter 1. Introduction

1.1 Atherosclerosis

Atherosclerosis, a disease of large and medium-size arteries (viz., aorta, coronary, carotid and other proximal arteries), is a chief cause of death in the United States and in most of the Western world (69). Severe atherosclerosis interferes with blood flow and leads to potentially harmful disease conditions such as myocardial infarction (heart attack) or cerebral ischemia (stroke). There exists an important relationship between the characteristics of blood flow in the arteries and the disease processes, not only in late/severe stages but also in the early stages of the disease. The initiation of atherosclerosis, also known as atherogenesis, starts at an early age; the time scale of disease development spans decades (59).

The earliest stages of atherosclerosis are thought to be the transport and accumulation of macromolecules like low density lipoprotein (LDL) cholesterol from the blood across the endothelium into the arterial sub-endothelial intima (SI) (71, 72). LDL is termed the "bad" cholesterol because it is found in high concentrations in atherosclerotic lesions. An LDL particle contains about 2000 cholesterol and cholesterol ester molecules and is approximately 22 nm in diameter. A phospolipid coat that surrounds these cholesterol molecules make them water/blood plasma soluble and thus make LDLs as the major carriers of cholesterol in the blood. The presence of apoprotein-B on the surface of an LDL, shown in Fig. 1.1, makes it's recognition possible by specific cell surface receptors. Cholesterol in moderate concentrations is needed by cells to produce cell membranes (81).

Once inside the SI layer, these macromolecules react with the extracellular matrix (ECM) that is mainly comprised of randomly-oriented proteoglycan (PG) and collagen (CG) fibers. It has been suggested that (74, 128) these binding interactions result in the formation of lipid packets, called liposomes (extracellular), that contain lipid from one or many LDL particles. The oxidation

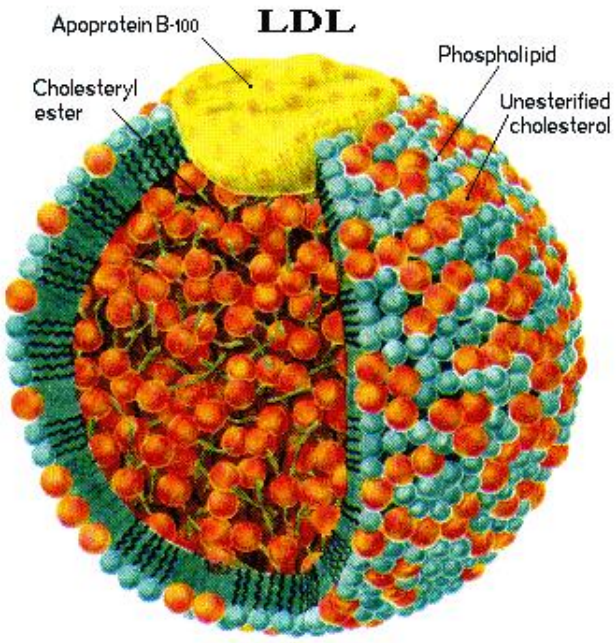

Figure 1.1: Low-density lipoprotein (LDL) molecule ($\sim$ 22 nm in diameter). Taken from http://www.cholesterol-and-health.org.uk/hdl-ldl.html

of LDL, perhaps by the endothelium (86, 88) or by the presence of reactive oxygen species inside the SI layer, initiates a cascade of inflammatory responses, including the adherence of blood borne monocytes to the luminal surface of the endothelial cell (EC). Monocytes transmigrate, possibly through endothelial junctions, into the SI region with high lipid concentration and become activated macrophages (10). The macrophage is a phagocytic scavenger and functions as an important part of the immune response system. It is thought to secrete chemoattractant factors and participate in the generation of reactive oxygen species (59). The interactions between LDL and ECM may increase the likelihood that the LDLs are chemically modified by oxidants within the arterial wall. The macrophages engulf oxidized LDL, not the native form of LDL, by the scavenger receptor pathway and result in the formation of lipid-laden macrophage foam cells (87). Though this could be a normal, phagocytic role of a macrophage, it appears that at some point in the disease process the macrophage/foam cells become overwhelmed and there is a breakdown that results in an increased amount of extracellular lipid and subsequently, in the development of fatty streaks or

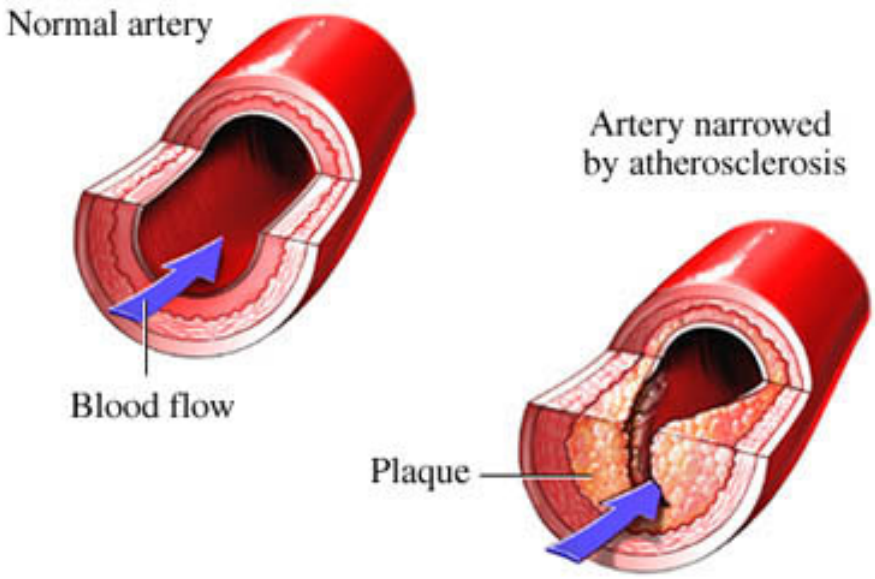

Figure 1.2: Comparison of blood flow in a normal and diseased artery. The atherosclerotic lesion that initially forms inside the artery wall infiltrates into the lumen and obstructs the blood flow as shown. Taken from http://www.nucleusinc.com

lesions inside the artery wall (86, 81). It is thus important to note that the deposition and oxidation of LDL particles in the SI trigger a complex cascade of biological interactions that eventually lead to the thickening and hardening of the vessel wall, including the formation of fatty lesions that slowly protrudes into the lumen and severely affects the blood flow to distant tissues. Furthermore, if unstable, part of the lesion can break off and completely block a small artery downstream, causing ischemic heart attack or stroke. The schematic depicting the obstruction of an artery due to atherosclerotic plaque formation and its contrast to a normal artery is shown in Fig. 1.2.

Many factors are known to influence atherogenesis, including food, a high cholesterol diet, high blood pressure, diabetes, cigarette smoking etc. It has been shown that different risk factors somehow lead to endothelial dysfunction (97) and thus increase its permeability to "bad" LDL cholesterol. Elevated LDL and/or reduced high-density lipoprotein (HDL) levels are the greatest risk factor for atherosclerosis. Although a number of risk factors, as mentioned above, have been identified, the exact mechanism by which they lead to atherosclerotic lesion formation

remains less clear. Non-pharmaceutical means such as eating a healthy (low cholesterol) diet, practicing regular exercise and not smoking are typically the first line of treatment used to slow-down or stop the progression of atherosclerosis. Pharmaceutical medications like statins that lower the blood concentration of LDL cholesterol and help slow, stop or even reverse the buildup of fatty streaks are commonly prescribed to patients with severe atherosclerosis.

The vascular fluid mechanics or hemodynamics is known to play an important role in the pathobiology of atherosclerosis. The nature of the blood flow in normal arteries, i.e., without any modifications due to disease, is by and large laminar except in the aorta, where high flow rates associated with exercise in adults can lead to turbulent conditions (59). It is known that atherosclerosis tends to be localized in regions of curvature and branching in arteries. The flow patterns in these regions are complex and the fluid shear stress differs from its normal spatial and temporal distribution patterns in straight vessel (60). The association of atherosclerosis with regions of altered fluid mechanics has motivated many investigations to explore the role of blood flow in the localization of this disease (5, 25). It has been suggested that the sites of atherogenesis are the sites of reduced wall shear stress (97). It is important to note that though the vascular fluid mechanics governs the transport of macromolecules from the bulk fluid phase (blood) to the endothelial surface, the accumulation of macromolecules takes place inside the arterial wall. Thus it also depends on the hindrance to passage of materials out of the vessel wall that is offered by underlying layers of the vessel wall (74, 97). This and the fact that initial lipid accumulation occurs in the SI suggest that the SI and media could be important structures contributing to local macromolecular uptake patterns and necessitates the consideration of arterial wall mechanics, along with the vascular fluid mechanics, to better understand the process of lipid accumulation inside the vessel wall.

1.2 Structure of artery wall

The artery wall is a layered structure, composed of five distinct layers. Each of these has its own unique function and characteristic transport properties. The innermost layer that is in direct contact with the blood is a monolayer of ECs that are normally joined together by tight junctions.

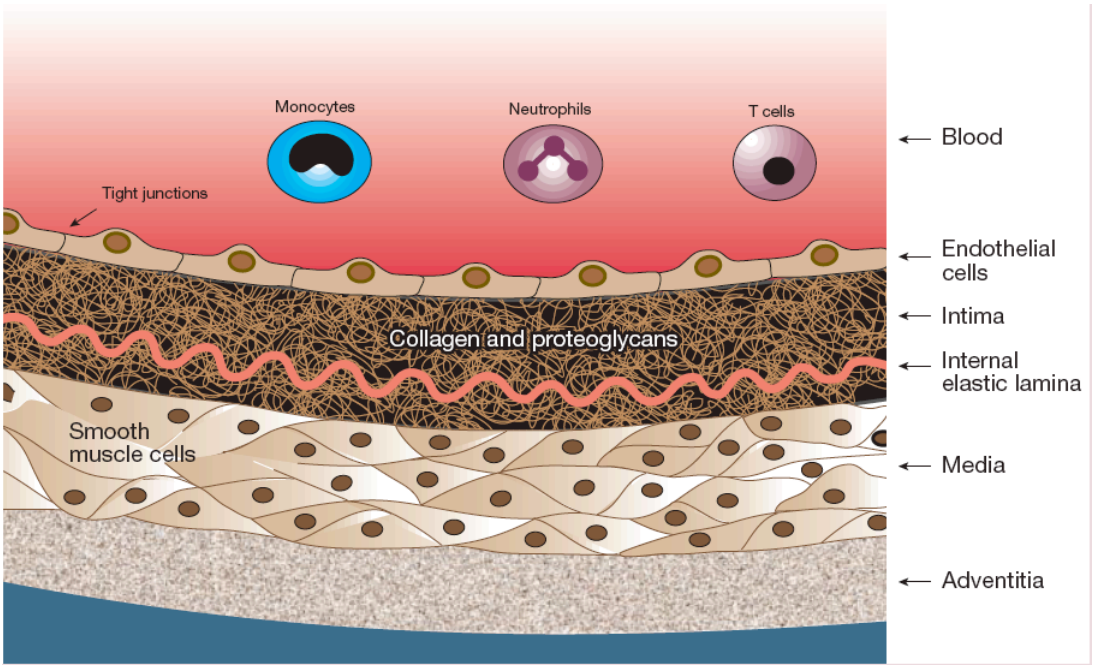

Figure 1.3: Structure of a normal large artery showing morphologically distinct layers, taken from Ref. (55)

Interendothelial junctions are typically 20 nm in width in regions of undamaged endothelium (30, 97). Figure 1.3 shows a cartoon of the vessel wall with various layers. Due to its strategic location, positioned between the flowing blood and the underlying vessel wall, ECs act as a barrier and limit the filtration of blood constituents into the vessel wall. It is also known to mediate the effects of circulating blood, including those due to hemodynamics, on vascular biology (59).

The plasma membrane of the ECs is covered by a thin layer of macromolecules known as the surface glycocalyx (GX) layer (not shown in Fig. 1.3). The major constituents of this layer are carbohydrates and glycoproteins, such as glycosaminoglycans (GAG), PGs and glycolipids (97). The polyanionic nature of these constituents imparts a net negative charge to the GX layer. The GX layer is postulated to play important roles in preventing interactions of red blood cells with the endothelium (75) and in the transduction of mechanical forces applied by vascular fluid mechanics to the surface of ECs (121, 111). Recent articles by Tarbell and Pahakis (99) and Weinbaum et al. (122) have reviewed the structure and function of the endothelial GX layer in great detail. The thickness of the GX layer has been controversial. *Ex vivo* electron microscopic studies in mouse

carotid arteries (109), and *in vivo* studies in venules (83, 20) and capillaries (114, 113) estimate the surface GX layer thickness of 0.5 μm to 1.0 μm. Recent observations of Squire et al. (84) in frog mesentery capillaries suggest a quasi-periodic bush-like structure of the GX layer with 10-12 nm diameter fibers separated by a distance of $\sim$ 20 nm in all directions. Using a structural model of the GX derived from the observations of Squire et al. (84) , Weinbaum et al. (121) have shown that the core proteins in the bush-like GX structure are sufficiently stiff and act as transmitters of fluid shear stress without significant deflection (99). They predict that the fluid shear force imposes a torque on stiff core proteins and suggest that the torque is transmitted to the underlying actin cortical cytoskeleton via transmembrane domains. They suggest that the resulting displacement of the actin filament can drive intracellular signaling. Hu and Weinbaum (32) have developed a cellular-level microstructural model and proposed that the endothelial surface GX layer act as a primary molecular filter for plasma proteins (e.g., oncatically active molecules like albumin $\sim$ 7 nm in diameter) and determine the effective oncotic force for water flow across the capillary endothelium. The influence of the GX layer in the transport of albumin will be discussed further in Chapter 3.

The thin SI layer (thickness less than 1 μm in healthy rats and rabbits) mainly comprises PG and CG fibers and separates the endothelium from the internal elastic lamina (IEL). Ultrastructure studies of rabbit aorta (24) have shown thick CG fibers ($\sim$ 20 nm in radius) interspersed with a mesh made of a large number of very thin ($\sim$ 2 nm in radius) PG fibers in the SI region. Huang et al. (36, 37) proposed and subsequently confirmed that the sparse SI layer undergoes compression with increasing lumen pressure. In rats, at low pressures, the thickness of the SI layer is found to be $\sim$ 1/2 μm (37). It should be noted that the SI layer shown in Fig. 1.3 is greatly exaggerated. The IEL in the aorta and other large arteries is $\sim$ 1 μm thick, continuous elastin sheet with numerous fenestral holes ($\sim$ 1 μm in radius (37)). Because of its structure, Huang et al. (36) propose that the IEL is impermeable to fluid and macromolecular transport except for its fenestra.

Adjecent to the IEL is the media, the thickest layer of the vessel wall ($\sim$ 150 μm in rat (78)). The media consists of smooth muscle cells (SMCs), repeated sheets of elastin fibers, and

a complex interstitial matrix containing CG, PG core proteins and GAGs (125, 46, 45, 117). The vascular SMCs, like all muscular cells, can contract and relax and thus provide contractile strength to the artery wall. The aorta, which receives blood directly from the heart, has a thick, strong wall to cope up with sudden high pressure produced during systole. The abundance of elastic material in the media region stretches the aortic wall in order for the vessel lumen to accommodate the change in blood volume during peak systole. The tensile strength of the collagenous connective tissue that surrounds the media region prevents over-distention of the elastic tissue (97). During diastole, the elastic recoil of these arteries maintains a continuous, though decreased, blood flow to smaller vessels. An anisotropic elastic model for the media layer of the artery wall, developed by Johnson and Tarbell (40), revealed that the volume of the media layer will not be significantly altered as the pressure is increased.

The outer adventitia layer of the wall of a large artery consists mostly of loose connective tissue that contains a drainage system of lymphatic vessels and a micro blood/nutrient supply system called the vasa vasorum. Because of its loose structure, the adventitia layer offers very little resistance to macromolecular and fluid transport through the vessel wall.

With the onset of atherosclerosis, there are some remarkable changes that take place within the vessel wall. As noted earlier, the transport and accumulation of macromolecules like LDLs in the SI and their subsequent interactions with the ECM can significantly alter the structural properties of the intima region. The thickening of the intimal region, observed in lesion-prone areas, occurs due to the accumulation of monocyte-derived macrophages and the proliferation and migration of vascular SMCs, emanating from the vessel media into the SI region, possibly through the IEL fenestrae (59).

1.2.1 Function of ECs

ECs line the inner layers of blood vessels like arteries, veins, arterioles and capillaries and act as a barrier between the blood and rest of the vessel wall. At the blood-artery wall interface, ECs are acted on directly by the hemodynamic stress imposed by flowing blood. This stress has two

components, a normal component, pressure and any normal stresses, and a tangential component, shear stress (59). ECs react to these fluid mechanical forces by releasing various substances that change the tone or firmness of the artery and serve as a mediator of hemodynamic or fluid mechanical effects. Endothelium-derived relaxing factor (EDRF), identified as Nitric oxide (NO), released by the ECs, regulates the vascular tone by dilating blood vessels. It thus has a direct functional influence on the vascular wall. It has been suggested that NO produced by ECs may scavenge oxygen free radicals, in doing so providing protection to the vessel wall (59). Under atherosclerotic condition, ECs cannot function properly, which results in reduced NO-induced vasodilation and thus stiffening of arteries.

1.2.2 Fluid mechanical effects on ECs and SMCs

The wall shear stress associated with blood flow through the lumen is known to affect ECs and may play an important role in arterial diseases. Specifically, the effects of shear stress on endothelial transport properties, viz. its hydraulic conductivity and permeability to solutes, are reviewed by Tarbell (97, 98). For a membrane (like the endothelium), one would normally think of its transport properties as constant parameters. However a remarkable feature of the endothelium is that its transport properties are sensitive to both the chemical and mechanical environment within which it resides (98). Endothelial cells exposed to normal blood flow experience a shear stress on the order of 10 $\mathrm{dyne/cm^2}$ (96). Shear stress on ECs can stimulate the release of diffusive substances like NO which, as noted earlier, causes SMC relaxation (59). The influence of shear stress on NO production provides a link between hemodynamics and its effect on the vascular tone, both of which are known to play important roles in disease progression. The influence of steady shear stress on tight and adherens junctions that link neighboring ECs is demonstrated by transport experiments on bovine aortic EC (BAEC) monolayers (21). These experiments showed a shear-induced reduction in occludin content (by $\sim 50\%$) and a decrease in the resistance offered by junctional strands or an increase in BAEC monolayer hydraulic conductivity (by 4.7 fold) after 3 hours of exposure to 20 $\mathrm{dyne/cm^2}$ shear stress. Other groups (39, 80) have also shown a shear-induced increase in

hydraulic conductivity (3 to 3.5-fold increase after 3 hours of exposure to steady shear stress of 20 $\mathrm{dyne/cm^2}$) of BAEC monolayers and in monolayer permeability to albumin . Though the majority of studies that looked into the influence of shear stress on endothelial transport are *in vitro* studies, the effect of shear stress in intact vessels (*in vivo* preparations) has also been observed. Lever et al. (48) found a 30% increase in the endothelial hydraulic conductivity in excised rabbit carotid arteries within 20 min of exposure to 1 $\mathrm{dyne/cm^2}$ shear stress. Although the relative increase in the hydraulic conductivity of whole vessels in response to shear stress is much less than above mentioned increase observed in BAEC monolayers *in vitro*, it should be noted that the SI and media layer of the arterial wall (not present in the *in vitro* set-up) contribute more than 50% of the overall resistance to water flux in an artery and thus the 30% increase observed by Lever et al. (48) may not reflect the change in endothelial hydraulic conductivity.

SMCs are also exposed to transmural (across the vessel wall) pressure-driven flow and its induced shear stress. Wang and Tarbell (117) have shown that, under physiological conditions, even though the superficial velocity of interstitial flow is very low (on the order of 10^{-6} cm/sec), the shear stress over the SMC surface is ~ 1 $\mathrm{dyne/cm^2}$, a level shown to affect SMC biology. Later, Tada and Tarbell (95) developed a 2-dimensional model to describe the interstitial flow through the media of an artery wall in the presence of the IEL. They modeled the IEL as an impermeable barrier to water flux, except for the fenestral pores that are uniformly distributed over the IEL. The media was modeled as a heterogeneous medium composed of a periodic array of cylindrical SMCs embedded in a fiber matrix representing the interstitial PG and CG fibers. They employed Brinkman equation to describe the porous media flow field and numerically solved the interstitial flow problem. By varying the area fraction and diameter of fenestral pores from 0.001-0.036 and 0.4-4 $\mu\mathrm{m}$, respectively, they predicted that the average shear stress on SMCs immediately below the IEL could be 10-60 times higher than on the cells residing further away from the IEL. They attributed this increase in the shear stress on SMCs residing in the proximity of the IEL to a dramatic increase in flow (concentrated water flux) emerging from the IEL fenestrae. In a subsequent study, Tada and Tarbell (96) found that the fluid shear stress on the bottom surface of

ECs, exerted by the lateral fluid flow in the SI between the basal endothelial surface and the IEL towards fenestration in the IEL, is on the same order as that acting on its top surface (10 $\mathrm{dyne/cm^2}$). Given the inhibitory effect of shear stress on vascular SMC proliferation (90, 108) and migration (77), high levels of shear stress can suppress these processes, which might otherwise contribute to atherosclerosis and intimal hyperplasia (82).

1.3 Transport across the endothelium

As noted earlier, the transport of LDL from the blood, across the endothelium, into the SI is an important process in atherogenesis. However, given the tightness of endothelial junctions, it is confounding how a large macromolecule like LDL ($\sim$ 22 nm in diameter) can penetrate the intact endothelium. The two most commonly accepted pathways for the transendothelial transport of macromolecules are through transcellular pathways by vesicular routes and transport across large paracellular channels. The relative contribution of these two pathways has been highly debated in the literature. Rosengren and coworkers (70) showed that impairing transcytosis, which involves shuttling of macromolecules back and forth within the cell, by inducing hypothermia in peritoneal microvessels of rats *in vivo* did not result in any appreciable decrease in overall LDL transport. They concluded that paracellular route is the dominant pathway for LDL transport. Recently, Cancel et al. (4) measured water, albumin and LDL fluxes across BAEC monolayers under both diffusive and pressurized (convective) conditions and estimated the contribution of vesicles to overall transendothelial LDL transport. They found that transcellular vesicular transport of LDL contributes less than 10% to the total LDL uptake. These predictions are consistent with the *in vivo* observations that LDL receptors (vesicular pathway) do not contribute significantly to LDL uptake in pressurized arteries (124, 98).

Weinbaum et al. (119) postulated that the dominant pathway for LDL transport across the endothelium is via rare "leaky junctions" associated with ECs in the state of cell turnover; i.e., either cell division (mitosis) or cell death (apoptosis) (118). These widened leaky junctions have dimensions on the order of 30-1000 nm (8, 97) and the leakage is found to last on an average

about one hour (in rats) before a well-formed new junction is established (11, 8). Tracer studies by Stemerman et al. (89), using horseradish peroxidase (HRP) and LDL, have shown that the transport of macromolecules across the endothelium of rabbit aortas occurred at focal leakage sites, rather than uniformly. Although the occurrence of these focal leaky sites surrounding isolated ECs ($\sim$ 1 in 2000-6000 cells in rats (11)), that allow LDL to pass through, is very rare, they can significantly increase the endothelial permeability to LDL.

Later on, Lin et al. (50, 51) substantiated Weinbaum et al.'s (119) leaky junction-cell turnover hypothesis by injecting rats with Evans blue albumin (EBA $\sim$7 nm in diameter) and Lucifer-yellow LDL (LY-LDL) and viewing their thoracic aortas *en face* using fluorescent microscopy. They reported that more than 99% and 80% cells in mitotic phase were associated with EBA and LY-LDL leakage, respectively. However, using quantitative autoradiography of the endothelium, Truskey et al.(105) showed that leaky sites associated with mitotic ECs do not account for all leaks. They found that such regions with higher permeabilities to ^{125}I-LDL account for only 25% of the total leaks. Chen and coworkers (9) also studied the relation between cell turnover and macromolecular leakage in rat thoracic aortas. They found the association of a great majority (more than 90%) of mitotic and dying ECs with focal HRP uptake. They also reported that these mitotic and dying ECs accounted for only 17% of the total leakage sites, indicating that significant leakage of HRP may occur through normal ECs.

It is noteworthy that the leaky junctions, which constitute the principle pathway for transport of LDL across the endothelial layer, are affected by local fluid mechanics. It is observed that elevated steady shear stress tends to be associated with suppression of both mitosis and apoptosis, whereas low shear stress and separated or disturbed flow are associated with an increase in the rate of these processes (22, 12). Therefore, leaky junctions would be more prevalent in regions of low shear stress and separated flow regions rather than in regions of higher, unidirectional shear stress. Interestingly, these are the precise locations where atherosclerotic plaques tend to be localized.

1.4 Transport models

In order to understand the transport characteristics of macromolecules through the vascular endothelium of the rat aorta, Chuang et al. (13) and later Shou et al. (79) injected HRP through femoral veins of the rat and allowed the tracer to circulate for various amounts of time before sacrificing the animal. Surprisingly, these experiments showed rapid early-time growth of the leakage spot and a longer time asymptotic behavior in which the leakage spot appeared to approach an equilibrium diameter. Specifically, the HRP tracer spots grew to 200 μm in diameter in the first 2 minutes of circulation time, reaching a value of $\sim$ 250 μm by four minutes that appeared to be growing slowly enough to look like an approach to a steady spot diameter. Many investigators in the past tried to explain the time dependent transport of tracer molecules with the help of mathematical models (104, 26, 27, 107, 119, 120, 123). Initial one-dimensional models, independent of (i.e., uniform in) the directions parallel to the endothelium, for macromolecular transport in the artery wall assumed that the primary transport in the SI is in a direction normal to the endothelial surface. These include one dimensional diffusion-based models and diffusion coupled with convection normal to the endothelium model (104, 26, 27). Clearly these models were not constructed to explain focal leaks and the lateral subendothelial spread of macomolecules away from these cellular level leakage sites. The two-dimensional time dependent models developed by Weinbaum and co-workers (119, 120, 123) were based on pure diffusion and neglected the unique structure of the IEL with its fenestra. Their inaccuracy in predicting the early rapid growth of the tracer spots necessitated the consideration of convection with diffusion.

Yuan et. al. (129), for the first time, came up with a 2-D convection-diffusion model over a periodic wall unit that considered the nonuniform subendothelial pressure field that arises from the different hydraulic resistances of normal and leaky endothelial cells. They also considered the unique structure of the internal elastic lamina (IEL), with its fenestrae, in modulating the horizontal transport of macromolecules after they have entered the subendothelial region. They treated the IEL as a discrete barrier for the trasmural flow and divided the arterial wall into four layers,

namely, the endothelium, the SI, the IEL and the media. Though this model considered the SI and media regions separately, it assigned the same transport parameters for these two regions. Due to higher hydraulic conductivity of leaky junctions compared to normal/tight junctions, Yuan et al. (129) postulated that the pressure drop across leaky junctions will be smaller than that across the normal endothelium. Thus, at constant luminal pressure, large lateral pressure gradients will exist in the SI between the exit of leaky junction and the remainder of periodic wall unit. The model suggested that the water flow in the SI, after crossing the leaky cleft, will primarily be parallel rather than normal to endothelial surface. Though this model did a slightly better job in qualitatively explaining the rapid early-time growth of HRP leakage spots (150-200 μm diameter after 1 min) observed in rabbit and rat aortas than earlier diffusion based models, it still under-predicted the experimentally observed growth of the HRP spots by an order of magnitude from 30 seconds to 4 minutes after injection.

The ultrastructure study of Frank and Fogelman (24), using an ultra-rapid freezing/ rotary shadow etching electro microscopic technique, showed the presence of proteoglycan (PG) and collagen (CG) fibers in the subendothelial region and revealed the unexpectedly far sparse structure of the SI than the medial matrix. Moreover, immunolocalization studies with monoclonal antibodies confirmed vastly different PG structures in the intima and media and evinced a continuation of the intima's PG matrix structure into the fenestral pores of the IEL (47). These inherent differences in the structural properties of the intimal and medial layers suggested large difference in the transport parameters, such as Darcy permeability K_P and macromolecular diffusivity D, of these two layers. Using these ultrastructural observations, Huang et al. (35) estimated that the SI is practically all void with over 90% space for albumin and 50% for LDL; however, the media is only about 8% void for albumin and less than 1% for LDL (35). Huang et al. (35) postulated that the intima was much more porous than media and, thus, offered much less hydrodynamic resistance than the media. They developed an *ab initio* theory to predict the permeability of the heterogeneous PG and CG matrix of the intima and found that the hydraulic conductivity and Darcy permeability of the intima (K_{P_i}) is one to two orders of magnitude greater than that of the media (K_{P_m}).

Using these different transport parameters, Huang et al.'s (35) theory predicted that, due to the difference between SI and media flow resistance and between leaky and normal junction hydraulic conductivity, macromolecules crossing the endothelium would have the tendency, in the vicinity of the leaky cell, to be transported extremely rapidly in the intima in a direction parallel to the endothelium away from the leak, instead of predominantly directly across the thickness of the vessel. Moreover, their predictions of the growth and concentration of HRP leakage spots showed excellent agreement with experimental values. The close agreement between the theoretical and experimental results for the growth of HRP and LDL leakage spots strongly supported the idea that the transport across the arterial wall is indeed convection driven and, in the SI near macromolecular leakage sites, predominantly in the direction parallel to the endothelium.

Zeng et al. (131) developed a detailed 2-D, wall structure-based filtration and macromolecular transport model, structurally similar to those proposed by Yuan et al. (129) and Hunag et al. (35), but with improved parameters that, due to the paucity of data available at the time, had to be guesstimated in earlier studies (129, 35). In addition to this, neither of the earlier studies (129, 35) had directly solved the equations of continuity and of solute conservation in the SI region. Owing to a very small ratio of SI thickness (0.2 - 1 μm (35)) to the mean distance between leaky cells (670 μm (35)), they replaced these equations by their integrals (normal to the endothelium) across the SI and thus transformed the boundary value (BV) problem in the SI simply into boundary conditions for the media BV problem. Zeng et al. (131) showed that, although this assumption holds in regions far from the leaky site, it introduces significant errors near the leak. Since all tracer enters via leaky junction in this model, even small error in advection and concentration near the leak can lead to inaccuracies in the larger solution. Zeng et al. (131) directly solved the SI and media problems with the appropriate parameters and without these and other simplifications and found a very good agreement with both Chuang et al.'s (13) and Shou et al.'s (79) HRP spot size data. Sun et al. (93) investigated the effects of transmural pressure and shear-dependent hydraulic conductivity of the endothelium on the arterial mass transport of LDL using a multilayered, coupled lumen-wall model. They showed that low wall shear stress weakens the convective clearance

effect of transmural flow and leads to focal LDL accumulation. Moreover, they found that there is a global LDL accumulation in the SI and inner media at high transmural pressure, associated with hypertension, due to a significant increase in LDL transendothelial flux.

1.5 Hydraulic conductivity

The above-mentioned transport studies strongly suggest that advection, by transmural pressure-driven water transport through leaky endothelial junctions, is responsible for the focal transport and subsequent spreading of macromolecules in the SI. Uniform transmural water transport through the normal endothelium augments this lateral spreading by dilution and flushing tracer that has entered the SI via the leaky junction pathway. That is, water is known to cross the normal endothelium uniformly e.g., through normal tight junctions. Thus water transport, together with the diffusion, can further transport lipoproteins that have already entered the vessel's intima. Hence, the total transmural water transport, and not just the portion through leaky junctions, appears to play a central role in delivering LDL cholesterol to and flush it from the subendothelial space. The water flow carries soluble tracers such as lipid into the arterial subendothelial intima and spreads it there, thereby giving it the chance to bind to extracellular matrix. Such binding might lead to, and possibly trigger, the start of lesion formation. The transmural flow dilutes LDL's local concentration, thereby likely slowing these binding reaction's kinetic rates, and flushes unbound LDL from the SI, and ultimately from the wall. Thus, it is critical to understand the nature and control of transmural plasma (i.e., water and small solutes) flow and its influence on the lipid transport in the vessel wall.

One indirect way of studying water flow through an arterial wall, and its pressure dependence, is by measuring an important transport property of the artery wall, called the hydraulic conductivity (L_P). The L_P is an experimentally measurable quantity and a constant of proportionality that relates the water flux to the driving force ΔP (a difference between lumen and adventitia pressure) for convection. Many researchers (110, 100, 3, 2, 78, 62) have employed various experimental methods to measure the L_P of aortas from various animal species as a function of transmural pressure *ex vivo*. Tedgui & Lever (100) and Baldwin & Wilson (2) have studied the ef-

fect of pressure on fluid filtration through the intact and denuded (de-endothelialized) whole rabbit aortic wall, while Shou et al. (78) and Nguyen (62) did analogous experiments on intact and denuded whole rat aortic wall. Comparison of the intact and the denuded vessel experimental results allows one to infer the contribution of the endothelium to the overall L_P of the vessel wall. Figure 1.4 plots the L_P results obtained by these researchers (100, 2, 78, 62).

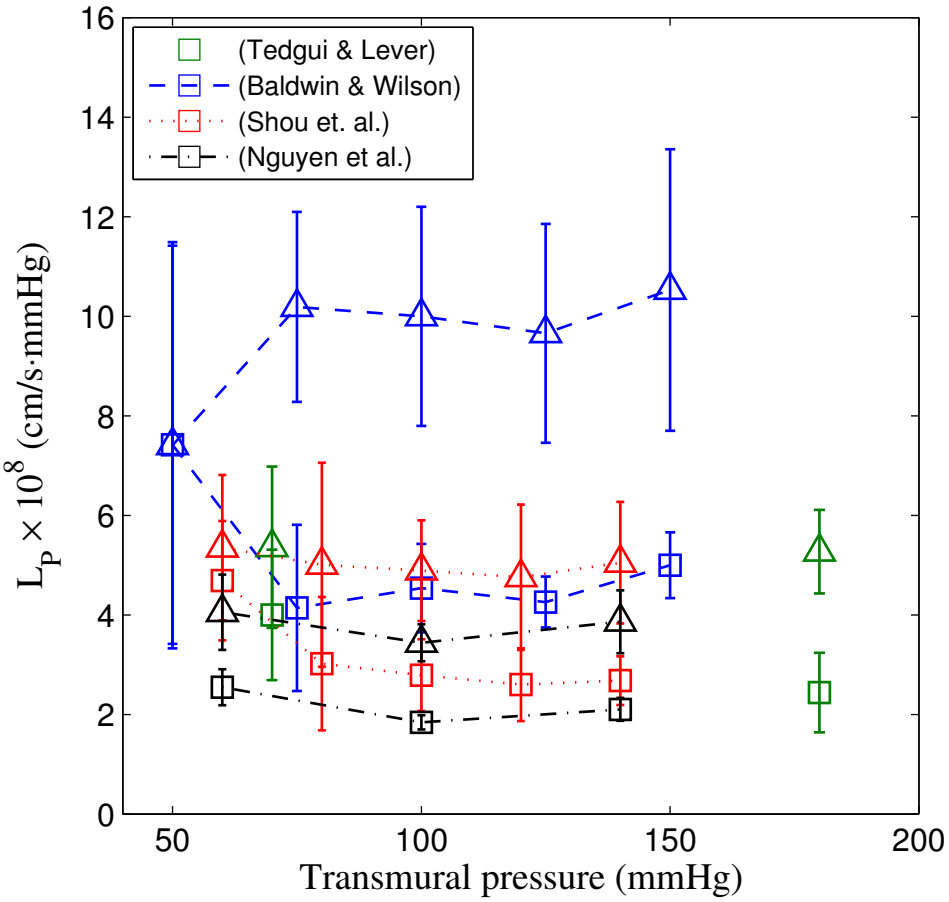

Figure 1.4: Hydraulic conductivity (L_P) as a function of transmural pressure. Reported above are results obtained by Tedgui & Lever (100) and Baldwin & Wilson (2) for rabbit aorta and by Shou et al. (78) and Nguyen et al. (62) for rat aorta, □ for intact and △ for denuded endotheliums. Error bars represent standard deviations.

Tedgui & Lever (100) found higher L_P at lower transmural pressure (70 mmHg) and lower L_P at higher pressure (180 mmHg). Their de-endothelialized arteries not only had higher L_P values (approximately double) than those of the intact vessels, but exhibited no significant dif-

ference at low and high pressures. Baldwin & Wilson (2) used Tedgui & Lever's (100) technique and repeated intact and denuded L_P measurements on same rabbit aortas (as opposed to Tedgui & Lever who used different portions of the same vessels to measure denuded L_P) at five different pressures. Baldwin and Wilson (2) found uniformly double L_P results compared to those obtained by Tedgui & Lever (100), but both results showed qualitatively similar trends. In this study as well, the L_P for an intact wall was found to be higher at lower pressures, but the increased pressure resolution showed that it decreased by $\sim 40\%$ from 50 to 75 mmHg and remained relatively constant at higher pressures. However, given these datas large experimental variation at 50 mmHg, one could not unambiguously infer a significant change in L_P upon endothelium removal at this pressure. Shou et al. (78) and Nguyen et al. (62) repeated these L_P measurements on the much smaller rat model and found Lp trends, both with and without endothelium, that agree quantitatively with Tedgui & Lever (100) and qualitatively with Baldwin & Wilson (2), suggesting that there is little species variation in L_P-trends in large arteries. They also had much lower error bars and therefore could indeed evince a measurable increase in L_P at 60 mmHg.

Due to the vast difference in tissue density, or its dual, tissue void space, between the sparse SI and the dense media, Huang et al. (36) postulated that the SI is very compressible and the media is relatively incompressible under physiological transmural pressures. They invoked this notion to explain the variation in L_P with increasing transmural pressure by attributing it to intimal compaction upon pressure loading. They postulated that initially at lower pressures the intima is not compressed, and hence allows a higher transmural water flux. However, an increasing pressure compresses the PG matrix in the SI, thereby decreasing the void space between the fibers and increasing its resistance for flow. Moreover, the compressed SI forces the endothelium to block flow into the IEL's fenestrae, which inhibits some of the flow through them. This inhibition drastically reduces the overall L_P of the vessel wall. The intima can achieve a maximum compression at which the PG matrix is maximally compressed and the much stiffer collagen fibers inhibit further compression. Beyond this maximum compression one expects very little change SI structure and thus in filtration properties; thus wall L_P remains constant at higher pressures. Endothelial removal

eliminates both a layer of resistance, and thus fenestral blocking potential, thereby increasing L_P and explaining the denuded vessel hydraulic conductivity's pressure insensitivity. Again, the media is assumed to be very dense compared with the intima and, therefore, the degree to which this layer compresses with increasing pressure within the physiological range is minimal.

Thus, in order to quantitatively explain the observed trends in hydraulic conductivity of an intact artery wall with transmural pressure, Huang et. al. (36) proposed a local (on the scale of single endothelial cell) two dimensional model for the filtration through fenestral pores in a compressible intima and included the variation of the SI's Darcy permeability K_P as a function of intimal compaction. They indeed found a dominant role for fenestral blockage upon pressure-induced intimal compaction and successfully explained the L_P variation observed by Tedgui & Lever (100) and Baldwin & Wilson (2). Later on, Huang et al. (37) experimentally confirmed their predicted intimal compression behavior with increasing pressure. Among other things, by improving the solution method, specifically by employing exact boundary conditions in the IEL fenestral hole as opposed to the approximate ones used by Huang et al. (36), we have explained all of the L_P results shown in Fig. 1.4 (see chapter 2).

Huang et al. (36) also predicted the effective L_P of the endothelium and SI ($L_{P_{e+i}}$) as a function of ΔP, and used these predictions from the local filtration theory in their earlier convective-diffusive transport model (35) to investigate the change in the time-dependent HRP concentration profiles and thus, leakage spot sizes with transmural pressure. They found that, due to pressure induced intima compaction and the resulting change in its transport properties, the long-time asymptotic spot size decreased by $\sim 50\%$ when the transmural pressure was increased from 50 to 100 mmHg (36). Moreover, the rise time required to achieve the asymptotic spot size was much shorter at 100 mmHg than that required at 50 mmHg.

Y. Sun (94) then combined Zeng et al.'s (131) corrected theory with appropriate rat parameters with Huang et al.'s (36) intima compression theory and predicted the effect of initma compression on HRP spot growth as a function of transmural pressure (ΔP). These predictions both qualitatively and quantitatively matched with those obtained by Huang et al. (36) previously

and suggested that the rise time and the asymptotic size of HRP spot growth in the intima decrease with increasing ΔP. They subsequently measured HRP spot growth in rat aorta at different acute transmural pressures and found good agreement between experimental observations and the predictions of the theory that incorporates intimal compaction under ΔP.

Dabagh and coworkers (18) constructed a multilayer model that took into account the presence of leaky and normal endothelial junctions and studied the effects of the increase in cell turnover and the compaction of the arterial wall layers on the transport of LDL with changes in pressure. They predicted that hypertension increases the endothelial permeability to LDL through its influence on cell turnover and results in the accumulation of LDL in the SI.

1.6 Aquaporin-1 and transcellular water transport

The transmural transport of blood plasma (which we refer to as water, since plasma is $\sim 95\%$ water) discussed in earlier sections assumes water flow through leaky and normal/tight junctions surrounding leaky and the far more numerous normal ECs, respectively. A membrane protein molecule called aquaporin-1 (AQP1), discovered by Agre and coworkers (67), acts a specific water channel and is found to be expressed in a variety of endothelial and epithelial cells (63, 102), as well as in red blood cells (56, 115) and plants (64). These highly selective passive water channels allow high throughputs of water ($\sim 3 \times 10^9$ molecules/sec) in response to, e.g., osmotic gradients, at little or no cost in ATP (58). In humans, AQP1 and AQP2 are abundant in the kidney, where 150-200 liters of water resorb from the primary urine per day. J. Toussaint of our group, using an immunohistochemical technique, has established that rat aortic endothelial cells (RAECs) avidly express AQP1 *ex vivo* (103), while Nguyen (62) and Xue (126) have identified the presence of AQP1s in BAEC and RAEC cultured monolayers, respectively. This discovery suggests the new possibility of transcellular water flow through AQP1s, alongside the generally accepted paracellular route. Furthermore, J. Toussaint (103) found that whole rat aortas upregulate the numbers of AQP1s that they express in response to a chronic increase in ΔP. More recently, C. Raval (68) has found that certain cAMP agonists upregulate endothelial AQP1 expression in BAEC monolayers

and whole rat aorta *ex vivo*.

Our group is interested in investigating the potential role of AQP1 in water transport across the endothelium and through the artery wall. T. Nguyen (62), S. Russell (73) and Y. Xue (126) showed that chemical blocking of AQP1 or knocking down AQP1 expression (using siRNA against AQP1) significantly reduces BAEC and RAEC monolayer hydraulic conductivities. Nguyen's (62) *in vitro* experiments showed an average 22.1% decrease in water flux for $HgCl_2$ treated (AQP1-blocked) BAEC monolayers compared to controls (without $HgCl_2$), whereas the siRNA studies showed $\sim 60\%$ and 62.4% drop in BAEC and RAEC monolayers relative to controls. Subsequent studies with tracer molecules that only cross the endothelium paracellularly (through junctions) showed no change in junctional transport, implying that the observed drop in L_P is primarily due to reduction in transcellular water transport.

Nguyen and Xue carried out *ex vivo* studies to measure the hydraulic conductivity of an excised vessel as a function of pressure, first with functioning AQP1s and then with chemically blocked AQPs1 (62), using $HgCl_2$ as a blocker (or with AQP1s knocked down (126)), on the same vessel. The statistically significant decreases of $\sim 32\%, 11\% \,\&\, 5\%$ in intact vessels' hydraulic conductivity, observed experimentally in case of blocked AQP1s (62), at 60,100,140 mmHg respectively, indicate that AQP1s seem to play an important role in transendothelial water transport. Since the wall's total resistance to flow, $1/L_P$, is the sum of the resistance of the endothelium plus SI and that of the media plus IEL, resistance in series, one finds that the endothelial L_P drops by 56%, 21% and 11%, respectively, at these pressures. AQP1 knockdown studies, which require a much more challenging experimental setup, showed a nearly identical drop in L_P at 60 mmHg in whole rat aortas *ex vivo* (126). The results of both of these experiments suggest a significant contribution of AQP1-mediated transcellular flow to overall water transport across the vessel wall. However, a strong pressure dependence of the decrease in L_P of the vessel wall suggests that the effect of AQP1 blocking on total L_P is not simply due to lower hydraulic conductivity of the endothelium (L_{P_e}), but something more subtle. Recall Huang et al.'s (36) intimal compression theory (without blocker) argued that at higher transmural pressures (beyond $\sim$ 80-90 mmHg) the intima

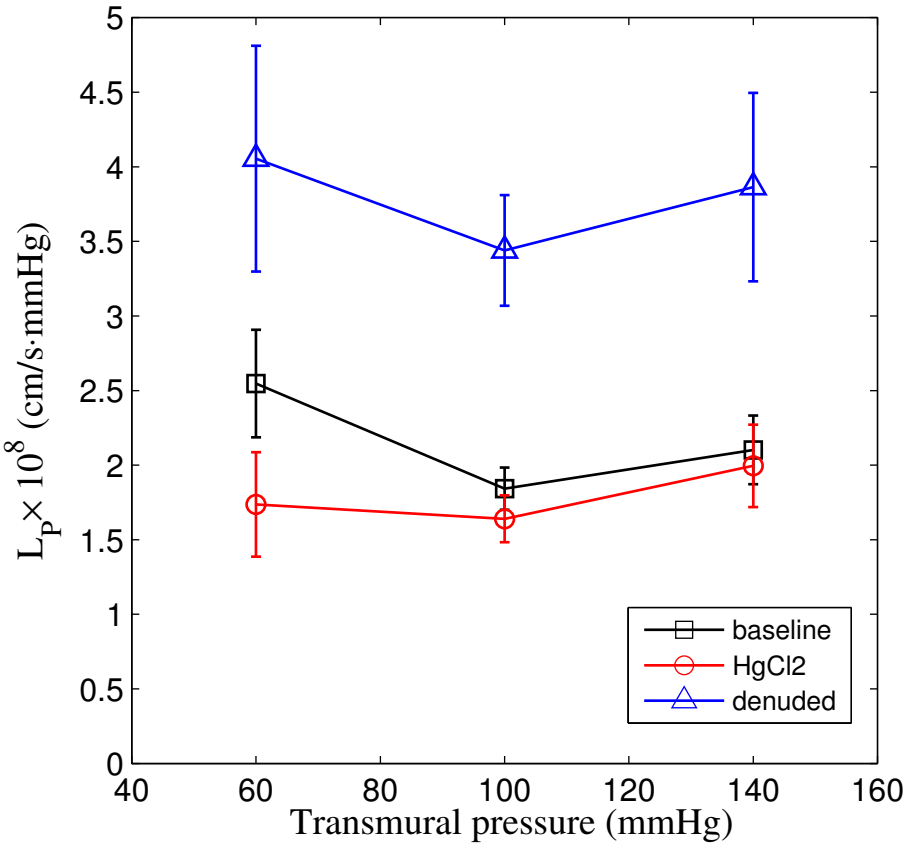

Figure 1.5: Nguyen's (62) hydraulic conductivity as a function of pressure for intact endothelium with and without $HgCl_2$ (baseline), and for denuded endothelium. Note that the baseline results are same as those shown in Fig. 1.4

remains fully compressed and therefore L_P becomes ΔP-independent. Note that, in the case of blocked AQPs, Nguyen (62) showed nearly ΔP-independent values of L_P that extend to much lower pressures ($\sim$ 60 mmHg), where the unblocked intima is not compressed. This suggests that AQP-blocking may lead to premature intima compaction at a lower overall ΔP.

1.7 Objectives of the study

Motivated by Nguyen's (62) intriguing experimental findings, the second chapter of this thesis seeks to theoretically explore the influence of blocking of AQP1s on the total hydraulic conductivity and the overall wall mechanics. Here we extend Huang et al.'s (36) local filtration model (that models only paracellular water transport) and include the effects of trancellular water flow through AQP1 water channels. We also include the effect of the GX layer that covers the luminal side of the EC on transport across the artery wall. The reason for this is that we believe this layer may play an important role in transport of oncotically active solutes like albumin from the blood into and through the vessel wall, something that Huang et al. (36) did not consider in their model. Chapter 3 extends the models from Chapter 2 to concentrate on oncotic issues, and therefore the earlier model sets the stage for this by including the surface GX layer.

Specifically, Chapter 2 proposes a new theory to explain the perplexing experimentally-observed (62) pressure-dependent effect of AQP-blocking on the L_P of whole rat aorta. One mystery that our theory addresses is why the drop in L_P is pressure dependent. It also extracts the percentage of the intrinsic endothelial L_P due to AQP1s. The idea behind the new model is that blocking the endothelial AQP1s will decrease the number of available pathways for water transport, thus increasing the resistance of endothelium, i.e., decreasing its intrinsic hydraulic conductivity (L_{P_e}). This will result in a decrease in intimal pressure ($\bar{P}_i$) at a fixed ΔP. Thus there is a larger endothelial force per unit area ($P_L^* - \bar{P}_i^*$), which can compress the intima and lead to IEL fenestral blockage at lower overall ΔP. In other words we speculate that, at low transmural pressures where the intima is normally uncompressed, blocking EC AQP1s can shift a larger portion of the overall ΔP from the media to the endothelium and thereby compress the intima without changing ΔP. We

characterize the transcellular water transport by attributing a fraction of the intrinsic L_{P_e} to AQP1s on an EC, denoted by $L_{P_{EC}}$ and see if this model quantitatively explains Nguyen's experimental data (62). If so, we would have both experimental and theoretical evidence of the effect of AQP1s or transcellular water transport on overall water flux across the artery wall. Once we successfully establish the mechanism of AQP1's action on the wall's mechanics, we would test the theory for an inverse effect i.e., instead of blocking, we will mimic the experimental effect of AQP1 upregulation by increasing $L_{P_{EC}}$ and see if the model provides us some interesting predictions and insights into such experiments. We anticipate that higher $L_{P_{EC}}$, or more AQP1s, will increase the overall L_P of the vessel wall. In addition, we anticipate that AQP1 upregulation will shift the dynamic range of intima compaction, i.e, the pressure range over which the SI goes form its uncompressed to its fully compressed state, to higher overall transmural pressures. We shall seek to identify a range of transmural pressures where an increase in the number of AQP1s would significantly raise the total wall L_P by a value that is greater than typical experimental variations observed in *ex vivo* set-up (see error bars in Figs. 1.4 and 1.5). Should we find such a pressure range, we shall make predictions for such new experiments. The reasons why we are interested in increasing the total L_P are: (a) increased transmural water flux that results from higher L_Ps has the potential to dilute and thus lower LDL's local concentration inside the artery's SI region; and (b) the enhanced convective water flux can flush unbound lipid or LDL from the SI deeper into the vessel wall, where it is unlikely to adhere, and possibly entirely out of the vessel wall. Both of these related processes can potentially lower the rates of LDL- SI ECM binding kinetics, a critical and possibly triggering event in lesion formation.

The first part of Chapter 2 explains the filtration model proposed by Huang et al. (36) with, as mentioned earlier, the addition of the GX layer and with the use of exact, rather than approximate, boundary conditions. We first present and solve the governing set of coupled partial differential equations (PDEs) both analytically (by using approximate boundary conditions instead of the pressure and velocity continuity in the fenestral hole, as in Huang et al. (36)) and by numerical finite difference and find the pressure distributions in both the subendothelial intima and

media. The numerical solution uses a *finite difference* method with a numerical implementation of the exact boundary conditions. This solution is new, and using it we can evaluate the quality of Huang et al.'s (36) approximate solution, which we have reproduced. Using this method, we will explain all of the experimental L_P results, cited earlier. Section 2.3 then extends Huang et al.'s (36) model by incorporating transcellular flow and estimates AQP1's contribution in overall transmural transport by comparing predictions of hydraulic conductivities for the case of blocked AQP1s with corresponding experimental observations of Nguyen et al. (62). Section 2.3.3 makes predictions for new experiments and section 3.3.12 compares the model's predicted hydraulic conductivities with the results of experiments that were designed to test these predictions and carried out (by C. Raval, Ph.D.) in our group.

The effect of osmotic pressure differences on the flow across the capillary endothelium has been well known for many years. However, in large blood vessels, due to higher hydrostatic pressures and the fact that the lumen and the *vaso vasorum* are both isotonic, the contribution of osmotic gradients in the wall is generally considered negligible (100, 38); thus the transmural water flux is thought to be controlled by only the hydrostatic pressure difference (ΔP) between the inside and the outside of the artery wall. Though we neglect the effect of osmotic pressure gradients in the transport models discussed in Chapter 2, the transmural pressure-driven trans-AQP1 mediated water flow presents an oncotic paradox, explained as follows. Normal EC junctions transport isotonic fluid, i.e., water and small solutes (e.g. albumin) responsible for osmotic pressure. In contrast, AQP1s specifically transport pure (hypotonic) water, excluding nearly everything else. This pure water trans-endothelial flow should both raise the albumin concentration on the lumen side and lower it on the SI side of the EC, thereby setting up an osmotic pressure difference ($\Delta\pi$) that acts against the ΔP-driven flow through the cell and prevents the SI from getting more hypotonic. One would expect this adverse $\Delta\pi$ to oppose and eventually even halt the ΔP-driven trans-endothelial flow. If so, why are the L_P values in Fig. 1.5 steady for hours, rather than decaying to zero? Since $\Delta\pi$ is acting against ΔP, wouldn't it grow to balance ΔP and turn off the transmural water flow completely? This is the focus of Chapter 3, where we investigate the effects of osmotic pressure

differences on the overall transport across the endothelium and through the entire vessel wall.

A number of theoretical and experimental studies on micro vessels have shown the significance of the surface GX layer in determining the effective oncotic force that drives water flow across the capillary endothelium (32, 33, 1, 132). Specifically, it has been suggested that the local hydrostatic and osmotic pressure differences across the surface GX layer, and not the global hydrostatic and osmotic pressure differences across the entire capillary wall between the plasma and tissue, determine the relevant Starling forces that drive water flow across the capillary endothelium. This led us to believe that the GX layer, which acts as a primary filter for oncotically active molecules like albumin, could have an impact on the transport of albumin across the arterial endothelium (or on $\Delta\pi$) and through the artery wall. To unravel the significance of such oncotic differences, we extend our transcellular filtration theory (discussed in section 2.3) and develop a model for water and small solute transport across the GX layer, across the endothelial interface and through the entire wall. This addition non-linearly couples the mass transfer, the fluid flow and the wall mechanics. The flow advects tracer into the wall while albumin differences across the endothelium set up a $\Delta\pi$ that sucks fluid back across the endothelium towards the lumen. Clearly the coupling of equations governing the water velocity with those governing species concentration makes calculations more complex. To circumvent this complexity and assuming minor contribution of osmotic effects, many researchers (93, 112, 18) have neglected the contribution of $\Delta\pi$ in their transport studies. To our knowledge, this is the first study that attempts to explore the effects of both the hydrostatic and osmotic pressure differences on the transport across the walls of larger blood vessels. Our approach is to solve the combined steady state filtration and mass transfer problem as the long-time solution of a fictitious unsteady problem that we attack with finite difference methods. Note that Hu and Weinbaum (32) have also considered the effects of both of these pressures and have done similar calculations to describe the transport across microvessel walls, which have a very different structure than bigger blood vessels.

One might speculate that the surface GX layer, that acts as a filter for albumin, could drastically lower the oncotic pressure that can build up adjacent to the lumen side of the EC.

Moreover, much of the isotonic fluid crossing the endothelium enters via the EC junction, and this fluid flows parallel to the endothelium in the ultra-thin, sparse SI until it finds the IEL fenestral hole to enter the dense media. From typical radial fluid velocities in the SI ($\sim 10^{-5}$-10^{-7} cm/s) and the EC radius ($\sim$ 10-15 μm), one can estimate that the solute entering the SI from its junction spends >100s in the SI. However, since the diffusive mixing (normal to the endothelium) time in the SI is much smaller (on the order or milliseconds for typical diffusivities of 10^{-7} cm^2/s), one might expect the diffusive mixing to elevate the albumin concentration and the π adjacent to the abluminal EC membrane. The solution of the combined filtration and mass transfer model will show us if/how oncotic gradients across an EC are reduced to a level consistent with observed transendothelial flows and if the model is able to resolve the above-mentioned oncotic paradox. This model will help us estimate the true hydraulic conductivity of the endothelium by including the effects of both ΔP and $\Delta\pi$. Using the combined model, we will predict the variation in the L_P of the vessel wall with transmural pressure and compare it with the predictions from our previous filtration model that neglected the oncotic effects. This comparison will tell us to what extent oncotic gradients affect the total L_P of the vessel wall. If the effect of oncotic gradients turns out to be significant, we will further explore what happens to the concentration of albumin or to $\Delta\pi$ with AQP1 upregulation. We shall also examine the relative importance of the GX layer on the overall transport by theoretically removing it from the model and comparing the resulting water flux with that estimated in the presence of the GX. If we find appreciable change, we shall again make predictions for new experiments.

Chapter 4 of this thesis focuses on theoretically exploring AQP1's role on tracer (e.g., HRP, LDL) transport across the arterial wall. We believe that endothelial AQP up-regulation, and the resulting increase in overall transmural flow, can not only decrease tracer's local concentration in the SI region (by dilution) but also flush out unbound tracer from the SI further into the media region. Since early lesion formation is known to occur in the SI, it would be particularly interesting to see if increased water flux can indeed lower LDL's concentration in the SI region. If the theory predicts a decrease in LDL concentration upon AQP up-regulation, for the reasons mentioned

before, it would suggest a potential route to lower the progression of pre-atherosclerotic events.

To investigate the effect of intima compression (or decompression upon AQP up-regulation) on tracer transport inside the arterial wall, we will combine our local filtration theory with Zeng et al.'s (131) 2-D, wall-structure based convection-diffusion model. Zeng et al. (131) made a number of improvements over earlier mathematical studies (129, 35) that investigated macromolecular transport through an artery wall and, as mentioned earlier, successfully explained a range of available tracer transport data (13, 79). For these reasons we have employed Zeng et al.'s (131) convection-diffusion model in our study. Our approach is similar but not identical to Y. Sun's (94) in combining our local filtration and Zeng et al.'s (131) convection-diffusion model. Unlike Y. Sun (94), for a given transmural pressure and intima compression (L_i^*), we do not use the predicted $L_{P_{e+i}}$ from the local filtration model into Zeng et al.'s (131) convection-diffusion model. Note that Zeng et al. (131) combined the effects of intima compression and fenestra blockage in a lumped parameter $L_{P_{nj}}$, similar but not identical to the $L_{P_{e+i}}$ obtained from local model. Since $L_{P_{e+i}}$ is a phenomenological and not a physical parameter, we first match the water flux calculated from both models and use the corresponding value of $L_{P_{e+i}}$ (as $L_{P_{nj}}$) in Zeng et al.'s (131) tracer transport model. In addition, we use fiber matrix theory to adjust tracer transport properties, like the diffusivity (D), retardation coefficient (f) and the available solute volume fraction (γ) with intima compression, something which Y. Sun (94) did not consider. Using the two models, we should see how the tracer transport and its concentration inside the artery wall, specifically in the SI, vary with transmural pressure. More importantly, we shall test the combined theory for the effect of AQP1 expression on overall macromolecular transport at different transmural pressures and see if we find interesting outcomes that can suggest possible strategies to help lower the progression of early pre-atherosclerotic events.

Chapter 2. Aquaporin-1 affects transmural pressure-induced aortic intima compression: Mathematical models

2.1 Introduction

Atherosclerosis, a disease of large blood vessels, is believed to be responsible for more than 50% of all deaths in the United States and in most Western countries (69). Its earliest stages are thought to be the transport and accumulation of macromolecules, like low-density lipoprotein (LDL) cholesterol, from the lumen into the subendothelial intimal (SI) region of the vessel wall, where it reacts with the collagen and/or proteoglycan fibers present in the SI extracellular matrix (ECM). Lodged lipid oxidizes and appears to cause endothelial cells to recruit blood-borne monocytes that transform into macrophages (10). These macrophages can engulf oxidized LDL and, when overloaded, can become necrotic foam cells (87), the earliest observable pre-lesion event. Atherosclerotic plaque can grow to a size where it can block the entire cross-section available for blood flow or, if it is of the vulnerable variety, it can rupture; the resulting lesion debris can block smaller blood vessels downstream, causing ischemic stroke or heart attack.

Macromolecules cross the endothelial layer at specific leakage sites that correspond to rare endothelial cells ($\sim$1 in 2000-6000 cells in rat (50, 51, 52)) with junctions wide enough for an LDL particle ($\sim$ 20-25 nm) to transport through it (119). Our group has shown (129, 35) that transmural pressure-driven water flow advects macromolecules through these focal leaks into the SI and subsequently spreads them radially from the leakage site in the SI. There they have the opportunity to bind to SI ECM, which might trigger lesion formation. On the other hand, since water, plasma's major constituent, can easily pass through the tight junctions between the normal endothelial cells, which vastly outnumber the leaky ones, the transmural pressure (across the vessel wall) drives far more water flow, albeit absent macromolecules, through the normal endothelium than through the leaky junction. This pressure driven water transport together with diffusion can

further transport LDL macromolecules that have already entered the vessel wall through leaky junctions; it can dilute the local LDL concentration in the SI, thereby slowing the ECM binding reactions' kinetic rates and flushing unbound LDL from SI, and ultimately from the wall. Clearly it is critical to understand the nature of the total transmural water transport, and not just the portion through leaky junctions.

Starling's law gives the overall water flux across the vessel wall as (85): $J_v = L_P(\Delta P - \sigma\Delta\pi)$, where L_P is the hydraulic conductivity of the vessel wall, σ is the osmotic reflection coefficient, and ΔP & $\Delta\pi$ are the hydrostatic and osmotic pressure differences across the vessel wall. Neglecting the osmotic forces (since large blood vessels are universally considered isotonic (38)), $J_v = L_P \times \Delta P$. Many research groups in the past (100, 2), including ours (78, 62), have measured the hydraulic conductivities of rabbit and rat aorta *ex vivo* over a range of transmural pressures. In all of these studies, L_P was found to be higher at low transmural pressures, it decreased with increasing transmural pressure and then, beyond a certain ΔP, remained practically constant to within experimental error to very high pressures for a vessel with intact endothelium. When one de-endothelializes the same vessel, L_P doubles, but remains pressure-insensitive to within experimental error over the entire pressure range. Ultrastructure studies (24) of the arterial wall show stark differences in structure between the SI and the media. Most importantly they indicate the far sparser intima relative to the media ECM: the media is less than 50% void, whereas Huang et al. (36) calculate a SI void space of 95%. This extreme sparseness of the SI suggests the possibility of structural SI variation in response to changes in the transmural pressure, i.e., Huang et al. (36) hypothesized that increasing transmural pressure compresses the sparse SI, leading to markedly different responses, as codified by L_P, to transmural pressure. This theory posits that at low transmural pressures the SI is relatively uncompressed and allows high throughputs of water. They proposed a local model for the filtration through the fenestral pores that predicted, and their experimental work subsequently proved (37), that an increased transmural pressure indeed compacts the SI proteoglycans (PGs). SI compaction reduces the ECM's inter-fiber distances, which lowers the SI's Darcy permeability (K_P). More critically, in the region near the IEL fenestral pores, SI

compression leads to partial or total fenestral blockage. According to their theory, this inhibition of water flow through the IEL is responsible for the major portion of the observed reduction in wall hydraulic conductivity with pressure. Once the PGs are fully compressed, the stiffer collagen (CG) fibers resist any further compression and there is little variation in L_P with further increase in pressure, which explains its pressure-insensitivity there. Endothelial removal eliminates both a layer of resistance and the potential for fenestral blockage and thus explains the higher L_Ps of denuded vessels and their pressure insensitivity. Huang et al. (36) also considered the variation of Darcy permeability (K_P) with SI compaction. Their model predictions for the variation of intact vessel wall L_P agreed very well with the experimental observations of Tedgui & Lever (100) and of Baldwin & Wilson (2).

Up to this point we have focused exclusively on plasma (which we refer to as water) transport around the normal and leaky endothelial cells (paracellular flow) via normal/tight or leaky junctions, respectively. Huang et al.'s (36) SI compaction theory calculated flows and resistance based on the premise that transmural water transport occurred only through leaky and normal/tight junctions between the ECs. We now consider the possibility of another route potentially available for water transport. A membrane protein called Aquaporin-1 (AQP1), a highly water-specific channel membrane protein in otherwise hydrophobic membranes, has caused tremendous excitement in the scientific community over the last twenty years. These water channels, found in variety of endothelial, epithelial and other cells (63), allow high throughputs of water ($3x10^9$ molecules/sec/channel) in response to osmotic gradients at little or no cost in ATP (58). Using immunohistochemical techniques, our group has successfully shown the presence and distribution of AQP1 in rat and bovine aortic endothelial cells both in cultured monolayers (62) and in whole rat aortas *ex vivo* (103). This discovery suggests the new possibility of water transport through the endothelial cell via AQP1s (transcellular flow), alongside the generally accepted paracellular route. Our group has studied the effect of AQP1s on the transport properties of the vessel wall using both *in vitro* and *ex vivo* techniques (62). Very low exposures to $HgCl_2$, known to chemically block AQP1s and titrated to a level that is reversible and causes no observable artifacts, is used to block

transcellular water flow, thereby assessing the relative contribution of the transcellular route to the overall water transport. Our group has repeated these experiments, both *in vitro* (73) and on whole rat aortas *ex vivo*, using siRNA against AQP1 (126), a much more challenging procedure, particularly in the *ex vivo* setting, and found nearly identical result. Both studies showed a significant decrease in the hydraulic conductivity for the blocked-AQP case. The water flux across the $HgCl_2$ treated BAEC monolayers (blocked-AQPs) showed an average $22.1\pm6\%$ decrease (62) compared to controls (without $HgCl_2$); the siRNA numbers showed a $62.4\pm1.7\%$ drop (126) relative to control. Studies with tracers that only cross the endothelium paracellularly show that these treatments do not impede junctional transport to within measurement accuracy.

These *ex vivo* studies were carried out to measure the hydraulic conductivity of an excised vessel as a function of pressure, first with functioning AQP1s and then with chemically blocked AQP1s, using $HgCl_2$ as a blocker (or with AQP1s knocked down), on the same vessel. The major contribution of AQP1s in the transmural water transport is clearly evident from the statistically significant decreases in the intact vessel's L_P of $\sim 32\pm4\%$, $11\pm2\%$ & $5\pm3\%$, for blocked AQP1s, at 60,100,140 mmHg respectively (62), with very similar results for the siRNA studies (126). Since the wall's total resistance to flow, $1/L_P$, is the sum of the resistance of the endothelium plus SI and that of the media plus IEL, resistance in series, one can calculate that these percentage decreases in total wall L_P correspond to drops in the endothelial L_P of $56\pm4\%$, $21\pm2\%$ and $11\pm3\%$, respectively, at these three pressures. Clearly AQP1-mediated transcellular flow contributes significantly to endothelial L_P. However it is confounding that this percentage decrease is apparently strongly pressure-dependent, which would not be the case for a simple material. In particular, whereas L_P in the absence of blocker is, as noted, pressure dependent at low pressures, when the AQP1s are blocked, the hydraulic conductivity turns out to be pressure independent at these lower pressures. Reasoning from the theory of Huang et al.'s (36), one is tempted to guess that, whereas in the absence of blocker, the SI reaches full compression somewhere between 80 and 100 mmHg, in the presence of blocker, the SI might fully compress at the lower pressure of 60 mmHg. That is, we might guess that AQP1-blocking or knockdown may lead to premature SI compaction at a lower

overall ΔP.

This Chapter proposes to extend Huang et al.s (36) local filtration theory by including transcellular flow, in order to test the possibility that AQP1 blocking or knockdown can indeed compact the SI at a lower ΔP. Specifically, we hypothesize that decreasing the number of functioning EC AQP1s will decrease the number of available pathways for water transport, thereby decreasing the intrinsic endothelial hydraulic conductivity L_{P_e} and SI pressure (P_i^*) at fixed ΔP. A Lower L_{P_e} increases the force per unit area $(P_L^* - \bar{P}_i^*)$ acting on the endothelium, which compresses the SI and leads to IEL fenestral blockage at lower overall ΔP. This scenario would explain the observed pressure-dependent effect of AQP blocking on vessel wall Ł$_P$. We shall compare the results of this theory with Nguyen's (62) experimental data.

Section 2.2 explains the filtration model proposed by Huang et al. (36). We first present and solve the governing set of coupled partial differential equations both analytically (in an approximate sense as explained by Huang et al. (36)) and with a full numerical finite difference implementation of the exact problem and find the pressure distributions in both the SI and media. In the former, we obtain analytical infinite sum solutions of the filtration problem in each region and, because of the complexity of the exact pressure and velocity continuity matching conditions in the fenestral hole, we match these solutions using approximate fenestral boundary conditions. In contrast, the new numerical finite difference solution implements the exact fenestral boundary conditions. With it we evaluate the quality of Huang et al.'s (36) approximate solutions, which we have reproduced. Section 2.3 then extends Huang et al.'s (36) model by incorporating transcellular flow. It compares the model's predicted hydraulic conductivities with experimentally observed data from our group and makes other predictions for future experiments.

Glossary:

a^*	Effective radius of proteoglycan aggregates
h_j	Ratio of thickness of region j to radius of fenestral pore
j	Region of artery wall ($j = g, i, m$ for GX, SI and Media respectively)
J_v	Water flux
k	Elastic coefficient of SI
K_{P_j}	Darcy permeability of region j

L^*_{i0}	Thickness of SI at zero luminal pressure
L^*_{ic}	Critical thickness of SI layer
L^*_j	Thickness of region j
L_p	Hydraulic conductivity
L_{p_e}	Intrinsic hydraulic conductivity of the endothelium
$L_{p_{EC}}$	Hydraulic conductivity of the endothelium attributed to its AQPs
$L_{p_{e+i}}$	Hydraulic conductivity of the endothelium + SI
L_{p_i}	Hydraulic conductivity of SI
L_{p_I}	Hydraulic conductivity of IEL
L_{p_m}	Hydraulic conductivity of media
$L_{p_{m+I}}$	Hydraulic conductivity of IEL + media
$L_{p_{nj}}$	Hydraulic conductivity of normal junction surrounding an EC
L_{p_t}	Total hydraulic conductivity of the vessel wall
P^*_j	Dimensional pressure in region j
P_j	Dimensionless pressure in region j
$\bar{P}^*_j$	Dimensional average pressure in region j
$\bar{P}_j$	Dimensionless average pressure in region j
P^*_L	Lumen pressure
P^*_{Lc}	Dimensional critical pressure
r	Dimensionless radial coordinate
r^*	Dimensional radial coordinate
r^*_f	Radius of fenestra
U^*_j	Dimensional lateral velocity in region j
U_j	Dimensionless lateral velocity in region j
R^*	Dimensional radius of EC
R	Dimensionless radius of EC
$\mathbf{V}$	Velocity vector
W^*_f	Dimensional water velocity through fenestra
W_j	Dimensionless normal velocity in region j
z	Dimensionless normal coordinate
z^*	Dimensional normal coordinate
ΔR^*	Dimensional width of normal junction
ΔR	Dimensionless width of normal junction
ΔP	Dimensionless pressure drop across a membrane
$\Delta\pi$	Dimensionless osmotic pressure difference across a membrane
μ	Viscosity of fluid
ξ^*_I	Dimensional radius of periodic wall unit
ξ_I	Dimensionless radius of periodic wall unit

Table 2.1: Measured hydraulic conductivity with and without endothelium in rabbit and rat aortas

Data	Pressure	Hydraulic Conductivity $\times 10^8$ (cm/s·mmHg)	
	(mmHg)	Intact endothelium	Denuded endothelium
Tedgui & Lever (100)	70	4.00±1.31	5.36±1.62
	180	2.44±0.80	5.27±0.84
Baldwin & Wilson (2)	50	7.42±4.00	7.41±4.08
	75	4.14±1.67	10.19±1.91
	100	4.54±0.89	10.00±2.20
	125	4.26±0.51	9.66±2.20
	150	5.00±0.66	10.53±2.83
Shou et. al. (78)	60	4.69±1.2	5.35±1.46
	80	3.02±1.34	5.01±2.05
	100	2.79±0.72	4.89±1.01
	120	2.6±0.73	4.76±1.46
	140	2.68±0.49	5.05±1.22
T. Nguyen (62)	60	2.547±0.361	4.055±0.277
	100	1.842±0.142	3.44±0.757
	140	2.102±0.23	3.864±0.371

values are mean ± SD

Table 2.2: Nguyen's data (62): Effect of AQP blocking on hydraulic conductivity of intact artery wall

Pressure (mmHg)	Hydraulic Conductivity, L_{P_t} $\times 10^8$ (cm/s·mmHg)	
	Unblocked AQPs	Blocked AQPs
60	2.547±0.36	1.736±0.35
100	1.842±0.14	1.64±0.16
140	2.102±0.23	1.995±0.28

values are mean ± SD

2.2 Filtration model: Paracellular flow

2.2.1 Model Description

Since the transport of macromolecules across the arterial wall is convection dominated, it is critical to understand the transmural water flow in detail. As noted in the previous section, water can enter the SI via the paracellular pathway, through both the tight and the far more numerous normal junctions and, due to the evidence noted above, through the transcellular pathway via AQP1s, as well. In this section we shall consider only the paracellular route. In the next section we will extend this model to include the transcellular pathway as well.

The transmural pressure, defined as the pressure difference between inside (lumen) and outside (adventitia) of the vessel, drives water through the glycocalyx (GX) layer on the luminal surface of the ECs into the SI through the intercellular junctions along the EC's perimeter. It then flows laterally (i.e., parallel to the endothelium) in the SI and enters the media through the fenestral openings in the IEL. SI compression at increased pressure narrows the cross-section for this lateral SI flow and causes the endothelium to partially or totally block the IEL fenestral entrance. The decreasing SI K_P and this alteration in flow, might lead to significant pressure gradients in the SI that can radically change the head losses incurred in traversing the SI and the IEL fenestrae. Thus, in order to understand the effect of SI compaction on the SI and fenestral flow, we consider

a local (on the scale of a single EC) model for SI flow into and through the fenestral hole. The model considered in this section is exactly that considered by Huang et al. (36) except for the consideration of the EC surface GX layer.

Figure 2.1 shows a representative local periodic wall unit of a circular cylinder of radius ξ_I^*=(R* + ΔR*/2), where R^* is the radius of an assumed round EC and ΔR^* is the width of normal intercellular junction or cleft. A round fenestral pore of radius r_f^* is ideally placed at the unit's center and a fluid source along the wall unit's perimeter represents the normal endothelial cell junction. This model considers a cell having normal tight junctions with its neighbors and the problem of water flow entering the SI through these normal clefts, as normal junctions vastly outnumber the leaky clefts by a factor of 2000-6000 and thus account for the overwhelming majority of water flow across the endothelium. Figure 2.1 greatly exaggerates the vertical scale of the SI, which is of the order of 0.2-0.5 μm in healthy rat aorta and the placement of fenestra beneath the center of the cell is also an obvious idealization. Note that experimental data (66) indicate that the number of fenestrae is between 0.1 and 10 times the number of ECs; we take an average number of one fenestra per EC (as in (36)), and locate it concentrically with the EC, which keeps the problem axisymmetric. The intima under the assumed non-deformable endothelium can be compressed upon pressure loading from L_{i0}^* (initial thickness at zero transmural pressure) to L_i^*. The IEL is treated as an impenetrable barrier of zero thickness except for its fenestral openings and any non-uniform deformation of the endothelium due to spatial differences in the transendothelial pressure is neglected. Due to the high density of the media, our model presumes that it does not undergo any compression upon pressure loadings and its filtration properties (e.g., Darcy permeability) are assumed to be uniform.

2.2.2 Mathematical formulation

Let j be a dummy index that takes values g for GX, i for SI and m for media, respectively. Let U_j^*, W_j^* be the dimensional lateral and normal velocities in the r and z directions of cylindrical coordinates and P_j^*, K_{P_j} be the pressure and Darcy permeability, respectively, in region j of thick-

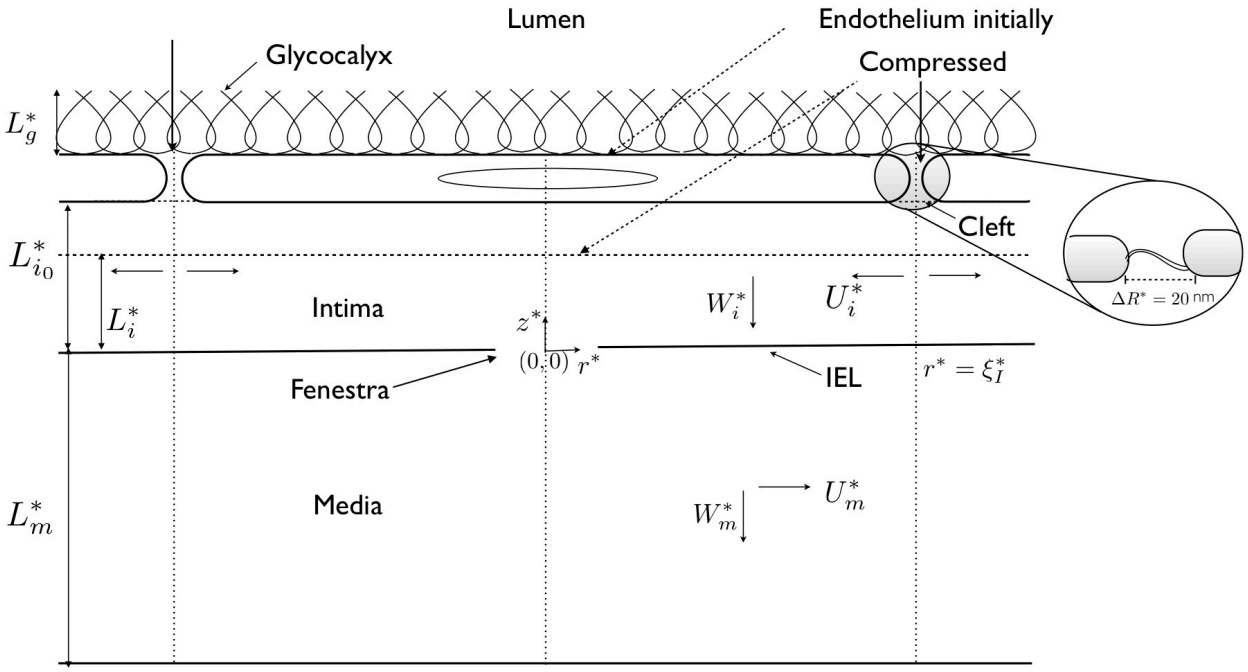

Figure 2.1: Schematic of periodic local wall unit around a fenestral pore. Intima under non-deformable endothelium is compressible; L_{i0}^*, intima thickness at zero transmural pressure, L_i^*, compressed intima thickness; water enters intima through clefts surrounding EC; see Glossary for definition of other abbreviations.

ness L_j^*. We neglect pressure pulsatility; thus let the time-invariant lumen pressure be P_L^*. We introduce the following non-dimensional (without superscript *) variables and parameters:

$$r = \frac{r^*}{r_f^*}, \qquad \xi_I = \frac{\xi_I^*}{r_f^*}, \qquad R = \frac{R^*}{r_f^*}, \qquad \Delta R = \frac{\Delta R^*}{r_f^*}, \qquad z_j = \frac{z_j^*}{L_j^*}$$

$$P_j = \frac{P_j^*}{P_L^*}, \qquad U_j = \frac{U_j^*}{\frac{K_{P_j}}{\mu}\frac{P_L^*}{r_f^*}}, \qquad W_j = \frac{W_j^*}{\frac{K_{P_j}}{\mu}\frac{P_L^*}{L_j^*}}$$

The continuity equations, in non-dimensional form, for the three regions are:

$$h_j^2\left(\frac{\partial U_j}{\partial r} + \frac{U_j}{r}\right) + \frac{\partial W_j}{\partial z_j} = 0 \quad (j = g, i, m) \tag{2.1}$$

where $h_j = \dfrac{L_j^*}{r_f^*}$ are the ratios of the thicknesses of the three regions to the radius of a fenestral pore. The water flow across the arterial wall through the SI, made up of ECM of PG and CG fibers, and the media which consists of smooth muscle cells (SMC), ECM and elastic layers, can be modeled as porous media flows governed by Darcy's law: $\mathbf{V} = \dfrac{-K_P}{\mu}\nabla P$ with an effective Darcy permeability for each region. We choose to use Darcy, rather than Brinkman's equation because it does not seem consistent to explicitly enforce no slip on the region boundaries when simultaneously lumping the no-slip on the far more ubiquitous fibers, elastic layers and cells into the bulk parameters K_{P_j}. Thus, Eq. 2.1 become:

$$h_j^2\left(\frac{\partial^2 P_j}{\partial r^2} + \frac{1}{r}\frac{\partial P_j}{\partial r}\right) + \frac{\partial^2 P_j}{\partial z_j^2} = 0 \quad (j = g, i, m) \tag{2.2}$$

The boundary conditions (in non-dimensional form) for this system of coupled PDEs are:

(a) The axisymmetry at $r = 0$ and periodicity at $r = \xi_I$ require:

$$\frac{dP_j}{dr} = 0 \text{ at } r = 0 \text{ and } r = \xi_I \quad (j = g, i, m) \tag{2.3}$$

(b) The pressure at the top of the GX layer equals the lumen pressure:

$$P_g = 1 \text{ at } z_g = 1 \tag{2.4}$$

(c) The adventitia is assumed to be at the reference pressure, thus

$$P_m = 0 \text{ at } z_m = -1 \tag{2.5}$$

(d) Mixed boundary conditions at the GX/EC boundary $(z_i = 1)$: The endothelium is assumed to be impermeable to water (this assumption is relaxed in the next section). The amount of water entering the SI through normal junctions is governed by the hydraulic conductivity of the normal junction $(L_{P_{nj}})$ and the pressure difference across it.

(d1) On the EC: $(0 < r \leq R)$

$$\frac{dP_j}{dz_j} = 0 \quad (j = g, i) \tag{2.6}$$

(d2) Inside the normal junction: $(R < r \leq \xi_I)$

$$W_g = W_i \tag{2.7}$$

$$-W_i = \frac{L_{P_{nj}} \mu L_i^* (P_g - P_i)}{K_{P_i}} \tag{2.8}$$

Note that, in previous studies (131), $L_{P_{nj}}$ is used to describe the area averaged hydraulic conductivity of the endothelium, equivalent to our L_{P_e} in this local model. Here we allow only junctional water transport, and so our L_{P_e} and $L_{P_{nj}}$ are related by the ratio of junctional to total endothelial areas; the next section includes a separate transcellular contribution, and both will contribute to an area averaged L_{P_e}.

(e) Mixed boundary conditions at the SI/media boundary $(z_i = 0)$: The IEL is assumed to be an impenetrable barrier except for its fenestral openings. Thus, water enters the media only through the fenestra where pressures and velocities are continues. This requires

(e1) In the fenstral hole: $(0 < r \leq 1)$

$$P_i = P_m \tag{2.9}$$

$$W_i = W_m \tag{2.10}$$

(e1) Outside the fenstral hole: $(1 < r \leq \xi_I)$

$$\frac{dP_j}{dz_j} = 0 \quad (j = i, m) \tag{2.11}$$

The model developed by Huang et al. (36) did not consider the effect of GX that ideally covers the luminal side of EC. Also, instead of periodicity at $r = \xi_I$ in the SI region (Eq. 2.3), they had assumed a ring source trough an endothelial cleft and the unknown pressure P_0 at $r = \xi_I$ was obtained by imposing the incompressibility of flow. So neglecting the GX region and reducing the model to exactly that given in Huang et al. (36), one can obtain the analytical solution of Eq. 3.2 in terms of infinite sums of zero order Bessel functions (J_0). The general solutions for pressure in the SI and media region are:

$$P_i(r, z_i) = P_0 \, + \, P_0 \sum_{n=1}^{\infty} \left(A_n \, \frac{\cosh[\, h_i \, \sqrt{\lambda}_n \, (z_i - 1) \,]}{\cosh(h_i \sqrt{\lambda}_n)} \cdot J_0(\sqrt{\lambda}_n \, r) \right) \tag{2.12}$$

$$P_m(r, z_m) = P_0(z_m + 1)C_0 \, + \, P_0 \sum_{p=1}^{\infty} \left(C_p \, \frac{\sinh[\, h_m \, \sqrt{\lambda}_p \, (z_m + 1) \,]}{\sinh(h_m \sqrt{\lambda}_p)} \cdot J_0(\sqrt{\lambda}_p \, r) \right) \tag{2.13}$$

where, λ_n and λ_p are the roots of the eigen value equations $J_0(\sqrt{\lambda}_n \, \xi_I) = 0$ (n = 1, 2, 3,.,∞) and $J_1(\sqrt{\lambda}_p \, \xi_I) = 0$ (p = 1, 2, 3,.,∞). The constants A_n and C_p in above solutions depend on the

boundary condition used in the fenestra. Huang et al. (36) employed following three approximate boundary conditions (in non-dimensional form) inside the fenestra region and Fig. 2.2 shows their effect on the pressure distribution.

(i) The z- velocity, (W_f), in the fenestra is constant and the pressures in the SI and media match only at the centerline i.e., $P_i = P_m$ at (r, z = 0)

(ii) W_f is constant and only the average pressure, ($\bar{P_i}$ = 2 $\int_0^1 P(r) r dr$), across the fenestra matches in the fenestral hole i.e., $\bar{P_i} = \bar{P_m}$ at $0 < r \leq 1$, $z = 0$

(iii) At $z = 0$, $W_f(r)$ fits a cubic polynomial that satisfies dW_f/dr=0 at r=0 and the pressure is continuous at r= 0, 0.5, 0.9 i.e.,

$W_f = (a_0 + c_0 r^2 + d_0 r^3) P_0$ and $P_i = P_m$ at $r = 0, 0.5, 0.9$; $z = 0$

2.2.3 Exact numerical solution of the boundary value problem:

We adopt a direct-discretization finite difference approach to solve the system of coupled PDEs (Eq. 3.2). Though the governing equations for the filtration problem are simple Laplace equations, the mixed boundary conditions (Eqs. 2.3-2.11) make it very difficult to obtain an exact analytical solution. This numerical method, in principle, allows us to use the exact boundary conditions as opposed to the approximate ones employed by Huang et al. (36). Since the thickness of the SI region (L_i^*) and the radius of the fenestral hole (r_f^*) are both small compared to both the radius of wall unit (ξ_I^*) and the length of media region (L_m^*), we use non-uniform grids in the r and z directions. We expect a steep pressure gradient near the fenestral hole and thus form a very dense grid near the hole with the smallest non-dimensional grid size (r^*/r_f^*) of 0.0005 (non-dimensional r, z_g, z_i and z_m vary from 0 to 15.0125, 0 to 1, 0 to 1 and 0 to -1, respectively) in the fenestral hole. Moreover, in order to resolve the pressure variations in the normal junction (width = 20

nm), we use extremely small grid near the junction with the smallest grid size being 8×10^{-10}. Since the coefficients $(L_i^*, L_m^*, K_{P_i}, K_{P_m})$ in the velocity matching condition (Eq. 2.10) differ by several orders of magnitude between regions being matched (see Sec. 2.2), one has to be very careful in selecting the mesh sizes in the z-directions near the fenestral hole. If the mesh size is not sufficiently small, the finite difference approximations used for the derivative dP/dz might lead to significant errors there. We chose the smallest grid size near the hole in SI and media to be 0.0005 and 0.000001 respectively. Similarly, the smallest grid sizes used in the z-directions close to the endothelial cell boundary are 0.0005 and 0.00006 in the SI and GX regions. The governing equations are discretized using following central difference formulae for non-uniform meshing:

$$\frac{\partial f}{\partial r}\Big|_i = \frac{f_{i+1} - f_{i-1}}{x_i + x_{i-1}}$$

$$\frac{\partial^2 f}{\partial r^2}\Big|_{i,j} = \frac{x_{i-1}f_{i+1,j} - (x_i + x_{i-1})f_{i,j} + x_i f_{i-1,j}}{\frac{1}{2}x_i x_{i-1}(x_i + x_{i-1})}$$

$$\frac{\partial^2 f}{\partial z^2}\Big|_{i,j} = \frac{y_{j-1}f_{i,j+1} - (y_j + y_{j-1})f_{i,j} + y_j f_{i,j-1}}{\frac{1}{2}y_j y_{j-1}(y_j + y_{j-1})}$$

where, $x_i = r_{i+1} - r_i,\ y_j = z_{j+1} - z_j$

The boundary conditions are discretized using second order difference formulae. This discretization procedure leads to a linear system of algebraic equations whose number equals the total number of mesh points. We solve the set of equations representing the three domains simultaneously using Matlab (Mathworks Inc). In order to test the accuracy of the solution, we adopt a successive mesh-refinement procedure until the difference between two consecutive computations is in the fourth significant digit.

Table 2.3: Parameters and constants used in the model

Constant/Paramteter	Value	Reference
a^*, nm	2.37	a
L_g^*, nm	200	(132)
L_{i0}^*, nm	500	(36)
L_m^*, μm	141(rat), 125(rabbit)	(36, 78)
R^*, μm	12	(123)
r_f^*, μm	0.8	(36)
ΔR^*, nm	20	(123)
K_{P_g}, cm^2	4.08×10^{-14}	b
K_{P_i}, cm^2	2.20×10^{-12}	(36),c
δ_{CG}, nm	170.35	d
δ_{PG}, nm	40	(36)
ϵ_{CG0}	0.95	(35)
ϵ_{PG0}	0.9883	a
μ, kg/m $\cdot$ sec	7.2×10^{-4}	(31)

a: calculated using the fiber matrix theory and as explained in (35)

b: estimated as explained in the text

c: uncompressed SI value at zero transmural pressure, corresponding values for compressed SI (L_i^*) are calculated as explained in the text and in Ref. (36)

d: calculated by assuming hexagonally packed collagen fibers of radius 20 nm (35) with initial volume fraction of 5% (35)

2.2.4 Constants and Parameters

Geometric parameters:

Most of the parameters used in this study are adopted from Huang et al. (36) and are given in table 2.3. Huang et al. (35) extracted from Frank and Fogelman's (24) freeze etchings that the average spacing, δ_{PG}, between PG fibers is approximately 30-40 nm. We use δ_{PG0} = 40 nm for the relaxed intima. Huang et al. (35) developed a fiber matrix theory to calculate the effective radius (a^*) of the PGs and the initial (at zero transmural pressure) void fraction (ϵ_{PG0}) for the PGs. We use Huang et al.'s (35) theory and estimate a^* and ϵ_{PG0} to be 2.37 nm and 98.83%, respectively. Using

these estimated numbers, one can calculate the Darcy permeability of a fiber matrix of PGs in the SI using the Carman-Kozeny expression (15, 16, 17) as:

$$K_{P_{(PG)}} = \frac{{a^*}^2\, \epsilon_{PG0}^3}{4\, G\, (1 - \epsilon_{PG0}^2)}$$

where G (the Kozeny constant) is obtained as explained in Ref. (29). The spacing δ_{CG0} between collagen fibers of radius 20 nm (35), assumed to form a parallel, triangular array of fibers with an initial volume fraction (ϵ_{CG0}) of 5% (35), is calculated to be 170.35 nm. Tsay and Weinbaum's correlation (106) gives the Darcy permeability of collagen matrix $K_{P_{(CG)}}$ in terms of fiber radius and the average fiber spacing as:

$$\frac{K_{P_{(PG)}}}{K_{P_{(CG)}}} = \left(\frac{r_{CG}^*}{a^*}\right)^{0.377} \left(\frac{\delta_{PG0} - 2a^*}{\delta_{CG0} - 2r_{CG}^*}\right)^{2.377}$$

We assume that the resistances due to the PG and collagen fiber populations act as resistors connected in series and thus compute the overall Darcy permeability of the SI region (K_{P_i}) as (49):

$$\frac{1}{K_{P_i}} = \frac{1}{K_{P_{(PG)}}} + \frac{1}{K_{P_{(CG)}}}$$

At zero transmural pressure, we calculate K_{P_i} as 2.20×10^{-12} cm^2, in agreement with Huang et al. (36). Since the SI undergoes compression upon pressure loadings, as evidenced by Huang et al. (37), the void fractions of PG (ϵ_{PG}) and CG fibers (ϵ_{CG}) are functions of transmural pressure via the intima thickness (L_i^*) as:

$$\epsilon_{PG} = 1 - \frac{L_{i0}^*}{L_i^*}(1 - \epsilon_{PG0}) \tag{2.14}$$

$$\epsilon_{CG} = 1 - \frac{L_{i0}^*}{L_i^*}(1 - \epsilon_{CG0}) \tag{2.15}$$

At a given compression, one can calculate the PG and CG void fractions and estimate the average spacing between these fibers, assuming they form a parallel, triangular array. Using these estimated

spacing, we compute K_P of the compressed intima as explained above. As shown by Huang et al. (36), we found that K_{P_i} decreases rapidly as the intima starts compressing with pressure loading. K_{P_i} at $L_i^* = 0.2L_{i0}^*$ and $L_i^* = 0.1L_{i0}^*$ are one (2.06×10^{-13} cm^2) and approximately two orders of magnitude (4.7×10^{-14} cm^2) lower than it's uncompressed value, respectively. This drastic change in K_P significantly affects the pressure and velocity distributions in the vicinity of the fenestra, as explained in the results section.

The major constituents of the GX layer that covers the luminal side of the EC are PGs with their glycosaminoglycan side chains and glycoproteins (97). Recent observations of Squire et al. (84) and Weinbaum et al. (122) suggested a bush-like structure for the GX layer with clusters of core proteins projecting normally from the EC surface. We model the GX layer as a fiber matrix with a Darcy permeability (K_{P_g}) defined as (106):

$$K_{P_g} = 0.0572\, a_f^2 \left(\frac{\Delta}{a_f}\right)^{2.377}$$

where a_f is the fiber radius (6 nm, (84)) and Δ is the open spacing between fibers (8 nm, (84)). Using these parameters, we compute K_{P_g} as 4.08×10^{-14} cm^2. Using Δ =20 nm, Dabagh and coworkers (18) calculated K_{P_g} as 3.6×10^{-13} cm^2. Assuming a regular 2-D hexagonal arrangement, we can compute the fiber volume fraction to be 0.326 and thus a void fraction of 0.674. With this void fraction and using Zhang et al.'s (133) relation between fiber radius, void fraction and the radius of fluid annulus, Liu et al. (53) estimated K_{P_g} as 6.04×10^{-14} cm^2. Seki and coworkers (92) calculated the Darcy permeability of the GX layer considering a flow perpendicular and parallel to the hexagonal array of cylindrical fibers as 3.16×10^{-14} cm^2 and 6.10×10^{-14} cm^2, respectively. Our value for K_{P_g}, mentioned above, lies in this range. Further, we assume that, since the GX lies between the lumen and the EC, increasing lumen pressure does not affect the GX layer and its structural properties are presumed to remain constant at all pressures.

Hydraulic conductivities:

As described in section 2.1, the hydraulic conductivity (L_P) is a crude, unit operations level linear proportionality that relates the driving pressure difference to the fluid velocity response that is constant for simple materials. In this problem we are concerned with the L_P's of the endothelium, the normal junction, SI, IEL, media, endothelium + SI, IEL + media, and total arterial wall, denoted as: L_{P_e}, $L_{P_{nj}}$, L_{P_i}, L_{P_I}, L_{P_m}, $L_{P_{e+i}}$, $L_{P_{m+I}}$, L_{P_t}, respectively. $L_{P_{m+I}}$ is the hydraulic conductivity of the denuded vessel representing the contributions of the IEL and the media. Tedgui & Lever (100) and Baldwin & Wilson (2) experimentally measured intact and denuded vessel hydraulic conductivities for rabbit aorta over a range of transmural pressure, while Shou et al. (78) and Nguyen et al. (62) did the analogous set of experiments on rat aortas. The latter three groups did measurements at all pressures and for the intact and denuded vessel, all on each vessel. These experimental measurements give us the values for L_{P_t} and corresponding $L_{P_{m+I}}$. $L_{P_{e+i}}$ is a phenomenological value derived from experiment: Just as for electrical resistances, we can consider the inverse of hydraulic conductivity $(1/L_P)$ as a form of a specific resistance offered by each layer of an arterial wall and assuming that the resistances of adjacent layer add as resistors connected in series, we have:

$$\frac{1}{L_{P_t}} = \frac{1}{L_{P_{e+i}}} + \frac{1}{L_{P_{m+I}}} \tag{2.16a}$$

$$\frac{1}{L_{P_{e+i}}} = \frac{1}{L_{P_e}} + \frac{1}{L_{P_i}} \tag{2.16b}$$

$$\frac{1}{L_{P_{m+I}}} = \frac{1}{L_{P_m}} + \frac{1}{L_{P_I}} \tag{2.16c}$$

Note that $K_{P_m} = L_{P_m} \times \mu \times L_m^*$, where μ is the viscosity of water and L_m^* is the thickness of media, which is 125 μm and 141 μm for rabbit and rat aorta respectively. Note that the rat aorta's media is the thicker one. This is because Shou et al. (78) measured the rat aortic thickness from vessels fixed after excision rather than measuring it by in situ fixation. In case of in situ

Table 2.4: Converged L_{P_m} values

Data	$L_{P_m} \times 10^8$ (cm/s·mmHg)
Tedgui & Lever (100)	11.00
Baldwin & Wilson (2)	19.87
Shou et. al. (78)	10.37
T. Nguyen (62)	7.50

fixation the vessel is still tethered and is in a stretched state inside the animal. Once excised, this stretching is released, the vessel retracts and, by mass conservation, becomes thicker. At steady state the water flow across each arterial layer must be the same. Thus, as explained by Huang et al. (36), by matching water fluxes across the IEL and using Eqs. 20 and 21 from Ref. (36) with the average $L_{P_{m+I}}$ for each data set given in table 2.1, we obtain $L_{P_m} = 11{\times}10^{-8}\ \mathrm{cm/sec \cdot mmHg}$ for Tedgui & Lever's data (100). This gives us K_{P_m} as $8.38{\times}10^{-15}\ \mathrm{cm}^2$, which is very close to $6.09{\times}10^{-15}\ \mathrm{cm}^2$ used by Tada et al. (96). The calculated values of L_{P_m} for other data sets are listed in table 2.4.

The pressure-independent intrinsic hydraulic conductivity of the endothelium L_{P_e} is also an unknown quantity. We assume that at very low pressures the intima is fully expanded and there is no fenestral blocking. As a result the combination of SI K_P and the squeezing flow into the IEL fenestra should yield only a negligible resistance. Thus, one can fix an estimate of the value of L_{P_e} by using the least compressed intima configuration for which experimental L_{P_t} data is available. One then calculates its $L_{P_{e+i}}$ by employing flow incompressibility, i.e., the overall water flow across the vessel wall must match the water flow across the endothelium as well as across the IEL, as:

$$L_{P_{e+i}} \left(\bar{P}_g|_{z_g=0} - \bar{P}_i|_{z_i=0}\right) \pi \xi_I^2 = \frac{2\pi K_{P_i}}{\mu\, L_i^*} \int_0^1 \left.\frac{dP_i}{dz_i}\right|_{z_i=0} r dr \tag{2.17}$$

where,

$$\bar{P}_g|_{z_g=0} = \frac{2}{\xi_I^2} \int_0^{\xi_I} \left. P_g \right|_{z_g=0} r dr \quad \text{and} \quad \bar{P}_i|_{z_i=0} = \frac{2}{\xi_I^2} \int_0^{\xi_I} \left. P_i \right|_{z_i=0} r dr \tag{2.18}$$

Table 2.5: Converged L_{P_e} values

Data	$L_{P_e} \times 10^8$ (cm/s·mmHg)
Tedgui & Lever (100)	16.41
Baldwin & Wilson (2)	35.80
Shou et. al. (78)	16.52
T. Nguyen (62)	8.29

Therefore, using Eqs. 2.16b and 2.17, one can obtain $L_{P_e} \geq L_{P_{e+i}}\big|_{\Delta P(min)}$. This approach is in the same spirit as that in (36), but is slightly more complicated because of the presence here of the GX layer.

To begin this calculation, we assume a value of the hydraulic conductivity of the normal junction $L_{P_{nj}}$, solve the whole system numerically using boundary conditions (Eqs. 2.3-2.11) and compare the calculated $L_{P_{e+i}}$ from Eq. 2.17 with the corresponding experimental value obtained using Eq. 2.16a and the data listed in Table 2.1. This procedure is repeated until the numbers from both experimental and model calculations match. $L_{P_{nj}}$ is nothing but the measured L_{P_e}, area-corrected to the junctions and can be expressed as:

$$L_{P_e} = \frac{L_{P_{nj}}\, 2\pi R^* \left(\Delta R^*/2\right)}{\pi \xi_I^{*2}}$$

Table 2.5 give the converged results for L_{P_e} for available experimental data. We use these converged values of L_{P_e} or ($L_{P_{nj}}$) for all our further calculations and predictions.

One test of the model it to use it to compute the total hydraulic conductivity (L_{P_t}) of the vessel wall and to compare these model predictions with experimental L_P data. An obvious way to find (L_{P_t}) is to use $L_{P_{e+i}}$ from Eq. 2.17 and to insert it into Eq. 2.16a with an averaged value of $L_{P_{m+I}}$ from the corresponding experimental data, as done in (36). The problem with this method is that $L_{P_{m+I}}$ does not enter into the calculation directly (other than in determining the bulk parameter K_{P_m}). The calculation yields a media pressure field from which one can use a balance to calculate a phenomenological $L_{P_{m+I}}$ needed for Eq. 2.16a at each ΔP, which neither needs to

be equal the averaged experimental value used to calculate K_{P_m} nor even to be ΔP-independent. In fact, $L_{P_{m+I}}$ calculated directly from the model turns out to be nearly constant at lower pressures, but it decreases significantly at higher transmural pressures. A better method for finding the fully model-generated value for L_{P_t} is to again appeal to incompressibility by equating the calculated velocities with the L_{P_t} expression for the total flow across the wall, i.e.,

$$L_{P_t}\,\pi\xi_I^2 = \frac{2\pi K_{P_i}}{\mu\, L_i^*}\int_0^1 \frac{dP_i}{dz_i}\Big|_{z_i=0} r dr \tag{2.19}$$

2.2.5 Results and discussion

Pressure drop across IEL:

Figures 2.2 and 2.3 depict the pressures, non-dimensionalized by the luminal pressure P_L^* (the adventitial pressure is taken to be zero), as a function of r^*/r_f^* for various given intimal compressions. They predict the pressure distributions above and below the IEL obtained using both the analytical series solution (Fig. 2.2) with Huang et al.'s (36) approximate boundary conditions described in section 2.2.2 and the finite difference solution that employs the exact boundary conditions (Fig. 2.3). These figures neglect the GX layer so as to facilitate comparison with Huang et al.'s (36) GX-free model. For the predictions shown in Fig. 2.3, we use the ring source at the normal junction instead of Eqs. 2.7 and 2.8, exactly as in Hunag et al. (36). Clearly, the finite difference solution gives us proper pressure (and flow rate) matching in the fenestral hole $(r^*/r_f^* \leq 1)$ region. Both figures show that the pressure decreases from the edge of wall unit to the center on the intimal side as the fluid approaches the fenestral hole and then decreases as r increases on the media side as the fluid exiting the fenestra spreads in the media. Both sets of curves display a qualitative change in the behavior of the pressure as the thickness of the intima decreases in response to an increasing transmural pressure. For L_i^* >200 nm, the pressure profile in the intima is almost flat and most of the pressure drop occurs in media. However, as the intima thins with increasing transmural pressure, say at L_i^* = 50 nm, most of the pressure drop shifts to the intima in a region of several pore radii from the fenestral opening. Thus the flow resistance shifts with pressure from the spreading

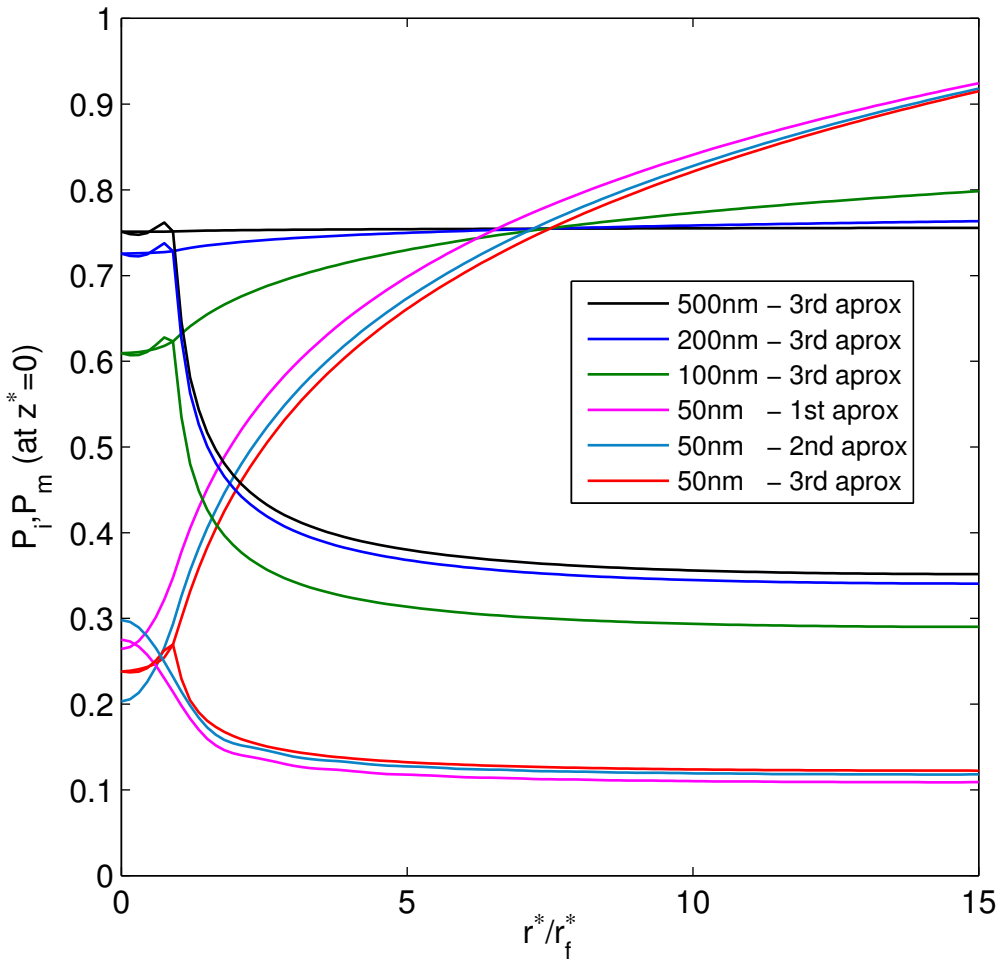

Figure 2.2: Local pressure distributions on the intimal side (P_i: the upper curve of a given color) and the medial side (P_m: the lower curve of a given color) of IEL for different intima thicknesses using Tedgui and Lever's (100) data with Huang et al.'s (36) approximate boundary conditions. L_{P_m} and L_{P_e} are given in tables 2.4 and 2.5, respectively; see Glossary for definition of other abbreviations.

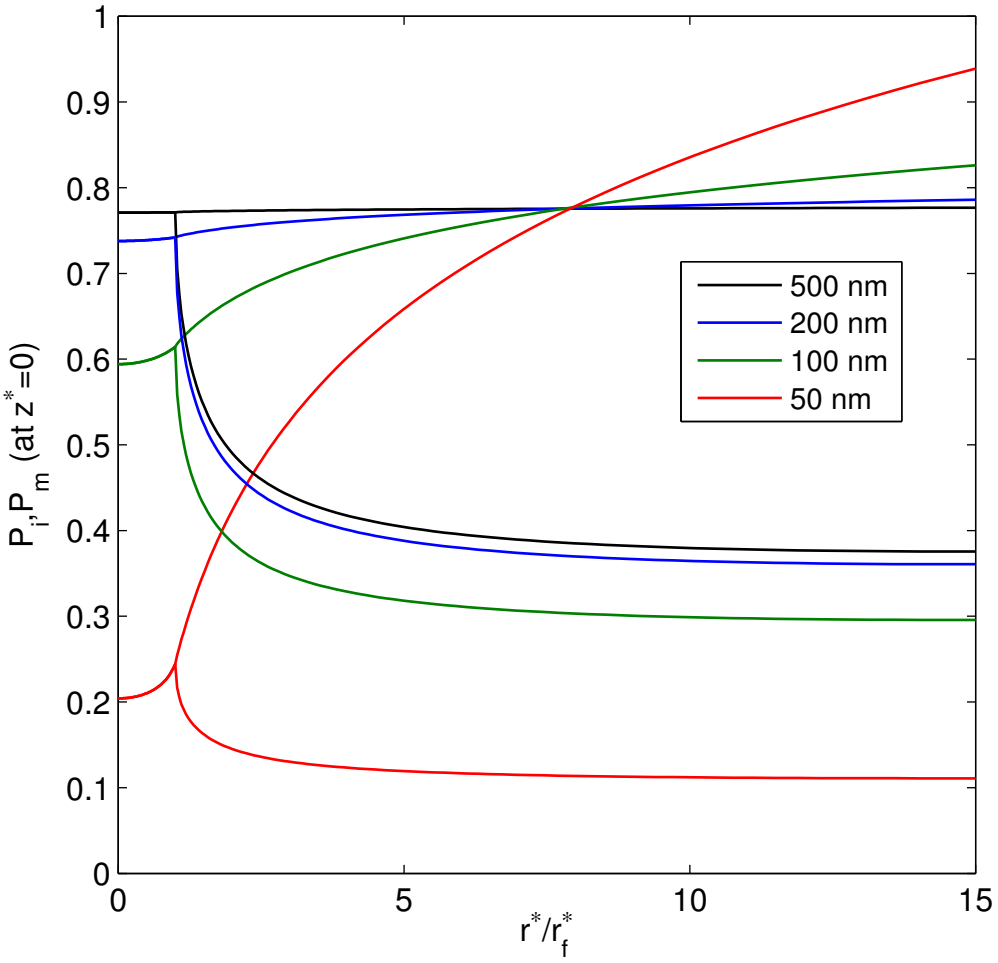

Figure 2.3: Local pressure distributions on the intimal side (P_i: the upper curve of a given color) and the medial side (P_m: the lower curve of a given color) of IEL for different intima thicknesses using Tedgui and Lever's (100) data with exact boundary conditions. L_{P_m} and L_{P_e} are given in tables 2.4 and 2.5, respectively; see Glossary for definition of other abbreviations.

flow in the media to the entrance flow into a partially blocked IEL fenestra. In other words, at 50 nm, the SI is fully compressed and the endothelial cell partially blocks the fenestra; water incurs a sharp pressure drop (red curve in Fig. 2.3) in traversing the SI.

Our calculations using Huang et al.'s (36) approximate boundary conditions resulted in very small differences from their predictions, which are likely due to different numbers of terms retained and different matrix inversion tool used. Figures 2.2 and 2.3 show very good qualitative agreement between the two solutions. However, in and near the fenestral hole and especially for compressed intimae, the predictions are off by approximately 10%. Also, the pressures at the edge of wall unit (junctional region) differ roughly by 3%. These two regions are where the pressures vary significantly in both the z direction and, for thinner SI, in the radial direction across the fenestra. It is worth noting that the separation of scales in most of the SI (i.e., the characteristic z-scale, L_{i0}, is far smaller than the characteristic r-scale, ξ_I, in the SI, except in these regions where the r-scale is the far smaller region width) means the z variation of the dynamic variables should be very small (i.e., not of leading order in the small ratio of these scales). This separation of scales is not valid in these two regions, and so z-variation becomes significant there. A comparison between the two solutions suggests that Huang et al.'s (36) third, three-point-matching approximation clearly performs the best, as anticipated. We have not yet predicted the intima compression for a given P_L^* and so cannot yet calculate the dimensional pressures. We will use Huang et al.'s (36) theory that relates intimal compression (L_i^*/L_{i0}^*) to the applied transmural pressure gradient, P_L^*, to calculate the dimensional pressure profiles.

We did not find any significant change in these pressure profiles with inclusion of the GX layer. The pressure distribution within the GX region (not shown) is uniform in both r and z directions at a value nearly equal to the lumen pressure except near the junction region, where one finds a small decrease ($< 1\%$) in pressure. This drop causes the average pressure in the SI to be $\sim$4% lower at large intima thicknesses (>100 nm) and at least 2-3% lower when the intima is relatively compressed (<100 nm) compared with Fig. 2.3. Interestingly, we find a non-negligible variation in the SI pressure in z-direction near the junctional region and it propagates

a short distance ($\sim 10\Delta R$) inside the intima, consistent with the separation of scales argument mentioned above. These calculations suggest that the surface GX layer provides little resistance to water flow; this result agrees well with the theoretical predictions of Seki and coworkers (92) who showed negligible resistance from the GX for flow though micro vessel walls. We anticipate that the GX layer may play a major role in transport of small oncotically-active protein molecules like albumin into and through the vessel wall; such effects are the subject of the next chapter. In the results that follow, we have included the GX layer and the model used is as shown in Fig. 2.1.

Hydraulic conductivity of the endothelium plus SI:

Figure 2.4 plots the model predictions for the variation of the hydraulic conductivity of the endothelium plus SI ($L_{P_{e+i}}$) calculated using Eq. 2.17 as a function of intimal compression. Thick intimae have a high $L_{P_{e+i}}$ that remains almost constant for ($L_i^*/L_{i0}^* > 0.4$), since for such thicknesses there is no fenestral blockage and $L_{P_{e+i}} \sim L_{P_e}$, the intrinsic endothelial conductivity. Compressed intimas with ($L_i^*/L_{i0}^* < 0.4$), on the other hand, decrease K_P and obstruct fenestral openings. These factors rapidly increase SI resistance, i.e., decrease its conductivity, e.g., $L_{P_{e+i}}$ decreases by $\sim$28% from $L_i^*/L_{i0}^* = 0.4$ to $L_i^*/L_{i0}^* = 0.15$.

Pressure dependent hydraulic conductivity:

In order to compare the predicted variation of the hydraulic conductivity of an intact arterial wall with the experimental L_P measurements from various groups, we model the SI matrix as a Hookean spring. The spring responds (with spring constant k) to the force per unit area ($\bar{P}_g^* - \bar{P}_i^*$) on the endothelium to get an implicit relation between intimal compression (L_i^*/L_{i0}^*) and the applied pressure difference (P_L^*) as:

$$P_L^*(\bar{P}_g^* - \bar{P}_i^*) = k\left(1 - \frac{L_i^*}{L_{i0}^*}\right) \tag{2.20}$$

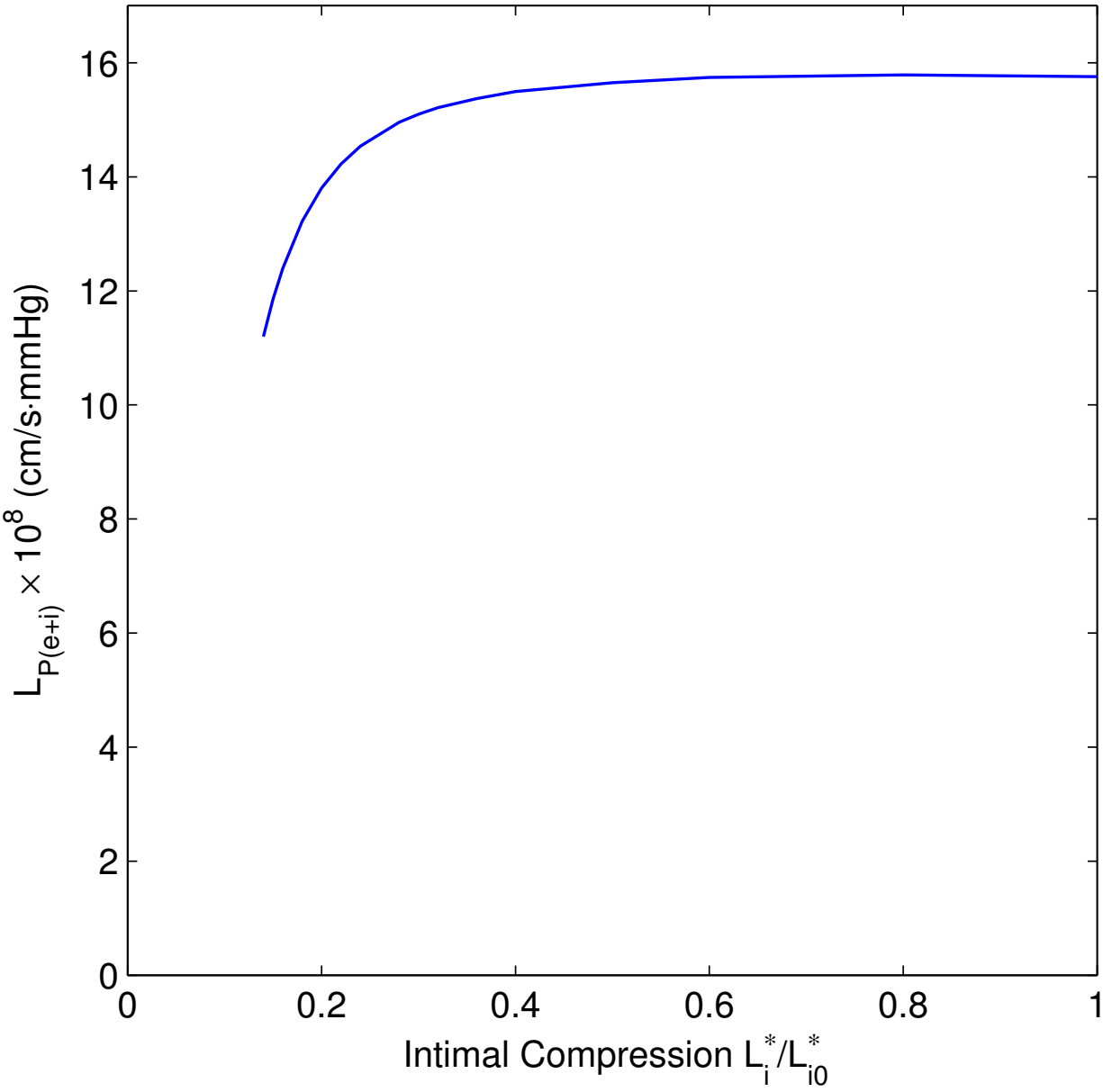

Figure 2.4: Predicted variation of the hydraulic conductivity of the endothelium plus intima as a function of intimal compression using Tedgui and Lever's data (100). L_{i0}^*= 500 nm. L_{P_m} and L_{P_e} are given in tables 2.4 and 2.5, respectively; see Glossary for definition of other abbreviations.

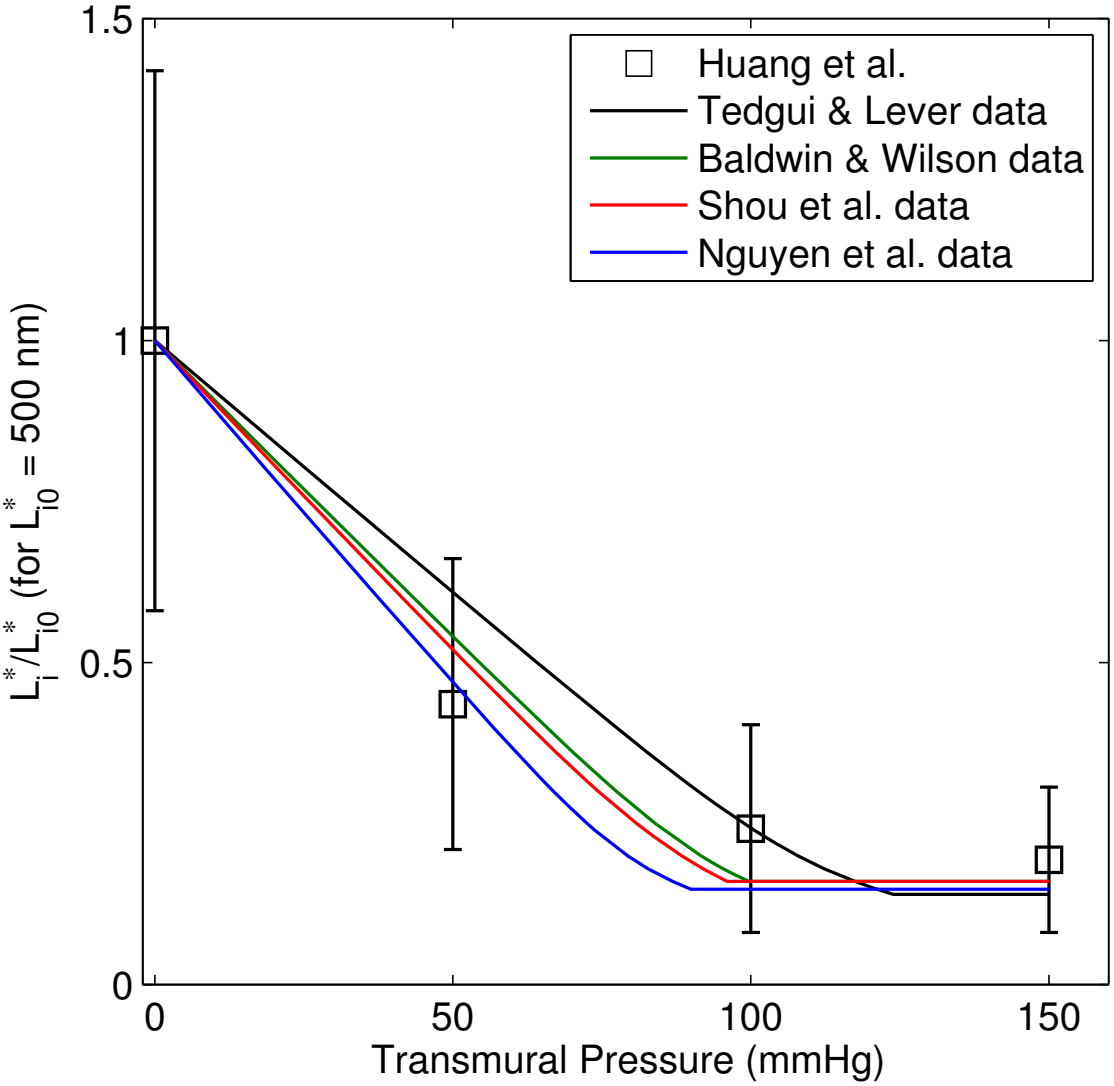

Figure 2.5: Nonlinear relationship between intimal thickness and transmural pressure and comparison with Huang et al.'s (37) experimental measurements of thickness of the SI of rat aorta. Error bars represent standard deviations. L_{P_m} and L_{P_e} for corresponding data sets are given in tables 2.4 and 2.5, respectively; see Glossary for definition of other abbreviations.

where, k is the transmural-pressure-independent intimal elastic coefficient $[\mathrm{mmHg}]$. Using Eqs. 2.19 and 2.18, we calculate L_{P_t} and $\bar{P}_i^*$ at different intimal thicknesses (L_i^*). We also have experimental data for L_{P_t} at various lumen pressures P_L^*. We choose a measured L_{P_t} corresponding to a particular pressure from the experimental data. We then try to find an intima thickness that predicts the same L_{P_t} from our model calculations. Using the values of L_{P_t}, P_L^* and L_i^* that correspond to the various experimental transmural pressures, we can plot the transendothelial pressure (Eq. 2.20) vs the endothelial displacement and use the best-fit value for its slope as the spring constant k.

Figure 2.5 plots the variation of the intimal thickness with increasing luminal pressure for four different data sets and compares them with the experimental data of Huang et al. (37), who measured the intimal thickness of rat aorta fixed at four different transmural pressures. J. Abrams (pending) did similar direct SI thickness measurements (with an improved procedure to find the region of interest in electron micrographs of sections of rat aorta using Matlab's image processing tool) at 50, 100 and 150 mmHg and found similar results with much better standard deviations than Huang et al.'s (37) measurements. The theory predicts the experimental data fairly well at 50 mmHg (see predictions for Shou et al.'s (78) and Nguyen et al's (62) L_P data for rat aorta). Even though at 100 mmHg, the predictions appear lower than the data, this difference is not significant and agreement with the data at 150 mmHg is very good. Given the complexity associated with measuring the thickness of the extremely irregular intima layer and the simplicity of our model, our model appears to capture the important physiological conditions that govern intima compression. The results show a nearly linear decrease in the intimal thickness for the lower range of transmural pressures ($\sim$ up to 60 mmHg for Baldwin & Wilson's (2) and Nguyen et al.'s (62) data and $\sim$up to 80 mmHg for Tedgui & Lever's (100) and Shou et al.'s (78) data, respectively). Further increase in luminal pressure causes a nonlinear flattening of the intimal thickness vs pressure until a critical pressure that corresponds to maximal compression, after which we allow no further compaction. Our model predicts the critical thickness L_{ic}^* (that corresponds to the critical pressure) to be $\sim 14\%$ and 16% of its unstressed value (L_{i0}^*), compared to Huang et al.'s (36) 13% and 16% for Tedgui & Lever (100) and Baldwin and Wilson's (2) data, respectively. For Shou et al. (78) and Nguyen et

al.'s (62) data, the corresponding numbers are 16% and 15% respectively.

Using Eq. 16, Figures 2.6 - 2.9 plot the calculated variation of L_P for the intact vessels, (L_{P_t}) and for denuded vessels, $(L_{P_{m+I}})$, as functions of the transmural pressure and compares model predictions for each of the four different experimental data sets. We assume same L^*_{i0} (500 nm) for rabbit and rat data. Recall that Huang et al. (36) estimated $L_{P_{e+i}}$ (see Eq. 10 in Ref. (36)) and used Eq. 2.16a with a constant, data set-specific value of $L_{P_{m+I}}$ for an intact vessel to predict the variation of L_{P_t} with transmural pressure. We found that (results not shown) this method of calculating L_{P_t} slightly under-predicts L_{P_t} (by 2%) at lower intima compressions, but leads to significant over-predictions (by as much as 8-20% between $L^*_i/L^*_{i0} \sim 0.2$-0.15) of L_{P_t} at higher compressions. The spring constants obtained from these data sets are 32.7, 23.68, 27.66, 30.6 mmHg, respectively. Note that the low k value corresponds to Baldwin and Wilson's (2) data on rabbits, which are uniformly about double the L_P values of the other three data sets, two for rats and one for rabbits. With these results, one can calculate the mean value of k for a sub-endothelial matrix as 28.7 $\pm$ 3.9 (SD) mmHg. The elastic modulus of the PG and CG fiber matrix in the alveolar walls of lung tissue has been reported to be 5 kPa (6) (or $\sim$ 35 mmHg), which is very close to our prediction (28.7 mmHg) noted above. Compared to Huang et al.'s 22 and 16 mmHg, for Tedgui & Lever (100) and Baldwin & Wilson's data (2), these numbers are significantly higher. This difference is likely due to different method used for the estimation of L_{P_t} (as mentioned earlier) and the implementation of fenestral boundary conditions. Higher value of k means, for the same level of compression, greater force/area on the endothelium. Since the critical thicknesses predicted by both models are about the same (see above), our predictions with higher k would correspond to lower pressure required to achieve the level of maximal SI compression. Consistently, the predicted critical pressures for Tedgui & Lever's (100) and Baldwin & Wilson's data (2), as Figs. 2.6 and 2.7 show, are 124 and 96 mmHg, which are lower than Huang et al.'s (36) corresponding predictions - 135 and 82 mmHg, respectively. Our calculations predict critical pressure of 100 mmHg for Shou et al.'s (78) and 90 mmHg for Nguyen et al.'s (62) data.

Overall we find a good agreement between the experimental results and the model pre-

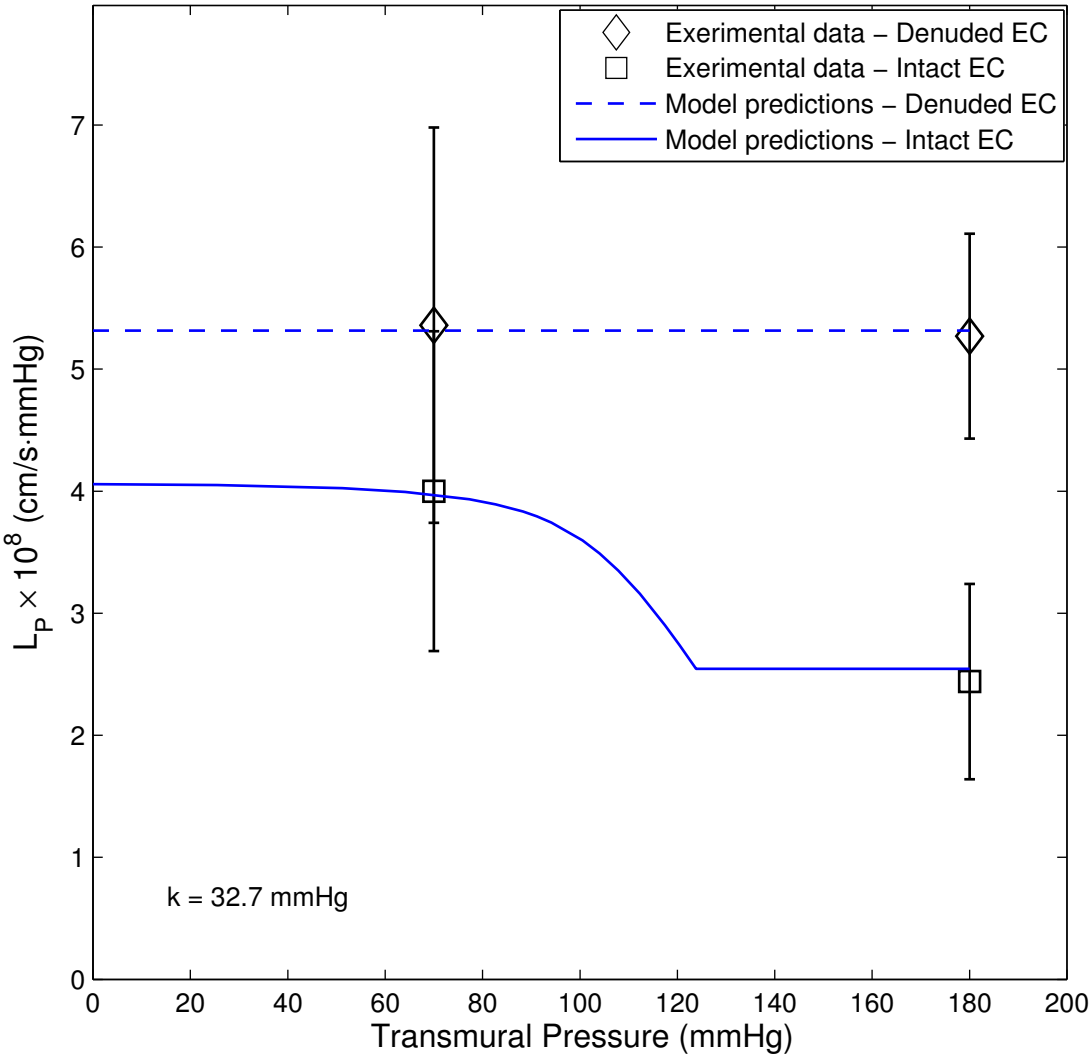

Figure 2.6: Comparison of the model's pressure-dependent hydraulic conductivity in the intact artery wall and pressure-independent hydraulic conductivity in the denuded artery wall with experimental measurements from Tedgui and Lever (100) on rabbit aortas. L_{P_m} and L_{P_e} are given in tables 2.4 and 2.5, respectively; see Glossary for definition of other abbreviations.

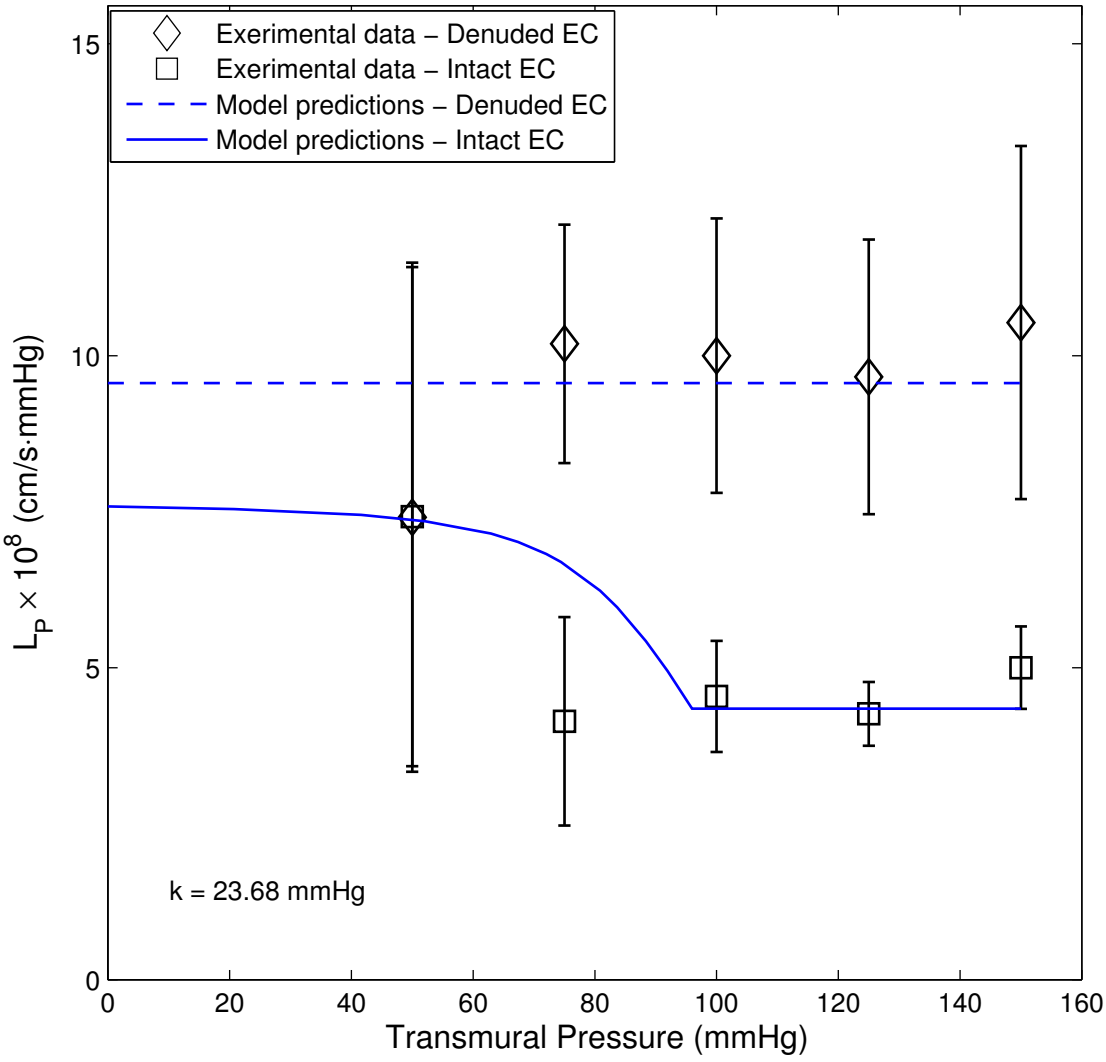

Figure 2.7: Comparison of the model's pressure-dependent hydraulic conductivity in the intact artery wall and pressure-independent hydraulic conductivity in the denuded artery wall with the experimental measurements from Baldwin and Wilson (2) on rabbit aortas. Note the relatively lower value of k corresponds to the uniformly higher L_P values in this relative to the other three sets of data. L_{P_m} and L_{P_e} are given in tables 2.4 and 2.5, respectively; see Glossary for definition of other abbreviations.

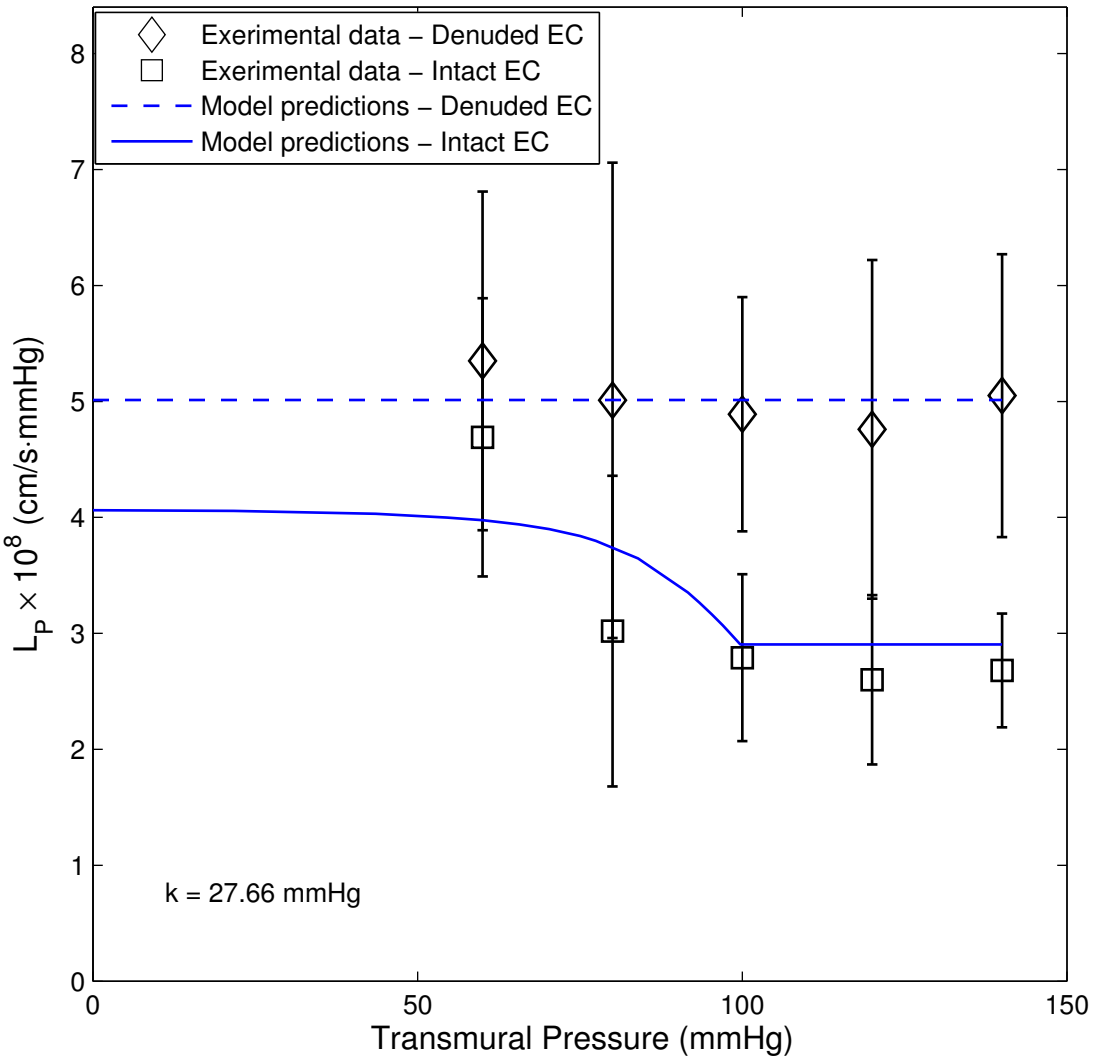

Figure 2.8: Comparison of the model's pressure-dependent hydraulic conductivity in the intact artery wall and pressure-independent hydraulic conductivity in the denuded artery wall with experimental measurements from Shou et al. (78) on rat aortas. L_{P_m} and L_{P_e} are given in tables 2.4 and 2.5, respectively; see Glossary for definition of other abbreviations.

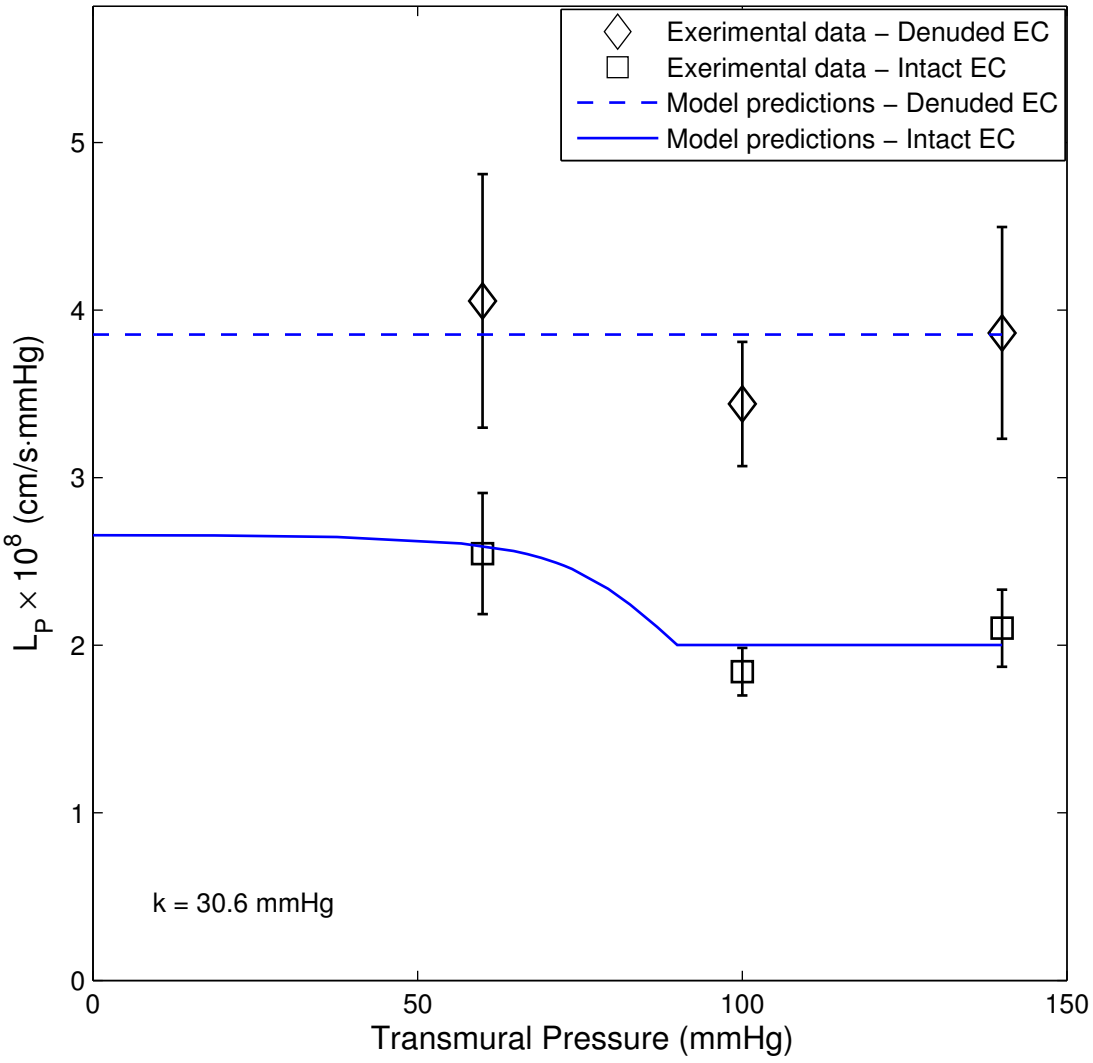

Figure 2.9: Comparison of the model's pressure-dependent hydraulic conductivity in the intact artery wall and pressure-independent hydraulic conductivity in the denuded artery wall with experimental measurements from Nguyen et al. (62) on rat aortas. L_{P_m} and L_{P_e} are given in tables 2.4 and 2.5, respectively; see Glossary for definition of other abbreviations.

dictions for each of the four data sets. As the figures display, $L_{P_{m+I}}$ of the denuded vessel is independent of transmural pressure, since there is nothing in the denuded vessel that compresses with pressure. However, when the vessel is intact, L_{P_t} appears to be constant until $\sim$ 60 mmHg, after which it drops by $\sim$ 40% in a non-linear fashion until the transmural pressure (or the force acting on the endothelium) reaches a critical limit - and the SI a limiting compression - after which our model does not allow any further SI compression. This renders L_{P_t} constant at higher pressures (beyond $\sim$ 100 mmHg). Thus, as per Huang et al.'s (36) theory, the compression of the SI and subsequent blockage of IEL fenestra indeed explains the experimentally observed marked drop in L_{P_t} with pressure and the 60-110 mmHg dynamic range over which L_{P_t} changes.

2.3 Filtration model: Transcellular flow

The experimental observations of Nguyen et al. (62), showing a marked decrease in L_{P_t} upon blocking of AQP1s, suggest a significant functional role of AQP1s or transcellular flow in determining and controlling the transmural water transport through rat arterial walls. What is disturbing here is the fact that the drops in L_{P_t}, as observed by Nguyen et al. (62), differ significantly at different transmural pressures. Huang et al.'s (36) SI compaction theory and section 2.2 calculate a critical average force per unit area $(\bar{P}_g^* - \bar{P}_i^*)$ on the endothelium to compress the SI which, under normal circumstances, occurs over a dynamic range of $\sim$60-100 mmHg. We propose that, by blocking the AQP1 channels, the available pathways for water transport across the endothelium are decreased, thereby decreasing L_{P_e} and consequently P_i. This increases the average force per unit area $(\bar{P}_g^* - \bar{P}_i^*)$ acting on the endothelium and shifts a larger fraction of ΔP from the media to the endothelium. As a result, the critical force per unit area acting on the endothelium obtains at a lower transmural pressure, which should shift the dynamic range of SI compression to lower overall transmural pressures. At higher luminal pressures, where partial/full fenestral blocking takes place even without reduction in functioning AQP1s, such a reduction should not lead to any significant additional compression, but rather would simply reflect a change in L_{P_e}. Thus we expect a much smaller variation in L_P at higher pressures upon AQP1 blocking, as observed by Nguyen et al. (62). In order to test the feasibility of our hypothesis, we incorporate transcellular flow into our earlier model and attempt to quantitatively explain the contribution of AQP1s to the vessel wall endothelium's hydraulic conductivity (L_{P_e}) and its ΔP-dependence.

2.3.1 Mathematical formulation

To account for the transcellular water flow, we extend our filtration model explained in section 2 by changing the boundary condition at the endothelium $(z_i = 1)$. The earlier model assumes that the endothelium is impermeable except for the junctional region. Here we allow a transcellular water flow, characterized by a hydraulic conductivity $L_{P_{EC}}$, of the endothelial cell due to its AQP1s in

addition to the water entering the SI through normal junction. The two of these together account for or add up to the endothelium's intrinsic hydraulic conductivity L_{P_e}. The boundary condition at $z_i = 1$ inside the normal junction is the same as given in Eqs. 2.7 and 2.8, however on the endothelium $(0 < r \leq R)$, water flux is governed by $L_{P_{EC}}$ as:

$$-W_j = \frac{L_{P_{EC}} \mu L_i^* (P_g - P_i)}{K_{P_i}} \text{ at } z_i = 1 \quad (j = g, i) \tag{2.21}$$

We express L_{P_e}, which is in principle an experimentally measured quantity, as a combination of $L_{P_{EC}}$ and $L_{P_{nj}}$ as:

$$L_{P_e}\, \pi \xi_I^{*2} = L_{P_{EC}}\, \pi R^{*2} + L_{P_{nj}}\, 2\pi R^* (\Delta R^*/2) \tag{2.22}$$

Note we have attributed half of the junctional area to the cell in question; the other half is, by symmetry, attributed to the neighboring cells. After replacing Eq. 2.6 by 2.21, we proceed to solve the Eq. 3.2 with the numerical implementation of the exact boundary conditions in the fenestral hole, as done previously. We use the same finite difference method as in section 2.2.

2.3.2 Constants and parameters

The parameters used for this model are same as those used in section 2.2, except $L_{P_{EC}}$, which does not appear in earlier model. Since we do not know the exact fraction of L_{P_e} due to AQP1s, we assume $L_{P_{EC}}$ to be various fractions of the experimentally-determined L_{P_e}, whose intrinsic value we have already calculated from our earlier model. Thus, using Eq. 2.22, one can find the (now lower) $L_{P_{nj}}$ corresponding to each assumed fraction.

2.3.3 Results and discussion

Pressure dependent hydraulic conductivity for unblocked AQP1s:

Functioning, unblocked AQP1s serve as available pathways for a substantial transendothelial water flow in addition to the intercellular junctions. We now use this new model to predict the variation

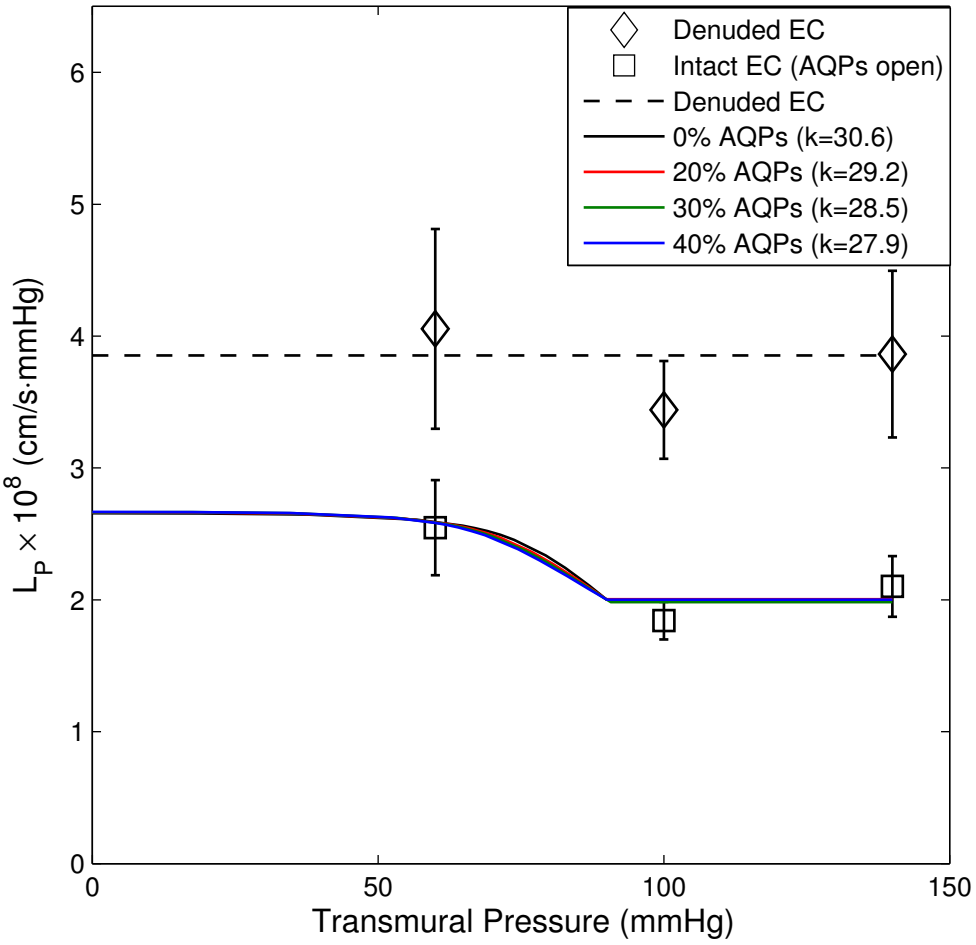

Figure 2.10: Effect of various AQP1 fractions (open or functioning) on the pressure dependent hydraulic conductivity of an intact artery wall and comparison with Nguyen et al.'s (62) experimental data. Symbols: experimental data, Lines: model predictions. Note that L_{P_e} in all of the four assumed fractions is the same, 8.29×10^{-8} $\mathrm{cm/sec \cdot mmHg}$; $L_{P_{EC}}$ and $L_{P_{nj}}$ are varied based on assumed AQP1 fraction and Eq. 2.22

Table 2.6: The effect of increasing AQP1s on water flux across the EC and normal junction

AQP1 expression	Q_{EC} (%)	Q_{nj} (%)
Baseline	30.21	69.79
25% more	35.11	64.89
50% more	39.37	60.63
100% more	46.41	53.59

Baseline assumes that AQP1s contribute 30% to L_{P_e}. Q_{EC} - water flux across the EC and Q_{EC} - water flux across the normal junction

of L_{P_t} with ΔP. We begin by assuming $L_{P_{EC}}$ as various fractions of L_{P_e} and predict the total L_{P_t} of the vessel wall at various SI thicknesses. For each fraction, we then scale the model to, e.g., Nguyen's (62) unblocked data (as explained in section 2.2.5), by finding the average compression that gives the L_{P_t} equal to the measured value at that transmural pressure. The slope of the resulting compressions vs the transendothelial force/area curve is the effective SI ECM spring constant (k) for each assumed AQP fraction of L_{P_e}. That is, since we are interpreting the experimental data based on an assumed fraction, each assumed fraction will give us a different value of this spring constant, i.e. a different SI spring. Knowing the spring constants and using Eq. 2.19 which predicts L_{P_t} for a given SI thickness and Eq. 2.20, we can find the variation of L_{P_t} vs ΔP and calculate/predict L_{P_t} at any ΔP.

Figure 2.10 depicts the variation in L_{P_t} with transmural pressure for various assumed fractions of L_{P_e} contributed by AQP1s. Note that the curve for 0% AQP1s i.e., no transcellular flow, is the same as that obtained in earlier model (see Fig. 2.9). The calculation assumes that all of these AQP1s are open and contribute to transcellular water flow. Since all of these curves have the same L_{P_e}, they are nearly identical. Notice though that as one increases the fraction of AQP1s from 0 to 40% at fixed L_{P_e}, the $L_P(\Delta P)$ curve does become slightly flatter in the dynamic pressure range of 60-100 mmHg. This is due to the fact that increasing L_{P_EC} lowers the pressure difference across the EC slightly for a given ΔP, and one needs a slightly higher ΔP to achieve the same trans-EC force/area. Viewed slightly differently, the increased flatness with increasing AQP1 fraction is the result of the shorter flow path traversed by the transcelluar, rather than the

junctional, portion of the water flow in the thinning intima, meaning less head loss and therefore less reduction in L_{P_t}. As expected, since L_{P_e} is the same for all of the assumed AQP1 fractions (see caption below Fig. 2.10), all of these curves result in roughly the same critical pressure (90 mmHg) after which no further compression is allowed. It is no surprise that one finds a different spring constant for each assumed AQP1 fraction (see Fig. 2.10); again, more AQP1s means a higher trans-EC flow, which reduces the pressure difference across the EC at a given ΔP. Since the matching to data occurs via ΔP, the system accomplishes the same compression at a lower trans-EC pressure, yielding a lower k with more AQP1s. Our calculations, incorporating transcellular flow, predict the spring constants for the four data sets given in Figs. 2.6-2.9 as 27.98, 19.17, 23.84 and 27.9 mmHg, respectively. Note that these numbers are smaller than those reported in Figs. 2.6 - 2.9, which do not include transcellular water flow.

Pressure dependent hydraulic conductivity for blocked AQP1s:

The hydraulic conductivities reported for blocked AQP1s (Nguyen et al. (62)) were measured using 5 μM $HgCl_2$. The inhibition of AQP1s by submillimolar concentrations of $HgCl_2$ had been amply demonstrated in red blood cells (RBC) (115). Titration curves taken on RBCs suggests that 5 μM would block less than 100%, and possibly as low as 1/3 of AQP1s (127). However, since a single molecular transcellular pathway may consist of more than one functioning AQP1 in series, it is possible that the number of molecular transcellular pathways blocked exceeds the number of functioning AQP1s blocked. Thus since we do not know the exact percentage contribution of AQP1s to the L_{P_e}, we choose a lower bound on it by assuming that 5 μM blocks all (100%) AQP1 pathways, and see how the model predictions for various assumed fractions compare with Nguyen et al.'s (62) blocked data. Given an assumed $L_{P_{EC}}$ (and corresponding $L_{P_{nj}}$ from Eq. 2.22), if the model predicts L_{P_t} values for maximum AQP1 blocking (by setting $L_{P_{EC}}$ =0, corresponding to 100% blocking) that are higher than the blocked experimental data, this would mean that we should have assumed a higher $L_{P_{EC}}$. Clearly blocking less than 100% of the AQP1s would result in higher L_{P_t} than 100% blockage. On the other hand, if for an assumed $L_{P_{EC}}$, we maximize

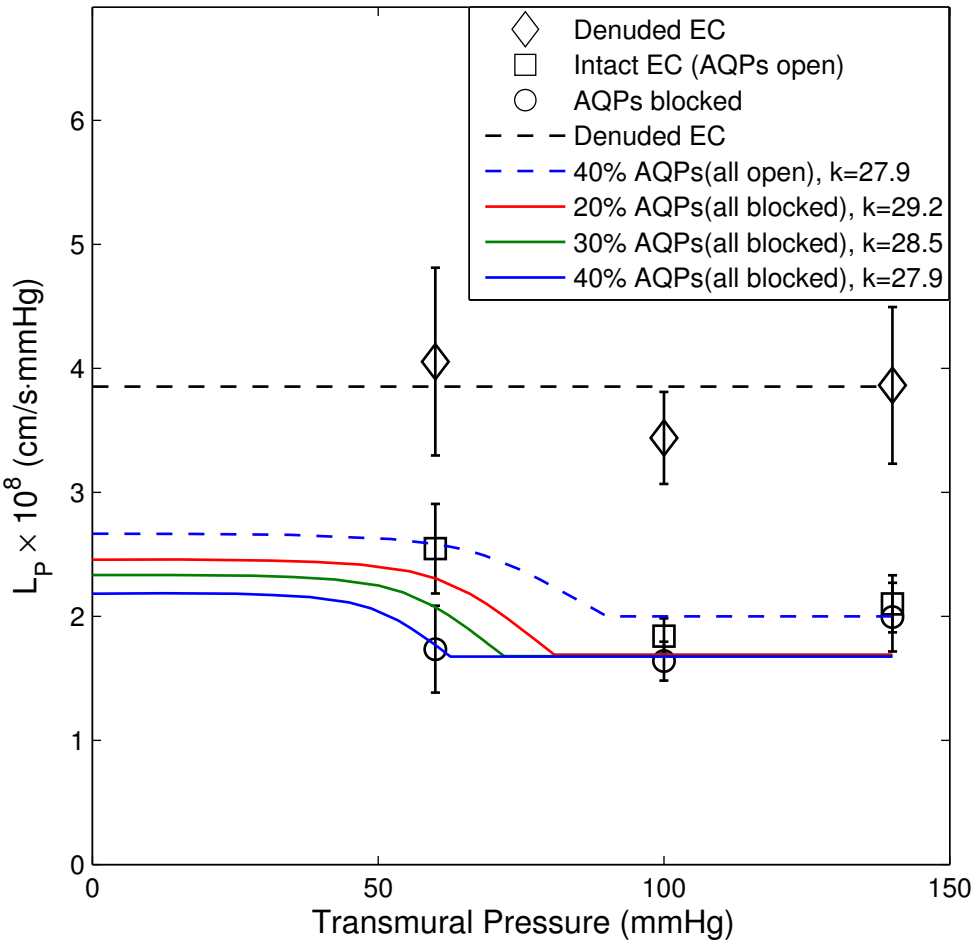

Figure 2.11: Effect of various AQP1 fractions and whether they are open or blocked on the pressure dependent hydraulic conductivity of an intact artery wall and comparison with Nguyen et al.'s (62) experimental data. Symbols: experimental data, Lines: model predictions. Note that blocking AQP1s (solid lines) for a given AQP1 fraction leaves $L_{P_{nj}}$ unchanged, but shuts off $L_{P_{EC}}$ (i.e., sets it to zero) and thus lowers L_{P_e}. $L_{P_{nj}}$ for each assumed fraction is the same as that used in Fig. 2.10; dashed blue curve is the same as 40% AQP1s curve in Fig. 2.9

blocking by setting $L_{P_{EC}}$= 0 and the model predicts L_{P_t} lower than experiment, we decrease the percentage of AQP1s blocked until we get a reasonable agreement with the experimental data. It is important to note that, in order to predict the hydraulic conductivity at the different pressures, we must retain the same spring constants obtained for the unblocked AQP1s.

Figure 2.11 compares the hydraulic conductivities in the presence of $HgCl_2$ at various $L_{P_{EC}}$ with Nguyen's (62) blocked data. For reference the figure also includes both the intact-unblocked and denuded vessel data and the corresponding theoretical curves, with the intact unblocked vessel theory computed for an AQP1 fraction of 40% of L_{P_e} from Fig. 2.10. The predictions in Fig. 2.11 clearly show a significant decrease in the hydraulic conductivity of the vessel wall with increased fraction of blocked AQP1s. As shown, for the case of 20% and 30% AQP1s, 100% of which are blocked, the model predictions for hydraulic conductivities are quite high while those for 40% AQP1s, 100% of which are blocked, are very close to experimental data. We now use these results to calculate the force acting on the endothelium. Note that the curves in Fig. 2.11 retain their shape, but shift to left as one blocks more AQP1s, meaning that the SI attains the maximum compression limit at much lower transmural pressures. Recall that Nguyen's (62) *in vitro* measurements showed that AQP1 blocking reduces water flux across BAECs by $\sim$22.1$\pm$6%, which reasonably agrees with our model's prediction that AQP1s likely account for more than 30% of L_{P_e}. Recall that Yan et al. (126) found that AQP1 knockdown lowers RAEC monolayer L_{P_e} by 62.4%, but that her tracer studies indicate that a portion of this drop appears to be due to a reduction in junctional transport with AQP1 knockdown. See Yan et al. (126) for details.

Experimental predictions: According to our theory, in the presence of $HgCl_2$, the SI is fully compressed at 60 mmHg, whereas it is only partially compressed, and not to an extent that causes fenestral blockage, in its absence. Thus we predict that direct measurement of SI thicknesses for vessels fixed under pressure, either with or without $HgCl_2$, should show this difference. The experimental measurements of J. Abrams (in preparation for a separate publication) showing $\sim$ 21% decrease in the SI thickness of rat aortas fixed at 50 mmHg with $HgCl_2$ (or blocked AQP1s)

and very small decrease in its thickness at 100 and 150 mmHg, are consistent with our hypothesis. We find that the force/area acting on the endothelium at 60 mmHg in the case of functioning AQPs is the same as that acting at 43 mmHg for the blocked case. That is, the theory predicts that, even with $HgCl_2$ treatment, the SI at 43 mmHg transmural pressure should experience the same level of compression and fenestral blockage as the untreated SI at 60 mmHg. $HgCl_2$ treatment will however still lower L_{P_e}, and thus the predicted L_{P_t} at 43 mmHg with $HgCl_2$ would be 2.11×10^{-8} $\mathrm{cm/sec \cdot mmHg}$, much higher than its value with blocker at 60 mmHg, but still less than the blocker-free 60 mmHg value of 2.58×10^{-8} $\mathrm{cm/sec \cdot mmHg}$.

A second prediction, is that, if one lowers the transmural pressure sufficiently, one should be able to decompress the SI and to raise L_{P_t} even in the presence of $HgCl_2$. The model predicts that the L_{P_t} in the presence of $HgCl_2$ increases from 1.75×10^{-8} to 2.18×10^{-8} $\mathrm{cm/sec \cdot mmHg}$ as the transmural pressure is reduced from 60 to 20 mmHg. Nguyen (62) carried out pilot measurement of L_{P_t} with $HgCl_2$ at 20 mmHg and found a value of 1.9×10^{-8} $\mathrm{cm/sec \cdot mmHg}$, which is greater than their L_{P_t} value at 60 mmHg (1.74×10^{-8} $\mathrm{cm/sec \cdot mmHg}$) and is quite consistent with our prediction.

We note also that Nguyen et al. (62) found an L_{P_t} value at a transmural pressure of 140 mmHg to be 1.995×10^{-8} $\mathrm{cm/sec \cdot mmHg}$ that was higher than the values at 60 and 100 mmHg, which showed no statistically significant difference. They carried out their controls for reversing the effects of $HgCl_2$ with 2-mercaptoethanol only at the two lower pressures and recovered L_P values within an average 5% of baseline values, suggesting negligible change in paracellular pathway upon $HgCl_2$ treatment. One reason for this discrepancy is the possibility that at this elevated pressure, the $HgCl_2$ was forced into the cells and caused some cellular damage. J. Abrams has found clear artifacts in ECs from rat aortas fixed at 150 mmHg and exposed to $HgCl_2$ for longer time (more than 30 mins), which were absent in ECs from the rat aortas fixed at 50 and 100 mmHg. Another possibility is that, since in the presence of $HgCl_2$ the force/area on the endothelium at fixed transmural pressure is far higher than in its absence, maybe this force at 140 mmHg was large enough to cause a slight stretching of the endothelium and therefore of all of the EC junc-

tions, thereby slightly elevating the junctional contribution to L_{P_e} and therefore to L_{P_t}. We find that, in order to exert the same force on endothelium as that exerted in case of blocked AQPs at 140 mmHg, one has to increase the transmural pressure to $\sim$ 200 mmHg. The forces acting at such high transmural pressures might cause some mechanical damage to the endothelium and can lead to the higher L_Ps, as seen by Nguyen (62). This calculation suggests that one should measure L_{P_t} without blocker at 200 mmHg and compare it to the L_{P_t} with blocker at 140 mmHg.

Effect of AQP1 up-regulation on force/area on EC:

Since decreasing functioning AQP1s decreases the critical ΔP for SI compression, could increasing functioning AQP1s increase this value, say, into the physiological range? This would increase L_{P_t} significantly there. Figure 2.12 shows the predicted effect of up-regulating AQP1s or, equivalently, of increasing the transcellular transport on the force acting on a unit area of endothelium. Note that each curve in figure 2.12 starts out almost linear, then flattens and finally climbs linearly again. The initial near-linearity reflects the fact that L_{P_e} remains fixed for each curve and the initial compression causes no fenestral blockage; thus the transendothelial pressure drop (or force/area) scales almost linearly with the transmural pressure. Beyond a certain point, the increased pressure compresses the SI, causing fenestral blockage, which lowers L_{P_t}. The higher driving pressure and the lower L_{P_t} nearly balance, meaning the trans-wall - equal to the trans-endothelial - flow hardly changes with increasing transmural pressure in this region. Since L_{P_e} is an intrinsic property that does not change with compression, this means that the transendothelial force/area hardly changes in this region. However, once full SI compression is reached, the geometry remains fixed and the transendothelial pressure drop (which is proportional to the transendothelial flow, equal to the transmural flow) simply scales exactly linearly with the transmural pressure. An increase in functioning AQP1s shifts the transendothelial force/area curves in Fig. 2.12 down. As above, this means that the more functioning AQP1s or the more transcellular transport pathways, the lower the force/area across the EC at each transmural pressure, as originally suspected. Phrased differently, as we block the AQP1s, there is more pressure drop and thus more force on the endothelium that

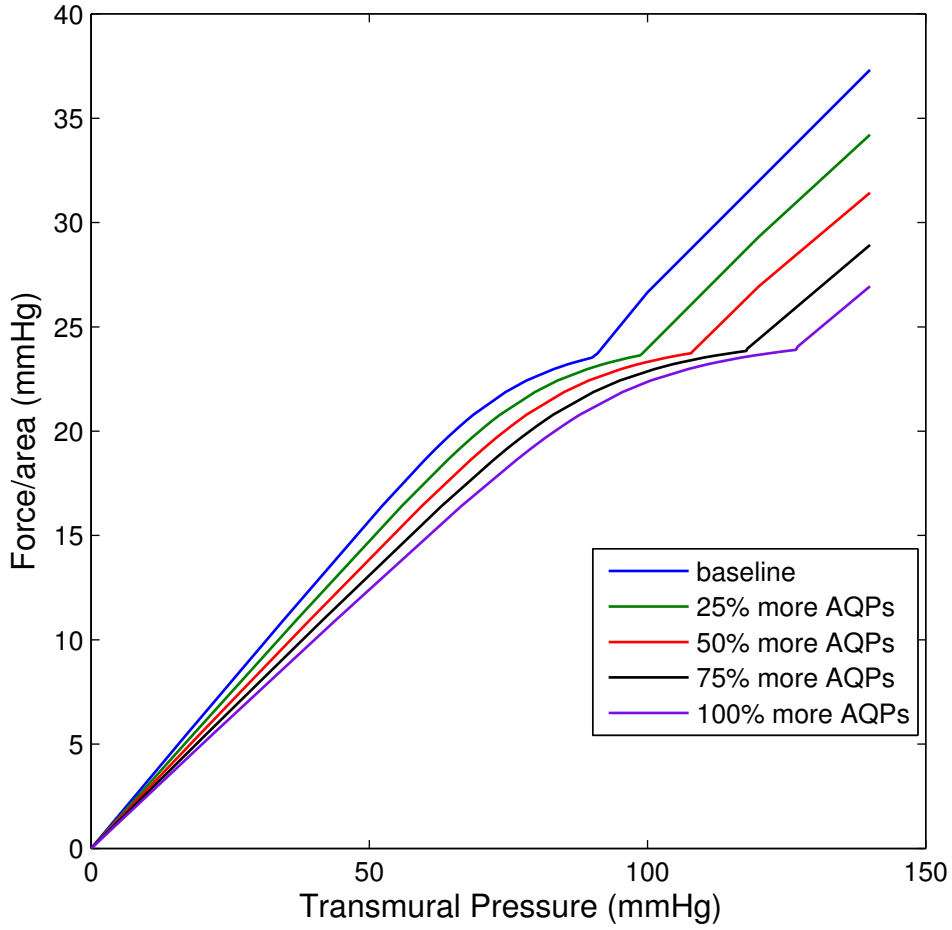

Figure 2.12: Effect of increasing the number of functioning AQP1s (their fraction of L_{P_e}) on the force per unit area acting on the endothelium. Baseline results assume that AQP1s contribute 40% to L_{P_e} (Eq. 2.22 gives corresponding $L_{P_{EC}}$ and $L_{P_{nj}}$); $L_{P_{nj}}$ (and thus k =27.9 mmHg) is fixed in all cases and $L_{P_{EC}}$ is varied based on the assumed fraction

compresses the SI. The right shift in force/area curve suggests that, if the endothelium expresses more AQP1s, the intima can sustain higher range of pressures before getting fully compressed and may be beneficial in flushing unbound lipid from the wall.

Effect of AQP1 up-regulation on L_{P_t}:

Figure 2.13 shows the model predictions for the effect of increasing (only) transcellular transport on the hydraulic conductivity of an intact vessel wall. Clearly, the L_{P_t} significantly increases with increasing the number of functioning AQP1s on the endothelium. Moreover, as Fig. 2.13 depicts, with more AQP1s, the $L_{P_t}(\Delta P)$ curve becomes flatter and shifts to right. For Nguyen's data (62), the critical pressures are found to be 91, 99, 108, 118 and 127 mmHg for every 25% increase in AQP expression respectively. It also means that the more active the transcellular pathways, the higher the transmural pressure needed to achieve the critical force/area for maximal SI compression, and consequently, the farther to the right, i.e., to higher transmural pressures, the dynamic range of L_{P_t} shifts. This could have implications for possible interventions to increase vessel wall L_{P_t}. These predictions suggest new experiments to investigate the effects of increasing EC AQP1s on L_{P_t}. One anticipates a significant increase in L_{P_t} with more EC AQP1s in the transmural pressure regime of $\sim$70-95 mmHg and a small change beyond 110 mmHg. My colleague C. Raval has recently performed these experiments and will present their very good agreement with this theory in a companion paper.

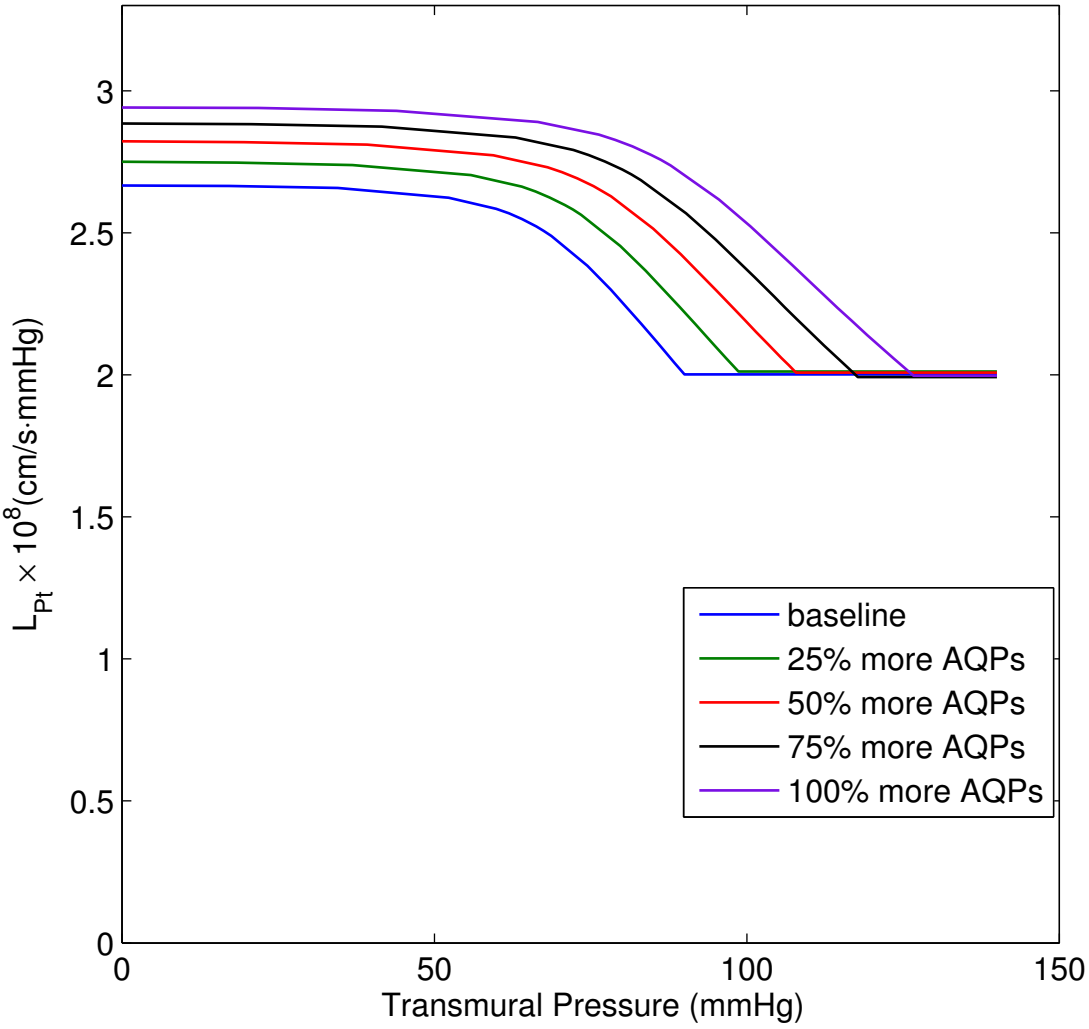

Figure 2.13: Effect of increasing the number of functioning AQP1s (their fraction of L_{P_e}) on the hydraulic conductivity of an intact artery wall. Baseline results assume that AQP1s contribute 40% to L_{P_e} (Eq. 2.22 gives corresponding $L_{P_{EC}}$ and $L_{P_{nj}}$); $L_{P_{nj}}$ (and thus k =27.9 mmHg) is fixed in all cases and $L_{P_{EC}}$ is varied based on assumed fraction

2.4 Conclusion

We have presented a pair of models for the filtration through the arterial wall and, in particular, through its fenestral pores and considered, for the first time, the role played by AQP1s in modulating the total hydraulic conductivity of an intact arterial wall with changes in transmural pressure. Our calculations showed a substantial decrease in L_{P_t} values upon increasing the percentage of blocked AQP1s, and that this decrease is the combined effect of lowering the intrinsic L_{P_e} and inducing fenestral blockage at a much lower transmural pressure than would be needed with functioning aortic endothelial AQP1s. The model provides several interesting results that compare favorably with experiment. First, the large predicted drop in L_{P_t} agrees with Nguyen's (62) experimental observations of the effect of blocking on L_P at different transmural pressures, supporting the hypothesis that AQP1s indeed play a significant role in overall transport across the arterial wall. Second, the theory predicts that AQP1s contribute at least 30% to the intrinsic hydraulic conductivity of the endothelium. Third, the force acting on the endothelium at 60 mmHg with functioning AQP1s is same as that at 43 mmHg for blocked AQP1s. This suggests that the SI in the presence of $HgCl_2$ should decompress at 43 mmHg to a level that the untreated SI is at 60 mmHg. Pilot data seems to agree at least qualitatively with the precise predictions for the extent to which L_{P_t} should increase with this drop in transmural pressure for the treated vessel. The theory has also made predictions for measurements of L_{P_t} at elevated pressures and with higher EC AQP1 expression. We anticipate that these new understandings of the nature of the transendothelial water flow may suggest new potential therapeutic targets for slowing the early progress of atherosclerosis.

Chapter 3. Interplay of flow and oncotically active solute transport across the endothelium

3.1 Introduction

The transport and accumulation of macromolecules like low density lipoprotein (LDL) cholesterol from the lumen into the subendothelial intima (SI) region of a arterial wall are thought to be critical pre-lesion events in atherosclerosis. These macromolecules react with and bind to SI extracellular matrix (ECM) (mainly comprised of proteoglycan (PG) and collagen (CG) fibers (24)) allowing them to oxidize *in situ*. Endothelial cells (EC) recruit blood-borne monocytes that mature inside the SI region to become macrophages (10) and engulf oxidized LDL. When overloaded, they form necrotic foam cells (87), a process known to trigger early atherosclerotic lesion formation. Many researchers, using both experimental (89, 11, 13, 34, 50, 51, 52) and theoretical (119, 129, 35) approaches, have studied the transport process by which macromolecules cross the aortic endothelium and enter the inner layers of the vessel wall. These studies (11, 50, 51, 52, 119) have shown that macromolecules cross the aortic endothelium at certain focal locations, widened junctions surrounding rare ($\sim$ 1 in every 2000-5000 ECs in rat aorta (50, 51, 52)) ECs. They have shown (129, 35) that macromolecular advection by transmural (across the vessel wall) pressure-driven plasma flow (water and solutes) is the dominant mechanism of this focal macromolecular transport and subsequent spread in the SI. Unlike macromolecules, water, because of its small size, can cross the normal tight junctions surrounding normal ECs that vastly outnumber the leaky ones and enter the vessel wall. Transmural pressure-driven leaky junction flow brings macromolecules into the SI through rare leaky junctions and advects them further inside the SI region, thereby increasing LDL-ECM interactions. On the other hand, transmural pressure-driven flow across the normal endothelium can also flush unbound LDL from the SI and ultimately from the vessel wall. Thus the overall water transport across the endothelium, and not just the portion through rare leaky junctions, affects LDL accumulation inside the vessel wall.

A wall parameter, the hydraulic conductivity (L_P), defined as the ratio of the transmural water flux to (hydrostatic-oncotic, the latter universally taken as zero in large artery walls (38)) pressure difference, characterizes the transmural water transport; in simple materials, it is pressure-independent. In contrast, experimental observations of Tedgui & Lever (100), Baldwin and Wilson (2), Shou et al. (78) and Nguyen et al. (62) have shown an interesting pressure dependence of the L_P in rabbit (100, 2) and rat (78, 62) aortic walls. A higher L_P obtains at lower transmural pressures and a lower L_P at higher transmural pressures. Huang et al.'s (36) intima compression theory postulated that the force acting on the endothelium with increasing transmural pressure can compress the sparse SI layer and decrease it's Darcy permeability (K_P). The predictions from Huang et al.'s (36) local filtration model, which we have reproduced and extended in our earlier study (Ch. 2), indeed suggest that the pressure-induced SI compression and more importantly, the consequent EC blocking of the fenestral openings in the internal elastic lamina (IEL) through which transmural flows must pass drastically reduces the L_P of the vessel wall. The SI can be compressed to a critical limit after which the stiffer collagen fibers in the SI do not permit further compression and L_P becomes pressure-invarient. Huang et al.'s (37) direct measurement of SI thickness in aortas fixed under pressure directly demonstrates this pressure-induced SI compression. Both Huang et al.'s (36) and our model's predictions (Ch. 2) explain these experimentally observed variation in the L_P very well.

The presence of aquaporin-1 (AQP1) in aortic ECs suggests a new possibility of water transport through the EC, alongside the generally accepted paracellular route (62, 103, 126). AQP1 is a membrane protein molecule that acts as a highly specific water channel and allows high throughputs of water (3×10^9 molecules/sec/channel) in response to osmotic gradients at little or no cost in ATP (58). Using immunocytochemical techniques, Nguyen et al. (62) and Yan et al. (126) have shown the presence of AQP1 in bovine aortic ECs (BAECs) and rat aortic ECs (RAECs) *in vitro*, respectively, while Toussaint et al. (103) used immunohistochemistry to demonstrate their presence in whole rat aorta *ex vivo*. By examining how a decrease in functioning AQP1s affects L_P, one can ascertain AQP1's functional role in trans-endothelial water transport.

Decreasing transcellular transport, either by using chemical agents that block AQP1 channels (62) or by using siRNA against AQP1 (73, 126), significantly reduces trans-endothelial water flux in both *in vitro* (62, 73, 126) and *ex vivo* (62, 126) studies. Our recent theory (Ch. 2) extended Huang et al.'s (36) theory to include trans-EC AQP1 flow and successfully explained these experimental findings, and, in particular, did so quantitatively for Nguyen et al.'s (62) and Yan et al.'s (126) *ex vivo* data. Taken together, these experimental and theoretical observations indeed substantiate the significance of AQP1-mediated transcellular flow in the overall water transport across the arterial wall.

Even though our filtration theory (Ch. 2) explains these *ex vivo* L_P observations extremely well, the transmural pressure driven trans-AQP1 mediated water flow presents an oncotic paradox. The idea is that normal EC junctions transport isotonic fluid, i.e., water and small solutes (e.g. albumin) responsible for oncotic pressure. In contrast, AQP1s specifically transport pure (hypotonic) water, excluding nearly everything else. This pure water inflow should both raise albumin concentration on the lumen side and lower it on the SI side of the EC, thereby setting up an oncotic pressure difference $(\Delta\pi)$ that acts against the ΔP-driven flow and prevents the SI from getting more hypotonic. This begs the question, how can the vessel maintain a steady trans-AQP1 water flow for many hours, as Nguyen et al.'s (62) chemical blocking of AQP1 experiments show, given its effect on SI tonicity? This question is the basic motivation behind the new model developed in this paper.

Above the EC lies a surface glycocalyx (GX) layer that can effect solute filtration. A number of theoretical and experimental studies on micro vessels have shown the significance of this GX layer in determining effective oncotic force that drives water flow across the capillary endothelium (32, 33, 1, 132). Hu and Weinbaum (32) have proposed that the endothelial surface GX layer acts as a primary molecular filter for oncotically active molecules like albumin and have suggested that the local hydrostatic and osmotic pressure differences across the surface GX layer, and not the global hydrostatic and osmotic pressure differences, which is very small across the capillary wall between the plasma and tissue, determine the Starling's forces for water flow across

the capillary endothelium. Motivated by these findings in microvessels, we hypothesize that the GX layer could have a significant impact on the transport of albumin across the walls of large arteries too. To unravel the effects of the oncotic forces on the transmural water transport across arterial walls where hydrostatic pressure differences are large and to resolve the above mentioned oncotic paradox, we develop a model for water and small solute transport across the GX layer, across the endothelial interface and through the entire wall. The filtration flow and the mass transfer problems for these regions are intimately and nonlinearly coupled: the flow advects tracer while albumin differences across the endothelium set up a $\Delta\pi$ that sucks fluid across the endothelium. We simultaneously solve the combined nonlinear steady state problem by treating it as the long-time solution of a fictitious unsteady problem with finite difference methods.

One might speculate that the surface GX layer, that acts as a filter for albumin, could drastically lower the oncotic pressure that can build up adjacent to the lumen side of the EC. Moreover, much of the isotonic fluid crossing the endothelium enters via the EC junction, and this fluid flows parallel to the endothelium in the ultra-thin, sparse SI until it finds the IEL fenestral hole to enter the dense media. From typical radial fluid velocities in the SI ($\sim$ 10^{-5}-10^{-7} cm/s (36)) and the EC radius ($\sim$ 10-15 μm), one can estimate that the solute entering the SI from its junction spends $>$100s in the SI. However, since the diffusive mixing (normal to the endothelium) time in the SI is much smaller (on the order of milliseconds for typical diffusivities of 10^{-7} cm^2/s), one might expect the diffusive mixing to elevate the albumin concentration and the osmotic pressure adjacent to the abluminal EC membrane. One expects both of these effects to mitigate the oncotic paradox. The solution of the combined filtration and mass transfer model will provide us the pressure, water velocity and albumin concentration profiles in the GX, SI and media region for each transmural pressure. The albumin concentration at the EC-GX boundary and the EC-SI boundary will allow us to calculate the oncotic pressure on each side of the EC and thus the overall oncotic pressure difference ($\Delta\pi = \pi_g - \pi_i$) across the EC. For a given applied transmural pressure difference ΔP, if the model predicts $\Delta\pi > \Delta P$ and $\pi_g > \pi_i$ then the resulting $\Delta\pi$ would suck fluid from the SI into the GX and oppose the ΔP driven flow that drives fluid from the lumen or GX into the

SI and across the vessel wall. However, if $\pi_g < \pi_i$ then the osmotic gradients would suck fluid in the same direction as ΔP driven flow. Since both hydrostatic and osmotic pressure differences govern the flow across the endothelium, the model will allow us calculate the true hydraulic conductivity of the endothelium from experimental measurements of the transendothelial flow. Using the combined model, we will predict the variation in the phenomenological L_P of the intact vessel wall with transmural pressure and compare it with the predictions from our previous filtration-only model (Ch. 2) that neglected oncotic effects. We shall calculate the various forces per unit area acting not only across the entire vessel wall, but also across the endothelium, viz., ΔP, $\Delta\pi$ and $\Delta P - \sigma\Delta\pi$ to better understand the fluid flow across the endothelium. We also consider the effects of AQP1 up-regulation on the concentration of albumin, the resulting osmotic pressures and the overall L_P of the vessel wall. To investigate the relative importance of the GX layer, we shall theoretically remove it from the model, thereby mimicking an enzymatic degradation process, and compare the water flux and forces acting across the EC with those estimated in the presence of the GX. The effect of pathologically relevant blood albumin concentration on the water flux across the vessel wall is also presented.

3.2 Mathematical model

3.2.1 Model Description

Fig. 3.1 is a schematic of the 2-D, axisymmetric (in cylindrical coordinates) model of water and solute flow through an arterial wall. As explained in our previous paper (Ch. 2), the transmural pressure difference drives water and small solute flow paracellularly through the normal/tight junctions surrounding an EC and water flow transcellularly through the EC via AQP1 channels. After entering the SI layer, lateral pressure gradients drive water and small solutes horizontally in the SI until they find the IEL fenestra and seeps into the media region. This water flow advects solutes such as dissolved albumin through the various layers of the vessel wall and together with diffusion, this advective albumin transport determines it's overall concentration within the vessel wall. The resistance offered by the adventitia layer, because of its loose structure, is much smaller compared to other layers and thus we do not include it in the transport model.

This flow model is same as the one used in our previous study (Ch. 2) which, by abuse of geometry, is assumed to be periodic on a cylindrical unit of radius ξ_I^*. An EC of radius R^* is surrounded by a normal junction of width ΔR^*. An IEL fenestra of radius r_f^* is ideally placed at the center of the periodic wall unit. We treat the IEL as a zero thickness impenetrable boundary except at it's fenestral openings. As per Huang et al.'s (36) intima compaction theory, the SI lies under a non-deformable endothelium and can be compressed upon pressure loadings from an initial thickness of L_{i0}^* (at zero transmural pressure) to $L_i^*(\Delta P)$. Due to its dense structure, we presume the media region is incompressible and thus its filtration properties are constant. Due to its small size (radius $\sim 3.5\ \mathrm{nm}$), albumin that has crossed the GX layer can traverse the normal junction (width $\sim 20\ \mathrm{nm}$) and enter the SI layer. Note that albumin can also enter the SI through the EC via vesicular transport governed by the permeability of EC to albumin. However it can not flow through AQP1s on the EC. Once inside the SI, pressure-ddriven water flow can advect albumin radially towards the fenestra and further into and through the media layer.

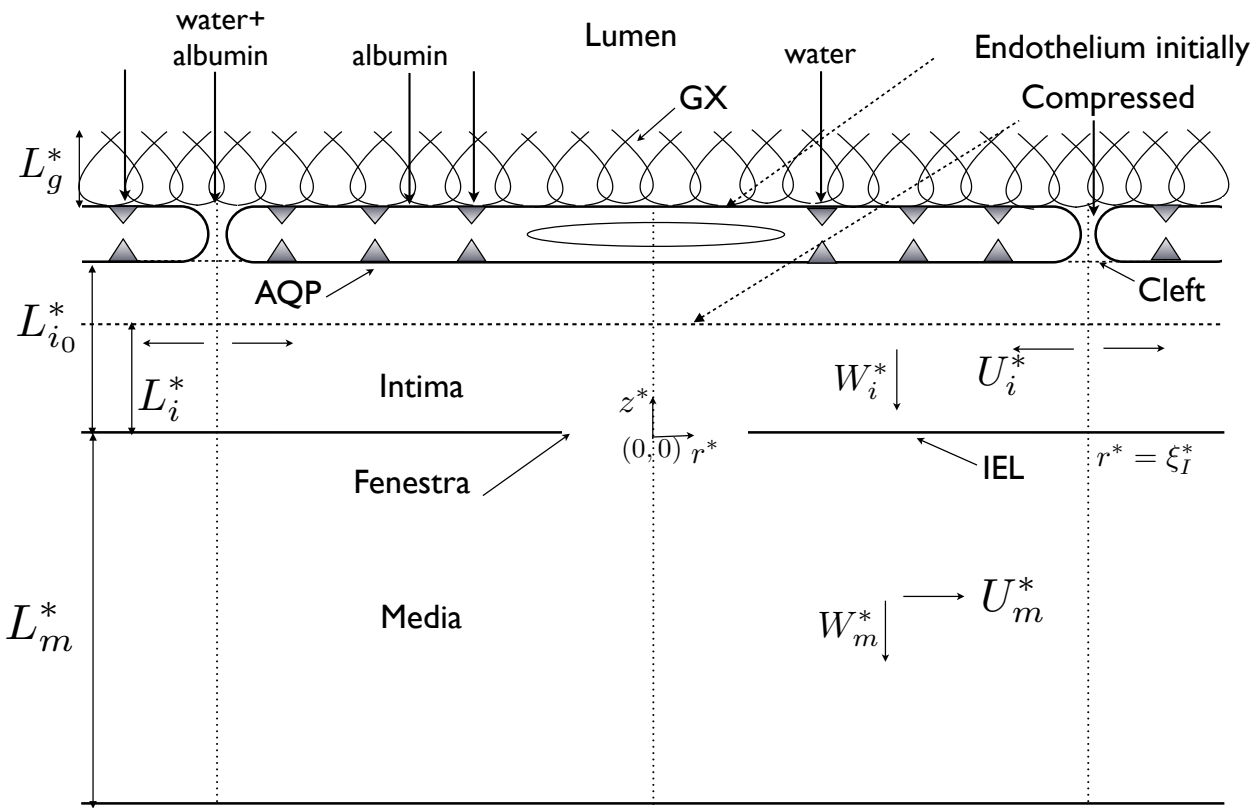

Figure 3.1: Schematic of the periodic local wall unit around a fenestral pore. Intima under non-deformable endothelium is compressible; L_{i0}^*, intima thickness at zero transmural pressure, L_i^*, compressed intima thickness; water and dissolved albumin enters the intima region through clefts surrounding EC, however, only pure water component of blood plasma flows through AQP1s on the EC. Note that albumin can cross the EC via vesicular route but it can not flow through AQP1s because of their specificity, see Glossary for definition of other abbreviations.

3.2.2 Filtration model

Let j be a dummy index that takes values g, i and m for GX, SI and media respectively. U^* and W^* are the local average velocities of water in the r and z directions, respectively, and together comprise the vector $\mathbf{V}^*$:=(U^*, W^*). P_j^*, K_{P_j} be the pressure and Darcy permeability, respectively, in region j of thickness L_j^*. We let the time-invariant lumen pressure be P_L^*. We introduce the following non-dimensional (without superscript *) variables and parameters:

$$r = \frac{r^*}{r_f^*}, \qquad \xi_I = \frac{\xi_I^*}{r_f^*}, \qquad R = \frac{R^*}{r_f^*}, \qquad \Delta R = \frac{\Delta R^*}{r_f^*}, \qquad z_j = \frac{z_j^*}{L_j^*}$$

$$P_j = \frac{P_j^*}{P_L^*}, \qquad U_j = \frac{U_j^*}{\frac{K_{P_j}}{\mu}\frac{P_L^*}{r_f^*}}, \qquad W_j = \frac{W_j^*}{\frac{K_{P_j}}{\mu}\frac{P_L^*}{L_j^*}}$$

The continuity equations, in non-dimensional form, for the three regions are:

$$h_j^2\left(\frac{\partial U_j}{\partial r} + \frac{U_j}{r}\right) + \frac{\partial W_j}{\partial z_j} = 0 \quad (j = g, i, m) \tag{3.1}$$

where $h_j = \dfrac{L_j^*}{r_f^*}$ are the ratios of the thicknesses of the three regions to the radius of a fenestral pore. The water flow across the arterial wall through the SI, made up of ECM of PG and CG fibers, and the media which consists of smooth muscle cells (SMC), ECM and elastic layers, can be modeled as porous media flows governed by Darcy's law: $\mathbf{V} = \dfrac{-K_P}{\mu}\nabla P$ with an effective Darcy permeability for each region. Thus, Eq. 3.1 become:

$$h_j^2\left(\frac{\partial^2 P_j}{\partial r^2} + \frac{1}{r}\frac{\partial P_j}{\partial r}\right) + \frac{\partial^2 P_j}{\partial z_j^2} = 0 \quad (j = g, i, m) \tag{3.2}$$

The boundary conditions (in non-dimensional form) for this system of coupled PDEs are:

(a) The axisymmetry at $r = 0$ and periodicity at $r = \xi_I$ require:

$$\frac{dP_j}{dr} = 0 \text{ at } r = 0 \text{ and } r = \xi_I \quad (j = g, i, m) \tag{3.3}$$

(b) The pressure at the top of the GX layer equals the lumen pressure:

$$P_g = 1 \text{ at } z_g = 1 \tag{3.4}$$

(c) The adventitia is assumed to be at the reference pressure, thus

$$P_m = 0 \text{ at } z_m = -1 \tag{3.5}$$

(d) Mixed boundary conditions at the GX/EC boundary $(z_i = 1)$: Starling's law sates that the flux across a semipermeable membrane is governed by the product of the hydraulic conductivity of the membrane and the difference between hydrostatic and the osmotic reflection coefficient times the oncotic pressure differences across it. To take this coupling into account, the following Eqs. 3.6 and 3.8 now include such terms and govern the water fluxes across the EC and the normal junction instead of Eqs. 2.21 and 2.8 in our previous study (Ch. 2) that neglect oncotic effects.

(d1) On the EC: $(0 < r \leq R)$

$$-W_j = \frac{L_{P_{EC}} \mu L_j^*}{K_{P_j}} \left[(P_g - P_i) - \sigma_{EC}(\pi_g - \pi_i) \right] \text{ at } z_i = 1 \ (j = g, i) \tag{3.6}$$

(d2) Inside the normal junction: $(R < r \leq \xi_I)$

$$W_g = W_i \tag{3.7}$$

$$-W_i = \frac{L_{P_{nj}} \mu L_i^*}{K_{P_i}} \left[(P_g - P_i) - \sigma_{nj}(\pi_g - \pi_i) \right] \text{ at } z_i = 1 \tag{3.8}$$

where σ_{EC} and σ_{nj} are osmotic reflection coefficients of albumin through the EC and normal junction, respectively. $L_{P_{EC}}$ is the hydraulic conductivity of the EC due to its AQP1s and $L_{P_{nj}}$ is the hydraulic conductivity of the normal junction. Note that, in previous studies (131), $L_{P_{nj}}$ is used to describe the area averaged hydraulic conductivity of the endothelium, equivalent to our L_{P_e} in this local model. The osmotic component $\Delta\pi$ $(\mathrm{cmH_2O})$ that affects the water flux across the EC and normal junction (as per Eqs. 3.6 and 3.8) is governed by the concentration of oncotically

active albumin $(\mathrm{gm/lit})$ as (32, 57):

$$\pi = 0.345C + 2.657 \times 10^{-3}\, C^2 + 2.26 \times 10^{-5}\, C^3 \tag{3.9}$$

(e) Mixed boundary conditions at the SI/media boundary $(z_i = 0)$: The IEL is assumed to be an impenetrable barrier except for its fenestral openings. Thus, water enters the media only through the fenestra where pressures and velocities are continues. This requires

(e1) In the fenstral hole: $(0 < r \leq 1)$

$$P_i = P_m \tag{3.10}$$

$$W_i = W_m \tag{3.11}$$

(e1) Outside the fenstral hole: $(1 < r \leq \xi_I)$

$$\frac{dP_j}{dz_j} = 0 \quad (j = i, m) \tag{3.12}$$

3.2.3 Albumin transport model

Let C_L^* be the lumen concentration of albumin and C_j^* be the dimensional albumin concentration per unit total volume (i.e., locally averaged over fluid and tissue phase) in region j. Let f_j be the retardation coefficient of albumin, γ_j the volume fraction available for albumin per unit total volume (fluid + tissue) and D_j^* be the effective diffusivity of albumin in region j. We introduce the following non-dimensional (without * variables):

$$C_j = \frac{C_j^*}{C_L^*}, \qquad P_{er_j} = \frac{f_j U_j^* r_f^*}{\gamma_j D_j^*}, \qquad P_{ez_j} = \frac{f_j W_j^* L_j^*}{\gamma_j D_j^*}$$

At steady state, the transport of albumin through the vessel wall is governed by the convection-diffusion equation as:

$$(f_j/\gamma_j)\mathbf{V}_j \cdot \nabla C_j^* = D_j^* \nabla^2 C_j^* \tag{3.13}$$

Using the non-dimensional variables defined above, we write Eq. 3.13 in non-dimensional form as: $(j = g, i, m)$

$$h_j^2 P_{er_j} \frac{\partial C_j}{\partial r} + P_{ez_j} \frac{\partial C_j}{\partial z_j} = h_j^2 \left(\frac{\partial^2 C_j}{\partial r^2} + \frac{1}{r} \frac{\partial C_j}{\partial r} \right) + \frac{\partial^2 C_j}{\partial z_j^2} \tag{3.14}$$

Note that each of the parameters h_j, f_j, γ_j and D_j^* is region dependent and, in the SI, depends on the level of SI compression. P_{er_j} and P_{ez_j} are peclet numbers in r and z direction, respectively, in region j. We employ following boundary conditions to solve Eq. 3.14:
Axisymmetry and periodicity imply zero mass flux at $r = 0$ and $r = \xi_I$ i.e.,

$$\frac{dC_j}{dr} = 0 \quad \text{at } r = 0 \text{ and } r = \xi_I \quad (j = g, i, m) \tag{3.15}$$

The concentration of albumin at the lumen-GX interface is equal to it's lumen, (C_L^*), and at the media-adventitia interface to its adventitia, (C_A^*) concentration.

$$\frac{C_g}{\gamma_g} = 1 \quad \text{at } z_g = 1,\ 0 < r < \xi_I \tag{3.16}$$

$$\frac{C_m}{\gamma_m} = 1 \quad \text{at } z_m = -1,\ 0 < r < \xi_I \text{ (assuming } C_L^* = C_A^*) \tag{3.17}$$

The boundary conditions at the GX-EC interface $(z_i = 1)$ turn out to be mixed: Since albumin can transfer across the EC by a vesicular pathway and the convective transport of water through the EC occurs via AQP1 channels, we model this vesicular transport as driven solely by an albumin concentration difference across the EC. In the normal junction, solute transport is governed by the

Kedem-Ketchalsky equation (43) along with the continuity of mass flux as:

(a) On the EC: $0 < r < R$ and $z_i = 1$:

$$\frac{dC_j}{dz_j} = \frac{Pe_{EC} L_j^*}{D_j^*} \left(\frac{C_g}{\gamma_g} - \frac{C_i}{\gamma_i} \right) \quad \text{at } z_i = 1 \quad (j = g, i) \tag{3.18}$$

(b) Inside the normal junction: $R < r < \xi_I$ and $z_i = 1$:

$$\frac{dC_i}{dz_i} - P_{ez_i} C_i = \frac{Pe_{nj} L_i^*}{D_i^*} \left(\frac{C_g}{\gamma_g} - \frac{C_i}{\gamma_i} \right) - \frac{W_i^* L_i^*}{D_i^*} (1 - \sigma_{nj}) \bar{C} \tag{3.19}$$

$$\frac{D_g^*}{L_g^*} \left(\frac{dC_g}{dz_g} - P_{ez_g} C_g \right) = \frac{D_i^*}{L_i^*} \left(\frac{dC_i}{dz_i} - P_{ez_i} C_i \right) \tag{3.20}$$

where Pe_{EC} and Pe_{nj} are the permeabilities of albumin through the EC and normal junction, respectively. Cancel et al. (4) have measured the diffusive permeability of albumin through vesicular pathway (our Pe_{EC}) in BAEC monolayers and also estimated its permeability through a large convective pore, similar to our normal junction. After making the area correction (see table 3.1), we estimate Pe_{nj} from the convective pore permeability value reported by Cancel et al. (4). Equation 3.20 imply mass flux continuity across the normal junction while Eq. 3.19 suggests that albumin's concentration across the normal junction is governed by both the diffusive and convective transport across it. The terms on right side of Eq. 3.19 represent the diffusive (first term) and convective (second term) transport of albumin. $\bar{C}$ in Eq. 3.19 is the average albumin concentration across the normal junction, defined as $\left(\frac{C_g}{\gamma_g} + \frac{C_i}{\gamma_i} \right)$.

The boundary condition at the SI-media interface $(z_i = 0)$ are also mixed: The IEL is assumed to be an impermeable barrier except for its fenestral openings. Thus, albumin can only enter the media through the fenestral hole where continuity of concentration and mass flux apply.

(a) Outside the fensetra: $1 < r < \xi_I$ and $z_i = 0$:

$$\frac{dC_j}{dz_j} = 0 \quad (j = i, m) \tag{3.21}$$

(b) Inside the fenestral hole: $0 < r < 1$ and $z_i = 0$:

$$\frac{C_i}{\gamma_i} = \frac{C_m}{\gamma_m} \tag{3.22}$$

$$\frac{D_i}{L_i^*}\left(\frac{dC_i}{dz_i} - P_{ez_i}C_i\right) = \frac{D_m}{L_m^*}\left(\frac{dC_m}{dz_m} - P_{ez_m}C_m\right) \tag{3.23}$$

3.2.4 Solution Method

The solution of Laplace's equation, $\nabla^2 P_j = 0$, and Darcy's law, $\mathbf{V}_j = \dfrac{-K_{P_j}}{\mu}\nabla P_j$, yields the water velocities (U^*, W^*) in each of the three regions required to solve Eq. 3.14. The details the finite difference scheme used to solve these PDEs to find the pressures and velocities can be found in our previous study (Ch. 2). Notice that the flux conditions (Eqs. 3.6 and 3.8) for the filtration problem depend on the albumin concentration, C, solution of the mass transfer problem and the solution of the mass transfer problem 3.13 depends on the solution $\mathbf{V}_j$ of the filtration problem, and Eq. 3.13 contains the product of these variables. This non-linear mixed-boundary value (Eqs. 3.18-3.23) problem is challenging. We use a time-dependent relaxation technique to solve this non-linear system of coupled PDEs, as used by Hu and coworkers (32) for solving a similar coupled system describing the concentration and flow fields in micro vessels. In this method, instead of solving the steady Eq. 3.14 directly, we solve an initial value problem for it's time-dependent counterpart (Eq. 3.24) until it reaches a steady state $(i.e., \dfrac{\partial C_j}{\partial t} \rightarrow 0)$ and thus obtain the solution of the original steady boundary value problem (Eq. 3.14).

$$\frac{\partial C_j}{\partial t} + h_j^2 P_{er_j}\frac{\partial C_j}{\partial r} + P_{ez_j}\frac{\partial C_j}{\partial z_j} = h_j^2\left(\frac{\partial^2 C_j}{\partial r^2} + \frac{1}{r}\frac{\partial C_j}{\partial r}\right) + \frac{\partial^2 C_j}{\partial z_j^2} \tag{3.24}$$

where t^* is non-dimensional time, defined as $t = \dfrac{t^*}{L^2/D}$.

We use a direct discretization approach on a non-uniform mesh to solve for the pressure and concentration distributions. The mesh size is carefully chosen to account for the large variations in the various parameters and length scales involved. Specifically, we create a very dense mesh near

the fenestra and around the normal junction where we expect large variations in pressures and concentrations. We employ central difference formulae to discretize diffusive terms in Eq. 3.24, and an upwind finite difference scheme for the advection terms to foster the stability of advection dominated transport. The boundary conditions are discretized using second order difference formulae. This discretization procedure leads a large number of linear algebraic equations (equal to the number of mesh points). Because of the matching conditions, we solve the corresponding set of equations for the three regions (GX, SI and Media, respectively) simultaneously using Matlab (Mathworks Inc) [1].

We begin by solving the steady uncoupled system and using that as our initial condition for the couple unsteady problem. That is, we initially set $C_j \equiv 0$ everywhere, solve for the pressure field ($\nabla^2 P_j = 0$) using the boundary conditions given in our previous study (Ch. 2) and compute the velocities using the Darcy's law. We then solve the steady convection-diffusion equation (Eq. 3.14) using these calculated velocities (U_j^*, W_j^*) as inputs to get the albumin concentration field. This concentration and velocity field serve as our initial conditions $(t = 0)$ for the unsteady problem (Eq. 3.24). With these velocities, the scheme computes the concentration at the next time step $(t = 1)$. It uses an implicit Euler scheme, which is unconditionally stable, to solve the unsteady convection-diffusion equation (Eq. 3.24). With these concentrations (at $t = 1$), we compute the new velocities by solving $\nabla^2 P_j = 0$ with the corrected boundary conditions (Eqs. 3.6 and 3.8). We use these new corrected velocities and concentrations at $t = 1$ as new initial condition to compute the concentrations at $t = 2$. This process is repeated until the difference in the concentration of albumin at $t = n$ and $t = n + 1$ is in the fourth significant digit.

Glossary:

a^*	Effective radius of proteoglycan aggregates
C_A^*	Dimensional concentration of albumin in adventitia
C_j^*	Dimensional concentration of albumin in region j
C_j	Dimensionless concentration of albumin in region j
C_L^*	Concentration od albumin in lumen

[1] Refer to our earlier study (Ch. 2) for more details on the numerical finite difference method

D_j	Effective diffusivity of albumin in region j
h_j	Ratio of thickness of region j to radius of fenestral pore
j	Region of artery wall ($j = g, i, m$ for GX, SI and Media respectively)
J_v	Water flux
k	Elastic coefficient of SI
K_{P_j}	Darcy permeability of region j
L^*_{i0}	Thickness of SI at zero luminal pressure
L^*_{ic}	Critical thickness of SI layer
L^*_j	Thickness of region j
L_p	Hydraulic conductivity
L_{p_e}	Intrinsic hydraulic conductivity of the endothelium
$L_{p_{EC}}$	Hydraulic conductivity of the endothelium attributed to its AQPs
$L_{p_{e+i}}$	Hydraulic conductivity of the endothelium + SI
L_{p_i}	Hydraulic conductivity of SI
L_{p_I}	Hydraulic conductivity of IEL
L_{p_m}	Hydraulic conductivity of media
$L_{p_{m+I}}$	Hydraulic conductivity of IEL + media
$L_{p_{nj}}$	Hydraulic conductivity of normal junction surrounding an EC
L_{p_t}	Total hydraulic conductivity of the vessel wall
Pe	Permeability
Pe_{EC}	Permeability of EC to albumin
Pe_{nj}	Permeability of normal junction to albumin
P_e	Peclet number
P_{er_j}	Peclet number in radial direction in region j
P_{ez_j}	Peclet number in z direction in region j
P^*_j	Dimensional pressure in region j
P_j	Dimensionless pressure in region j
$\bar{P}^*_j$	Dimensional average pressure in region j
$\bar{P}_j$	Dimensionless average pressure in region j
P^*_L	Lumen pressure
P^*_{Lc}	Dimensional critical pressure
r	Dimensionless radial coordinate
r^*	Dimensional radial coordinate
r^*_f	Radius of fenestra
U^*_j	Dimensional lateral velocity in region j
U_j	Dimensionless lateral velocity in region j
R^*	Dimensional radius of EC
R	Dimensionless radius of EC
$\mathbf{V}$	Velocity vector
W^*_f	Dimensional water velocity through fenestra
W_j	Dimensionless normal velocity in region j
z	Dimensionless normal coordinate
z^*	Dimensional normal coordinate
f_j	filtration/retardation coefficient of albumin in region j

γ_j	Volume fraction of albumin per unit total volume of region j
σ_{EC}	Osmotic reflection coefficient of albumin through EC
σ_{nj}	Osmotic reflection coefficient of albumin through normal junction
π_j	Dimensionless osmotic pressure in region j
ΔR^*	Dimensional width of normal junction
ΔR	Dimensionless width of normal junction
ΔP	Dimensionless pressure drop across a membrane
$\Delta\pi$	Dimensionless osmotic pressure difference across a membrane
μ	Viscosity of fluid
ξ_I^*	Dimensional radius of periodic wall unit
ξ_I	Dimensionless radius of periodic wall unit

3.2.5 Constants and parameter values

Geometric parameters

Table 3.1 summarizes values of parameters and constants used in this study and their sources. Note that most of the geometric parameters used in this study are same as those employed in our previous study (Ch. 2) and also by Huang et al. (36). Our earlier study (Ch. 2) describes in detail the estimation of parameters required to solve the flow (filtration) problem. Here we will only describe the calculation for the mass-transfer model parameters.

Ogston et al. (65) derived the diffusion coefficient for a solute of radius r_s in a fiber matrix in terms of its diffusion coefficient D_f in free space as:

$$D = D_f \exp\left[-(1-\epsilon)^{1/2}\left(1+\frac{r_s}{r_f}\right)\right] \tag{3.25}$$

where ϵ is the fractional void volume and r_f is the fiber radius. The free diffusivity (D_f) of albumin (r_s = 3.5 nm (14)) is 6.8$\times10^{-7}$ cm^2/s (116). Based on the structural observations of Squire et al. (84) and Weinbaum et al. (122) and, as explained in our previous study (Ch. 2), one can estimate the void fraction (ϵ) of cylindrical GX fibers ($r_f = 6\,\mathrm{nm}$ (84)), arranged in a hexagonal array, to be 0.674. Thus Eq. 3.25 gives the diffusivity of albumin in GX region (D_g^*) as 2.75$\times10^{-7}$ cm^2/s. Using fluorescence correlation spectroscopy, Stevens and coworkers (91) found the diffusivity of

Table 3.1: Parameters and constants used in the model

Constant/Paramteter	Value	Reference
a^*, nm	2.37	(Ch. 2), a
L_g^*, nm	200	(132)
L_{i0}^*, nm	500	(36)
L_m^*, μm	141(rat), 125(rabbit)	(36, 78)
R^*, μm	12	(36)
r_f^*, μm	0.8	(36)
ΔR^*, nm	20	(36)
K_{P_g}, cm^2	4.08×10^{-14}	(Ch. 2)
K_{P_i}, cm^2	2.20×10^{-12}	(36, 41), b
γ_g	0.94	c
γ_i	0.94	b,c
γ_m	0.08	(101)
f_g	0.99	c
f_i	0.99	b,c
f_m	0.3	c
D_g^*, cm^2/s	2.75×10^{-7}	c
D_i^*, cm^2/s	3.76×10^{-7}	b,c
D_m^*, cm^2/s	1.296×10^{-8}	c
Pe_{EC}, cm/s	12×10^{-7}	(4)
Pe_{nj}, cm/s	1.21×10^{-3}	(4), d
σ_{EC}	1	e
σ_{nj}	0.17	(4)
μ, $\mathrm{kg/m}\cdot\mathrm{sec}$	7.2×10^{-4}	(31)
$L_{P_{EC}}$, $\mathrm{cm/sec}\cdot\mathrm{mmHg}$	3.38×10^{-8}	f
$L_{P_{nj}}$, $\mathrm{cm/sec}\cdot\mathrm{mmHg}$	6.09×10^{-5}	g

a: calculated using the fiber matrix theory and as explained in Ref. (35)

b: uncompressed SI value at zero transmural pressure, corresponding values for compressed SI (L_i^*) are calculated as explained in our previous study (Ch. 2)

c: estimated as explained in the text

d: estimated by making area correction A_{EC}/A_{nj} to the value 20×10^{-7} reported in Ref. (4)

e: since albumin can not flow through AQP1s

f: estimated from converged L_{P_e} and assuming AQP1's contribution to be 40% to L_{P_e}

g: estimated from L_{P_e}, $L_{P_{EC}}$ and Eq. 3.31

albumin in lung endothelial GX to be 4×10^{-7} cm^2/s, which is very close to our estimated value. To account for the presence of CG fibers along with PGs in the SI region, Huang et al.'s (35) fiber matrix theory replaces D_f in Eq. 3.25 and computes effective diffusivity in the SI region as:

$$D_i^* = D_f(\epsilon_{CG} + \epsilon_{PG} - 1) \exp\left[-(1-\epsilon_{CG})^{1/2}\left(1 + \frac{r_s}{r_{CG}}\right)\right] \exp\left[-(1-\epsilon_{PG})^{1/2}\left(1 + \frac{r_s}{a^*}\right)\right] \tag{3.26}$$

where ϵ_{CG} and ϵ_{PG} are void fractions of CG and PG fibers, respectively. r_{CG} is the radius of the collagen fibers (20 nm (35)) and a^* is the effective radius of the PG fibers (2.37 nm (Ch. 2)). At zero transmural pressure, ϵ_{CG} = 0.95 (35) and ϵ_{PG} = 0.99 (Ch. 2) and Eq. 3.26 yields D_i^* as 3.76×10^{-7} cm^2/s. Since PG and CG fibers are not known to swell, we do not account for the effect of swelling on the diffusivity of albumin in the SI region. Tedgui and Lever (101) measured the diffusivity of albumin in rabbit thoracic aorta as 7.2×10^{-9} cm^2/s. Since the media region consists of parallel layers of elastic sheets, the diffusivity of albumin in the direction parallel (here the r direction) to these elastic sheets must be higher than its diffusivity in the normal direction (here the z direction). Huang et al. (35) suggested a factor of 3 difference in these diffusivities. Using these numbers and considering contributions from radial (D_{mr}^*) and normal (D_{mz}^*) components, we estimate the effective diffusivity (D_m^*) of albumin in the media as 1.296×10^{-8} cm^2/s. Huang and Tarbell (38) accounted for the presence of smooth muscle cells (SMC) inside the media and derived an expression for the effective diffusivity (see Eqs. 50 and 51 in Ref. (38)). Assuming that the SMCs account for 40% of the media volume (38) and using Huang and Tarbell's theory (38), we estimate D_m^* as 1.21×10^{-9} cm^2/s. Karner and coworkers (42) use D_m^* as 1.48×10^{-7} cm^2/s in their study. Thus our value for D_m^* seems to be in the range of what has been used in the literature.

Curry (15) calculates the retardation coefficient f_j from the partition coefficient ψ_j as:

$$f_j = 1 - (1 - \psi_j)^2 \tag{3.27}$$

where $\psi_j = \gamma_j/\gamma_{wj}$ in region j is defined as the ratio of the fractional available volume for a solute (γ_j) to that available for water (γ_{wj}). The partition coefficient for a solute of radius r_s, in the randomly oriented fiber matrix, derives from (15):

$$\psi = \exp\left[-(1-\epsilon)^{1/2}\left(\frac{2r_s}{r_f} + \frac{r_s^2}{r_f^2}\right)\right] \tag{3.28}$$

where ϵ is the fractional void volume and r_f is the fiber radius.

For the sparse SI layer, $\gamma_{wi} \sim 1$ (35) and thus $\gamma_i \sim \psi_i$. Thus at zero transmural pressure, Eq. 3.28 yields the fractional volume available for albumin (γ_i) as 0.94 and from Eq.3.27, $f_i = 0.99$. Huang et al.'s (36) intimal compression theory, and their subsequent experimental evidence (37), argues that the SI layer, due to its sparse structure, undergoes compression upon pressure loading. The resulting change in the porosity of the SI layer should also alter the transport properties, like the diffusivity (D^*), retardation coefficient (f), available volume fraction (γ), of a tracer flowing through it. We use Eqs. 3.26 - 3.28 to also predict the variation of the transport parameters (f_i, γ_i, D_i^*) in the SI region by using the corresponding fractional void volumes $(\epsilon_{PG}, \epsilon_{CG})$ at different SI compressions. Our previous study (Ch. 2) explains in detail the calculation of these fractional void volumes for the compressible SI region.

Since the fractional void volume of the GX layer having fibers of radius 6 nm (84) is 0.674, Eq. 3.28 gives $\psi_g = 0.61$. Assuming $\gamma_{wg} \sim 1$ as in (19), we get $\gamma_g = 0.61$ and $f_g = 0.85$ from Eq. 3.27. Tedgui and Lever (101) measured the volume fraction of albumin in the media (γ_m) as 0.08 and together with $\gamma_{wm} \sim 0.5$ (35), Eq. 3.27 gives f_m = 0.3. Our model assumes that the GX and the media regions do not undergo any structural change upon pressure loadings, and thus $f_g, f_m, \gamma_g, \gamma_m, D_g^*$ and D_m^* are constant at all pressures.

Hydraulic conductivities:

Unlike the phenomenological $L_{P_{e+i}}$, the intrinsic hydraulic conductivity of the endothelium, (L_{P_e}), is a pressure-independent input parameter to the model. Its estimation begins by matching the experimental water flux (J_v^{exp}) at very low transmural pressures (where there is no fenestral blocking and where the SI offers negligible flow resistance) with that obtained from the model (J_v^{model}) at $L_i^* = L_{i0}^*$ to find L_{P_t}. The matching equations are:

$$J_v^{exp} = L_{P_t}\left[(P_L^* - P_A^*) - \sigma(\pi_L^* - \pi_A^*)\right] \tag{3.29}$$

$$J_v^{model} = \frac{\displaystyle\int_0^{\xi_I^*} W^* r^* dr^*}{\displaystyle\int_0^{\xi_I^*} r^* dr^*} \tag{3.30}$$

where P_L^* and π_L^* are the hydrostatic and osmotic pressures in the lumen while P_A^* and π_A^* are corresponding pressures in the adventitia region. L_{P_t} is the hydraulic conductivity of an intact artery wall. Tedgui & Lever (100) and Baldwin and Wilson (2) measured the L_{P_t} of rabbit aorta while Shou et al. (78) and Nguyen et al. (62) did analogous measurements on rat aorta at several transmural pressures. Table 1 in our earlier study (Ch. 2) lists all these data sets. The experimental measurements of L_{P_t} (78, 62) all used the same concentration of albumin (40 $\mathrm{gm/l}$) in the perfusate and superfusate solutions. Thus the oncotic pressures in the lumen and adventitia must be the same i.e., $\pi_L^* = \pi_A^*$ and J_v becomes $J_v^{exp} = L_{P_t}(P_L^* - P_A^*)$

We assume L_{P_e} equals the area-weighted average of the hydraulic conductivity of the normal junction ($L_{P_{nj}}$) and that of the EC ($L_{P_{EC}}$):

$$L_{P_e}\pi {\xi_I^*}^2 = L_{P_{EC}}\pi {R^*}^2 + 2\pi R^*(\Delta R^*/2)L_{P_{nj}} \tag{3.31}$$

To compute the L_{P_e}, we start by assuming that water enters the SI region through only normal junction i.e., we set $L_{P_{EC}}$= 0. With an assumed value of $L_{P_{nj}}$ (roughly estimated from Eq. 3.31 by

setting $L_{P_{EC}}$ = 0 and using $L_{P_{e+i}}$ in the place of L_{P_e} that is available from the experimental L_P data at lowest transmural pressure) and an uncompressed intima thickness (L^*_{i0}), we solve the flow and the mass transfer problem simultaneously as discussed in section 3.2.4 and compare the water flux obtained using Eq. 3.30 with experiments at low transmural pressures. This procedure is repeated until the numbers from both experiments and model calculations match. For Nguyen et al.'s (62) data, the converged L_{P_e} is 8.44$\times 10^{-8}$ $\mathrm{cm/s \cdot mmHg}$. Note that our previous filtration theory (Ch. 2) calculates L_{P_e} as 8.29$\times 10^{-8}$ $\mathrm{cm/s \cdot mmHg}$, $\sim 2\%$ lower than current calculations. Since this parameter is intrinsic, we retain this value of L_{P_e} for all intima compressions and pressures.

The Darcy permeability of the media region (K_{P_m}) is estimated from its hydraulic conductivity (L_{P_m}) as: $K_{P_m} = L_{P_m} \times \mu \times L^*_m$, where μ is the fluid viscosity and L^*_m is the thickness of the media. As shown by Huang et al. (36), the L_P of the media is obtained by invoking the flow incompressibility and equating the water fluxes across the IEL and media. Using this method, we obtain L_{P_m} as 7.5$\times 10^{-8}$ $\mathrm{cm/sec \cdot mmHg}$ (Ch. 2) for Nguyen et al.'s (62) data.

3.3 Results and discussion

3.3.1 The effect of $\Delta\pi$ on pressure distribution in the SI

Figure 3.2 shows the pressure distribution inside the SI layer (non-dimensioanlized by the lumen pressure, P_L^*) underneath the EC (at $z_i = 1$) and compares the predictions of the current model with those of our earlier (Ch. 2) filtration-only model. At low transmural pressure, the SI is relatively uncompressed and, because of its sparse nature, offers very little resistance to water flow. This results in an almost r-independent pressure distribution in the SI; see Fig. 3.2(a). However, at higher transmural pressures, the increasing force acting on the endothelium compresses the SI region and decreases it's Darcy permeability (K_P). The decrease in K_P, along with the IEL fenestral blockage by the ECs, drastically increases the resistance to water flow and results in a significant pressure drop as water radially traverses the SI from the normal junction to the fenestra, as shown in Fig. 3.2(b).

Without mass transfer, the SI pressure does not change with pressure until a SI compression is reached (at 60 mmHg) where the blocking of the IEL fenestrae begins to impede fenestral flow, as seen by the significant departure of the pressure curve from the horizontal. At lower transmural pressures, as Fig. 3.2(a) shows, the pressure inside the SI region predicted using the coupled filtration & mass-transfer model is significantly higher than the predictions from our filtration model (Ch. 2). We find that the average pressure in the intima obtained using current model is approximately 25%,16%, 13%, 11% and 8% higher than the predictions of filtration model, at 10, 20, 30, 40 and 50 mmHg, respectively. The reason behind these higher predictions, which requires the estimation of oncotic forces, will be discussed later. With increasing transmural pressure, the difference between the predictions of the two models gets smaller (up to $\sim$4% at 70 mmHg), and practically no difference is seen at 80 and 90 mmHg, see Fig. 3.2(b). These predictions suggest that oncotic forces have a strong effect on the SI pressure distribution at lower pressures than at higher transmural pressures.

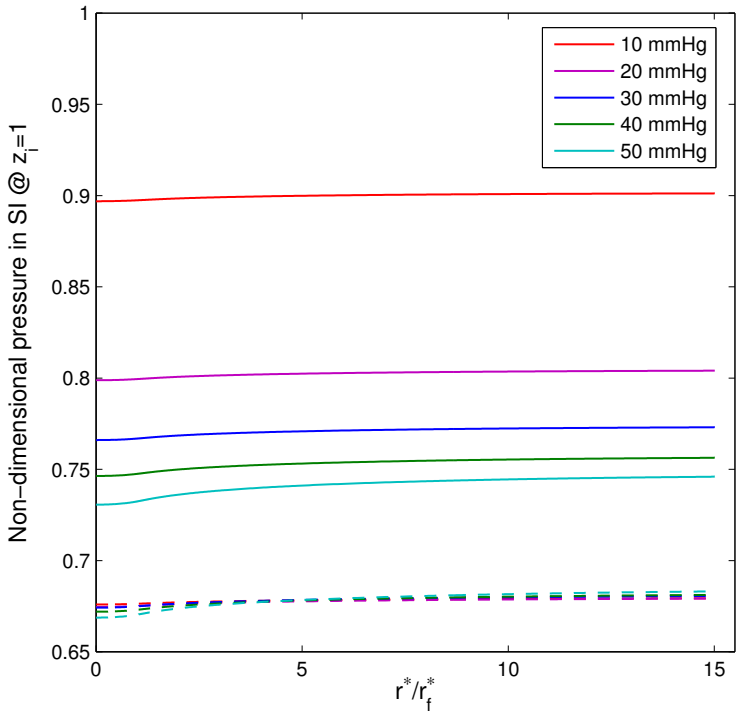

(a) P_L^* = 10 - 50 mmHg

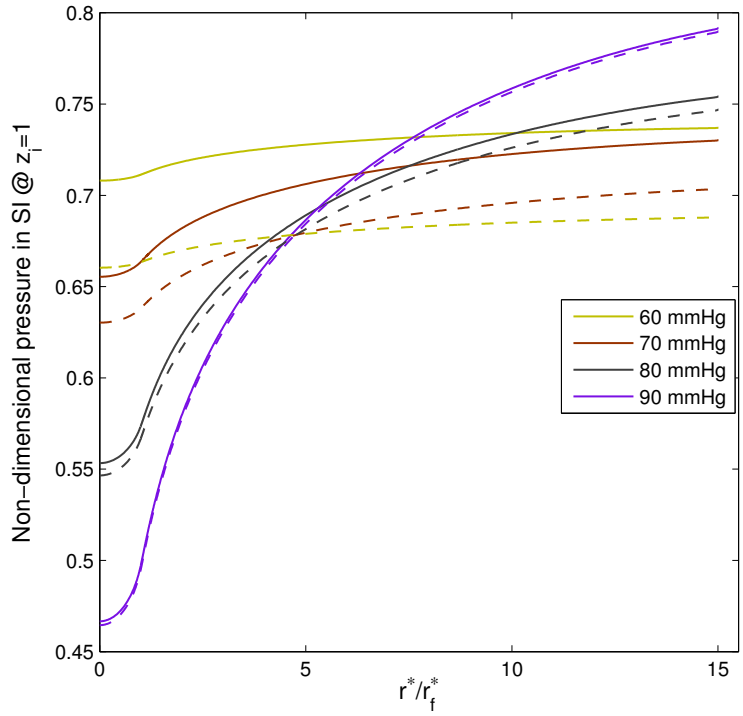

(b) P_L^* = 60 - 90 mmHg

Figure 3.2: Non-diemsional pressure in SI at z_i =1 as a function of radial distance at various transmural pressures. Solid lines - with mass transfer, dashed lines - filtration only

3.3.2 Velocity near fenestra

Figure 3.3 shows the normal velocity in the SI, in the fenestra region, at different z-locations at and above the IEL. Because of the assumed impermeability of IEL outside of the fenestra and thus the zero flux condition used in our model there (see Eq. 3.12), the normal velocity, shown by the blue curve in Fig. 3.3, is zero over the IEL surface $(r^*/r_f^* > 1)$. Interestingly, since the Darcy flow satisfies potential flow equation, the flow exiting the fenestra results in a velocity overshoot very close to it's edge $(r^*/r_f^* \sim 1)$, shown by a peak in Fig. 3.3 at $z_i = 0$. Note that, for potential flow, the normal velocity diverges at the corner of the fenestra and the IEL and thus results in a singularity there. We numerically avoid this singularity by positioning a grid point very close to, but not at the edge of the fenestra $(r^*/r_f^* = 1)$. The resulting velocity overshoot plotted at this grid point is finite, as shown in Fig. 3.3. This peak velocity rapidly decreases in a very short distance from the edge of fenestra (between 0.98$< r^*/r_f^* <$1) and looses it's r-dependence further inside the fenestra $(r^*/r_f^* < 0.9)$. Others have seen hints of this singularity in analogous flows. Feng and Weinbaum (23) used Brinkman's equation to describe the flow through an orifice surrounded by a fibrous structure and presented an analytical solution of the boundary value problem. They showed that as the Darcy permeability of the fiber structure gets smaller (approaching values typical of biological tissue), the flow approaches a Darcy potential flow. Their results exhibited a velocity minimum at the center of orifice and a sharp increase in velocity near its edge. Tada and Tarbell (96) numerically solved the interstitial flow through the SI and media of an artery wall and investigated the water flow distribution through the fenestral pores. They also found a sharp velocity overshoot near the edge of fenstra as water exits the fenesta and enters the media region. Overall, our result showing a marked velocity overshoot close to the edge of fenestra is to be in good agreement with these literature models.

The velocities above the IEL also clearly demonstrate a z-dependence in the SI, especially near the fenstra. These profiles have a minimum above the singularity at the fenestral edge, whose magnitude decreases and eventually disappears with z. That is, the normal velocity in the fenestra becomes r-independent away from the IEL surface; see $z_i = 40\Delta z_i$ curve in Fig. 3.3. Note that

the normal velocities on the right side of fenestra ($r^*/r_f^* > 1$) are distinctly non-zero near the edge of fenestra ($\sim 1 < r^*/r_f^* < 1.15$) and asymptote to zero as r increases ($r^*/r_f^* > 1.15$). This result means that the SI flow looses it's z-component and becomes purely radial (radial slit flow with wall slip) away from the fenestra.

Fig. 3.4 shows the effect of increasing lumen pressure on the exit velocity through the fenestra. The peak overshoot and the overall velocities in the fenestra region ($r^*/r_f^* < 1$) increase as the lumen pressure is raised. The distance from the edge of fenestra over which the velocity profiles relax to their r-independent values also increases with increasing lumen pressure. The increasing intimal compression and resulting fenestral blockage upon pressure loadings significantly increases the resistance to incoming water flow near the fenestra. This results in significant pressure gradients not only in radial but also in the normal (z) direction and consequently in higher normal velocities in the fenestra region, as depicted in Fig. 3.4.

3.3.3 Velocity streamlines

Figure 3.5 shows streamline contour plots of the water flow in the SI region at different transmural pressures with corresponding SI thicknesses. In all four panels in Fig. 3.5, a flow from the right converges into the fenestra ($r = r^*/r_f^* < 1$) and enters the media (not shown). The stream lines at low transmural pressures and thick SI, Figs. 3.5(a) and (b), have highest curvature near the fenestral edge. Higher transmural pressures and thus pressure gradients compress the SI, i.e., force the flow faster through a thinner SI; the result is a predominantly radial flow up until the fenestral edge, where it abruptly changes direction, while maintaining a much stronger radial component than the lower pressure curves (Figs. 3.5(c) and (d)).

3.3.4 Peclet number in radial direction

Let the radial Peclet number (P_{er}) be the radial velocity in the SI non-dimensionalized as $P_{er} = \dfrac{f_i |U_i^*| r_f^*}{\gamma_i D_i}$, where $|U_i^*|$ is the absolute radial velocity in the intima. Figure 3.6 plots (P_{er}) beneath the EC ($z_i = 1$) with increasing transmural pressure. The Peclet number curves reach

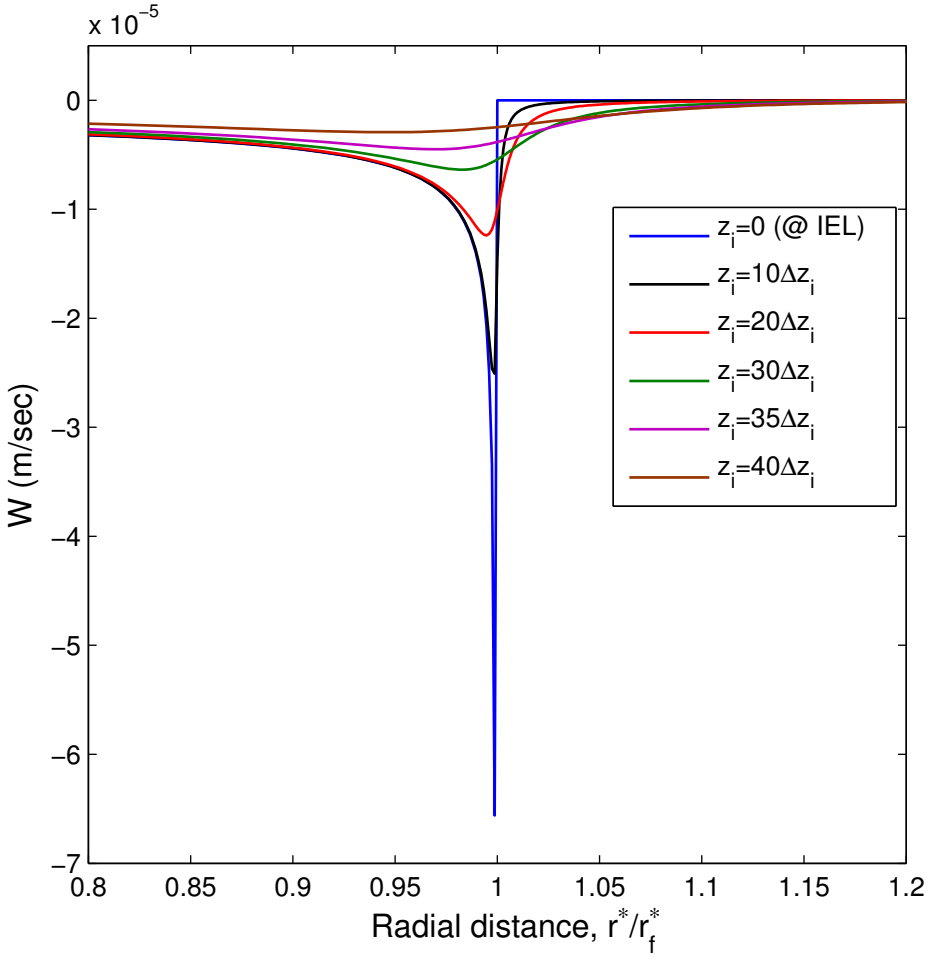

Figure 3.3: Normal velocity (W) at $(z_i = 0)$ and above the IEL $(z_i > 0)$ in the SI as a function of radial distance. Note that W is negative because the water flow is in the negative z direction. The IEL is at $z_i = 0$ and the fenestra is located between $0 < r^*/r_f^* < 1$, Δz is the distance between grid points in the z direction, P_L^* =60 mmHg.

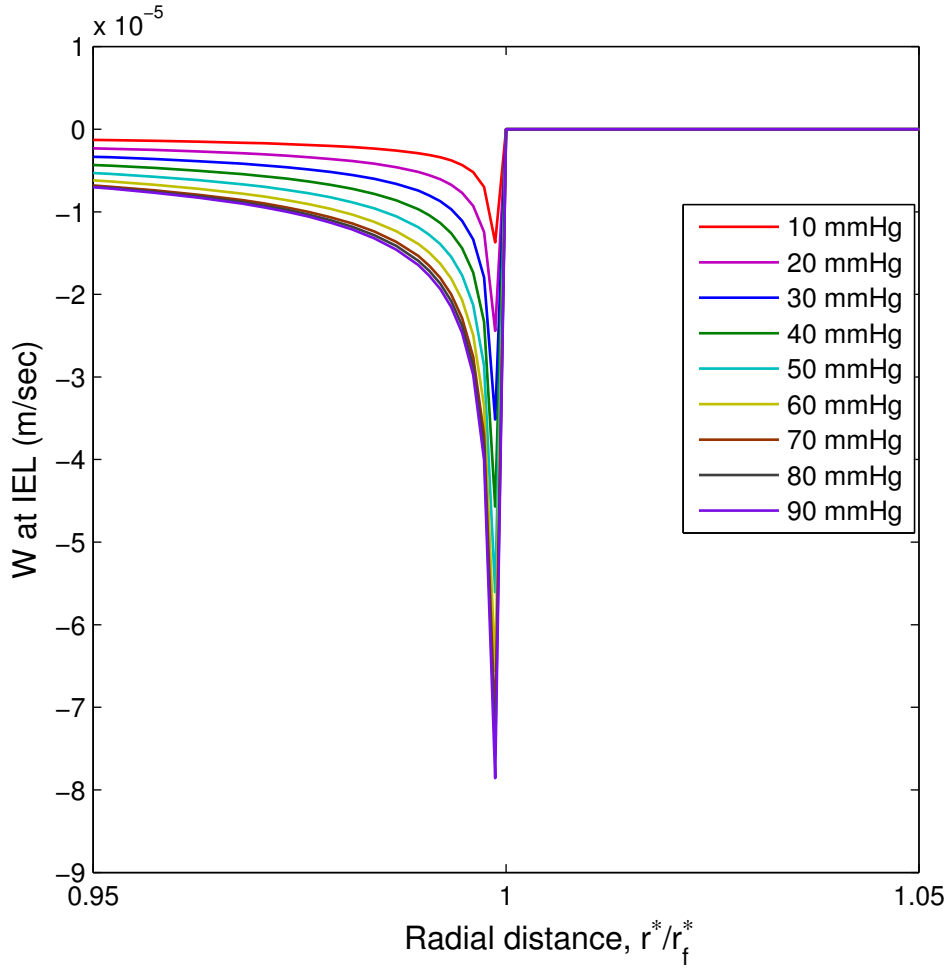

Figure 3.4: Effect of increasing transmural pressure on the exit normal velocity from the fenstra as a function of radial position. Tthe IEL is at $z_i = 0$ and th efenestra is located between $0 < r^*/r_f^* < 1$

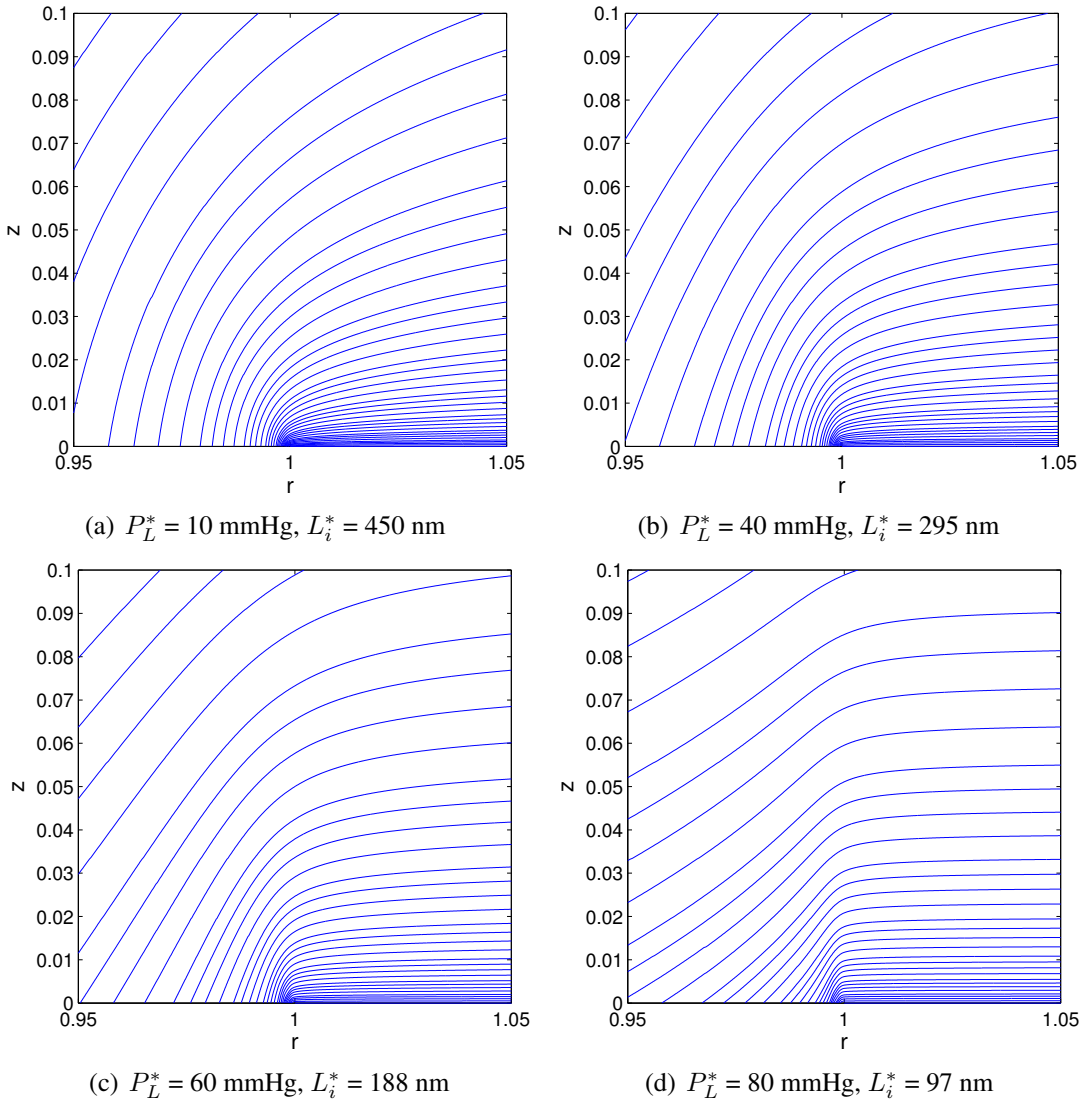

(a) P_L^* = 10 mmHg, L_i^* = 450 nm

(b) P_L^* = 40 mmHg, L_i^* = 295 nm

(c) P_L^* = 60 mmHg, L_i^* = 188 nm

(d) P_L^* = 80 mmHg, L_i^* = 97 nm

Figure 3.5: Streamline contour plots of the interstitial flow in the SI near the fenestra at four transmural pressures. In all the panels, the flow direction is from right to left. Fenestra is located at $r < 1,\ z = 0$

.

a maximum near the edge of fenestral pore ($r^*/r_f^* = 1$) as the radial flow converges and decay to zero due to axisymmetry at the center of the domain ($r = 0$). The maximum radial velocity/ radial pressure gradients near the edge of fenestra increases with transmural pressure. The Peclet numbers at low transmural pressures (up to $\sim$ 40 mmHg) are very small ($P_{er} \ll 1$) and almost uniform in r. This implies that at lower pressures diffusion dominates advection in the transport of albumin through porous SI region. However, at higher transmural pressures, P_{er} is substantially higher as water travels radially in the SI and advection competes with and dominates diffusive transport. The region where advection dominates diffusion ($P_{er} > 1$) extends to $r^*/r_f^* \sim 3.5$ in the SI at 90 mmHg, and decreases to ~ 2 at 80 mmHg.

3.3.5 Concentration of albumin in SI:

Fig. 3.7 plots the concentration of albumin (non-dimensionalized by the lumen concentration) in the SI beneath the EC, as a function of r at various transmural pressures, with the albumin concentration in the GX for reference. The GX concentration exhibits negligible pressure or r-dependence. The results with L_g^*= 500 nm (not shown) are not significantly different from the ones obtained with L_g^*= 200 nm. At most, near the normal junction region, the difference is in the fourth significant digit and much smaller everywhere else, suggesting a minor dependence on the thickness of the GX layer.

Surprisingly, as Fig. 3.7 shows, the concentration of albumin in the SI is everywhere greater than unity (the lumen concentration) at transmural pressures from 10 to 60 mmHg. For higher transmural pressures, the concentration is significantly higher in the fenestral region ($0 < r^*/r_f^* < 1$), but decreases to values below one away from the fenestra, despite the fact that most of the fluid and solute enter the SI through the junctions, far from the fenestra. This points to media involvement. By varying the media void space we find an unexpectedly strong effect on albumin's SI concentration. The small media filtration coefficient ($f_m = 0.3$) of albumin causes the media to act like a coffee filter, inhibiting the motion of albumin through it, with the filter cake backing up into the SI. This is the meaning of the high concentrations (> 1) and concentration maxima above

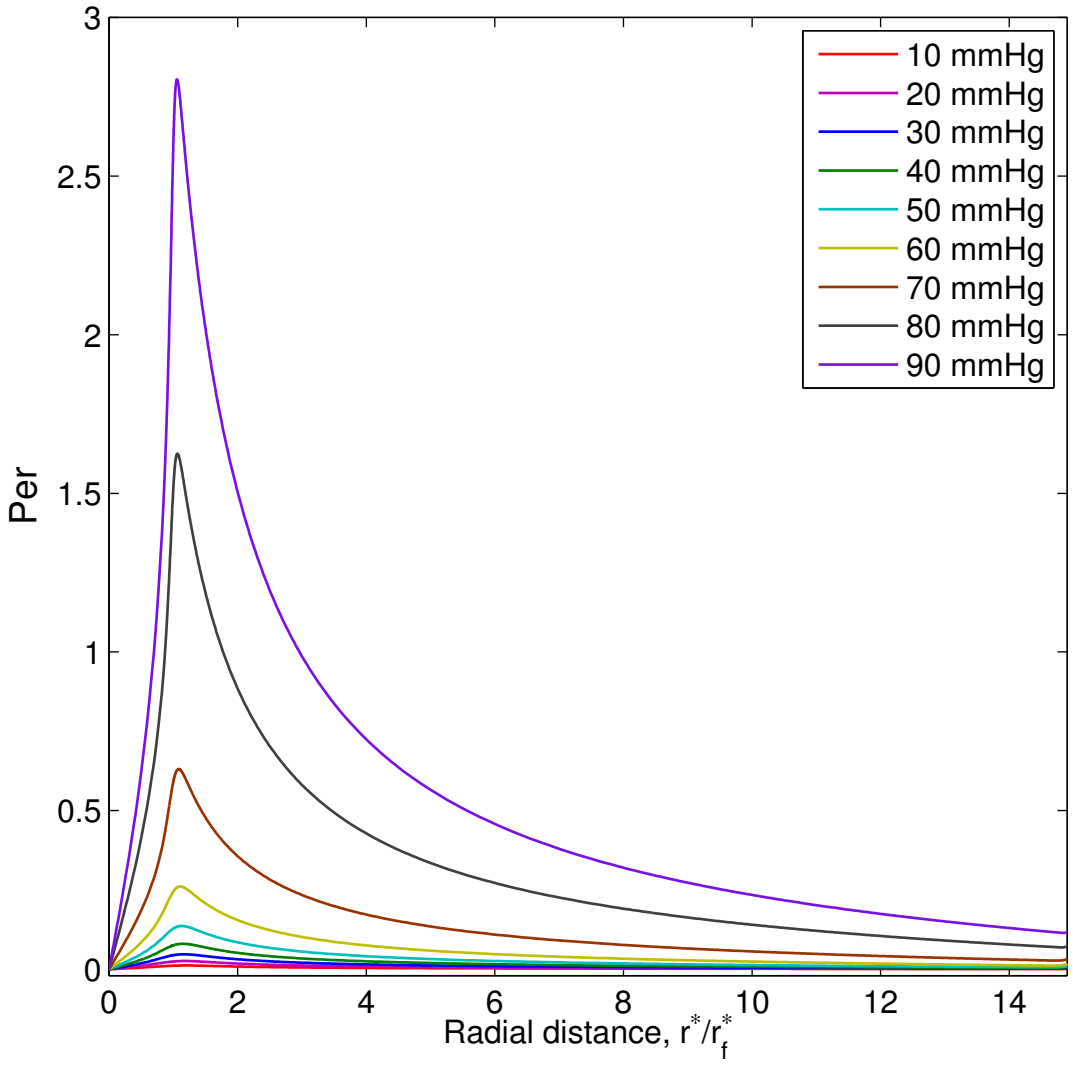

Figure 3.6: Effect of increasing transmural pressure on the Peclet numbers (scaled radial velocities) in the SI at $z_i = 1$ as a function of radial distance. The fenestra is located between $0 < r^*/r_f^* < 1$.

the fenestra in Fig. 3.7.

At low transmural pressures (up to 30 mmHg), the SI concentration profiles are nearly r-independent. Since P_{er} is very small at such low pressures (Fig. 3.6), the diffusion dominated transport smoothes and flattens out albumin's SI concentration. With increasing lumen pressure, the concentration of albumin increases in the direction of flow (from the junction towards the fenestra) to a maximum at $(r = 0)$. The larger Peclet numbers at higher transmural pressures (Fig. 3.6) due to both higher radial velocities and lower solute diffusivities in the compressed SI, more effectively advect albumin toward the fenestra in the SI, against back-diffusion, resulting in smaller regions with albumin concentrations above one.

Gibbs-Donnan equilibrium affects the plasma osmolality by altering the distribution of Na^+ and Cl^- ions in the plasma and in the interstitial fluid to maintain electroneutrality (61). The negatively charged protein molecules in the plasma space (including albumin) attract cations like Na^+ and K^+ and thus lead to higher concentration of these diffusible cations compared to the concentration of diffusible anions in the plasma compartment. The electrostatic forces arising here dominate the effects of concentration gradients in determining the movement of Na^+ ions. As a result purely of this Gibbs-Donnan effect, at equilibrium in a non-flowing system, the total osmolar concentration in the plasma becomes slightly greater than that in the interstitial space, where the albumin space is less than one, than what is purely due to this albumin space mismatch. These diffusible ions augment the usual colloid osmotic forces deriving from anionic proteins in the lumen (Typically, for a 20 mmHg oncotic pressure difference due large protein molecules like albumin, the Gibbs-Donnan effect contributes an additional 5-10 mmHg.), which results in a greater water content of the lumen relative to that of the vasculature tissue than what would be predicted on the basis of protein concentration alone (7). This effect becomes more pronounced with increasing albumin concentration.

In contrast to the equilibrium, no flow case discussed above, in our system, our calculations show that the transmural flow causes the SI region, which is $\sim 95\%$ void and, varies from $\sim$ 95-80% for different transmural pressures, to attain albumin concentrations that exceed the lumen

concentration. Let us examine the Donnan consequences of this imposed concentration difference. Recall, the SI ECM contains large amount of negatively-charged proteins such as proteoglycans. It is likely that these negative charges, along with those of the accumulated albumin, further enhance the Donnan effect in the SI above that in the lumen. Thus at lower transmural pressures where oncotic forces are comparable to hydrostatic forces (see Fig. 3.8), the Donnan effect would further increase the $\Delta\pi$ across the EC and lead to even higher overall driving forces for transmural water flow than what our model predicts. At higher transmural pressures (beyond 70 mmHg), where oncotic forces become less significant relative to hydrostatic forces, the augmentation of the Donnan effect very likely also becomes less significant. However, at higher transmural pressures, which result in significant SI compression, the SI concentration of the negatively charged PG fibers increases. This should increase the fractional augmentation to $\Delta\pi$ due to the Donnan effect at these higher transmural pressures, but since $\Delta\pi$ is small at these pressures, we do not expect a significant effect due to this augmentation.

Perhaps much more interesting, Figure 3.7 shows that the SI albumin concentration exceeds its GX concentration for all r at all transmural pressures. At lower pressures this difference is nearly uniform in r and is higher than the difference at higher pressures, where the main difference between the two concentrations is only near the fenestra region. This means that the oncotic pressures in the SI beneath the EC is in fact significantly *higher*, not lower as one would naively think, than the oncotic pressure in the GX on the luminal side of the EC. Thus, the resulting oncotic forces drive water flow from the lumen across the EC AQP1s into the SI, i.e., in the same direction of ΔP driven flow, and not the other way around. This resolves the apparent paradox of ΔP being able to drive the steady trans-EC AQP1 hypotonic pure water flow into the SI without creating a large oncotic counter-gradient.

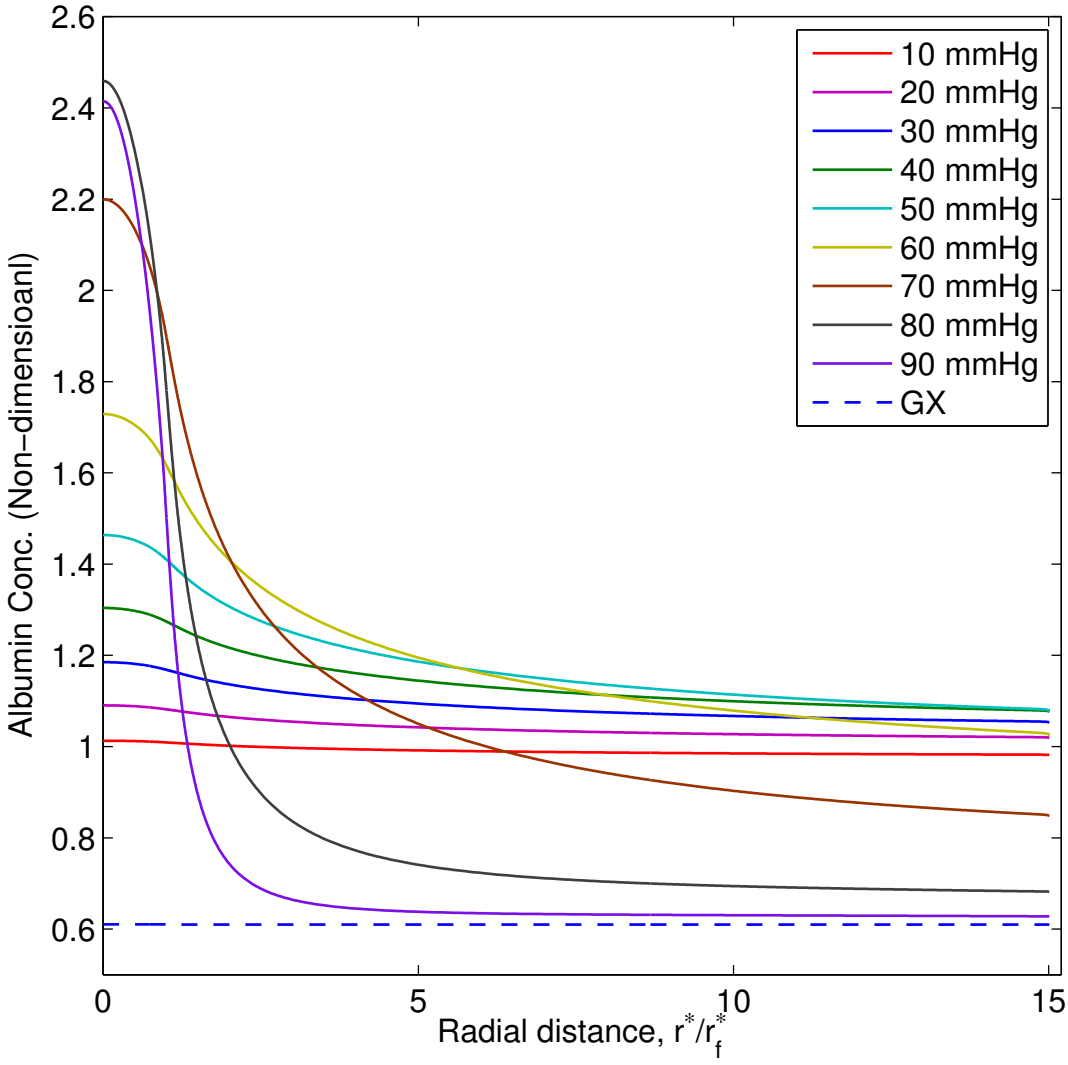

Figure 3.7: The effect of increasing transmural pressure on the non-dimensional concentration of albumin in the SI at $z_i = 1$ as a function of radial distance. The fenestra is located between $0 < r^*/r_f^* < 1$. The dashed line represents the albumin concentration in the GX.

3.3.6 Driving forces across the EC:

Let the area averaged hydrostatic and oncotic pressures be:

$$\bar{P}_j = \frac{\int_0^{\xi_I} P_j \, r \, dr}{\int_0^{\xi_I} r \, dr}, \qquad \bar{\pi}_j = \frac{\int_0^{\xi_I} \pi_j \, r \, dr}{\int_0^{\xi_I} r \, dr} \quad (j = g, i)$$

Fig. 3.8 plots the variation in the hydrostatic and the oncotic force per unit EC area (henceforth the per-unit-area will be understood), i.e. hydrostatic ($\Delta P = \bar{P}_g - \bar{P}_i$) and oncotic ($\Delta\pi = \bar{\pi}_g - \bar{\pi}_i$) pressure differences across the EC, as a function of transmural pressure.

The hydrostatic force across the EC increases linearly at low transmural pressures up to $\sim$ 60 mmHg. The rate of increase then decelerates as the SI compresses and the ECs begin to block the fenestae. Beyond the SI compression limit $\sim$ 90 mmHg, no further compression occurs and a linear increase resumes. Interestingly, the oncotic forces across the EC are negative at all transmural pressures i.e., the oncotic pressure difference itself is always pushing fluid from the GX into the SI region, as does the hydrostatic pressure difference. In fact, the hydrostatic and oncotic forces are of similar sizes, meaning the resulting force $(\Delta P - \sigma\Delta\pi)$ is then nearly double the ΔP alone, until about 60 mmHg; neglecting oncotic forces can significantly under-predict the driving force and the overall water flux across the EC. As shown in Fig. 3.7, the increasingly higher SI concentrations of albumin found at lower transmural pressures (from 10 - 50 mmHg) increase the magnitude of oncotic forces in Fig. 3.8. Beyond 60 mmHg, the decrease in overall concentration of albumin (see Fig. 3.7) reduces the oncotic pressure (π_i) in the SI region and lowers the magnitude of oncotic forces to 2-3% of ΔP, i.e., hydrostatic forces dominate oncotic forces, for transmural pressures $>$ 80 mmHg.

3.3.7 Hydraulic conductivity: AQP1s open

Figure 3.9 predicts the variation in the intact wall's L_P with pressure and the effect of various assumed AQP1 contributions ($L_{P_{EC}}$) on it. In all of these predictions, L_{P_e} is fixed and Eq. 3.31

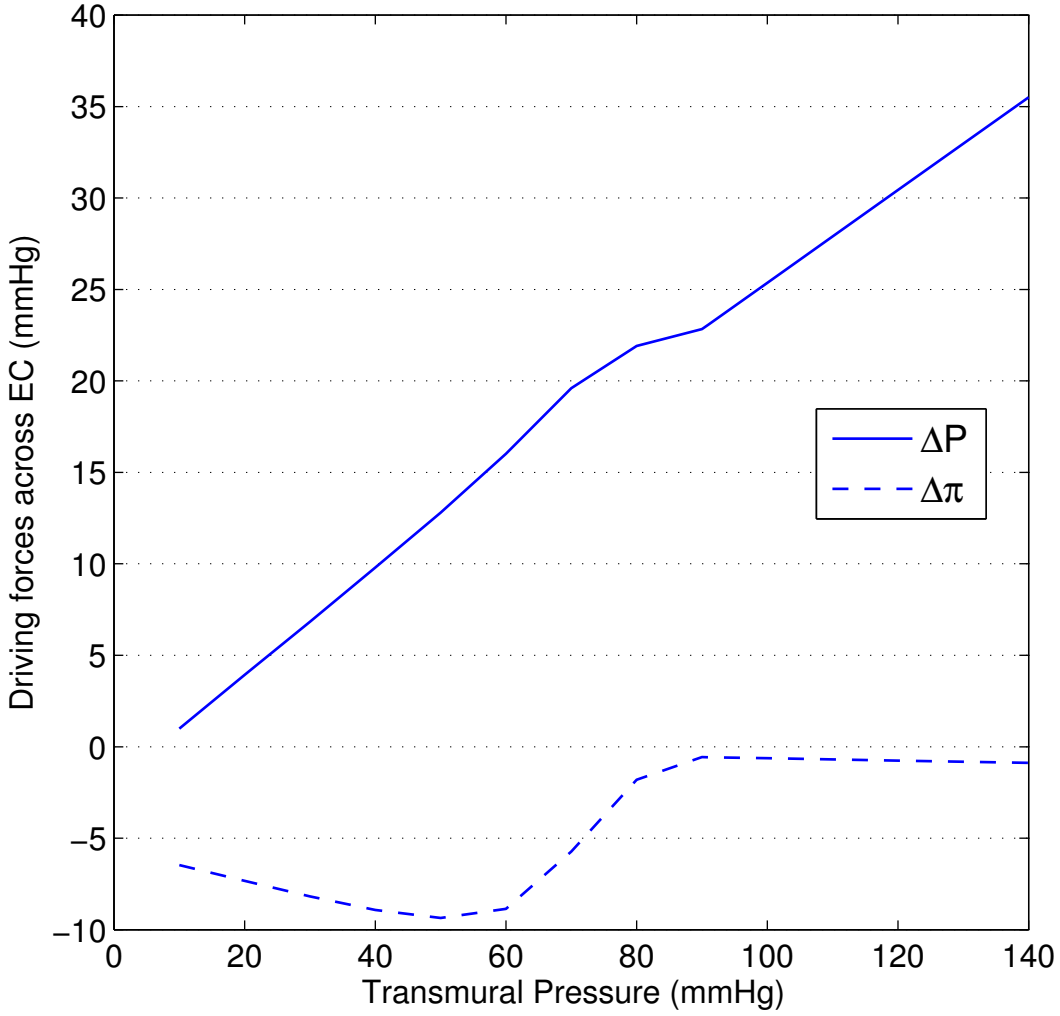

Figure 3.8: Variation in hydrostatic (ΔP) and oncotic $(\Delta\pi)$ forces per unit EC area across the EC with increasing transmual pressure. $\Delta P := (\bar{P}_g - \bar{P}_i)$ and $\Delta\pi := (\bar{\pi}_g - \bar{\pi}_i)$. $\bar{P}$ and $\bar{\pi}$ are the area averaged hydrostatic and oncotic pressures, as defined in the text. $\Delta\pi$ is negative, i.e., $\bar{\pi_g} < \bar{\pi}_i$, meaning that oncotic forces are pushing fluid from the GX towards the SI, at all trasmural pressures.

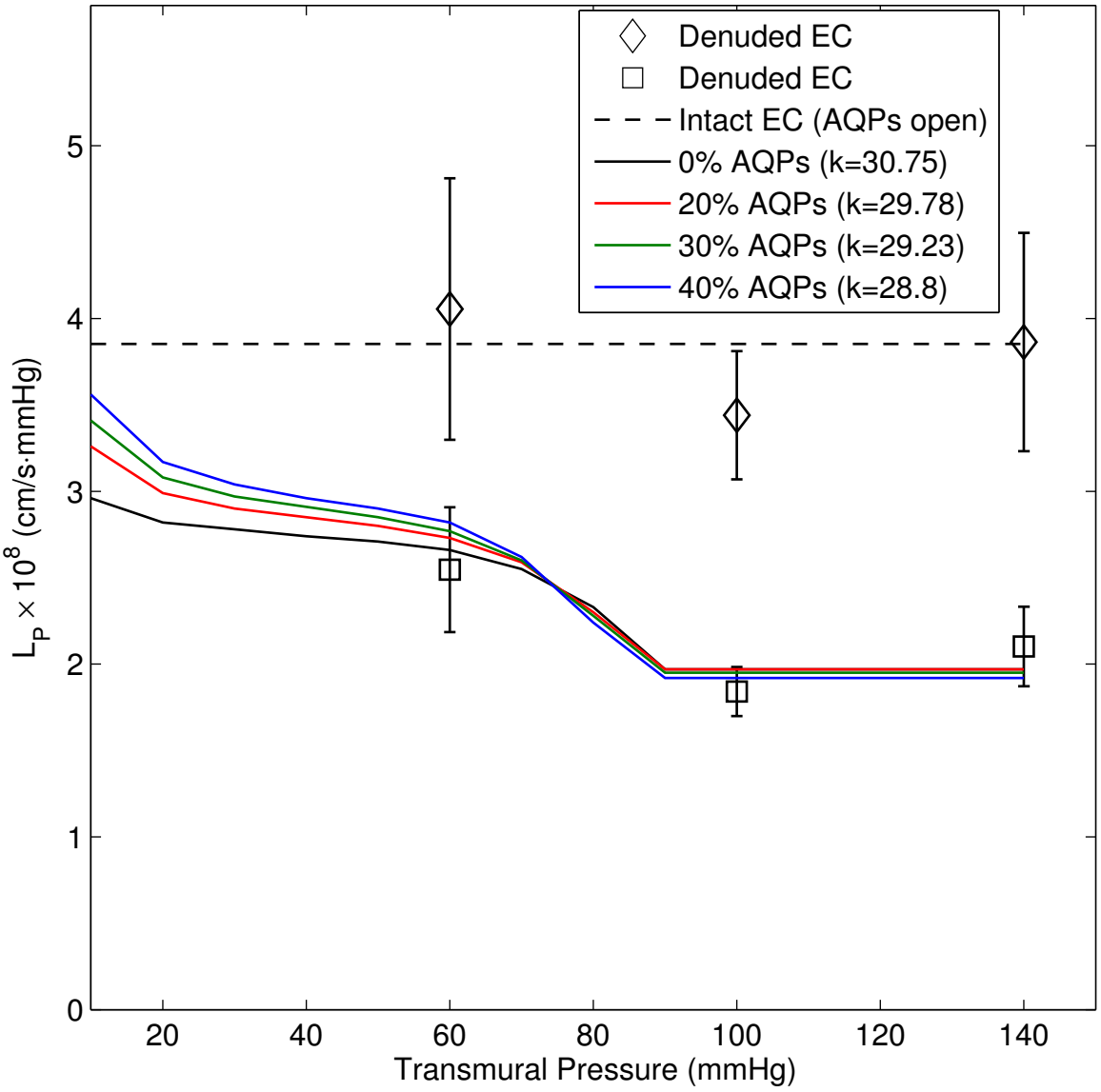

Figure 3.9: Hydraulic conductivity of the intact artery wall with open/functioning AQP1s and of the denuded artery wall, both compared with Nguyen's data (62). Lines - model predictions, symbols - experimental data. L_{P_e} is fixed at all assumed AQP1 fractions and Eq. 3.31 gives its corresponding decomposition into $L_{P_{EC}}$ and $L_{P_{nj}}$

decomposes it into $L_{P_{EC}}$ and $L_{P_{nj}}$ for each fraction of L_{P_e} due to AQP1s. For each assumed AQP1 fraction, we calculate J_v across the vessel wall (using Eq. 3.30) at the experimental transmural pressures and compare these predictions with the corresponding experimental J_v observations (62). The SI thickness for a particular transmural pressure is varied until the experimental and model J_vs match. As explained in our previous study (Ch. 2), we assume the SI acts as a Hookean spring (with transmural pressure-independent spring constant or SI elastic coefficient k in mmHg) that compresses upon pressure loading to give an implicit relation between force per unit area acting on the EC and the SI compression as:

$$P_L^*(\bar{P}_g - \bar{P}_i) = k\left(1 - \frac{L_i^*}{L_{i0}^*}\right) \tag{3.32}$$

According to Eq. 3.32, for each assumed AQP fraction, a plot of SI compression (from the converged J_v values) vs transendothelial force/area gives us an effective spring constant (k). The spring constant decreases with increasing AQP1 contribution to L_{P_e} (see legend in Fig. 3.9) because the larger the AQP1 fraction the lower the force on the endothelium corresponding to a given experimental compression. With an effective k for a given AQP1 fraction, one can estimate J_v and thus L_P at any transmural pressure by finding a SI thickness that satisfies both sides of Eq. 3.32.

The L_P of an intact artery wall for a given AQP1 fraction, plotted in Fig. 3.9, decreases quickly at very low transmural pressures (< 20 mmHg), then more slowly until ~ 60 mmHg. Beyond 60 mmHg, a sharp decrease in L_P occurs, as previously, due to SI compression and fenestral blockage, until the SI reaches its critical compression limit, corresponding to the lowest experimental L_P value. Beyond that, the stiff collagen fibers in the SI (24) prevent further compression and render L_P constant (36, 41). Overall we find good agreement between our model predictions and Nguyen et al.'s (62) experimental L_P observations. Recall that our predictions for the hydraulic conductivity of the intact vessel wall obtained using the filtration-only model (see Fig. 2.10 in Ch. 2) did not exhibit any appreciable dependence of the fraction of AQP1s on L_{P_t}. In contrast, the predictions from the coupled filtration and mass-transfer model, shown in Fig. 3.9,

do exhibit an increase in L_P with increasing transcellular water transport (and corresponding decrease in junctional water transport) from 0 to 40%. This is due to the oncotic forces that act in the same direction as hydrostatic force and raise the overall water flow across the endothelium and the vessel wall. The oncotic forces increase (results not shown) with increasing $L_{P_{EC}}$, raising L_Ps as Fig. 3.9 shows. At higher transmural pressures ($>$ 70 mmHg), the oncotic forces become far less significant (see Fig. 3.8) and the drop in L_P in Fig. 3.9 is simply due to fenestral blockage with hydrostatic pressure-induced SI compression. Note that this observed drop in L_P is sharper than our earlier prediction (Fig. 2.10 in Ch. 2). Moreover, increasing EC AQP1s render this drop even sharper. Removing the endothelial layer eliminates EC AQP1s and also the possibility of both SI compression and subsequent fenestra blockage. Denudation then result in constant (higher) L_Ps, as confirmed by experimental observations of Nguyen (62) shown in Fig. 3.9.

3.3.8 Hydraulic conductivity: AQP1s blocked

It is well-known that submillimolar concentration of $HgCl_2$ and other salts such as $AgCl_2$ can chemically block water transport through aquaporins by associating with the cystene group at the pore entrance and that this blocking is reversible by reduction of this association with 2-mercaptoethanol (56). One group has also reported a similar effect with the far more easily reversible (by dilution) tetraethyl ammonium chloride (TEA-Cl). Submillimolar concentrations of $HgCl_2$ have also been shown to inhibit the AQP1 expression in red blood cells (115). To minimize the toxicity effects associated with $HgCl_2$, Nguyen et al. (62) used micromolar $(5\,\mu\mathrm{M})$ concentration of $HgCl_2$ and investigated the role of AQP1s in the overall transport across the artery wall. Their results show a marked decrease of $\sim 32\pm4\%$ in the hydraulic conductivity of the intact vessel wall at 60 mmHg and smaller ($\sim 11\pm2$ & $5\pm2\%$) yet still statistically significant decreases at 100 and 140 mmHg upon chemical blocking of AQP1s. Note that all nine measurements (including the three for the denuded vessel) were taken on each vessel and the error bars on the data shown in Fig. 3.10 represent standard deviations among vessels from different animals. A plot of the statistics of the percentage drop in L_P for each vessel upon chemical blockage (62) indeed clearly shows these

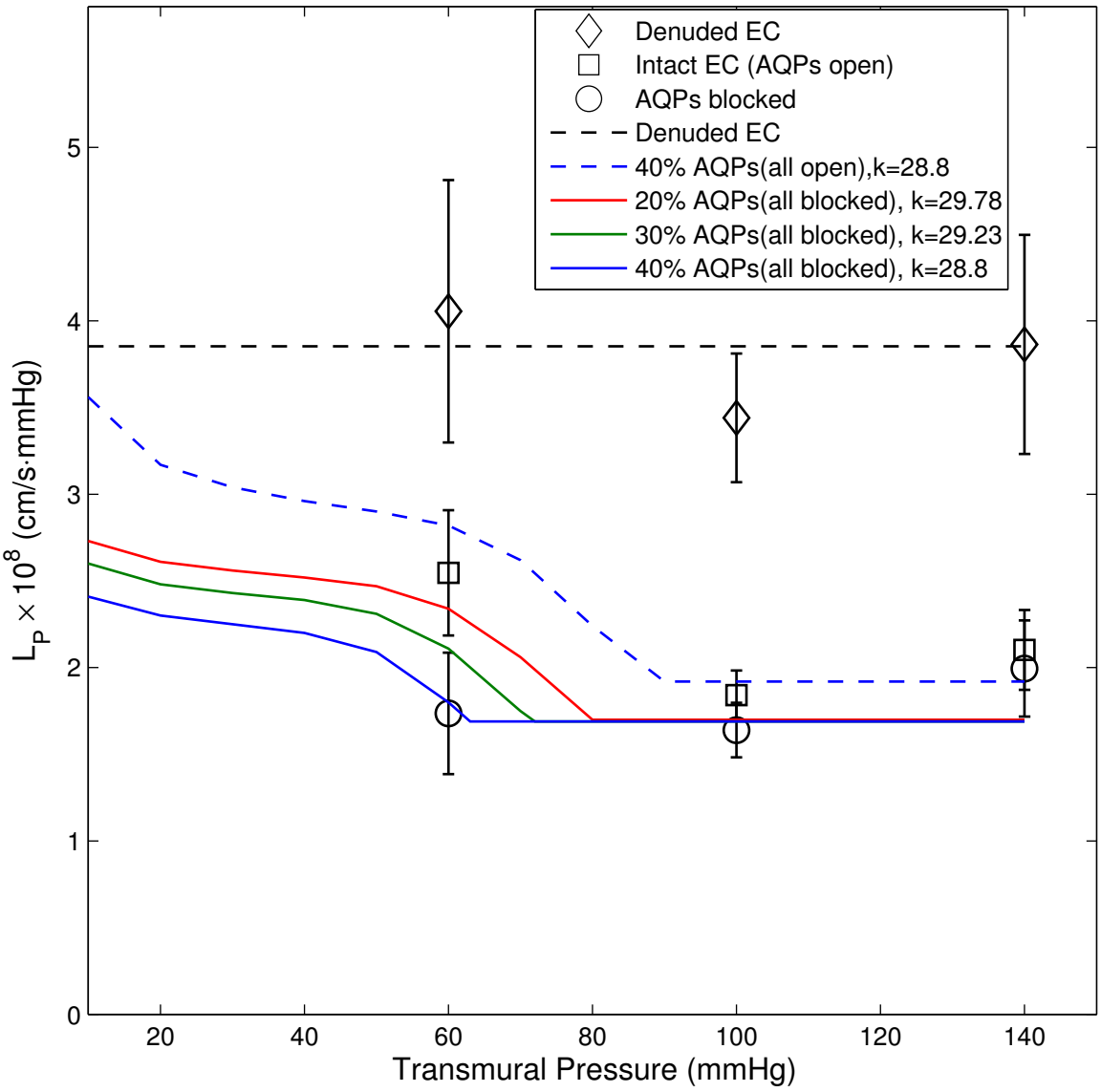

Figure 3.10: Hydraulic conductivity of the intact artery wall with blocked/non-functioning AQP1s and comparison with Nguyen's blocked AQP1 data (62). Lines - model predictions, symbols - experimental data. The $L_{P_{EC}}$ portion of L_{P_e} is set to be zero to mimic the experimental blocking of AQP1s with $HgCl_2$ (solid lines). Keeping the same L_{P_e}, Eq. 3.31 gives corresponding $L_{P_{nj}}$ for an assumed AQP1 fraction. For comparison, the dashed blue curve represents L_P for (functioning) AQP1s that contribute 40% to L_{P_e}. It is the same as the solid blue curve in Fig. 3.9.

statistical significances.

It is known that $HgCl_2$ at these concentrations is known to block only about 1/3 of available AQP1 channels (127). However, since a transendothelial pathway for water transport must involve at least two, and maybe more AQP1 molecules in series, in order to investigate the significance of AQP1s in overall water transport, we assume that this treatment with $HgCl_2$ blocks all AQP1 pathways across the EC; therefore we set $L_{P_{EC}} = 0$. We begin by assuming a fixed fraction of the total trans-endothelial L_{P_e} due to AQP1s ($L_{P_{EC}}$) and corresponding $L_{P_{nj}}$ from Eq. 3.31. Using this value of $L_{P_{nj}}$ and by setting $L_{P_{EC}} = 0$, we estimate L_{P_t} at various transmural pressures as explained in section 3.3.7. We retain the same spring constants obtained for open/unblocked AQP1s (given in Fig. 3.9) to predict SI compression and L_{P_t} values when blocking AQP1s. As in our previous study (Ch. 2), for an assumed AQP1 fraction, if the predicted L_{P_t} (with $L_{P_{EC}} = 0$) is less than the corresponding experimental value at 60 mmHg, we increase the AQP1 fraction until the predicted L_{P_t} matches the experimental value. Clearly, if the predicted L_{P_t} that corresponds to 100% blockage of AQP1s (i.e., with $L_{P_{EC}} = 0$) is higher than the experimental L_{P_t}, blocking less than 100% AQP1s ($L_{P_{EC}} > 0$) would further increase the L_{P_t} predictions. On the other hand, if the model predicts L_{P_t}s lower than the experimental value, one can decrease the percentage of blocked AQP1 pathways until one finds a reasonable agreement with the experimental data.

Figure 3.10 compares the model predictions for the effect of AQP1 blocking on L_{P_t} with Nguyen et al.'s (62) experimental blocked AQP1 data along with the unblocked values that assume a 40% AQP1 contribution to L_{P_e}. Predictions are shown for different AQP1 fractions of L_{P_e}. L_{P_t} clearly decreases with an increase in the fraction of blocked AQP1s; these decreases evince AQP1s' significance in water transport across the vessel wall. The L_{P_t}s predicted by assuming 20% and 30% contribution of AQP1s to L_{P_e} are higher than the experimental data at 60 mmHg. Our predictions for the case of AQP1s contributing 40% to L_{P_e} show a good agreement with Nguyen et al's (62) data and thus suggest that AQP1s contribute at least 30% to the phenomenological L_{P_e}. Notice that as more AQP1s are blocked the L_{P_t} curves appear to shift to the left. This means that the dynamic range over which the SI goes from an uncompressed to fully compressed state,

or the region where L_{P_t} drops drastically, shifts to lower transmural pressures. These results are consistent with predictions from our earlier filtration-based model (Ch. 2) and further confirm the hypothesis that reducing transcellular transport increases the force acting on the endothelium, with the critical force for SI compression achieved at lower overall transmural pressures.

Relative to the filtration-only model (see Fig. 2.11 in Ch. 2), the current model's predictions for the phenomenological L_{P_t} in the case of blocked AQP1s are slightly higher for pressures below 60 mmHg because of the oncotic forces across the EC that act there. We found that (results not shown) the oncotic forces for blocked AQP1s are smaller than those obtained with functioning AQP1s. This suggests that the increase in L_{P_t} predicted by the current model for blocked AQP1s is smaller than that seen in Fig. 3.9. At high transmural pressures, oncotic forces have a negligible effect and ΔP dominates the overall response. Thus, for a given blocked AQP1 fraction, the L_{P_t} predictions in the dynamic range from both models match very well. The range in which hydrostatic forces start to dominate over oncotic forces (60 - 90 mmHg in Fig. 3.8) also shifts to lower transmural pressures (results not shown) as more AQP1s are blocked. In other words, for the case of AQP1s contributing 20% to L_{P_e} and all of them blocked, the oncotic forces are comparable to the hydrostatic forces up to 60 mmHg. However, when AQP1s contributing 40% to L_{P_e} are blocked, the hydrostatic forces start to dominate at as low as 45 mmHg.

At higher transmural pressures, where partial/full fenestral blocking takes place even with intact AQP1s, the blocking of AQP1s would not lead to any significant additional SI compression, but rather would simply reflect a change in L_{P_e}. Thus we expect only a small variation in L_{P_t} at higher pressures upon AQP1 blocking. Our model predictions shown in Fig. 3.10 and the corresponding experimental data at 100 and 140 mmHg further confirm this hypothesis. Our theory predicts that the force/area acting on the EC at 70 and 60 mmHg with functioning AQP1s is the same as that acting at 50 and 43 mmHg, respectively, when the AQP1s are blocked. It means that the SI with $HgCl_2$ treatment should experience the same level of compression and fenestra blockage at 50 and 43 mmHg as the untreated SI at 70 and 60 mmHg, respectively. More to the point, Fig. 3.10 predicts, e.g., that L_{P_t} with $HgCl_2$ should be higher at 20 mmHg than at 60 mmHg,

but lower than without $HgCl_2$ at 60 mmHg. We also found that one needs a transmural pressure of $\sim$ 210 mmHg in order to exert the same force/area on the EC with functioning AQP1s as that exerted in the case of blocked AQP1s at 140 mmHg. We believe that the forces acting on the EC at such high pressures can cause mechanical stretching of endothelium and it's junction, potentially leading to an increase in the junctional contribution to L_{P_e} that can slightly raise L_{P_t}. This might explain the slight rise in L_{P_t} found by Nguyen et al. (62) at 140 mmHg compared to it's value at 100 mmHg. An alternate explanation for this slight rise comes from experimental work done by J. Abrams in our group (not shown). He has found indications of slight mercury toxicity at 140 mmHg, but not at the lower pressures.

3.3.9 The effect of AQP1 up-regulation on P_{er}:

Figures 3.11(a)-(d) show the effect of increasing endothelial AQP1 expression on the radial Peclet numbers $\left(P_{er} = \dfrac{f_i|U_i^*|r_f^*}{\gamma_i D_i}\right)$, a non-dimensional radial velocity $|U_i^*|$, in the SI underneath the EC (z_i = 1) for ΔPs of 60 - 90 mmHg. To asses how AQP1 expression affects this Peclet number, we keep the normal junction contribution, $L_{P_{nj}}$, to L_{P_e} fixed and only increase the AQP1 contribution, $(L_{P_{EC}})$. As previously discussed, all curves have a sharp maximum near the fenestral edge. At each transmural pressure, P_{er} decreases as the endothelial AQP1 expression increases and a smaller fraction of the water entering the SI enters at the junction. As $r \rightarrow$0, the curves for different AQP fractions converge since the overall flow there becomes independent of the AQP1 fraction. Figs. 3.11(a)-(d) show that P_{er} near the edge of fenestra decreases with increasing AQP1 fraction from $\sim$ 0.26 to 0.14, 0.63 to 0.19, 1.6 to 0.3 and 2.8 to 0.9 at 60, 70, 80 and 90 mmHg, respectively. Advective transport of albumin from the junction through the SI region becomes less significant as more AQP1s increase transcellular flow. This makes sense because, with more (uniformly distributed) AQP1s, the overall pressure in the SI rises and results in smaller radial gradients compared to the case with fewer AQP1s. At lower transmural pressures ($<$ 60 mmHg), we found a similar effect of AQP1 expression on P_{er} (results not shown). However, as Fig. 3.6 shows, since diffusion is the primary mechanism for the transport of albumin at such low pressures with

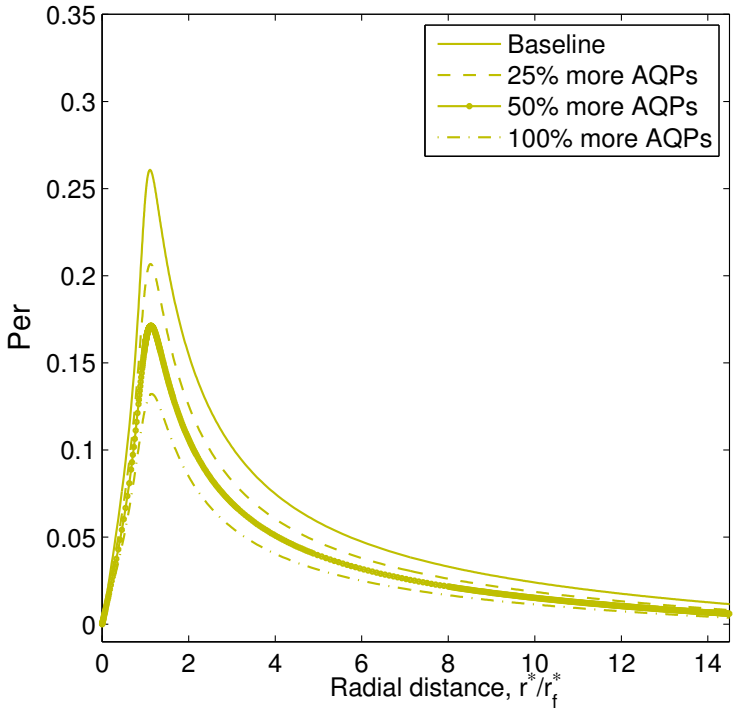

(a) $P_L^* = 60$ mmHg

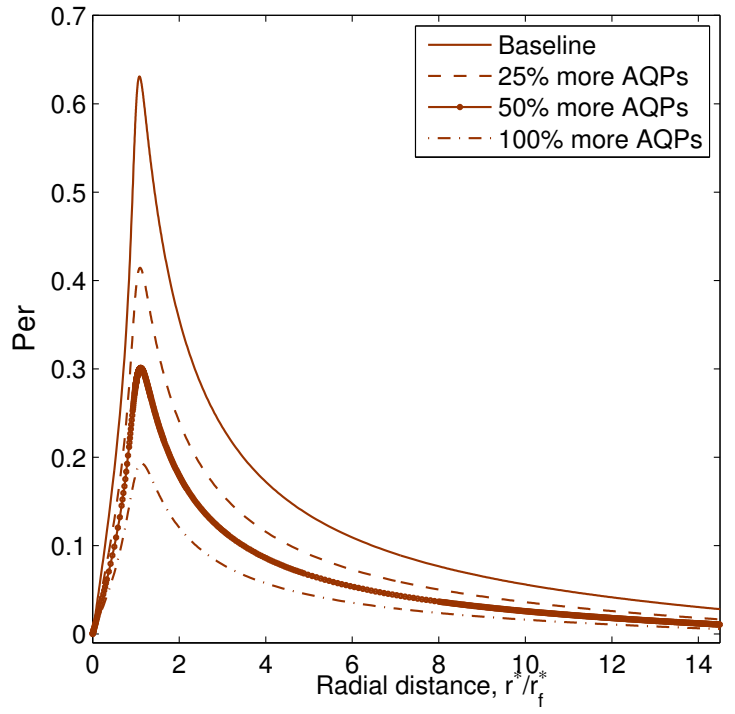

(b) $P_L^* = 70$ mmHg

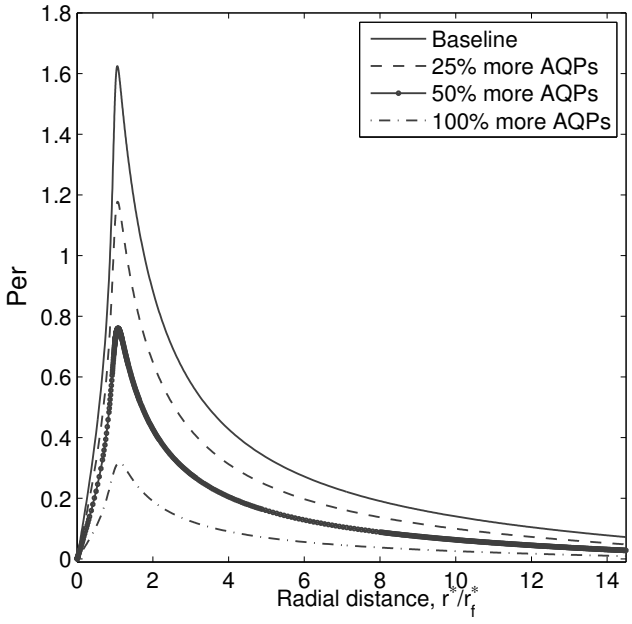

(c) P_L^* = 80 mmHg

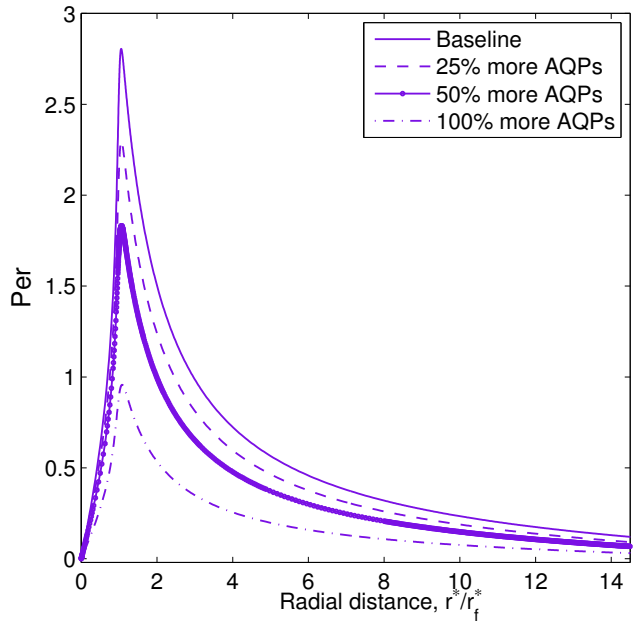

(d) P_L^* = 90 mmHg

Figure 3.11: The effect of increasing the number of AQP1s (incrementing $L_{P_{EC}}$ by 25, 50 and 100%) on the Peclet numbers in the SI region at $z_i = 1$ as a function of radial distance. Baseline curves for each pressure assume that AQP1s contribute 40% to L_{P_e} and are the same as those shown in Fig. 3.6. Again, the fenestra is located between $0 < r^*/r_f^* < 1$. The junctional contribution to L_{P_e} is fixed in these predictions.

baseline AQP1 expression, increasing the number of AQP1s causes only a negligible difference at those pressures.

3.3.10 The effect of AQP1 up-regulation on the albumin concentration in the SI

The effect of increasing endothelial AQP1 expression on the (non-dimensional) SI albumin concentration beneath the EC ($z_i = 1$) is plotted in Figs. 3.12(a)-(d) for transmural pressures from 60 - 90 mmHg. As with P_{er}, we have kept $L_{P_{nj}}$ fixed and only increased $L_{P_{EC}}$. Baseline curve in each of these figures assume AQP1s are responsible for 40% of L_{P_e} and are same as those shown in Fig. 3.7 at the corresponding pressures.

The concentration of albumin in the SI layer increases with increasing AQP1s and the concentration profile becomes flatter. Naively, with more AQP1s, one would anticipate that the concentration of albumin in the SI would decrease since more incoming water flow through the increased number of AQP1s should dilute albumin's concentration. The results in Fig. 3.12 belie this argument. Recall our hypothesis and our earlier model (Ch. 2) argue that, at a given transmural pressure, increasing the number of AQP1s reduces the pressure drop and hence the force per unit area acting on the endothelium. This reduced force/area decompresses the SI and increases the albumin transport parameters, such as f_i, γ_i and D_i, in the SI. We find that the increase in γ_i as the SI decompresses is primarily responsible for this increased albumin concentration. Moreover, the $(C_g/\gamma_g - C_i/\gamma_i)$ term on the right side of Eq. 3.19 suggests that an increase in γ_i increase the mass flux of albumin into the SI, which can lead to the higher SI concentrations seen in Figs. 3.12(a)-(d) with more AQP1s. The increased diffusivity and decreased P_{er} shown in Figs. 3.11(a)-(d) at the corresponding pressures explain the increased flatness of concentration profiles with more AQP1s.

The concentration profile in Fig. 3.12(d) shows a steep drop near the edge of the fenestra even after a doubling of the AQP1 expression on the EC. At such high pressures, even with twice the number of AQP1s, the force acting on the EC can compress the SI and produce substantial radial pressure gradients near the fenestra region. As confirmed by Fig. 3.11(d), the corresponding P_{er} are still high, i.e., advective albumin transport is still important. Increasing the AQP1 expres-

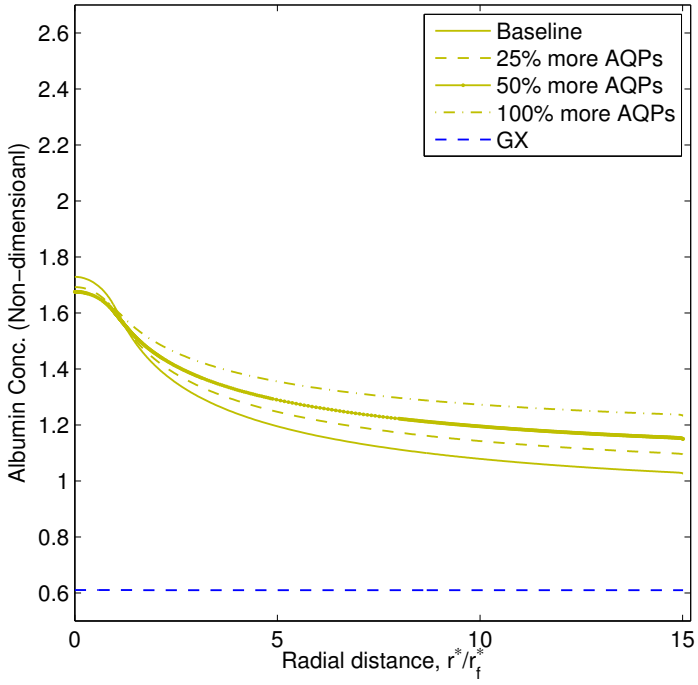

(a) $P_L^* = 60$ mmHg

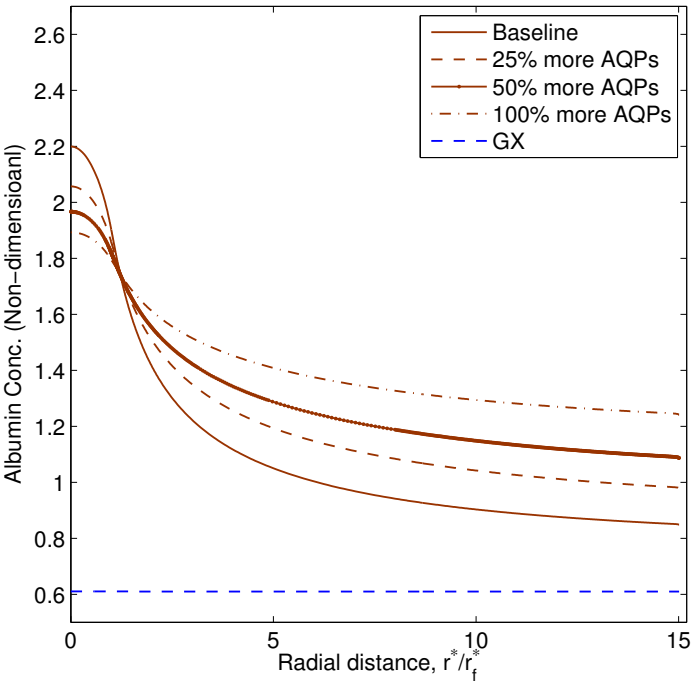

(b) $P_L^* = 70$ mmHg

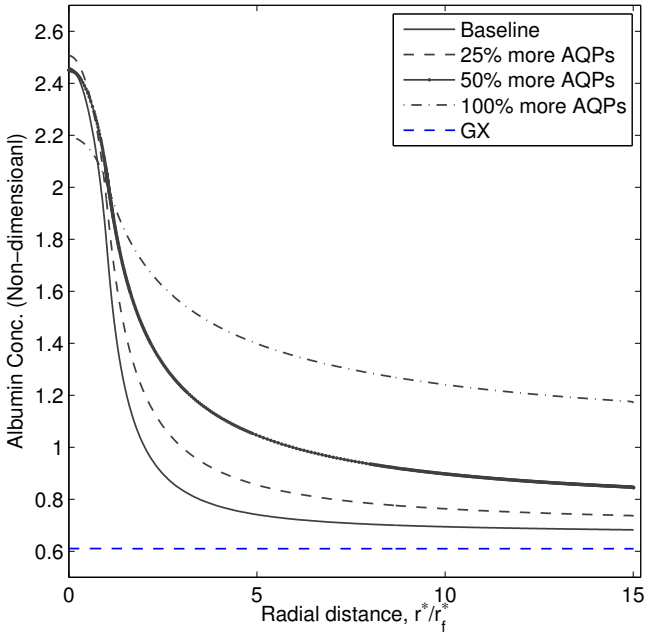

(c) P_L^* = 80 mmHg

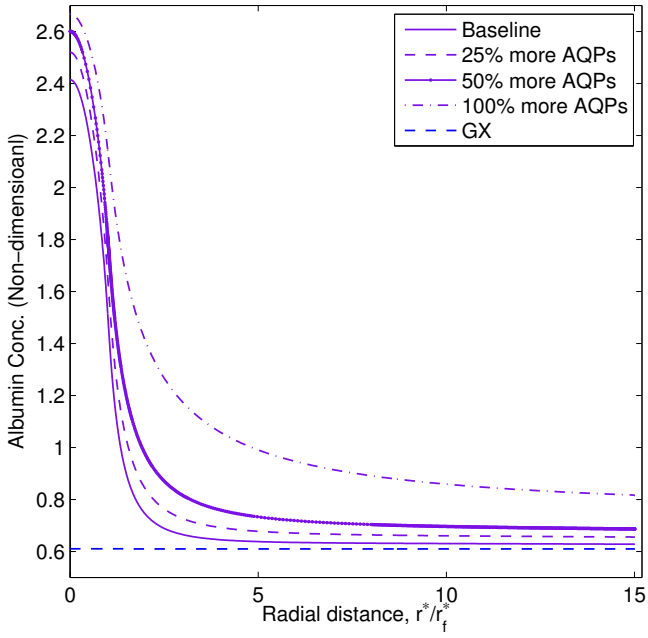

(d) P_L^* = 90 mmHg

Figure 3.12: The effect of increasing AQP1 expression on the concentration of albumin in the SI at $z_i = 1$ as a function of radial distance. Baseline curves for each pressure assume that AQP1s contribute 40% to L_{P_e} and are same as those shown in Fig. 3.7. Dashed blue line in each figure represents the concentration of albumin in the GX above the EC. The fenestra is located between $0 < r^*/r_f^* < 1$. The junctional contribution to L_{P_e} i.e., $L_{P_{nj}}$ is fixed in these predictions.

sion at transmural pressures less than 60 mmHg (results not shown) also had similar but small effect on SI albumin concentration. At such low force/area on the EC, the SI is relatively uncompressed even at baseline AQP1 expression and increasing it barely changes SI thickness, i.e., γ_i. These findings confirm that the difference in albumin concentration across the EC increases with increased AQP1s. This will strongly impact the oncotic forces across the EC discussed in the next section.

3.3.11 The effect of AQP1 up-regulation on forces across the EC

Figure 3.13 shows the predicted variations in hydrostatic and oncotic forces across the EC with transmural pressure and at various AQP1 expressions. These area averaged forces are calculated as explained in section 3.3.6. Consistent with our previous theory (Ch. 2), the transendothelial force/area (ΔP), at a given applied transmural pressure, decreases significantly with increasing endothelial AQP1 expression (see solid curves in Fig. 3.13). With more AQP1s, or more transport pathways across the EC, the overall pressure inside the SI ($\bar{P}_i$) increases and the pressure drop ($\bar{P}_g - \bar{P}_i$) or force/area on the EC decreases, as seen in Fig. 3.13. The curves in Fig. 3.13 shift to right, meaning that it takes higher pressures to achieve the critical trans-endothelial force to compress the SI, with more AQP1s. Inversely, with less AQP1s, the force/area on the EC increases and the SI reaches the critical compression limit, at much lower transmural pressures.

Fig. 3.13 shows that increasing endothelial AQP1 expression also shifts the $\Delta\pi$ curves downwards i.e., increases the magnitude of the osmotic forces. This is a direct consequence of the higher albumin concentration in the SI region that results with more AQP1s, as shown in Fig. 3.12. As with ΔP, higher AQP1 expression shifts the $\Delta\pi$ curves to right. This means that the regime where the hydrostatic and oncotic forces are comparable shifts to higher transmural pressures with more AQP1s. For example, at baseline AQP1s, both ΔP and $\Delta\pi$ are comparable up to $\sim$ 60 mmHg. Beyond that, $\Delta\pi$ drops sharply and ΔP dominates. With double baseline AQP1, $\Delta\pi$ matches ΔP at least up to 80 mmHg. Overall, these findings suggest that the oncotic pressure gradients become increasingly important as endothelial AQP1 expression increases. The larger

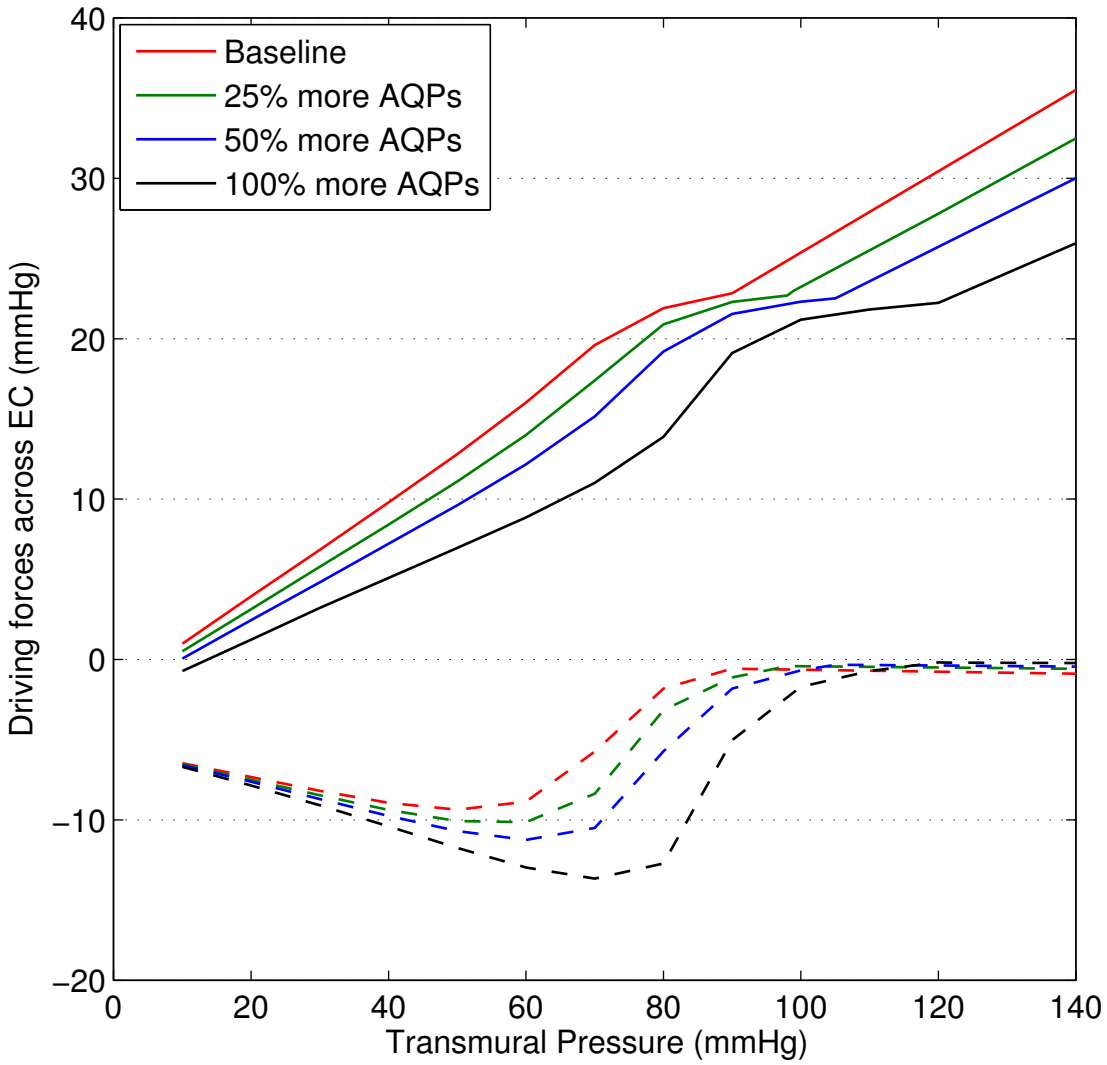

Figure 3.13: The effect of increasing endothelial AQP1 expression on the hydrostatic (ΔP, upper solid curves) and oncotic forces ($\Delta\pi$, lower dashed curves) per unit area across the EC as a function of transmual pressure. The same color for ΔP and $\Delta\pi$ curves represents equal AQP1 expressions. The curves for baseline AQP1 expression assume AQP1s contribute 40% to L_{P_e} and are the same as those shown in Fig. 3.8. The junctional contribution to L_{P_e} is fixed in these predictions and the contribution due to AQP1s increases in increments of 25%. $\Delta P = \bar{P}_g - \bar{P}_i$ and $\Delta\pi = \bar{\pi}_g - \bar{\pi}_i$. $\Delta\pi$ is negative for each AQP1 expression; thus $\bar{\pi}_g < \bar{\pi}_i$ at all trasmural pressures.

oncotic forces seen with more AQP1s, which act in the same direction as ΔP, enhance the overall driving force $(\Delta P - \sigma\Delta\pi)$ and thus the fluid flow across the EC and ultimately through the vessel wall.

3.3.12 The effect of increasing AQP1s on L_{P_t}:

Fig. 3.14 displays the variation of the intact artery wall hydraulic conductivity with transmural pressure and with increasing endothelial AQP1 expression. It compares these L_{P_t} predictions (solid curves) with those from our earlier filtration based model (dashed curves) and with the experimental observations of Nguyen et al. (62) and Raval et al. (68), the latter experiments planned based on our models' predictions. The baseline measurements of Nguyen et al. (62) for the case of unblocked or functioning AQP1s are the same as those shown in Fig. 3.9.

The predictions for AQP1 up-regulation from both models shown in Fig. 3.14 are qualitatively very similar. At fixed transmural pressure, more AQP1s increase L_{P_t} and shift the L_{P_t}-ΔP curve to the right. This effect is exactly the opposite of that of AQP1 down-regulation shown in Fig. 3.10 and for the same reason. As Fig. 3.13 shows, the force/area across the endothelium significantly decreases with more EC AQP1s, thereby decompressing the SI at higher ΔP and increasing L_{P_t}.

Our earlier model's (Ch. 2) L_{P_t} predictions are significantly lower than those of the current mass transfer model below $\sim$ 75-85 mmHg. These discrepancies again derive from the oncotic gradients across the EC. As Fig. 3.13 shows, since the oncotic pressure gradients act in the same direction as transmural pressure gradients (ΔP), the overall driving force, $(\Delta P - \sigma\Delta\pi)$, across the EC is greater than ΔP, the driving force used in our earlier model. Thus more water flows through the EC and hence through the vessel wall and results in higher L_{P_t}s for the same ΔP. For a fixed AQP1 fraction, we find the difference between the two models is maximum at low pressures, where oncotic differences are significant, and decreases at higher pressures as oncotic differences become negligible compared with hydrostatic pressure differences. Since the effect of oncotic gradients extend to higher transmural pressures with more AQP1s (see Fig. 3.13), the

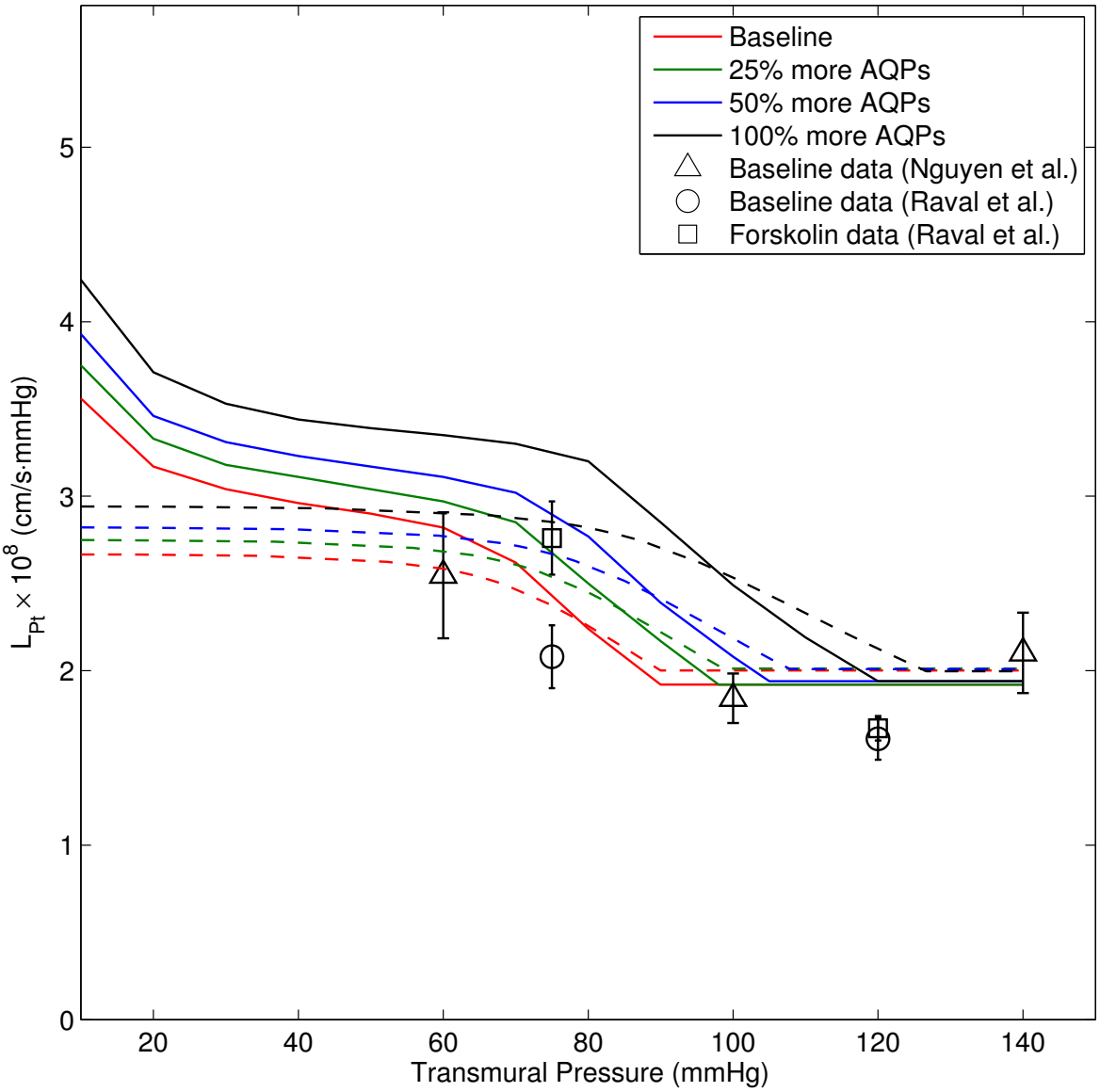

Figure 3.14: The effect of increasing endothelial AQP1 expression on the hydraulic conductivity of an intact artery wall as a function of trasmural pressure. A comparison among the current mass-transfer based model (solid curves), our earlier filtration-only model (dashed curves) from Ch. 2 and the experimental data from Nguyen et al. (62) and Raval et al. (68). The same color for solid and dashed lines represents equal AQP1 expression. All simulations use the same $L_{P_{nj}}$ value, but vary $L_{P_{EC}}$ and thus L_{P_e} according to increase in AQP1 expression. Baseline curves assume that AQP1s contribute 40% to L_{P_e}.

upper edge of the dynamic range of the two L_{P_t} predictions differ, with those of the current model slightly lower, and showing a sharper drop.

Based upon both theories' predictions in Fig. 3.14, an increase in AQP1 expression should have a particularly large effect on L_{P_t} in its dynamic range and only a negligible effect (relative to measurement error) to its right. Thus, measurement of L_{P_t} at 75 mmHg on the same vessel with baseline and elevated AQP1 expression should show a significant rise in L_{P_t} with increased AQP1, while at 120 mmHg, it should show no measurable change. Based on these predictions, Raval et al. (68) measured L_{P_t} of the intact artery wall *ex vivo* with normal functioning AQP1s at 75 and 120 mmHg. They then treated these vessels with forskolin, a chemical reagent that they showed up-regulates the AQP1s expression in AECs, and repeated these L_{P_t} measurements on the same vessels. They observed a $\sim$ 30% increase in L_{P_t} at 75 mmHg and a negligible change at 120 mmHg. Comparison of the 75 mmHg values with the filtration theory's predictions suggest forskolin up-regulated EC AQP1 numbers by 50-100%, while the newer theory suggest closer to 50% up-regulation. However, if we notice that Raval's baseline L_{P_t} values at both 75 and 120 mmHg are both a bit lower than Nguyen et al.'s baseline values [2], and try to infer the extent of AQP1 up-regulation from the difference of the 75 mmHg L_{P_t} value from baseline, one estimates from either theory that forskolin has at least doubled EC AQP1 transcellular pathways. This is consistent with the quantitative immunohistochemical slides of Raval et al. (68) that, while not yet quantitated, clearly show far brighter AQP1 staining after forskolin treatment than control.

3.3.13 The effect of GX removal on albumin concentration and the associated driving forces:

In order to simulate the experimentally observed effect of GX degrading enzymes such as heparinase, condroitinase, pronase and hyaluronse on overall wall transport, we eliminate the GX layer

[2] We could not scale our model to Raval et al.'s (68) data since they did not measure the L_{P_t} at lower transmural pressures, the values used to estimate the L_{P_e}. Though both set of experiments used same species of animal models, there could be variations from animal to animal that can result in slightly different L_{P_e} or a small systematic bias of each experimenter could account for these differences. We suspect that if the model is scaled to Raval et al.'s (68) data, assuming that their L_P value at 60 mmHg is lower than that of Nguyen et al. (62), the curves in Fig. 3.14 would simply shift down.

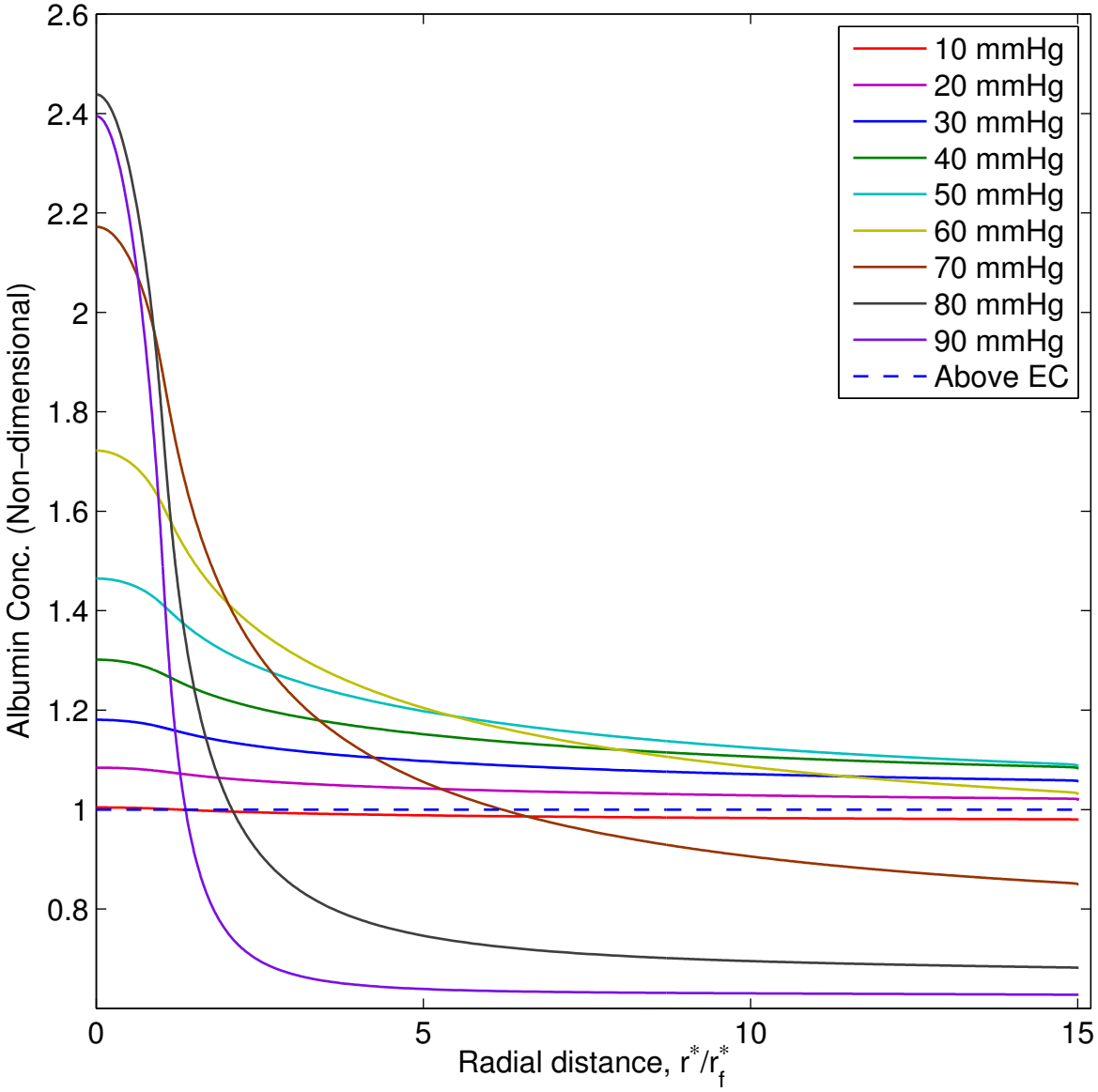

Figure 3.15: Non-dimensional SI albumin concentration as a function of radial distance in the absence of GX and at various transmural pressures. Dashed line shows the albumin concentration just above the EC (there is no GX here). The fenestra is between $0 < r^*/r_f^* < 1$.

from the model considered in Fig. 3.1. Removal of the GX changes the boundary conditions used at the EC surface. In the absence of the GX region, the variables P_g and π_g in Eqs. 3.6 and 3.8 would take their corresponding lumen values. Similarly, for the mass-transfer problem, the C_g/γ_g term in Eqs. 3.18 and 3.19 would change to 1 in non-dimensional form since $\gamma_L = 1$.

Figure 3.15 shows the concentration of albumin in the SI in the absence of GX with increasing transmural pressures. The concentration profiles are very similar to those in Fig. 3.7 for each transmural pressure, evincing only a minor effect of the GX on the SI concentration of albumin. As explained in section 3.3.5, due to the dense media structure, we find an accumulation of albumin in the SI upstream of the fenestral hole. The major contrast with Fig. 3.7 is the albumin concentration just above the EC (in this case lumen). In Fig. 3.7, this value was uniformly lower than the SI albumin concentration at all pressures, whereas here it is equal to one ($\sim 70\%$ higher than with a GX layer) everywhere and higher than the 10 mmHg curve and substantial parts of the curves above 60 mmHg. As we shall now see, this has substantial oncotic consequences.

Figure 3.16 shows model predictions for the forces acting across a unit area of the EC in the presence (blue curves) and absence (red curves) of the GX layer and their variation with transmural pressure. Upon GX degradation, the hydrostatic force, shown by the solid red curve in Fig. 3.16, is higher than the corresponding force with the GX intact. This suggests that the SI would compress more at a fixed transmural pressure without GX than with it, and thus the dynamic range of the L_{P_t} vs ΔP curve should shift leftwards upon GX degradation. On the other hand, whereas the oncotic forces across the EC, with its GX intact, are negative (they suck fluid from the lumen into the SI) at all transmural pressures, upon GX removal, they are negative up to ~ 65 mmHg and positive (opposing ΔP) beyond. This follows directly from the albumin concentration above the EC (the dashed lines in Figs. 3.7 and 3.15). Since GX degradation hardly affects the SI albumin concentrations, the rise in the dashed line with GX degradation subtracts a uniform constant from $\Delta\pi$, as seen in Fig. 3.15.

These findings imply that the overall driving force $(\Delta P - \sigma\Delta\pi)$ per unit area across the EC is much higher in the presence of the GX than in it's absence (dot-dashed curves in Fig. 3.16).

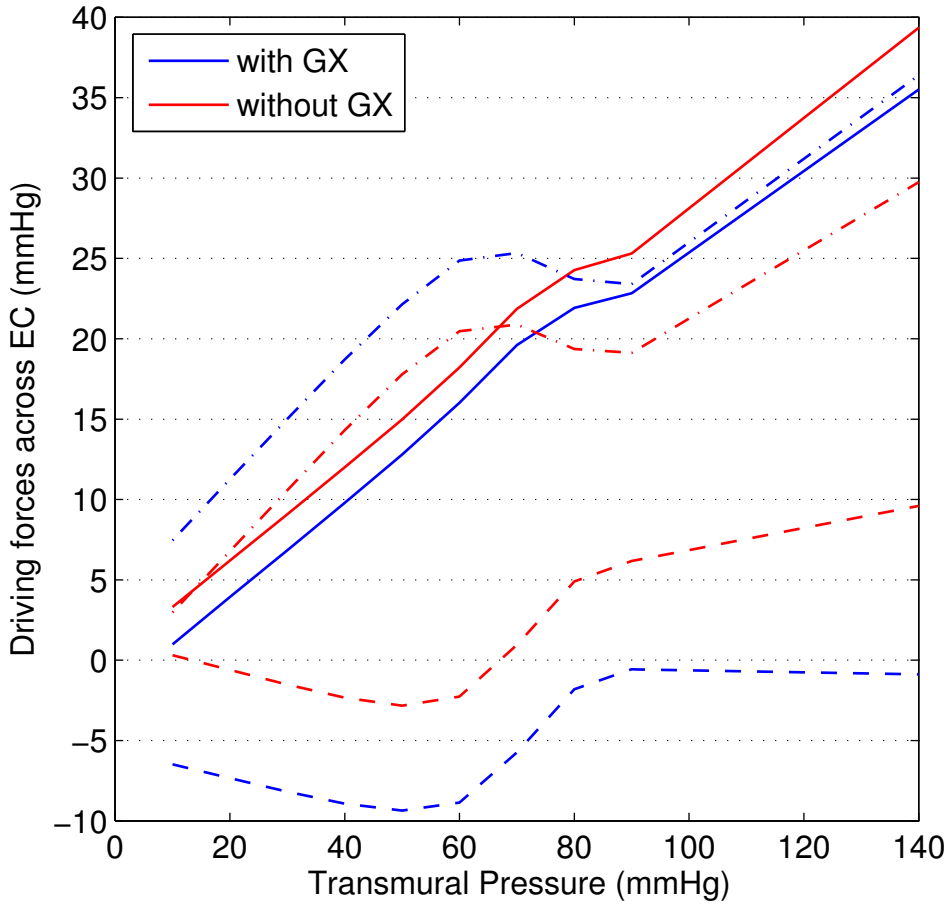

Figure 3.16: Force per unit area across the EC with varying transmural pressure with (blue curves) and without (red curves) GX layer. Solid curves: hydrostatic force (ΔP), dashed curves: osmotic force $(\Delta\pi)$ and dot-dashed curves: overall driving force per unit area acting across the EC $(\Delta P - \sigma\Delta\pi)$. The ΔP and $\Delta\pi$ curves with the GX region are the same as those in Fig. 3.8. Both set of curves assume that AQP1s contribute 40% to L_{P_e}.

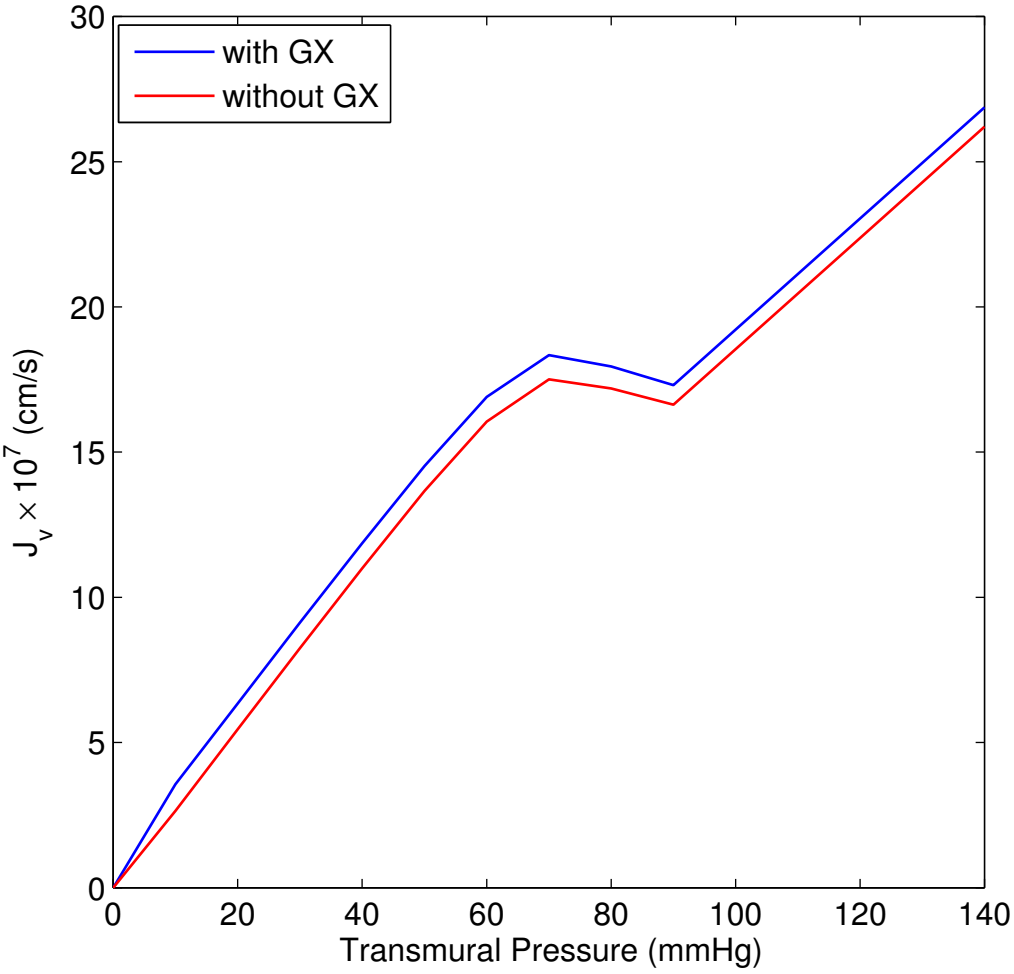

Figure 3.17: Transmural water flux across the vessel wall (J_v) in the presence and absence of the GX layer and its variation with transmural pressure. AQP1s contribute 40% to L_{P_e}.

That is, it predicts (see Fig. 3.17) somewhat counter-intuitively, a slightly higher water flow across the EC and thus through the vessel wall with intact than with degraded GX. It is not clear, however, whether this predicted difference is large enough to be unambiguously measured.

As discussed in Chapter 1, several studies, both *in vitro* and *in vivo*, have shown shear induced increase in endothelial L_P. This L_P response is stimulated by shear-induced NO production and mediated by the cell surface GX (98). Lopez et al. (54) measured the response of BAEC L_P to a step increase in luminal shear stress from 0 to 13.3 $\mathrm{dyn/cm^2}$ after pre-treatment of the monolayers with GX-digesting enzymes. They observed that heparinase and hyaluronidase completely blocked shear-induced NO production and increased monolayer L_P. That is, the monolayer J_vs were lower in the absence of the GX layer. Though these results are qualitatively similar to our findings, the response in vessel walls appears to be governed by oncotic forces and may not be correlated to the responses seen in these monolayer studies.

3.3.14 The effect of varying lumen albumin concentration on J_v:

Patients can sometimes experience elevated lumen albumin concentrations and Fig. 3.18 examines the predicted effect of such an elevated (from 20 to 100 gm/lit) concentration on J_v, the water flux across the vessel wall, vs transmural pressure. For a fixed albumin concentration, fluid flux increases nearly linearly with ΔP until the SI compression begins to block IEL fenestrae, when the increase in J_v slows down and, can even decrease. That is, in the dynamic range of L_{P_t}, it appears possible that as one increases ΔP where L_{P_t} decreases, the product $L_{P_t}\Delta P$ can decrease briefly. This effect is far more pronounced at higher albumin concentrations. Beyond maximal SI compression, the wall behaves like a simple material and J_v simply rises linearly with ΔP. At all pressures, fluid flux increases with increasing lumen albumin concentration, but much more so below the ΔP for maximal SI compression. This increase results from an increase in oncotic forces (not shown). J_v at one half (20 gm/lit) or at normal (40 gm/lit) lumen albumin concentrations do not differ significantly. However in pathological conditions such as hyperalbuminemia in which albumin's blood concentration raises to abnormally higher values (100 gm/lit), the model predicts

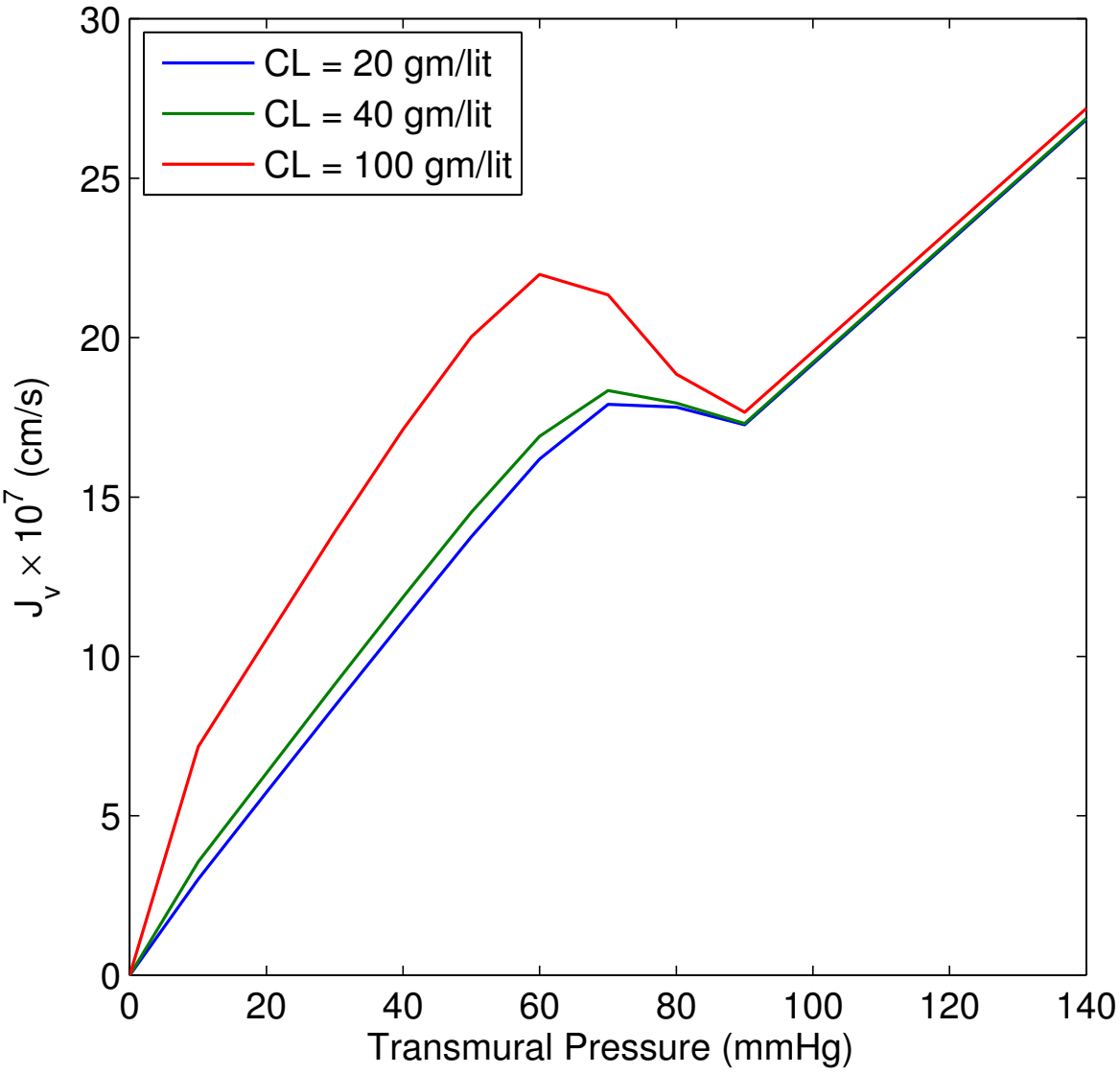

Figure 3.18: The predicted change in water flux across an artery wall vs transmural pressure and with increasing lumen albumin concentration. The GX layer is kept intact in these predictions

a substantial increase in J_v for pressures up to 60 mmHg and a sharp decrease from 60-90 mmHg. These predictions suggest new experiments to test the effect of oncotic gradients on the fluid flux across the vessel wall and predicts a range of albumin concentration that can lead to appreciable, i.e., experimentally measurable changes in J_v. Below about 70 mmHg, the elevated J_v might in fact be athero-protective, since it increases trans-SI water flow that potentially could dilute unbound SI LDL and potentially wash it from the SI before it can bind to SI ECM. Unfortunately this potential benefit disappears by 90 mmHg, which is still a bit below the physiological mean arterial pressure.

3.4 Conclusions

To our knowledge, the present two-dimensional coupled filtration and mass transfer model, for the first time considers the effect of oncotic forces within the vessel wall on the overall transport across large artery walls. It shows that, even though the oncotic differences between the lumen and the adventitia may be negligible or zero, they may still play a nontrivial role within such vessels, at least at low transmural pressures (up to 60 mmHg). One of its very interesting and surprising findings is that the dense structure of the media region acts to strongly filter albumin to the point that, under steady conditions, it generates an SI albumin build-up to values high enough to suck water from the lumen into the SI. This effect overcomes the tendency of hypotonic transenodthelial flow to result in oncotic differences pulling in the opposite direction. This effect resolves the oncotic paradox that motivated this work.

The present model provides several interesting - and experimentally testable - insights concerning the interactions between hydrostatic and oncotic forces that determine the fluid flow across the arterial endothelium. For example, the model predicts that the variation in L_{P_t} of the vessel wall with transmural pressure, both for the case of functioning and blocked AQP1s, agree well with Nguyen et al.'s (62) experimental observations. Although the precise numbers differ in magnitude, this model's predictions agree qualitatively with those of our earlier model (Ch. 2) that AQP1s contribute at least 30% to the phenomenological endothelial L_P at low transmural pressures. It predicts that neglecting oncotic gradients underestimates the overall inherent L_{P_t} of the vessel wall up to 60 mmHg and that endothelial AQP1 up-regulation increases vessel wall L_{P_t} even more than what our filtration-only model predicted; the difference is due to oncotic forces. A further prediction that AQP1 up-regulation would increase the dynamic range of L_{P_t} vs ΔP motivated Raval et al.'s (68) experiments with forskolin that confirmed these predictions and implied that forskolin at least doubles EC AQP1 expression. The model explains that GX removal results in a marked decrease seen in the overall driving forces per unit EC area across the EC. The difference in albumin concentration across the EC is much larger, and thus results

in increased transmural water flow, with intact vs degraded GX. Given AQP1's presence in the high-pressure cardiac endocardium, heart, lung and renal epithelia, resolving and understanding how mass-transfer-induced osmotic gradients interact with the flows that advect those solutes may have far broader and illuminating implications.

Chapter 4. The effect of aquaporin-1 on macromolecular transport through the artery wall

4.1 Introduction

Atherosclerosis, a disease of large arteries and the aortic valve (71, 76), is a leading cause of death in the US and in most of the Western countries. It appears to begin with the transport and accumulation of low density lipoprotein (LDL) cholesterol from the blood into the vessel wall. Once inside the subendothelial intima (SI) layer, the LDL cholesterol interacts with the subendothelilal extracellular matrix (ECM), mainly comprised of the proteoglycan (PG) and collagen (CG) fibers, and gets oxidized, perhaps by the presence of oxygen free radicals. Blood-borne monocytes enter the arterial intima in regions with high subendothelial lipid concentration, becoming macrophages that normally, along with media derived smooth muscle cells (SMC), attempt to scavenge the extracellular cholesterol (10). However, when overwhelmed, macrophages progress to form foam cells, and this accumulation of lipid and necrotic cells inside the SI appears to result in atherosclerotic lesion formation (86, 81). Eventually, such fatty lesions lead to stenoses that compromise the cross section for blood flow and cause potentially harmful disease conditions such as myocardial or cerebral ischemia. Worse still, unstable plaques may rupture and release large particles in blood stream that can completely block smaller blood vessels, resulting in heart attack or stroke.

Given the tight structure of the aortic endothelium, it is quite puzzling to ascertain how a macromolecule like LDL (average diameter $\sim$ 22 nm) can get through this barrier and enter the vessel wall. Many researchers in the past, using both experimental (89, 11, 13, 34, 50, 51, 52) and theoretical (119, 129, 35) approaches, have studied the transport of such macromolecules from the blood, through the endothelium, and into the inner layers of the vessel wall. These studies (119, 89, 11, 50, 51, 52) have revealed that macromolecules cross the aortic endothelium at certain focal locations, with widened endothelial junctions surrounding rare endothelial cells (EC) ($\sim$ 1 in every 5000 cells (50, 51, 52)) that are either dividing or dying.

Chuang et al. (13) studied the subendothelial spread of horseradish peroxidase (HRP) with increasing tracer circulation time. They found that localized HRP spots in the aorta initially grew very rapidly and then appeared to slow down, reaching almost $\sim 250\ \mu\mathrm{m}$ in diameter after 4 min circulation time. This spot size growth is too fast to be consistent with a diffusion-dominated mechanism for any reasonable diffusivity. Yuan et al. (129) developed a two-dimensional (2-D), convection-diffusion, wall-structure based model that explicitly includes the endothelium, SI, internal elastic lamina (IEL), and media layers of the vessel wall. Although their model could not explain the HRP spot growth seen in Chuang et al. (13), it demonstrated that the transmural (across the vessel wall) pressure driven plasma (henceforth called water) flow advects macromolecules through rare leaks and spreads them inside the SI and further into the vessel wall and theryby substantiated the significance of convection in overall macromolecular transport in the vessel wall. By examining the ultrastructural observations of Frank and Fogelman (24), that revealed surprisingly sparse SI structure than the media matrix in rabbit aorta, Huang et al. (35) developed a heterogeneous fiber matrix theory that calculates the SI Darcy permeability (K_{P_i}) and tracer diffusivity (D_i) to be 10-100 times the measured media values. Using these new parameters in Yuan et al.'s (129) 2-D convection-diffusion model, Huang et al. (35) found strong advective macromolecular transport parallel to the endothelium in the SI (due to the difference between leaky and normal junction hydraulic conductivities and between the SI and media flow resistances) and successfully explained Chuang et al.'s (13) HRP spot growth data.

As noted earlier, the transmural pressure-driven (ΔP) water flow brings macromolecules through rare leaky junctions and advects them further inside the SI region, thereby increasing LDL-ECM interactions. However, the majority of transendothelial water flow that occurs through normal junctions, surrounding normal ECs, can flush unbound LDL from the SI and ultimately from the vessel wall. Thus the overall water transport across the endothelium, and not just through rare leaky junctions, seems to affect the LDL accumulation inside the vessel wall. The hydraulic conductivity (L_P) is the measure of overall transmural water flux through the vessel wall. Together with the transport parameters of the individual layers of the vessel wall (e.g., K_P, D etc.), the L_P

decides the filtration/convection pattern inside the vessel wall. Tedgui & Lever (100), Baldwin and Wilson (2), Shou et al. (78) and Nguyen et al. (62) have reported higher L_Ps at low transmural pressures and lower L_Ps at high transmural pressures in rabbit (100, 2) and rat (78, 62) aortic walls. Moreover, endothelial denudation roughly doubled the L_P in these experiments and rendered it pressure insensitive. To explain this pressure-dependent behavior of the L_P, Huang et al. (36) postulated, and their subsequent experiments proved (37), that at high transmural pressures, the force acting on the endothelium compresses the sparse SI layer. This compression would decrease the intima's inter-fiber spacing, thereby decreasing its transport parameters (e.g., K_P) and, more importantly, cause the endothelium to partially block some of the IEL's fenestra. This latter effect could lower wall hydraulic conductivity drastically. They developed a local filtration model, on the scale of a single EC, and showed that the pressure induced intima compression and the subsequent IEL fenestra blockage indeed reduces the wall L_P, consistent with above-mentioned experimental observations. In addition to this, the local filtration theory (36) also predicted the effective L_P of the endothelium and SI ($L_{P_{e+i}}$) as a function of ΔP, which the authors used as an input in their earlier convective-diffusive transport model (35) to investigate the change in the time-dependent HRP concentration profiles and thus, leakage spot sizes with transmural pressure. They found that, due to pressure induced intima compaction and the resulting change in its transport properties, the long-time asymptotic spot size decreased by $\sim 50\%$ when the transmural pressure was increased from 50 to 100 mmHg (36). Moreover, the rise time required to achieve the asymptotic spot size was much shorter at 100 mmHg than that required at 50 mmHg.

Zeng et al. (131) developed a detailed 2-D, wall structure-based filtration and macromolecular transport model, structurally similar to those proposed by Yuan et al. (129) and Hunag et al. (35), but with subsequently measured parameter data (37) and some improved parameter values that were guesstimated in earlier studies (129, 35). Neither of earlier studies (129, 35) explicitly solved the equations of continuity and of solute conservation in the SI region. These studies replaced above-mentioned equations by their integrals across the SI owing to a very small ratio of the SI thickness (0.2 - 1 μm (35)) to the mean distance between leaky cells (670 μm (35)).

Zeng et al. (131) found that this assumption holds in regions far from the leaky site, but introduces significant errors near the leak, a critical region in this model where all tracer enters the vessel wall. Zeng et al. (131) directly solved the SI and media problems with the appropriate parameters and without these simplifications and found a very good agreement with both Chuang et al.'s (13) and Shou et al.'s (79) HRP spot size data in rabbit and rat aortas, respectively. Y. Sun (94) then combined Zeng et al.'s (131) corrected theory with appropriate rat parameters with Huang et al.'s (36) intima compression theory and predicted the effect of initma compression on HRP spot growth as a function of transmural pressure. Specifically, Y. Sun (94) used parameters like the SI thickness (L_i^*), K_{P_i} and $L_{P_{e+i}}$ at a given ΔP and their variation with transmural pressure from Huang et al.'s (36) local filtration theory, in Zeng et al.'s (131) 2-D convection-diffusion model and predicted spot growth at various ΔP. These predictions both qualitatively and qualitatively matched with those obtained by Hunag et al. (36) previously. They subsequently measured HRP spot growth in rat aorta at different acute transmural pressures and found good agreement between experimental observations and the predictions of the theory that incorporates intimal compaction under ΔP. In the present study, we will combine the predictions from our previous local filtration model (Ch. 2) with Zeng et al.'s (131) convection-diffusion model to predict the effect of pressure induced intima compression on the concentration and transport of macromolecules like HRP and LDL inside the artery wall. Our approach differs from Sun's (94) in two ways: (a) We do not use the predicted $L_{P_{e+i}}$ as it is from the local filtration model into Zeng et al.'s (131) convection-diffusion model. Rather we use that value of $L_{P_{e+i}}$ which matches the estimated water flux from the two models (see section 4.2.4 for more details). (b) We vary the tracer transport properties, like the diffusivity (D), retardation coefficient (f) and the available solute volume fraction (γ) with intima compression, something which Sun (94) did not consider.

The presence of aquaporin-1 (AQP1) in aortic ECs suggests a new possibility of water transport through the EC, alongside the generally accepted paracellular route (62, 103, 126). AQP1 is a membrane protein molecule that acts as a specific water channel and allows high throughputs of water (3×10^9 molecules/sec/channel) in response to osmotic gradients at at little or no cost in

ATP (58). Using immunocytochemical techniques, Nguyen et al. (62) and Yan et al. (126) have shown the presence of AQP11 in bovine aortic ECs (BAECs) and rat aortic ECs (RAECs) *in vitro*, respectively, while their presence in the rat aorta *ex vivo* has been demonstrated by Toussaint et al. (103). Moreover, the functionality of AQP1s in trans-endothelial water transport is demonstrated in both *in vitro* (62, 73, 126) and *ex vivo* (62, 126) studies. Specifically, it has been shown that decreasing transcellular transport, either by using chemical agents that block AQP1 channels (62) or by using siRNA against AQP1 (73, 126), significantly reduces trans-endothelial water flux. We proposed a new theory in our earlier study (Ch. 2) to explain AQP1's role in trans-endothelial and overall water flux across the vessel wall. Our predictions showed a significant decrease in the L_P of the vessel wall with less trancellular flow and agreed well with Nguyen et al.'s (62) and Yan et al.'s (126) corresponding experimental observations. More interestingly, it predicted higher overall L_P with more AQP1s at any given ΔP.

In this paper we test the combined theory for the effect of AQP1s on overall macromolecular transport at different transmural pressures. We hypothesize that with higher endothelial AQP1 expression, the overall L_P would be higher and thus the resulting water flow can dilute LDL's local concentration in the SI and flush unbound lipid from the vessel wall. This can decrease the rates of LDL-SI ECM interactions and as such may slow down the progression of pre-atherosclerotic events.

4.2 Mathematical formulation

In order to investigate AQP1's effect on the transport of macromolecules inside the artery wall, we employ the same structural model as used by Zeng et al. (131). As noted earlier, this model is similar but not identical to the one used by Yuan et al. (129) and Hunag et al. (35). The schematic of the idealized multi-layer, 2-D convection-diffusion model is depicted in Fig. 4.1. It models the artery wall in four different layers: the endothelium, the SI, the IEL and the media. The adventitia is not included in the model since its loose connective tissue plays a minor role in transport. Leaky junctions surrounding rare ECs constitute a major pathway for the transport of macromolecules (e.g., LDL) across the endothelium, whereas transmural water flow occurs through both normal and leaky junctions. Moreover, from the evidence suggested in the introduction, water can also flow transcellulary through AQP1 channels. We assume that water and advected macromolecules, after entering the SI region, seep through the IEL fenestrae into the media region. The rare ECs with transiently leaky junctions are assumed to be arranged in a periodic surface array, each surrounded by a uniform endothelium of normal permeability. The 2-D model has its origin at the center of the leaky cell and, by abuse of geometry, is axisymmetric on a periodic cylindrical unit. As shown, the z-axis is perpendicular to the endothelium and with negligible radius of curvature of the vessel wall with respect to its thickness, the endothelium is assumed flat. The radius, ξ_I^*, of the periodic unit is half the average distance between leaky ECs. The EC turnover parameter ϕ describing the frequency of the leaky sites is defined as R_1^{*2}/ξ_I^{*2}, where R_1^* is the average effective radius of an EC. The leaky junction has a width of ΔR^* and is equal to $R_2^* - R_1^*$, where R_2^* is the average outer leak radius.

Glossary:

a^*	Effective radius of proteoglycan aggregates
C_j^*	Dimensional concentration in region j
C_j	Dimensionless concentration in region j
C_L^*	Concentration in lumen
D_j^*	Effective diffusivity in region j
j	Region of artery wall ($j = i, m$ for SI and media respectively)
k	Endothelial mass transfer coefficient

K_{P_j}	Darcy permeability of region j
L_j^*	Thickness of region j
L_I^*	IEL thickness
L_p	Hydraulic conductivity
$L_{p_{e+i}}$	Hydraulic conductivity of the endothelium + SI
L_{p_I}	Hydraulic conductivity of IEL
$L_{p_{lk}}$	Hydraulic conductivity of leaky junction
L_{p_m}	Hydraulic conductivity of media
$L_{p_{m+I}}$	Hydraulic conductivity of IEL + media
$L_{p_{nm}}$	Hydraulic conductivity of normal endothelium
L_{p_t}	Total hydraulic conductivity of the vessel wall
P_e	Peclet number
$P_{e_{jr}}$	Peclet number in radial direction in region j
$P_{e_{jm}}$	Peclet number in z direction in region j
P_j^*	Dimensional pressure in region j
P_j	Dimensionless pressure in region j
P_A^*	Adventitia pressure
P_L^*	Lumen pressure
r	Dimensionless radial coordinate
r^*	Dimensional radial coordinate
a_f^*	Radius of fenestra
U_j^*	Dimensional lateral velocity in region j
U_j	Dimensionless lateral velocity in region j
R^*	Dimensional radius of EC
R	Dimensionless radius of EC
$\mathbf{V}$	Velocity vector
W_j	Dimensionless normal velocity in region j
z	Dimensionless normal coordinate
z^*	Dimensional normal coordinate
f_j	filtration/retardation coefficient in region j
γ_j	Volume fraction of a solute per unit total volume of region j
γ_{wj}	Volume fraction of water per unit total volume of region j
ψ_j	Solute partition coefficient in region j
ϕ_I	IEL fenestra fractional area
ΔR^*	Dimensional width of leaky junction
ΔR	Dimensionless width of leaky junction
μ	Viscosity of fluid
ξ_I^*	Dimensional radius of periodic wall unit
ξ_I	Dimensionless radius of periodic wall unit

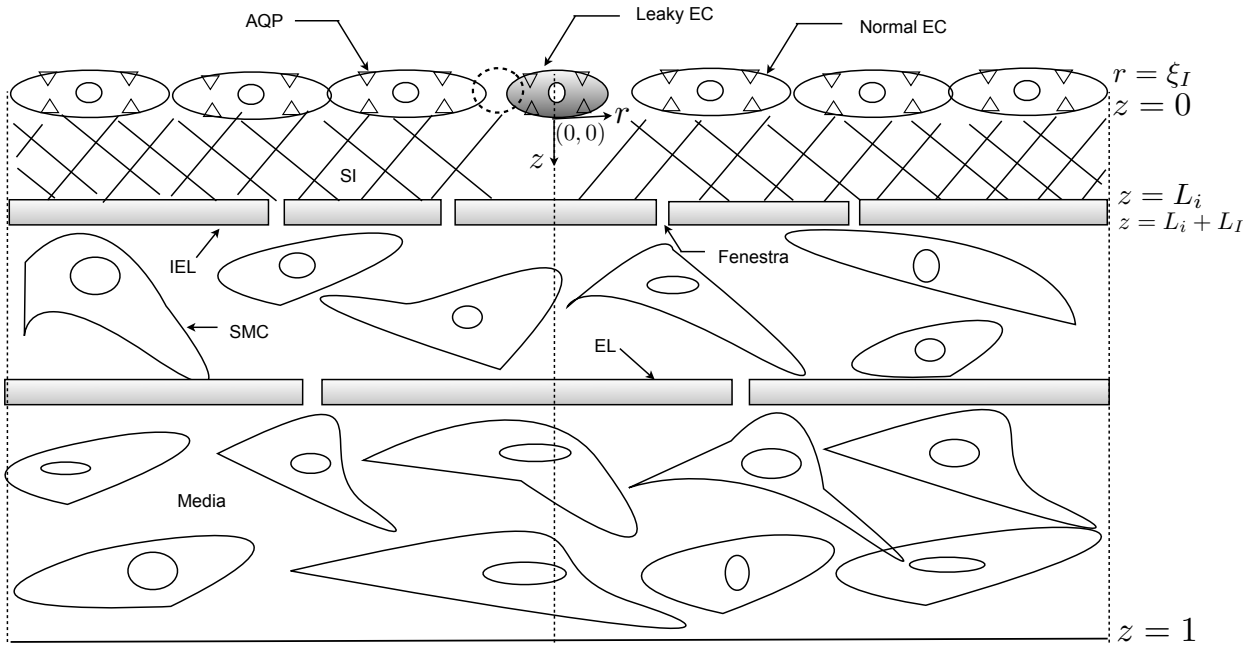
AQP
Leaky EC
Normal EC
$r = \xi_I$
$z = 0$
r
$(0,0)$
z
SI
$z = L_i$
$z = L_i + L_I$
IEL
Fenestra
SMC
EL
Media
$z = 1$

(a)

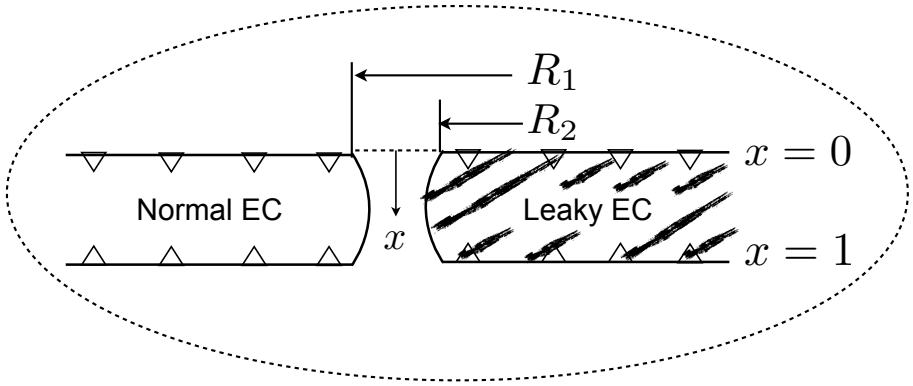
R_1
R_2
$x = 0$
Normal EC
Leaky EC
x
$x = 1$

(b)

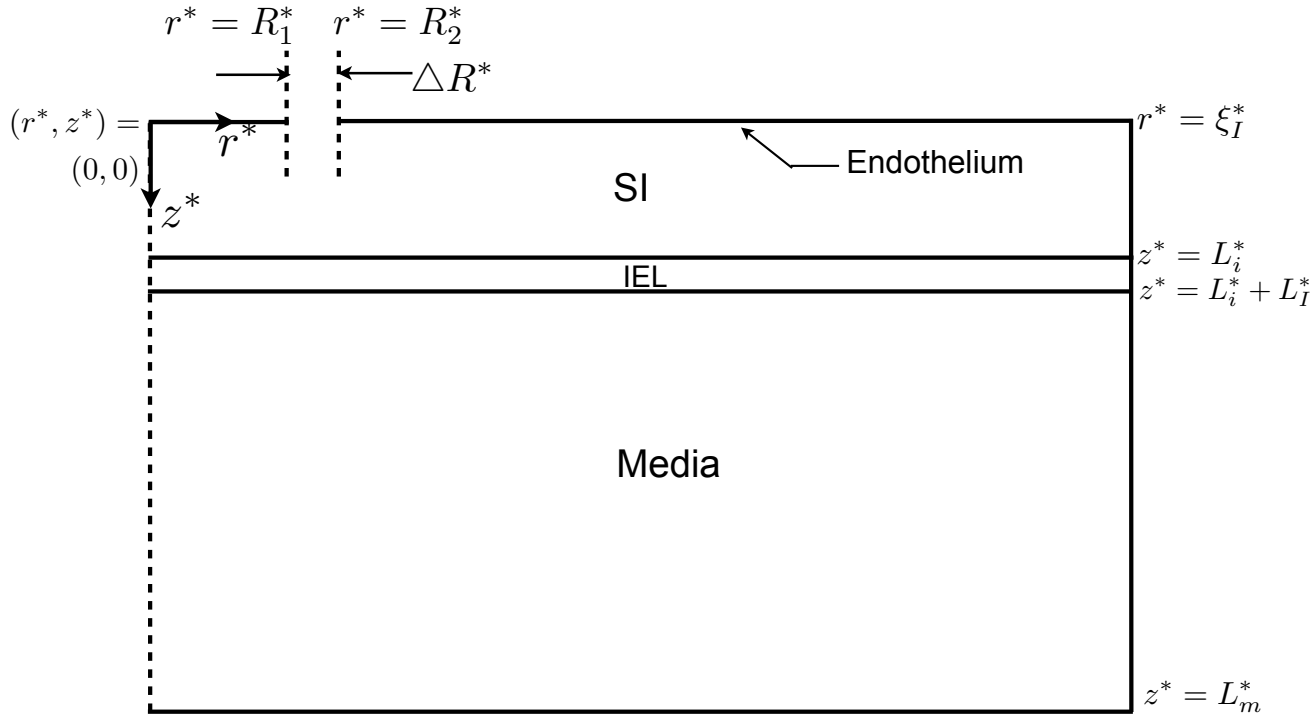

(c)

Figure 4.1: Schematic of the periodic wall unit representing different layers of the vessel wall with non-dimensional variables (a). Macromolecules enter the vessel wall through leaky junctions surrounding leaky EC, while water flows through normal junctions surrounding normal ECs and transcellularly via AQP1 channels, as shown. The SI under non-deformable endothelium is compressible upon pressure loadings. Finer scale, 1-D convection-diffusion model of the leaky cleft by Tzeghai et al. (107) used for Eq. 4.13 which enters as a boundary condition at the EC (b). Idealized mathematical diagram with dimensional variables (c). Note that the IEL shown in Fig. 4.1(c) has a finite thickness (L_I^*). For the current level of modeling, we assume the IEL as a boundary separating the SI and media, with an infinitesimal thickness. However we use constitutive equations (quasi-steady, 1-D, advection-diffusion model as in Ref. (107)) to estimate the solute flux across the IEL with a finite thickness. EC, endothelial cell; SI, subendothelila intima; IEL, internal elastic lamina; SMC, smooth muscle cell; EL, elastic lamellae. See Glossary for definitions of parameters.

4.2.1 Filtration model

The leaky ECs have much wider junctions, and therefore greater hydraulic conductivity, than the normal ECs and thus the pressure drop across the leaky junction is much smaller than that across the normal junctions. Hence, there exists a large pressure gradient parallel to the endothelium in the SI between the exit of the leaky junction and the normal junctions, indicating that water crossing the leaky cleft will spread laterally in the SI while seeping through the fenestrae in the IEL to enter the media.

Let P_L^* and P_A^* be the lumen and adventitia pressure respectively. Thus, ΔP = P_L^* - P_A^*. Let U_j^* and W_j^* be the dimensional lateral and normal velocities of water, respectively. Let $L_{P_j}^*$ and $K_{P_j}^*$ be the hydraulic conductivity and Darcy permeability, respectively, in region j of thickness L_j^*. Let j be the dummy index that takes values i and m for the SI and media, respectively. We introduce following non-dimensional (without *) variables and parameters ($j = i, m$).

$$r = \frac{r^*}{L_m^*}, \qquad z = \frac{z^*}{L_m^*}, \qquad \xi_I = \frac{\xi_I^*}{L_m^*},$$
$$U_j = \frac{U_j^*}{L_{P_m}^* \Delta P}, \qquad W_j = \frac{W_j^*}{L_{P_m}^* \Delta P},$$
$$P_j = \frac{P_j^* - P_A^*}{\Delta P}, \qquad K_{P_j} = \frac{K_{P_j}^*}{K_{P_m}^*}, \qquad L_{P_{lk}} = \frac{L_{P_{lk}}^*}{L_{P_m}^*}, \qquad L_{P_{nm}} = \frac{L_{P_{nm}}^*}{L_{P_m}^*}$$

where $L_{P_m}^* = \dfrac{K_{P_m}^*}{\mu\, L_m^*}$ and μ is the fluid (water) viscosity. The subscripts lk and nm denote leaky and normal endothelium, respectively.

Assuming incompressibility, the water flow through the SI and media satisfies equation of continuity, i.e.,

$$\nabla \cdot \mathbf{V}_j = 0, \quad (j = i, m) \qquad \text{(non-dimensional form)} \tag{4.1}$$

Due to porous structure of the intima and media region, the flow through arterial wall obeys Darcy's

law. It has been shown that Darcy approach is a good approximation for complex layered structures with different ECMs (35, 36, 130, 44). Darcy's law suggests that the flow through a porous medium is proportional to the applied pressure gradient and is given by:

$$\mathbf{V}_j^* = \frac{-K_{P_j}^*}{\mu} \nabla P_j^*, \quad (j = i, m)$$

Therefore in non-dimensional form,

$$\mathbf{V}_j = -K_{P_j} \nabla P_j, \quad (j = i, m) \tag{4.2}$$

Substituting Eq. 4.2 into Eq. 4.1 gives the governing equation for filtration model

$$\nabla^2 P_j = 0, \quad (j = i, m) \qquad \text{(non-dimensional form)} \tag{4.3}$$

Since the governing equations are second order Laplace equations, we need four boundary conditions (two each in r and z direction) for each region. We employ following boundary conditions (in non-dimensional form) to solve Eq. 4.3.

Axisymmetry at $r = 0$ and periodicity at $r = \xi_I$ require no fluid flux, thus

$$U_j = -K_{P_j} \frac{\partial P_j}{\partial r}, \quad (j = i, m) \text{ at } r = 0, \xi_I \tag{4.4}$$

Starling's law relates water velocity across the endothelium W_i to the local pressure drop (assuming negligible osmotic gradients) as:

$$W_i = L_{P_{nm}}(1 - P_i) \text{ at } R_2 < r < \xi_I \text{ and } z = 0 \tag{4.5a}$$

$$W_i = L_{P_{lk}}(1 - P_i) \text{ at } R_1 < r < R_2 \text{ and } z = 0 \tag{4.5b}$$

$$W_i = 0 \text{ at } 0 < r < R_1 \text{ and } z = 0 \tag{4.5c}$$

$L_{P_{nm}}$ in Eq. 4.5a is an area-averaged hydraulic conductivity representing contributions from normal junctions and ECs. Note that $L_{P_{nm}}$ is similar to the hydraulic conductivity of endothelium and SI ($L_{P_{e+i}}$) used in our previous local filtration theory (Ch. 2).

Since the IEL fenestrae are located randomly relative to the leak, we use an effective L_P (L_{P_I}) to describe the water flow across the IEL, which together with incompressibility gives us:

$$W_i\big|_{z=L_i} = W_m\big|_{z=L_i+L_I} = L_{P_I}(P_i\big|_{z=L_i} - P_m\big|_{z=L_i+L_I}) \tag{4.6}$$

At the media-adventitia boundary, the pressure is constant and is equal to the reference pressure, thus

$$P_m = 0 \quad \text{at } z = 1 \tag{4.7}$$

Yuan et al. (129) modeled the water flow through leaky junction (of length L_l^*) as steady 1-D slit flow and calculated its hydraulic conductivity as:

$$L^*_{P_{lk}} = \frac{\Delta R^{*2}}{12\mu L_l^*} \tag{4.8}$$

They also modeled the water flow through the IEL fenestra by considering a cylindrical slab with a circular fenestral pore in its center and estimated the L_P of the IEL. Zeng et al. (131) details Yuan et al.'s (129) method to calculate the L_{P_I}.

4.2.2 Macromolecular transport model

We are interested in studying the macromolecular transport (i.e., its concentration and potential washout) through the artery wall. We assume that initially the artery wall is tracer or macromolecule free and introduce a step change in the system by adding a tracer in the lumen at $t = 0$.

The transport problem of interest is an initial value problem that starts with zero tracer concentration everywhere and is given by following convection-diffusion equation:

$$\frac{\partial C_j^*}{\partial t^*} + (f_j/\gamma_j)\mathbf{V}_j^* \cdot \nabla C_j^* = D_j^* \nabla^2 C_j^*, \quad (j = i, m) \tag{4.9}$$

Notice that Darcy's law, after solving the filtration problem (Eq. 4.3), yields velocities ($\mathbf{V}^*$) required to solve the mass transfer problem (Eq. 4.9). We introduce following new non-dimensional (without *) variables and parameters to solve Eq. 4.9.

$$C_j = \frac{C_j^*}{C_L^*}, \qquad t = \frac{t^*}{L_m^{*2}/D_{mz}^*}, \qquad D_j = \frac{D_j^*}{D_{mz}^*},$$
$$P_{e_{jr}} = \frac{f_j U_j^* L_m^*}{\gamma_j D_{mz}^*}, \qquad P_{e_{jz}} = \frac{f_j W_j^* L_m^*}{\gamma_j D_{mz}^*}$$

where C_L^* is the solute concentration in the lumen. C_j^* is the dimensional solute concentration in region j, locally averaged over both tissue and fluid phase. D_j^* is the effective diffusivity of the solute in region j, t is the dimensionless time, normalized by solute's diffusivity in the media region (z-direction) and the media thickness. f_j, the retardation coefficient, represents the ratio of solute to water velocities; and γ_j is the fractional volume available for macromolecules per unit total tissue volume. $P_{e_{jr}}$ and $P_{e_{jz}}$ are the velocity variables, further non-dimensionalized in a manner appropriate for mass transfer studies, in the form of Peclet numbers in r and z directions, respectively. Using these non-dimensional variables and parameters, we write the dimensionless form of Eq. 4.9 as:

$$\frac{\partial C_j}{\partial t} + P_{e_{jr}} \frac{\partial C_j}{\partial r} + P_{e_{jz}} \frac{\partial C_j}{\partial z_j} = D_{jr} \left(\frac{\partial^2 C_j}{\partial r^2} + \frac{1}{r} \frac{\partial C_j}{\partial r} \right) + D_{jz} \frac{\partial^2 C_j}{\partial z_j^2}, \quad (j = i, m) \tag{4.10}$$

We employ following initial and boundary conditions to solve the governing initial boundary value problem (Eq. 4.10).

As mentioned earlier, for an initially tracer/solute free tissue, the initial condition introduces a tracer at $t = 0$:

$$C_j = 0 \text{ at } t = 0,\ j = i, m \tag{4.11}$$

The axisymmetry at $r = 0$ and periodicity at $r = \xi_I$ require no solute flux at these locations i.e.,

$$\frac{\partial C_j}{\partial r} = 0 \text{ at } r = 0 \text{ and } r = \xi_I,\ j = i, m \tag{4.12}$$

In order to explain the macromolecular transport through the endothelium (via leaks) and the IEL (through the fenestrae), we note that these holes are far smaller and occupy only a small fraction of the total surface area. The non-dimensional tracer flux through such a hole requires a local model on that scale. Tzeghai et al. (107) describe the local macromolecular flux through a fenetra by a 1-D, quasi-steady, advection-diffusion model through a slit. Following Tzeghai et al. (107) and Zeng et al. (131), we calculate the local macromolecular flux at the leaky junction exit as:

$$q_l^*|_{x^*=L_l^*} = \frac{C_L^* D_l^*}{L_l^*} P_{el} \left(\frac{e^{P_{el}} - C_{ls}}{e^{P_{el}} - 1} \right) \tag{4.13}$$

where

$$C_l = \frac{C_l^*}{C_L^*}, \quad x = \frac{x^*}{L_l^*}, \quad P_{el} = \frac{f_l W_l^* L_l^*}{\gamma_l D_l^*}$$

C_l^* is the dimensional solute concentration in the leaky junction, C_{ls} is the dimensionless solute concentration at the SI side of the leaky junction. The x-direction is perpendicular to the endothelium along the junction, as shown in Fig. 4.1(b). W_l^* in the leaky junction is uniform and thus the Peclet number in the leaky junction (P_{el}) is constant unlike $P_{e_{jr}}$ and $P_{e_{jz}}$, which are variables. f_l, γ_l and D_l^* are the retardation coefficient, fractional available volume and diffusion coefficient in the leaky junction, respectively.

The concentration (per unit void volume) is continuous at the leaky junction-SI interface, thus:

$$\frac{C_i}{\gamma_i} = \frac{C_{ls}}{\gamma_l} \text{ at } R_1 < r < R_2 \text{ and } z = 0 \tag{4.14}$$

Substituting C_{ls} from Eq. 4.14 into Eq. 4.13, we make use of solute flux continuity at the leaky junction-SI interface as:

$$q_l^*|_{x^*=L_l^*} = q_{iz}^*|_{z^*=0} = \frac{f_i}{\gamma_i} W_i^* C_i^* - D_{iz}^* \frac{dC_i^*}{dz^*} \tag{4.15}$$

Writing Eq. 4.15 in non-dimensional form:

$$\frac{D_l^*}{L_l^*} P_{el} \left(\frac{e^{P_{el}} - C_{ls}}{e^{P_{el}} - 1} \right) = \frac{D_{2z}^*}{L_m^*} \left(P_{e_{iz}} C_i - D_{iz} \frac{dC_i}{dz} \right) \text{ at } R_1 < r < R_2 \text{ and } z = 0 \tag{4.16}$$

Thus Eqs. 4.14 and 4.16 together constitute a boundary condition at the leaky junction-SI interface. Outside the leaky junction, a mass transfer coefficient k describe the diffusive transport across the normal endothelium. Hence, given the local concentration definitions (based on all phases, tissue and fluid, present locally), we have following additional boundary conditions on the endothelial surface ($z = 0$).

$$- D_{iz} \frac{dC_i}{dz} = \frac{kL_m^*}{D_{mz}^*} \left(1 - \frac{C_i}{\gamma_i} \right) \text{ at } R_2 < r < \xi_I \text{ and } z = 0 \tag{4.17}$$

$$- D_{iz} \frac{dC_i}{dz} = 0 \text{ at } 0 < r < R_1 \text{ and } z = 0 \tag{4.18}$$

Since the fractional area of the fenestra ($\phi_I = a_f^2/\xi_I^2$), where a_f is the radius of the fenestra, is far smaller ($\ll 1$), we assume that there is no interaction among IEL fenestrae and thus the local average solute flux across the IEL (q_I^*) is proportional to fractional fenestral area.

$$q_I^* = \phi_I q_f^* \tag{4.19}$$

where q_f^* is the solute flux through the fenestra. A similar subscale model, as that for the leaky cleft (107), is used to estimate q_f^* as:

$$q_f^*|_{z^*=L_i^*} = \frac{C_L^* D_I^*}{L_I^*} P_{eI} \left(\frac{e^{P_{eI}} C_{Is} - C_{Im}}{e^{P_{eI}} - 1} \right) \tag{4.20}$$

where

$$C_I = \frac{C_I^*}{C_L^*}, \quad P_{eI} = \frac{f_I W_I^* L_I^*}{\gamma_I D_I^*}$$

C_I^* is the dimensional solute concentration in the IEL. C_{Is} and C_{Im} are dimensionless entrance (SI) and exit (media) solute concentrations in the IEL fenestra, respectively. W_I^* is the normal velocity through the IEL. L_I^*, P_{eI}, f_I, γ_I and D_I are the height, Peclet number, retardation coefficient, fractional available volume and effective diffusion coefficient in the IEL, respectively. The conservation boundary conditions at the IEL are

$$q_{iz}^*|_{z^*=L_i^*} = q_{mz}^*|_{z^*=L_i^*+L_I^*} = q_I^* \tag{4.21}$$

One can write the Eq. 4.21 in non-dimensional form as:

$$\frac{D_{2z}^*}{L_m^*} \left(P_{e_{iz}} C_i - D_{iz} \frac{dC_i}{dz} \right) = \frac{D_{2z}^*}{L_m^*} \left(P_{e_{mz}} C_m - D_{mz} \frac{dC_m}{dz} \right) = \frac{D_I^*}{L_I^*} P_{eI} \left(\frac{e^{P_{eI}} C_{Is} - C_{Im}}{e^{P_{eI}} - 1} \right) \tag{4.22}$$

The SI and media concentration matching conditions are:

$$\frac{C_i}{\gamma_i} = \frac{C_{Is}}{\gamma_I} \text{ at } z = L_i \tag{4.23}$$

$$\frac{C_{Im}}{\gamma_I} = \frac{C_m}{\gamma_m} \text{ at } z = L_i + L_I \tag{4.24}$$

The concentration at the media-adventitia boundary is assumed to be zero, thus

$$C_m = 0 \text{ at } z = 1 \tag{4.25}$$

4.2.3 Solution methods

We use direct discretization, finite difference on a non-uniform mesh approach to solve for pressure and concentration distributions. Even though the 2-D Laplace equation (Eq. 4.3) has a direct analytical solution in terms of Bessel functions, the IEL matching conditions (Eq. 4.6) makes its implementation cumbersome (131). Moreover, since the width of the leaky cleft is four orders of magnitude smaller than the model's radial dimension, one needs to retain extremely large number of Bessel terms [$O(10^4)$] to resolve the scales over which dynamic variables change near the leaky junction (131) and can significantly increase the computational cost.

We improve the computational efficiency by developing a non-uniform mesh for the finite difference solution, which is very dense near the leak and sparse far from it. The discretized model becomes a large number of simultaneous linear algebraic equations, equal to the total number of mesh points, which can be solved with MATLAB (The MathWorks, Inc.). As in Zeng et al. (131), the unsteady macromolecular transport model is solved using the Hopscotch method, a fast second order partial differential equation solver. This method is fast, efficient and unconditionally stable (28).

4.2.4 Constants and parameters

Geometric parameters

The baseline values of constants and parameters used in the model are summarized in table 4.1. Note that most of the geometric parameters used in this study are same as those employed by Zeng et al. (131). We use Huang et al.'s (35) heterogeneous fiber matrix theory to estimate the Darcy permeability (K_{P_i}) of an uncompressed SI K_{P_i} to be 2.20×10^{-12} cm^2. Huang et al. (36) and our previous study (Ch. 2) discuss the effect of the intima thickness on K_{P_i} and estimate its variation

with transmural pressure.

Curry (15) calculates the retardation coefficient f_j from the partition coefficient ψ_j as:

$$f_j = 1 - (1 - \psi_j)^2, \quad (j = i, m) \tag{4.26}$$

where $\psi_j = \gamma_j/\gamma_{wj}$ in region j is defined as the ratio of fractional available volume for a solute (γ_j) to that available for water (γ_{wj}). The partition coefficient for a solute of radius r_s, in the randomly oriented fiber matrix, can be obtained as (15):

$$\psi = \exp\left[-(1-\epsilon)^{1/2}\left(\frac{2r_s}{r_f} + \frac{r_s^2}{r_f^2}\right)\right] \tag{4.27}$$

where ϵ is the fractional void volume and r_f is the fiber radius.

For the sparse SI layer, $\gamma_{wi} \sim 1$ (35) and thus $\gamma_i \sim \psi_i$. Thus at zero transmural pressure, since $\epsilon = 0.99$ (Ch. 2) and $r_f = 2.37$ nm (Ch. 2), Eq. 4.27 gives the fractional volumes (γ_i) for HRP (r_s = 3 nm (35)) and LDL (r_s = 11 nm (35)) as 0.95 and 0.65, respectively, and Eq. 4.26 predicts their retardation coefficients (f_i) as 1.0 and 0.88, respectively. The volume fraction of albumin in the rabbit thoracic media (γ_m) was measured by Tedgui and Lever (101) as 0.08. Since albumin ($r_s \sim$ 3.5 nm (14)) and HRP are similar in size, we set γ_m for HRP equal to that for albumin, and together with $\gamma_{wm} \sim 0.5$ (35), Eq. 4.26 gives f_m = 0.3. Using γ_m for HRP and molecular radii of HRP and LDL, Zeng et al. (131) estimated the media LDL distribution volume to be 0.025. Thus, from Eq. 4.26, we estimate f_m for LDL to be 0.0975.

Ogston et al. (65) have derived the diffusion coefficient for a solute of radius r_s in a fiber matrix in terms of its diffusion coefficient D_f in free space as:

$$D = D_f \exp\left[-(1-\epsilon)^{1/2}\left(1 + \frac{r_s}{r_f}\right)\right] \tag{4.28}$$

where ϵ is the fractional void volume and r_f is the fiber radius. Free diffusivity of albumin is D_f = 6.8$\times 10^{-7}$ cm^2/s (116). Using Stokes-Einstein (15, 29) size scaling ($D_{HRP}/D_{albumin} \sim r_{albumin}/r_{HRP}$), we find D_f for HRP as 7.93$\times 10^{-7}$ cm^2/s. In order to account for the presence of PG and CG fibers in the SI, Huang et al.'s (35) fiber matrix theory replaces D_f in Eq. 4.28 and computes effective diffusivity in the SI region as:

$$D_i = D_f(\epsilon_{CG} + \epsilon_{PG} - 1) \exp\left[-(1-\epsilon_{CG})^{1/2}\left(1 + \frac{r_s}{r_{CG}}\right)\right] \exp\left[-(1-\epsilon_{PG})^{1/2}\left(1 + \frac{r_s}{a^*}\right)\right] \tag{4.29}$$

where ϵ_{CG} and ϵ_{PG} are void fractions of CG and PG fibers, respectively. r_{CG} is the radius of collagen fibers (20 nm (35)) and a^* is the effective radius of PG fibers (2.37 nm (Ch. 2)). At zero transmural pressure, with $\epsilon_{CG} = 0.95$ (35) and $\epsilon_{PG} = 0.99$ (Ch. 2), Eq. 4.29 yields D_i for HRP and LDL as 4.51$\times 10^{-7}$ cm^2/s and 7.43$\times 10^{-8}$ cm^2/s, respectively. Due to similar matrix structures (47), as per Zeng et al. (131), we assume IEL fenestrae transport parameters to be equal to the SI parameters, $f_I = f_i$, $\gamma_I = \gamma_i$, $\gamma_{wI} = \gamma_{wi}$, $D_I^* = D_i^*$.

Equations 4.26 - 4.29, with corresponding fractional void volumes $(\epsilon_{PG}, \epsilon_{CG})$ at different SI compressions, predict the variation in γ_i, f_i and D_i with transmural pressure. Our previous study (Ch. 2) explains in detail the calculation of these fractional void volumes for compressible SI region.

Hydraulic conductivities

Many research groups (100, 2, 78, 62) have measured the hydraulic conductivity (L_P), defined as the ratio of transmural water flux to the difference between applied hydrostatic and osmotic pressure difference, of the intact ($L^*_{P_t}$) and denuded ($L^*_{P_{m+I}}$) aortic walls at various transmural pressures. In the filtration problem discussed in Section 4.2.1, the input parameters are: the hydraulic conductivity of the leaky junction ($L^*_{P_{lk}}$), the hydraulic conductivity of the normal endothelium ($L^*_{P_{nm}}$) and the hydraulic conductivity of the IEL (L_{P_I}). We estimate $L_{P_{lk}}$ using Eq. 4.8 and L_{P_I} as

Table 4.1: Parameters and constants used in the model

Constant/Parameter	Value	Reference
L_i^*, μm	0.5	(36), a
L_l^*, μm	2.0	(123)
L_I^*, μm	1.0	(129)
L_m^*, μm	141	(78)
R_1^*, μm	15	(123)
K_{P_i}, cm^2	2.20×10^{-12}	(36, 41), b
$L_{P_I}^*$, $\mathrm{cm/sec \cdot mmHg}$	9.7×10^{-8}	(Ch. 2)
$L_{P_m}^*$, $\mathrm{cm/sec \cdot mmHg}$	1.04×10^{-7}	(Ch. 2)
ΔR^*, nm	20	(123)
a_f^*, μm	1.0	(37)
ξ_I^*, μm	670	(131)
ϕ_I	0.043	(37)
γ_i	0.95 (HRP), 0.65 (LDL)	b, c
γ_m	0.08 (HRP), 0.025 (LDL)	(101, 131)
f_l	1.0	(129)
f_i	1.0 (HRP), 0.88 (LDL)	(35), b
f_m	0.3 (HRP), 0.0975 (LDL)	(35)
D_f^*, $\mathrm{cm}^2/\mathrm{sec}$	7.93×10^{-7} (HRP), 2.06×10^{-7} (LDL)	c, (105)
D_i^*, $\mathrm{cm}^2/\mathrm{sec}$	4.51×10^{-7} (HRP), 7.43×10^{-8} (LDL)	b, c
D_m^*, $\mathrm{cm}^2/\mathrm{sec}$	8.4×10^{-9} (HRP), 5.4×10^{-10} (LDL)	(105, 35, 131)
D_{mr}^*/D_{mz}^*	3.0	(129)
μ, $\mathrm{kg/m \cdot sec}$	7.2×10^{-4}	(31)

a: at zero transmural pressure

b: corresponds to uncompressed SI at zero transmural pressure, values corresponding to compressed SI are calculated as explained in our previous study (Ch. 2)

c: estimated as explained in the text

explained by Zeng et al. (131). Assuming that layers of the vessel wall act as resistances connected in series, we write:

$$\frac{1}{L_{P_t}^*} = \frac{1}{L_{P_{e+i}}^*} + \frac{1}{L_{P_{m+I}}^*} \tag{4.30}$$

where $L_{P_{e+i}}^*$ is the phenomenologically-derived hydraulic conductivity of the endothelium plus the SI layer that takes into account the effects of pressure induced intima compression and fenestra blockage. Zeng et al. (131) have lumped these effects and used an effective $L_{P_{nm}}^*$, instead of $L_{P_{e+i}}^*$,

in their model. For a given transmural pressure, our local filtration model (Ch. 2) predicts the $L^*_{P_{e+i}}$ along with the corresponding SI thickness (L^*_i) and the Darcy permeability ($K^*_{P_i}$). However, given the dissimilarity in the two model structures, we do not simply use the predicted $L^*_{P_{e+i}}$ from our local model (Ch. 2) in the place of $L^*_{P_{nm}}$ in Eq. 4.5a, but match water fluxes from two models. That is, for a given transmural pressure, we first estimate the water flux from the local model and find the value of $L^*_{P_{nm}}$ that predicts the same water flux from the current filtration model (away from the leak), but importantly with the same L^*_i and $K^*_{P_i}$ as used in the local model. Given our local filtration model's ability to predict the variation in $L^*_{P_{e+i}}$ with transmural pressure, and also with varying endothelial AQP1 expressions, we can test the current theory for the effect of pressure and endothelial AQP1 expression on the transport of macromolecules inside the artery wall.

4.3 Results and Discussion

4.3.1 Pressure Distribution

Figure 4.2 plots the non-dimensional pressure in the SI at $z = 0$ (P_{SI}) and at the IEL-media interface (P_{Im}) as a function of radial distance from the center of the leaky cell. It also shows the effect of increasing endothelial AQP1 expression (or the resulting increase in $L_{P_{e+i}}$) on P_{SI} and P_{Im}. The pressure curves in the SI attain maximum values at the leaky cleft (r^*/R_1^*= 1) and decay to lower and almost r-independent values far away from the leak (r^*/R_1^* >10). The large difference between the hydraulic conductivities of the leaky and normal junction ($L_{P_{lk}} \sim 5000 L_{P_{nm}}$) results in a significant pressure drop across normal endothelium compared to that under the leak. These pressure gradients drive the water flow radially (parallel to the endothelium) in the SI, generating radial velocities (U_i, as shown in Fig. 4.3) that radially advect tracer molecules in the SI further away from the leak. This advective transport can explain the early rapid spot growth seen by Chuang et al. (13) and Shou et al. (79). The pressure profiles shown in Fig. 4.2 loose their r-dependence far away from the leak and the model reduces to 1-D with almost all of the flow occurring normal to the endothelium. The pressure distribution in the media region (see lower red curves in Fig. 4.2) is almost independent of r direction. However, we find a clear rise in pressure (P_{Im}) near r^*/R_1^*= 1 , and as pointed out by Zeng et al. (131), it suggests that the impact of the leaky junction extends beyond the SI region. Due to lower Darcy permeability of the media (K_{P_m}), this rise however disappears within a short distance from the IEL (not shown), and P_{Im} becomes r-independent.

It should be noted that the non-dimensional peak pressure in the SI reported by Zeng et al. (131) is small ($\sim$ 0.7) compared with our predictions ($\sim$ 0.9). This difference could be attributed to higher values of L_i^* and $K_{P_i}^*$ used by Zeng et al. (131). For the transmural pressure difference of 100 mmHg, our local filtration model (Ch. 2) predicts L_i^*= 75 nm and $K_{P_i}^*$= 1.22 $\times$ 10^{-13} cm^2, compared to Zeng et al.'s (131) L_i^*= 200 nm and $K_{P_i}^*$= 1.08 $\times$ 10^{-12} cm^2. Lower $K_{P_i}^*$, resulting from intima compression, would mean that the water flow entering from the leaky junction will

experience greater resistance and will result in higher pressure near the leak, as shown in Fig. 4.2 (though the results shown in Fig. 4.2 use ΔP^* =80 mmHg, the results for ΔP^* =100 mmHg are qualitatively similar with non-dimensional peak pressure $\sim$ 0.9). It is also interesting to note that the distance from the peak in which P_{SI} curves reach their lower constant values decreases with increasing ΔP^*. For example at ΔP^*= 80 mmHg, P_{SI} attains a constant r-independent value at $r^*/R_1^* \sim 6$ (see solid blue curve in Fig. 4.2), which decreases to $r^*/R_1^* \sim 4$ at 100 mmHg (not shown). This suggests that the resulting radial pressure gradients would be larger, and thus radial velocities that advect tracers away from the leak would be higher at higher ΔP^*. This can explain shorter rise times required to achieve the asymptotic spot size at higher transmural pressures, as observed by Hunag et al. (36) and Y. Sun (94).

Figure 4.2 also shows the effect of increasing transcellular water flow through AQP1s on P_{SI} and P_{Im}. The lowest value of $L_{P_{e+i}}$ in Fig. 4.2 represents the least endothelial AQP1 expression (baseline) that corresponds to AQP1s contributing 40% to the intrinsic hydraulic conductivity of the endothelium (L_{P_e}). As Fig. 4.2 shows, both P_{SI} and P_{Im} increase with increased endothelial AQP1 expression (50% and 100% more than baseline). Our local filtration theory argues that with more EC AQP1s, there is less force per unit area on the endothelium and the intima is relatively uncompressed. The resulting increase in $K_{P_i}^*$ due to higher L_i^* decreases intima's resistance to water flow and thus lowers the overall pressure drop across it. We find approximately 13% and 18% increase in P_{SI} (far from the leak) for 50% and 100% increase in the endothelial AQP1 expression, respectively, at ΔP^*= 80 mmHg. The corresponding numbers at ΔP^*= 60 mmHg are only 6% and 9%, respectively. The smaller increase in P_{SI} seen at 60 mmHg can be explained as follows. At lower transmural pressure, due to less force, the intima is already decompressed with baseline EC AQP1 expression and thus increasing AQP1 expression and decompressing it more would decrease intima's resistance by a small amount. However at higher transmural pressures, say 80 mmHg, the force on the endothelium is enough to compress the intima. In this case, with more EC AQP1s, the resulting decrease in the force decompresses the intima from a compressed state and thus significantly decreases its overall resistance to water flow and results in higher pres-

sures shown in Fig. 4.2. The same line of reasoning can also be used to explain why the increase in pressure with 100% more AQP1s is not significantly higher than the increase seen with 50% more AQP1s. It is also interesting to note that the peak pressure in the intima increases slightly with AQP1 expression though the hydraulic conductivity of the leaky junction is unchanged. This again could be attributed to the change in L_i^* and corresponding increase in $K_{P_i}^*$. If $K_{P_i}^*$ is higher, as noted earlier, there will be less pressure drop across the leaky junction and a corresponding increase in P_{SI} as shown.

4.3.2 Lateral and Normal velocity

The lateral velocity in the SI (U_i) and its variation with increasing AQP1 expression is plotted in Fig. 4.3 as a function of radial distance r. The radial pressure gradients shown in Fig. 4.2 generate significant radial velocity near the leaky junction (r^*/R_1^*= 1), which uniformly decays to zero as the distance from leak increases (where P_{SI} becomes r-independent). We find that with more AQP1s the peak velocity near the leak decreases. This is consistent with smaller pressure gradients obtained with increasing $L_{P_{e+i}}$ or decreasing intima's resistance, shown in Fig. 4.2. The decrease in radial velocity would mean slower advective transport of tracer inside the SI and possibly smaller spots.

Figure 4.4 shows the effect of increasing EC AQP1 expression on the normal velocity (W_I^*) across the IEL. Due to significantly higher L_P of the leaky junction, W_I attains a maximum near r^*/R_1^* = 1 and decreases to lower and r-independent values far from the leak. In other words, the effect of leaky junction becomes negligible beyond $r^*/R_1^* > 10$ and the 2-D model reduces to 1-D in z. As seen from Fig. 4.4, the average velocity away from the leak increases with more AQP1s on the endothelium and this increase is proportional to the corresponding increase in P_{SI} as $W_I = L_{P_{e+i}}(1 - P_{SI})$. Hence for the reasons mentioned earlier, we find greater increase in W_I with more EC AQP1s at higher transmural pressures (80 and 100 mmHg) that at 60 mmHg. Interestingly, the peak velocity decreases with increasing $L_{P_{e+i}}$ and is consistent with higher peak pressures obtained with more AQP1s, as shown in Fig. 4.2. The increase in W_I and thus in overall

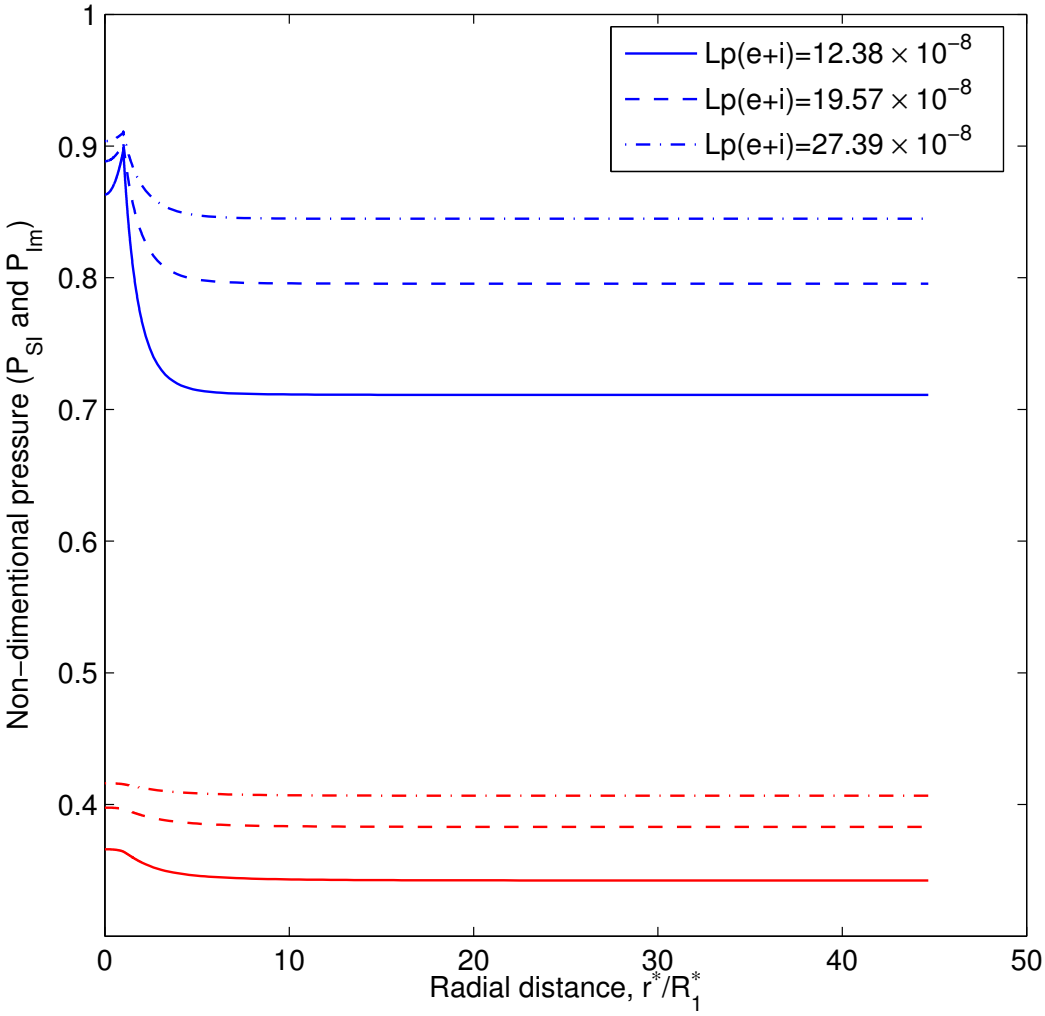

Figure 4.2: Non-dimensional pressure in the SI at $z = 0$ (P_{SI} - upper blue curves) and at the interface of IEL and media (P_{IM} - lower red curves) as a function of radial distance r from the center of the leaky cell with increasing endothelial AQP1 expression. Radial distance r^* in this and subsequent plots is normalized by the radius of an EC (R_1^*), as opposed to $r = r^*/L_m^*$, to focus on the junctional region. Thus the leaky junction is at $r^*/R_1^* = 1$. Pressure is normalized by the transmural pressure drop ΔP^*= 80 mmHg. All $L_{P_{e+i}}$ values are in $\mathrm{cm/sec \cdot mmHg}$. $L_{P_{e+i}}$ = 12.38$\times 10^{-8}$ (solid lines) corresponds to the baseline endothelial AQP1 expression (i.e., $L_{P_{EC}}$ = 40% of L_{P_e}; prediction from our local model (Ch. 2)), whereas 19.57$\times 10^{-8}$ and 27.39$\times 10^{-8}$ represent 50% (dashed lines) and 100% (dot-dashed lines) more endothelial AQP1 expression than the baseline case, respectively.

transmural flow can significantly influence the concentration of tracer molecules inside the SI. For example, increased transmural flow can dilute tracer's local concentration in the SI and flush unbound tracer from the SI further into the vessel wall.

4.3.3 HRP concentration distribution

Figures 4.5(a)-(c) plot non-dimensional radial HRP concentration distribution in the SI (C_{SI}) at $z = 0$ and at the IEL-media interface (C_{Im}) for transmural pressure difference of 60, 80 and 100 mmHg, respectively. At each ΔP^*, the effect of increasing EC AQP1 expression is also shown. For a short circulation time (4 min), it is assumed that HRP enters the vessel wall through leaky junction only and the transport of HRP across the normal endothelium is neglected i.e., we set k= 0 in Eq. 4.17.

For each transmural pressure, both C_{SI} and C_{Im} are higher near the leak ($r^*/R_1^* \sim 1$) and decay to low values away from it ($r^*/R_1^* \gg 1$). Due to very low distribution volume of HRP in the media region (γ_m= 0.08), a significant concentration drop is seen across the IEL ($C_{Im} \ll C_{SI}$) in Figs. 4.5(a)-(c). We find that C_{SI}, especially near the leak, and C_{Im} increase with transmural pressure (see solid blue curves in Figs. 4.5(a)-(c)). Note that L_{P_t} decreases but the overall transmural flow, given by $L_{P_t}\Delta P$, increases with transmural pressure. Naively, one might think that increased transmural flow should lower HRP's concentration in the SI rather than raising it. However, the change in properties of the SI upon pressure induced intima compression, namely the decrease in γ_i and D_i, restricts HRP's transport through the intima and leads to higher C_{SI} values with increasing ΔP^*. It is also interesting to note that the radial distance required for C_{SI} and C_{Im} curves to attain their constant values decreases with increasing ΔP^*. This is a direct consequence of the increased SI resistance, due to its compression, to the flow at higher pressures.

Note that our C_{SI} and C_{Im} values at 100 mmHg shown in Fig. 4.5(c) are higher, especially near the leaky junction ($r^*/R_1^* \sim 1$), than those reported by Zeng et al. (131) (see Fig. 5 in Ref. (131)). Moreover, their C_{SI} and C_{Im} curves for the rat aorta reach constant-lower values at $r^*/R_1^* \sim 10$, much higher than our predictions of $r^*/R_1^* \sim 5$. We believe the discrepancy

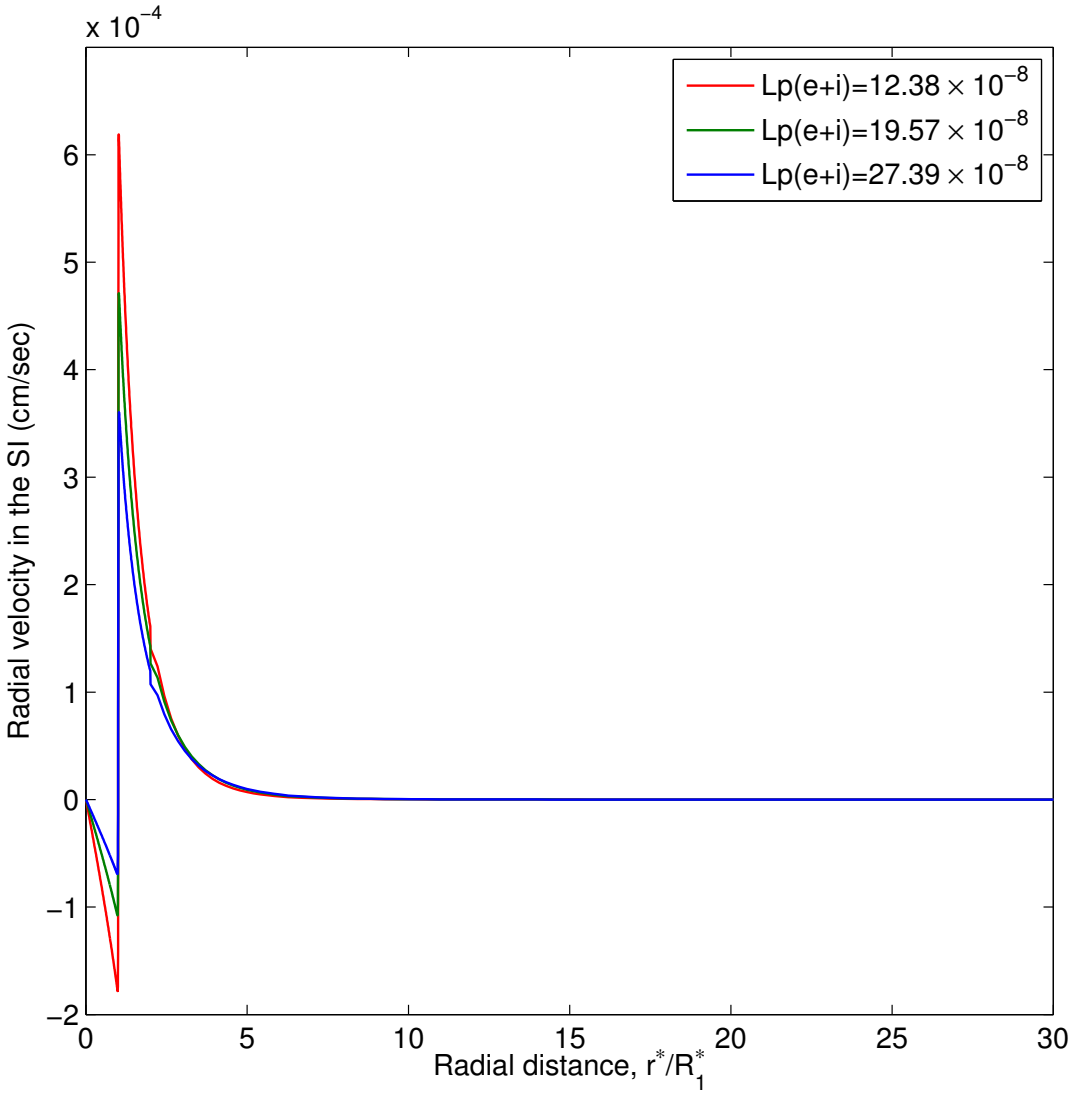

Figure 4.3: Radial velocity in the SI (U_i) as a function of radial distance r from the center of the leaky cell and its variation with increasing endothelial AQP1 expression at ΔP^*=80 mmHg. $L_{P_{e+i}}$ values are as described in Fig. 4.2

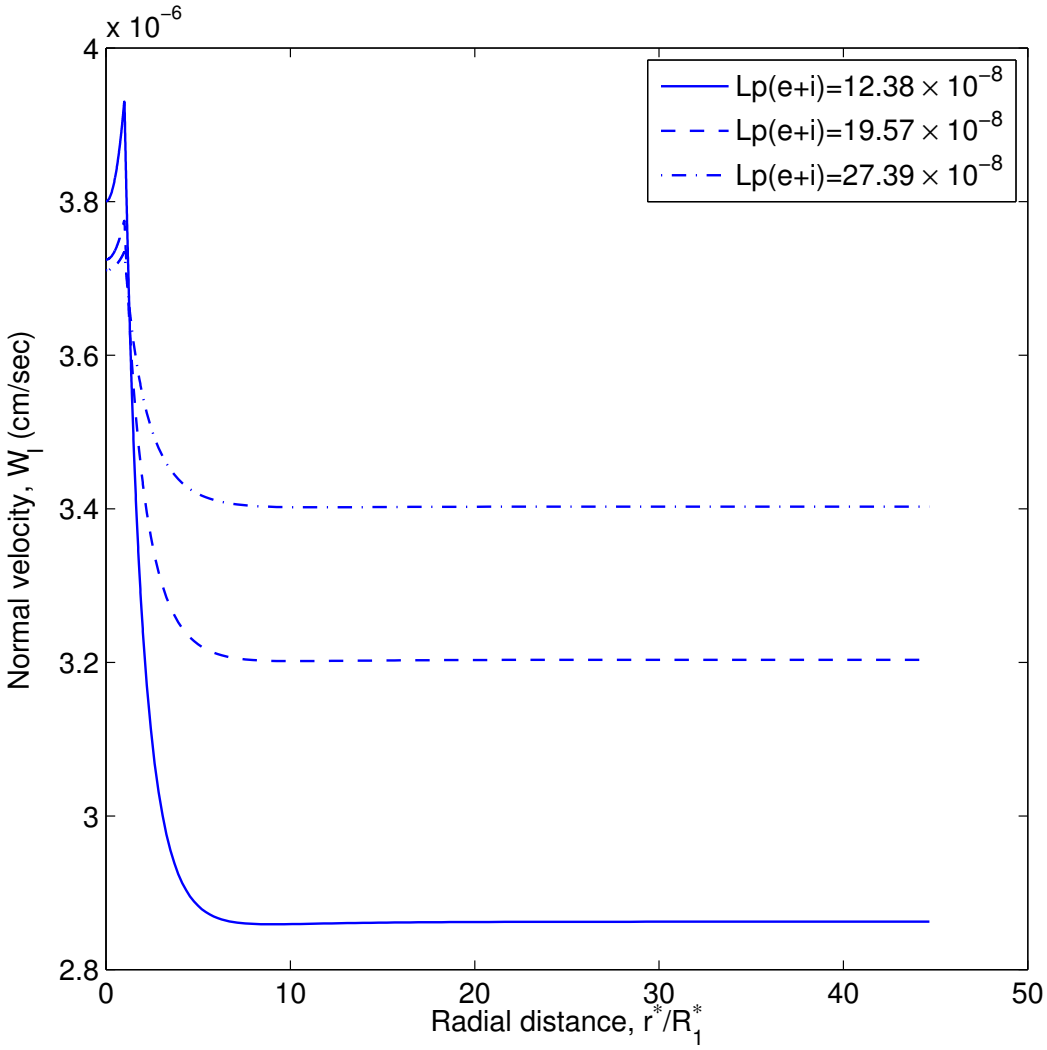

Figure 4.4: Normal velocity across the IEL (W_I) as a function of radial distance r from the center of the leaky cell and its variation with increasing endothelial AQP1 expression at ΔP^*=80 mmHg. $L_{P_{e+i}}$ values are as described in Fig. 4.2

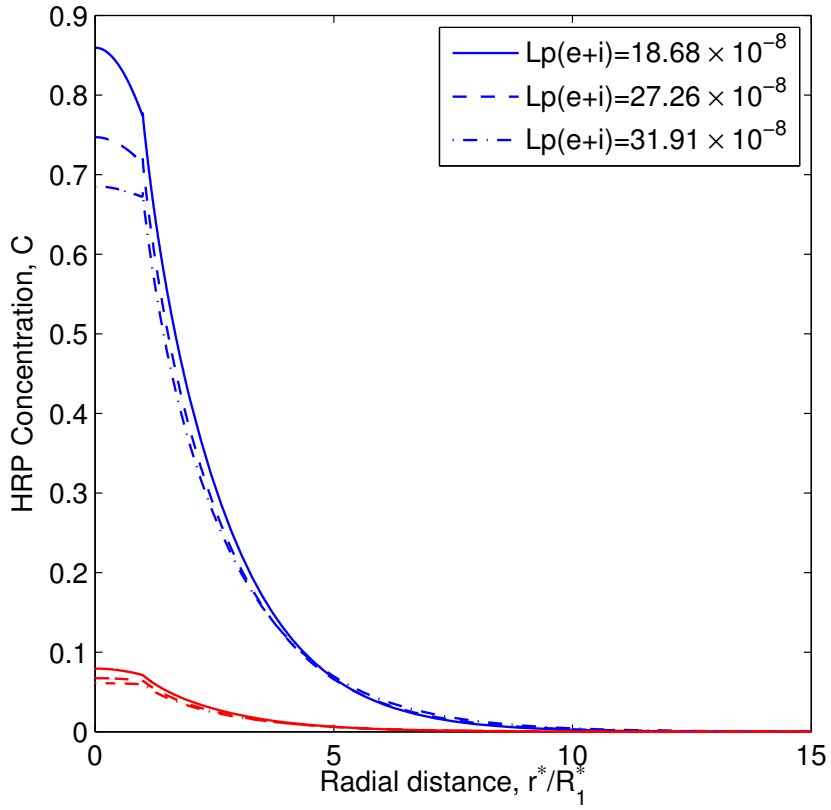

(a) P_L^*=60 mmHg

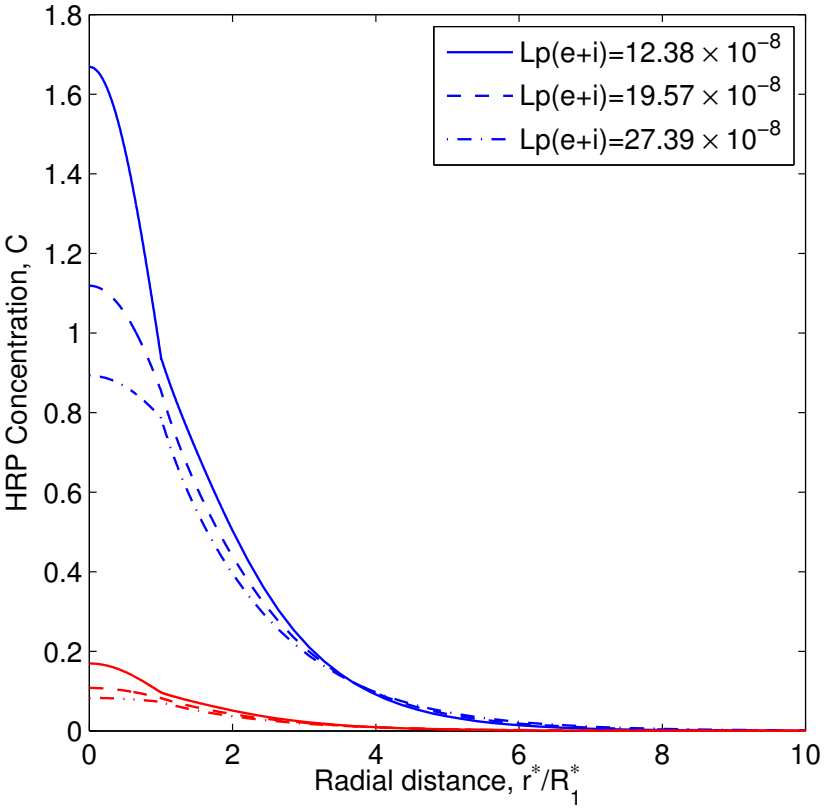

(b) P_L^*=80 mmHg

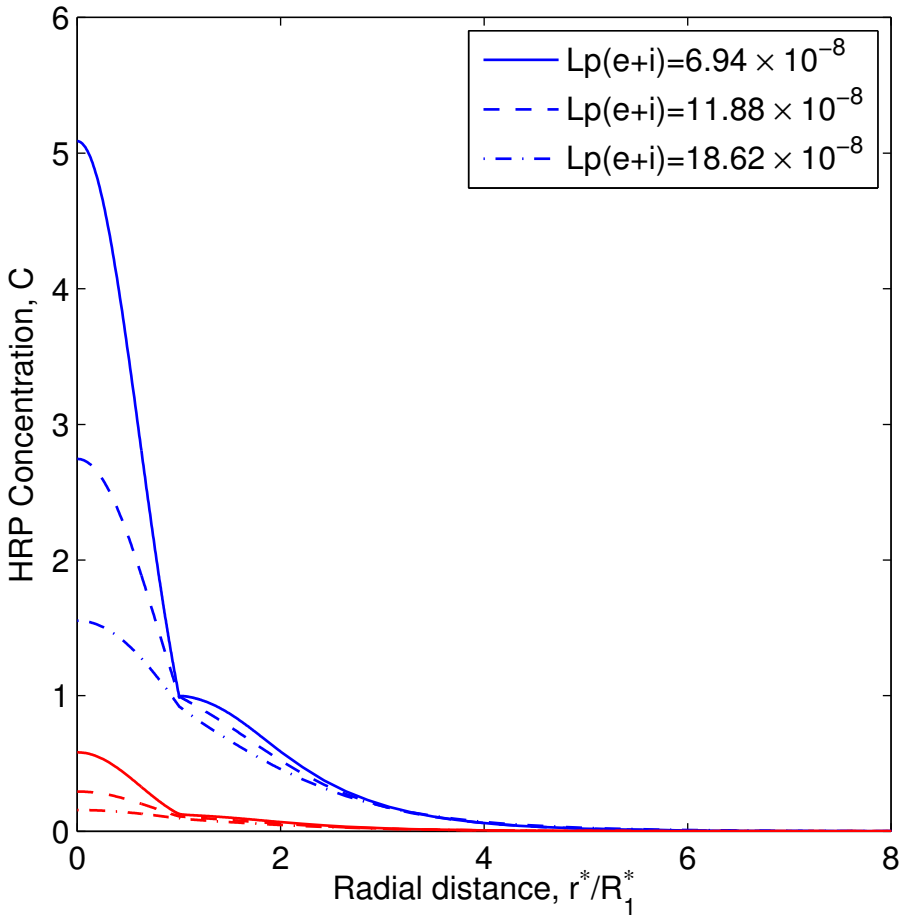

(c) P_L^*=100 mmHg

Figure 4.5: Non-dimensional concentration distribution of HRP at 4-min circulation in the SI at $z = 0$ (C_{SI}, upper blue curves) and at the IEL-media interface (C_{Im}, lower red curves) as a function of radial distance from the center of the leaky cell and its variation with increasing endothelial AQP1 expression. Note that the leaky junction is at r^*/R_1^*=1. All $L_{P_{e+i}}$ values are in $\mathrm{cm/sec \cdot mmHg}$. Solid, dashed and dot-dashed blue and red curves in each figure represent namely the baseline, 50% more and 100% more endothelial AQP1 expressions, respectively. Note that $L_{P_{e+i}}$ values for the same AQP1 expression decrease with increasing transmural pressure.

between the two predictions is due to the difference in SI parameter values used. Zeng et al.'s (131) HRP parameters in the SI are: f_i= 1, γ_i= 1 and D_i^*= 4.12$\times 10^{-7}$ cm^2/s. However, based on the discussion in section 4.2.4, we use f_i= 0.92, γ_i= 0.73 and D_i^*= 1.28$\times 10^{-7}$ cm^2/s at ΔP^*= 100 mmHg. Due to our small parameter values, there is an increased filtration of HRP in the SI and together with intima's increased resistance to flow it results in higher concentration of HRP inside the SI.

Interestingly, as Figs. 4.5(a)-(c) show, increasing EC AQP1 expression results in an opposite effect i.e., both C_{SI} and C_{Im} decrease with more AQP1s on the endothelium. At a given ΔP^*, more EC AQP1s mean higher $L_{P_{e+i}}$ and thus greater overall transmural flow. This increase in flow not only dilutes HRP's concentration in the SI but also flushes it from the SI further into the media region. Consistent with the results shown in Figs. 4.2 and 4.4, we find a greater effect of increasing EC AQP1s, or raising transcellular water flow, at higher transmural pressures than at 60 mmHg.

Figures 4.6(a)-(c) plot the variation of area averaged (integrated in r) non-dimensional concentration of HRP (C_{Int}) across the depth of the vessel wall at ΔP^*= 60, 80 and 100 mmHg, respectively. These figures also depict the effect of increasing EC AQP1 expression on C_{Int} at each pressure. In all of these results, we find a huge drop in C_{Int} within a very short distance of $z^*/L_m^* \sim$ 0.001-0.007, corresponding to the location of the IEL. The large difference between the distribution volume of HRP in the SI (γ_i) and the media (γ_m) across the IEL results in the observed drop in C_{Int}. As expected, increasing EC AQP1s had a small effect on C_{Int} at 60 mmHg. However, at 80 and 100 mmHg, a significant decrease in C_{Int} results with more EC AQP1s. Note that the difference between C_{Int} with 50% more AQP1s and with 100% more AQP1s is higher at 100 mmHg than 80 mmHg (see dashed and dot-dashed curves on Figs. 4.6(b) and 4.6(c)). This implies that the intima with 50% more AQP1s is still relatively compressed at 100 mmHg than at 80 mmHg.

Figure 4.7 shows the percentage decrease in absolute concentration of HRP in the SI (averaged in both r and z) with higher EC AQP1s from its value at the baseline case. Interestingly,

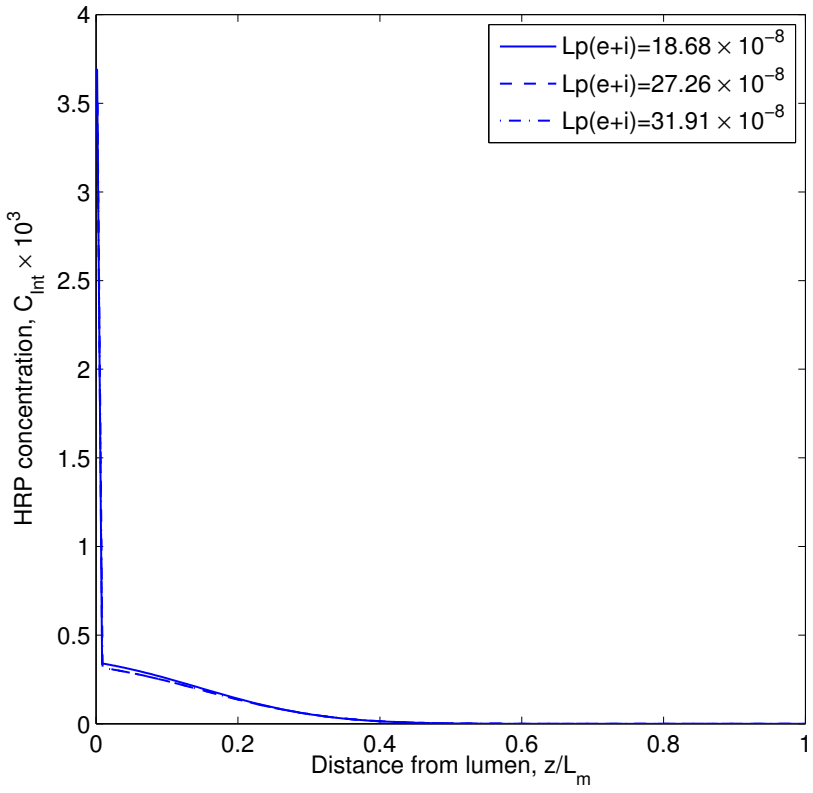

(a) P_L^*=60 mmHg

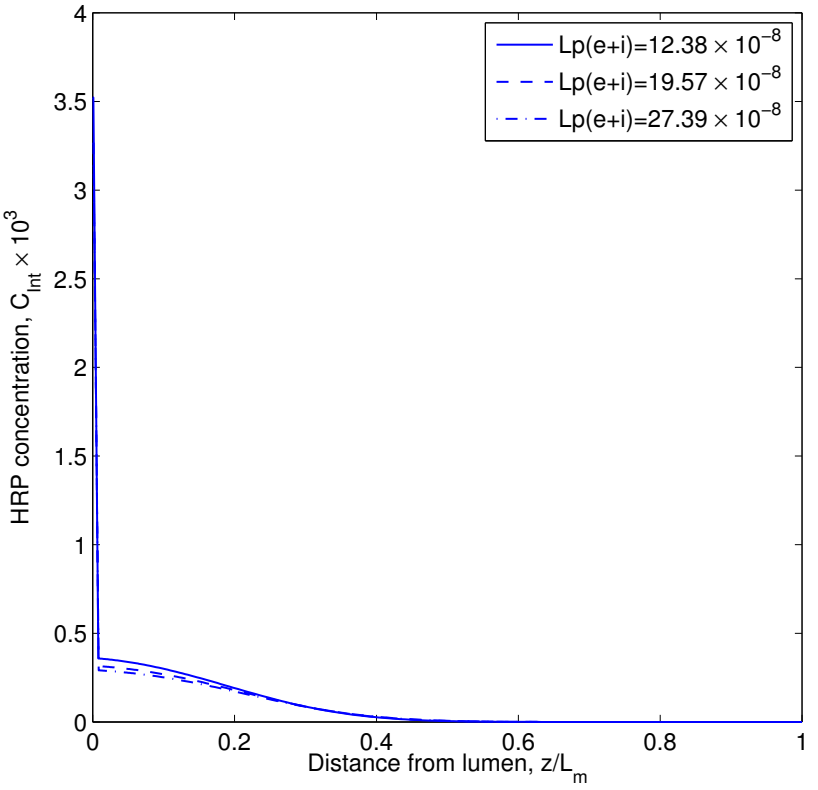

(b) P_L^*=80 mmHg

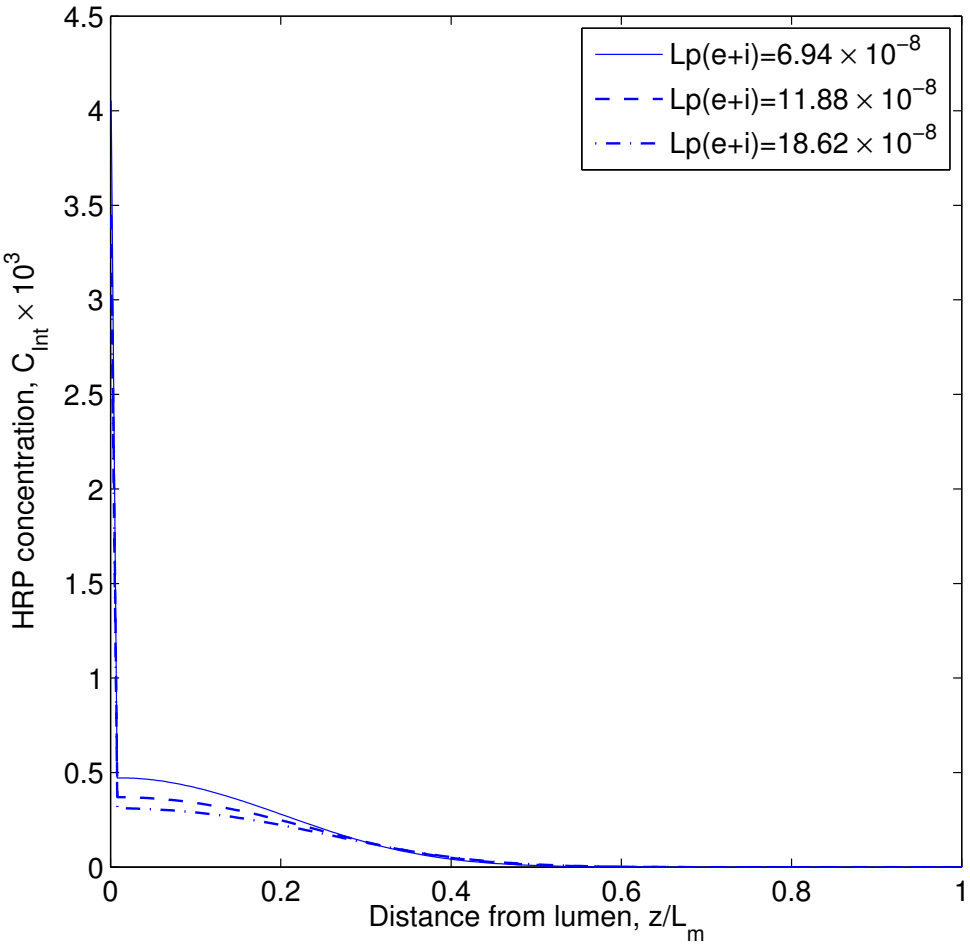

(c) P_L^*=100 mmHg

Figure 4.6: Non-dimensional concentration distribution of HRP (averaged in r) at 4-min circulation as a function of z (across the vessel wall) and its variation with increasing endothelial AQP1 expression. Note that the IEL is located between $z^*/L_m^* \sim 0.001$ to $z^*/L_m^* \sim 0.007$, a region where drastic drop in concentration is seen. All $L_{P_{e+i}}$ values are in $\mathrm{cm/sec \cdot mmHg}$. Solid, dashed and dot-dashed blue and red curves in each figure represent namely the baseline, 50% more and 100% more endothelial AQP1 expressions, respectively.

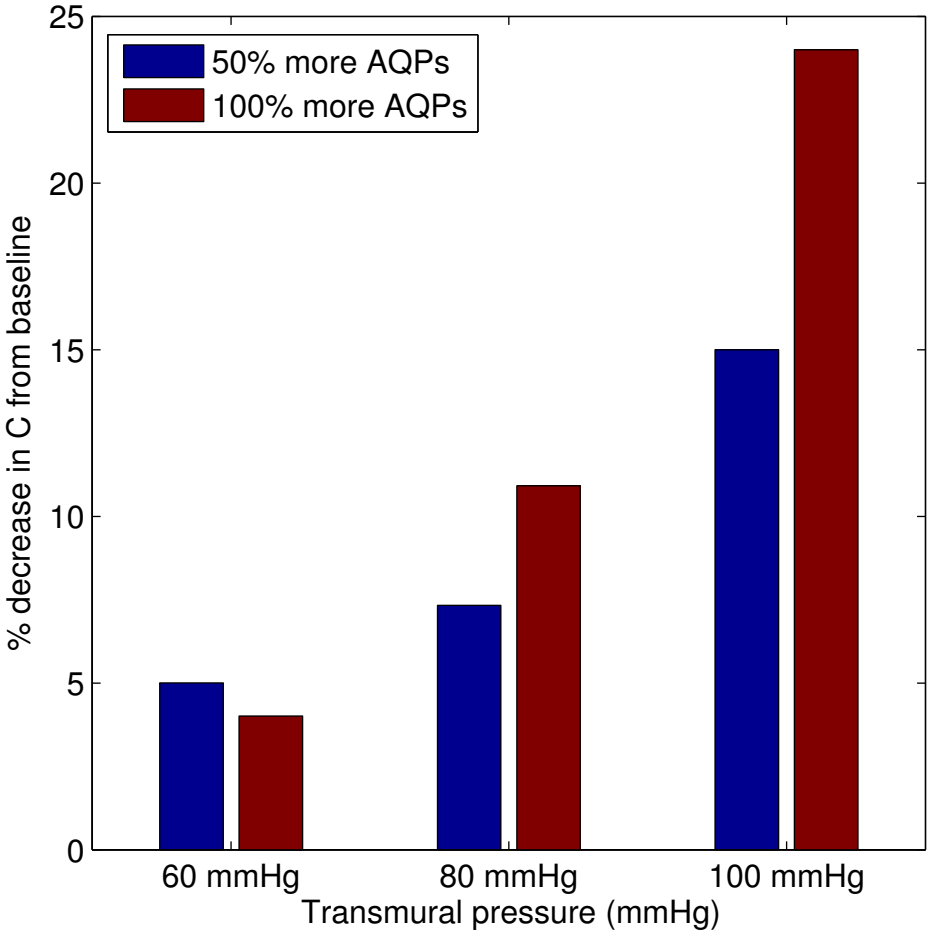

Figure 4.7: Percentage decrease in non-dimensional averaged concentration (area averaged on both r and z) of HRP in the SI at 4-min circulation with higher (50 and 100% more) AQP1 expression from the concentration at baseline AQP1 levels.

tough the absolute concentration of HRP is greater in the SI region at higher pressure, we find a substantial decrease in HRP's SI concentration at 100 mmHg upon increasing endothelial AQP1 expression. We find 15% and 24% decrease in HRP's SI concentration by 50% and 100% increase in EC AQP1s, respectively, at 100 mmHg. The corresponding numbers at 80 mmHg are 7% and 10%, respectively. Note that at 60 mmHg, the decrease in HRP's SI concentration is smaller when AQP1's contribution is increased by 100% from the baseline value, compared to the decrease with 50% more AQP1s. This small increase in HRP's concentration (or corresponding reduction from the baseline concentration) can be explained on the basis of relatively higher concentration of HRP in the region between $5 < r^*/R_1^* < 10$ for 100% more AQP1s, as shown in Fig. 4.5(a). Though the concentration in the leaky junction area ($0 < r^*/R_1^* < 1$) is less with 100% more AQP1s, the small increase in HRP's concentration over the larger area ($5 < r^*/R_1^* < 10$) results in a slight increase in its overall concentration in the SI and a corresponding decrease from the baseline as shown in Fig. 4.7.

4.3.4 LDL concentration distribution

The non-dimensional concentration of LDL in the SI (C_{SI}) as a function of radial distance at z = 0 and at the IEL-media interface (C_{Im}) and its variation with increasing AQP1 expression for transmural pressures of 60 and 80 mmHg is shown in Figs. 4.8(a) and 4.8(b), respectively. Due to its large size, LDL enters the SI through leaky junction only and thus we neglect its transport through normal endothelium and set k = 0 in Eq. 4.17. As in the case of HRP, LDL's concentration is higher near the leak ($r^*/R_1^* \sim 1$) and decays to low values away from it ($r^*/R_1^* \gg 1$). Again, due to a significant change in the fractional available volume for LDL, we find a huge drop in its concentration across the IEL. Interestingly, raising endothelial AQP1 expression lowers LDL's concentration inside the SI region (see dashed and dot-dashed blue curves in Figs. 4.8(a)-(b)). Lower LDL concentration can reduce the rates of LDL-SI ECM binding kinetics and possible slow down the formation of lipid liposomes and eventually the progression of pre-atherosclerotic events.

Figures 4.9(a)-(b) plot the area averaged (integrated in r) concentration of LDL (C_{Int})

across the depth of the vessel wall and its variation with increasing EC AQP1 expression. As Fig. 4.9(b) displays, there is a significant decrease in LDL's overall concentration with more EC AQP1s or higher $L_{P_{e+i}}$. We found $\sim$ 52 and 58% decrease in LDL's overall SI concentration (integrated in both r and z) at 80 mmHg as the endothelial AQP1 expression is raised by 50 and 100% from the baseline case. The corresponding decreases at 60 mmHg are only 6 and 4% respectively. Note, however, that LDL's concentration in the leak, with baseline AQP1 expression (lowest $L_{P_{e+i}}$), is much greater at higher pressure, see corresponding solid blue curves in Figs. 4.8(a) and 4.8(b). We found that this unreasonably high concentration of LDL results from the low volume fraction of LDL (γ_i) obtained at high pressures. Recall that, for a given transmural pressure, γ_i estimated from Eq. 4.27 depends on the intima thickness (or ϵ) at that pressure. Our local filtration model(Ch. 2) predicts an average intma thickness for a given transmural pressure. However, given the dissimilarities in hydraulic conductivities of leaky and normal endothelial junctions, and the resulting pressure drops across them, we believe that the SI under the leaky junction may not be compressed to the same extent as the SI under the normal endothelium. This suggests that γ_i under the leaky junction (the region of unreasonably higher LDL concentration) may be higher than its value further away from the leak. In order to implement this idea, one needs to consider the radial variation in γ_i and see its effect on LDL's concentration. This is the ongoing work and will be included in a publication based on this chapter, but is not being included in this thesis.

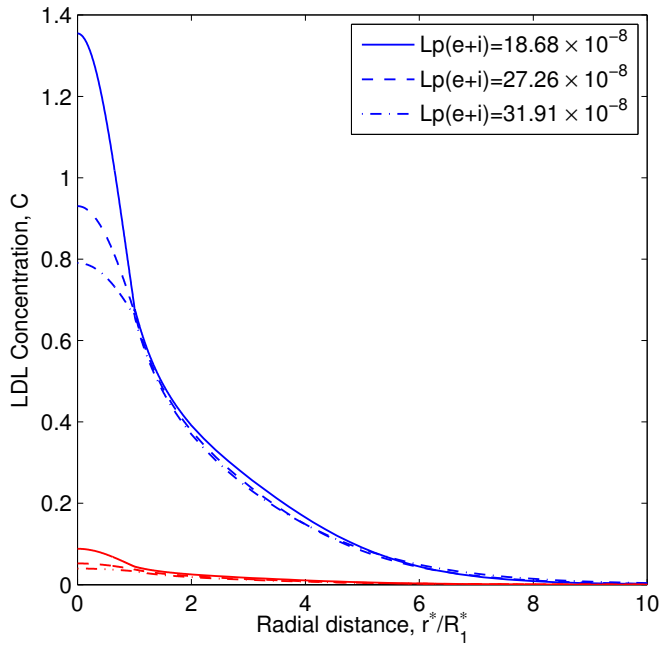

(a) P_L^*=60 mmHg

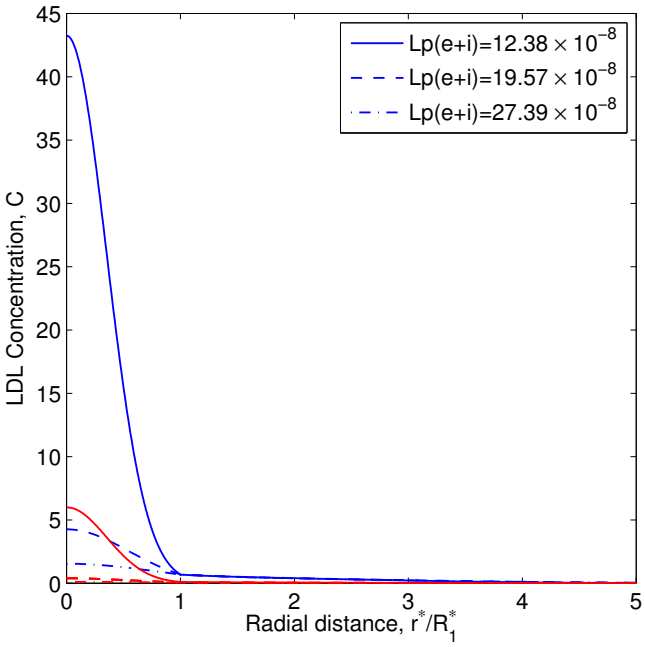

(b) P_L^*=80 mmHg

Figure 4.8: Non-dimensional concentration distribution of LDL at 10-min circulation in the SI at $z = 0$ (C_{SI}, upper blue curves) and at the IEL-media interface (C_{Im}, lower red curves) as a function of radial distance from the center of the leaky cell and its variation with increasing endothelial AQP1 expression. Note that the leaky junction is at r^*/R_1^*=1. $L_{P_{e+i}}$ values are as discussed in Fig. 4.5.

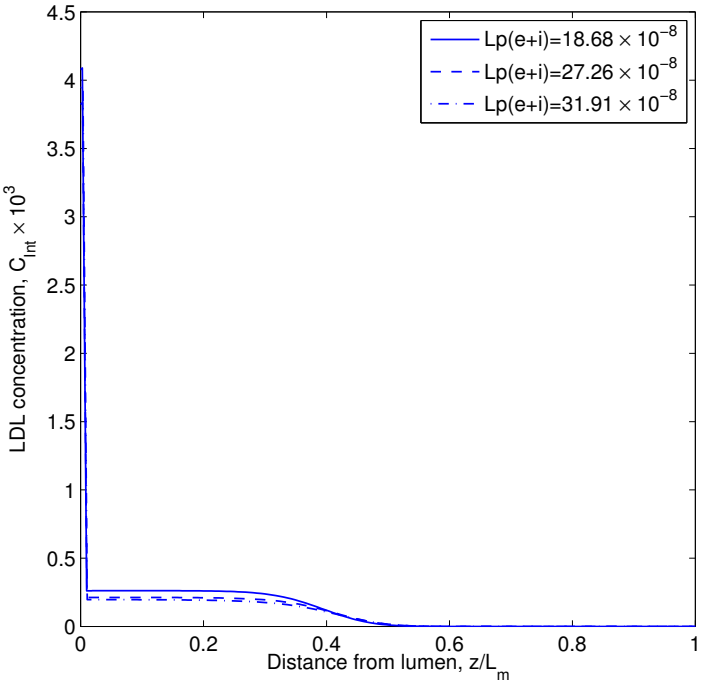

(a) P_L^*=60 mmHg

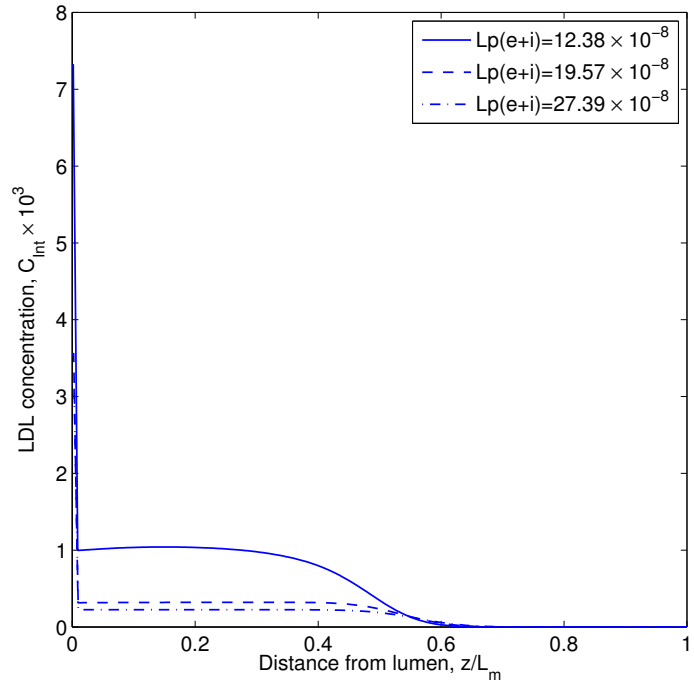

(b) P_L^*=80 mmHg

Figure 4.9: Non-dimensional concentration distribution of LDL (averaged in r) at 10-min circulation as a function of z (across the vessel wall) and its variation with increasing endothelial AQP1 expression. Note that the IEL is located between z^*/L_m^*=0.001 to z^*/L_m^*=0.007, a region where drastic drop in concentration is seen. $L_{P_{e+i}}$ values are as discussed in Fig. 4.6.

4.4 Conclusion

The present study seeks to gain insights into the effects of varying endothelial AQP1 expression on overall transmural flow and macromolecular transport across the vessel wall. We employ Zeng et al.'s (131) 2-D, wall-structure based convection-diffusion model, incorporating appropriate parameters and improvements over earlier (129, 35) models, to investigate AQP1's effect on the tracer transport with the predictions from our local filtration theory (Ch. 2) serving as inputs to this model. The results suggest a pressure-dependent increase in overall transmural flow upon increasing endothelial AQP1 expression. More interestingly, the tracer concentration in the SI region exhibit a pressure-dependent decrease with more EC AQP1s, and the effect is greater at higher pressures. These results suggest new experiments to study the effects of AQP1 up-regulating agents (like cAMP agonists) on tracer accumulation inside the vessel wall and provide useful predictions about suitable pressure range to test these effects. Since early lesions are known to develop inside the SI region, the decrease in LDL's SI concentration can lower SI ECM-LDL interaction rates and slow down lipid accumulation inside the artery wall. Thus raising endothelial AQP1 expression might serve as a potential avenue to slow down the progression of atherosclerotic lesion formation.

Chapter 5. Summary and outlook

The objective of this study is to understand the nature of the transmural water flow in large arteries, a critical consideration in the early events of atherosclerosis. This convection dominated water flow carries macromolecules like LDL into the subendothelial space, where they can bind to the fiber matrix and can start the cascade of processes that lead to atherosclerotic lesion formation. In addition, it can also dilute LDL's concentration, thereby, likely slowing down its binding reaction kinetics and ultimately flushing it from the wall. The near physical nature of these processes - rather than biological - enables us to implement basic engineering science principles like the fluid mechanics, mass transfer theory and to have an engineering perspective on the extremely complicated disease processes. The ultimate goal of this approach is to come with new strategies to prevent or, potentially, cure such diseases.

The hydraulic conductivity (L_P), the ratio of the transmural water flux to the hydrostatic minus the oncotic pressure difference across the vessel wall, is used to quantify this transmural water flow. In order to quantitatively explain the experimentally observed transmural pressure dependence of the hydraulic conductivity, we begin this thesis by improving on Huang et al.'s (36) transmural flow model and successfully explain all of the available L_P data, including that measured after Huang et al.'s (36) study. Specifically, in the first part of Chapter 2, we reproduced the filtration model for paracellular water flow proposed by Huang et al. (36), both with their approximate and with the fully correct mixed boundary conditions that required more computational power than was available for the earlier work. After verifying consistency with Huang et al. (36) (very small differences arose likely due to different numbers of terms retained and different matrix inversion tool used), we found that their approximate boundary conditions did quite well, with the largest deviations ($\sim$10%) occurring in the junction and fenestral ($r^*/r_f^* \leq 1$) regions, particularly for compressed intimae. Their third, three-point-matching approximation clearly performs

the best, as anticipated. Our L_P predictions with exact implementation of fenestral boundary conditions showed good agreement with the experimental measurements by Tedgui & Lever (100), Baldwin & Wilson (3), Shou et al. (78) and Nguyen (62). These results further emphasize Hunag et al.'s (36) hypothesis that increased transmural pressure compacts the intima near IEL fenestral pores and causes the associated hydraulic conductivity changes.

The discovery of the presence of special water channel protein called aquaporin-1 (AQP1) in the rat aortic endothelium and Nguyen's (62) experimental results showing markedly lower hydraulic conductivity when these water channels are blocked using $HgCl_2$, motivated us to develop a new theory to explain the experimentally observed variations in hydraulic conductivity with transmural pressure and with the reduction in functioning aquaporins in the aortic endothelium. We have extended Huang et al.'s (36) filtration model and considered, for the first time, the role played by AQP1s in modulating the total hydraulic conductivity of an intact arterial wall with changes in transmural pressure. Not surprisingly, our calculations showed a substantial decrease in L_{P_t} values upon increasing the percentage of blocked AQP1s. We found that such blocking, when done at pressures where the subendothelial intima would otherwise be uncompressed, can cause the SI compression and initiate fenestral blocking. The consequent large drops in L_{P_t} agrees with Nguyen's (62) observations of the effect of blocking on L_{P_t} at different transmural pressures and supports the hypothesis that AQP1s certainly play a significant role in overall transport across the arterial wall. After characterizing AQP1's mechanism of action, this theory provides several interesting predictions, some for new experiments. In particular, we find that increasing the number of functioning EC AQP1s increases the total hydraulic conductivity of the vessel wall and shifts the dynamic range of intima compression to higher transmural pressures. Based on these predictions, my colleague C. Raval has recently performed these experiments and their agreement with this theory is discussed in Chapter 3. Since higher L_Ps, and thus higher transmural water flow, can dilute LDL's local concentration in the SI and potentially wash these macromolecules further away from the SI where they are unlikely to bind to the ECM, increasing EC AQP1 expression could be beneficial, particularly for those whose hypertension put them at higher risk. Finally in Chapter

2, we predict that AQP1s contribute at least 30% to the phenomenological and intrinsic hydraulic conductivity of the endothelium.

Chapter 3 of this thesis focuses on the oncotic paradox that arises with the transmural pressure driven trans-AQP1 mediated water flow and develops new mathematical model to investigate the role of oncotic forces in trans-endothelial and transmural water flow across the walls of large arteries. The oncotic pressure difference, governed by the concentration of albumin, sucks fluid across the endothelium. The fluid flow, driven by hydrostatic and oncotic pressure difference, governs the concentration of albumin. The resulting non-linearity of fluid flow and mass transfer of albumin provides significant calculational challenges. Our results indicate a surprising finding that the dense media region acts to strongly filter the albumin and, under steady conditions, leads to albumin build-up inside the SI region. This increases the albumin concentration in the SI side of the EC compared to the luminal side of the EC and the resulting oncotic pressure difference sucks fluid in the direction of ΔP-driven flow and not the other way around. We find that oncotic forces indeed play a role in the walls of bigger arteries and neglecting their contribution can underestimate overall water flow at low transmural pressures. The model also predicts that removal of the surface GX layer lowers the oncotic force across the endothelium and reduces overall water flux across the vessel wall. This study also suggests new experiments to investigate the role of GX degrading enzymes like hyaluronidase, heparinase with varying lumen albumin concentration on transmural flow across arterial walls and predicts a pressure range to see an appreciable effect. Given AQP1's presence in the high-pressure cardiac endocardium, heart, lung and renal epithelia, resolving and understanding how mass-transfer-induced oncotic gradients interact with the flows that advect those solutes may have far broader and illuminating implications.

Chapter 4 then combines our local filtration model with Zeng et al.'s (131) 2-D, wall-structure based convection-diffusion model and discuses the effects of varying endothelial AQP1 expression, or transcellular flow, on overall transmural flow and macromolecular transport across the vessel wall. The predictions from our local filtration theory (Ch. 2) serve as inputs to Zeng et al.'s (131) tracer transport model that incorporates appropriate parameters and improvements

over earlier (129, 35) macromolecular transport models. The results suggest a pressure-dependent increase in overall transmural flow and a pressure-dependent decrease in the tracer (e.g., HRP, LDL) concentration upon increasing endothelial AQP1 expression. These results suggest new experiments to study the effects of AQP1 up-regulating agents (like cAMP agonists) on tracer accumulation inside the vessel wall and provide useful predictions about suitable pressure range to test these effects.

As noted in Chapter 4, lower γ_i resulting from compressed intimae at higher transmural pressures, lead to significantly high LDL concentrations inside the SI, particularly under the leak, that may not be physiologically reasonable. In future we would address this issue as follows. The larger width and significantly higher hydraulic conductivity of the laky junction would mean less pressure drop, and hence less force/area, across the leaky junction than that across the normal endothelium. This suggests that the intima beneath the leaky junction may not be as compressed as the intima under normal endothelium. We will improve on our current theory, which assumes uniform SI compression under both the leaky and normal endothelium, by including radial variation in γ_i with transmural pressure. If we succeed in finding physiologically relevant LDL concentrations, our theory would be able to predict the effect of increasing transmural flow via more EC AQP1s on LDL's transport at high transmural pressures too.

Clearly, the next step in this study would be to test AQP1's effect on lipid accumulation kinetics inside the aortic wall. The binding of LDL to sub-endothelial extra cellular matrix appears to form lipid packets, labeled extracellular liposomes. This LDL binding and modification precedes blood born monocyte entry and foam cell formation in lipid rich SI region, a critical event in atherosclerosis. Thus it is important to study the lipid accumulation and the roles of different factors that can influence this accumulation. We hypothesize that a decrease in LDL's SI concentration, resulting from increased trascellular flow though AQP1s, can lower SI ECM-LDL interaction rates and slow down lipid accumulation inside the artery wall. Moreover, since higher endothelial AQP1 expression would decompress the intima, the LDL-ECM binding constant that depends on the concentration of the ECM, would be lower with more EC AQP1s and can further slow down SI

lipid accumulation. To test this hypothesis, we would input the LDL concentration profiles from current combined theory at different transmural pressures and endothelial AQP1 expressions into the extracellular lipid liposome formation and growth model developed by Yin et al. (128). Should we find significant decrease in lipid accumulation with increasing endothelial AQP1 expression, it would substantiate the possibility of considering AQP1s as a future therapeutic target to slow down the progression of atherosclerotic lesion formation.

Appendix A.

A.1 Approximate Analytical Solution of the Boundary Value Problem:

Here we discuss the analytical method to obtain the pressure distribution in the intima and media region using Huang et al.'s (36) approximate boundary conditions, briefly discussed in section 2.2.2. The boundary value problem governing the pressure distributions in these two regions (Eqs. 3.2 in section 2.2.2) are:

$$h_i^2 \left(\frac{\partial^2 P_i}{\partial r^2} + \frac{1}{r} \frac{\partial P_i}{\partial r} \right) + \frac{\partial^2 P_i}{\partial z_i^2} = 0 \tag{A.1}$$

$$h_m^2 \left(\frac{\partial^2 P_m}{\partial r^2} + \frac{1}{r} \frac{\partial P_m}{\partial r} \right) + \frac{\partial^2 P_m}{\partial z_m^2} = 0 \tag{A.2}$$

Huang et al. (36) assumed that the endothelial cleft (normal junction) acts as a ring source at $r = \xi_I$, where flow is fully radial $\left(\text{i.e., } \frac{dP_i}{dz_i}\Big|_{r=\xi_I} = 0 \right)$. Thus, the boundary condition at $r = \xi_I$ becomes:

$$P = P_0 \quad \text{at} \quad r = \xi_I \tag{A.3}$$

The unknown pressure P_0 is independent of z_i and it's value is obtained by employing the incompressibility as:

$$L_{P_{nj}} \left(P_L^* - P_0^* \right) 2\pi R^* \frac{\triangle R^*}{2} = -2\pi \int_0^{r_f^*} W_{f_i}^* \, r^* dr^* \tag{A.4}$$

In non-dimensional form Eq. A.4 becomes:

$$L_{P_{nj}} \left(1 - P_0 \right) 2\pi R \frac{\triangle R}{2} = \frac{-2\pi K_{P_i}}{\mu \, L_i^*} \int_0^1 W_{f_i} \, r dr \tag{A.5}$$

We use separation of variables to solve the boundary value problem (Eqs. A.1 and A.2). Thus,

$$P_i(r, z_i) = \sum_{n=1}^{\infty} R_n(r) \cdot Z_n(z_i)$$

$$P_m(r, z_m) = \sum_{p=1}^{\infty} R_p(r) \cdot Z_p(z_m)$$

Using r boundary conditions (Eq. 2.3 and Eq. A.3), we get:

$$P_i(r, z_i) = P_0 + \sum_{n=1}^{\infty} \Big(A_n \cosh(h_i \sqrt{\lambda_n}\ z_i) + B_n \sinh(h_i \sqrt{\lambda_n}\ z_i) \Big) \cdot R_n(r) \tag{A.6}$$

$$P_m(r, z_m) = (\ C_0\ z_m + D_0\ ) R_0 + \sum_{p=1}^{\infty} \Big(C_p \cosh(h_m \sqrt{\lambda_p}\ z_m) + D_p \sinh(h_m \sqrt{\lambda_p}\ z_m) \Big) \cdot R_p(r) \tag{A.7}$$

where the eigen values λ_n and λ_p are roots of following eigenvalue equations:

$$J_0(\sqrt{\lambda}_n\, \xi_I) = 0 \qquad (n = 1, 2, 3, ..., \infty)$$
$$J_1(\sqrt{\lambda}_p\, \xi_I) = 0 \qquad (p = 1, 2, 3, ..., \infty)$$

where, J_0 and J_1 are zero- and first-order Bessel functions, respectively. Note that the model problem for the media region (Eq. A.2) has a zero eigenvalue because it has homogeneous Neumann conditions at both $r = 0$ and $r = \xi_I$. The eigen functions are given by:

$$R_n(r) = \frac{\sqrt{2}\, J_0(\sqrt{\lambda}_n\, r)}{\xi_I\, J_1(\sqrt{\lambda}_n\, \xi_I)}$$

$$R_0(r) = \frac{\sqrt{2}}{\xi_I}$$

$$R_p(r) = \frac{\sqrt{2}\, J_0(\sqrt{\lambda}_p\, r)}{\xi_I\, J_0(\sqrt{\lambda}_p\, \xi_I)}$$

The constants $A_n, B_n, C_0, D_0, C_p, D_p$ are to be obtained from the z-boundary conditions. The mixed boundary conditions on the pressure and on its gradient (the matching of the pressure and velocity in the fenestra and the homogeneous Neumann conditions outside of it, Eqs. 2.9 and 2.10), make it difficult to find the exact solution of the coupled boundary value problem. Thus, in order to simplify the problem, Huang et al. (36) introduced three separate approximate velocity and pressure matching conditions in the fenestral hole instead of Eqs. 2.9 and 2.10. The general solution of the Eqs. A.1 and A.2 with all boundary conditions except Eqs. 2.9 and 2.10 is:

$$P_i(r, z_i) = P_0 \; + \; P_0 \sum_{n=1}^{\infty} \left(A_n \, \frac{\cosh[\, h_i \, \sqrt{\lambda}_n \, (z_i - 1) \,]}{\cosh(h_i \sqrt{\lambda}_n)} \cdot J_0(\sqrt{\lambda}_n \, r) \right) \tag{A.8}$$

$$P_m(r, z_m) = P_0(z_m + 1)C_0 \; + \; P_0 \sum_{p=1}^{\infty} \left(C_p \, \frac{\sinh[\, h_m \, \sqrt{\lambda}_p \, (z_m + 1) \,]}{\sinh(h_m \sqrt{\lambda}_p)} \cdot J_0(\sqrt{\lambda}_p \, r) \right) \tag{A.9}$$

The unknown coefficients A_n and C_p depend on which of the three approximate matching conditions (discussed in section 2.2.2) one requires equations A.8 & A.9 to satisfy.

A.2 Determination of constants in Eqs. A.8 & A.9

Using change of variables and boundary conditions at $z_i = 1$ & $z_m = -1$, Eqs. A.6 and A.7 $\Rightarrow$

$$P_i(r, z_i) = P_0 + \sum_{n=1}^{\infty} \Big[\; A'_n \, \cosh\Big(h_i \sqrt{\lambda_n} \; (z_i - 1)\Big) \; \Big] \cdot R_n(r) \tag{A.10}$$

$$P_m(r, z_m) = (\, C'_0 \, z_m + 1 \,) R_0 + \sum_{p=1}^{\infty} \Big[\; C'_p \, \sinh\Big(h_m \sqrt{\lambda_p} \; (z_m + 1)\Big) \; \Big] \cdot R_p(r) \tag{A.11}$$

$$\frac{dP_i}{dz_i} = \sum_{n=1}^{\infty} \Big[\; A'_n \, h_i \sqrt{\lambda}_n \sinh\Big(h_i \sqrt{\lambda_n} \; (z_i - 1)\Big) \; \Big] \cdot R_n(r) \tag{A.12}$$

$$\frac{dP_m}{dz_m} = \; C'_0 \, R_0 + \sum_{p=1}^{\infty} \Big[\; C'_p \, h_m \sqrt{\lambda}_p \cosh\Big(h_m \sqrt{\lambda_p} \; (z_m + 1)\Big) \; \Big] \cdot R_p(r) \tag{A.13}$$

Huang et al.'s (36) First Approximation:

Velocity in the fenestra (W_f^*) is constant and pressure in the SI and media matches only at the centerline i.e., $P_i^* = P_m^*$ at $(r^*, z^*) = 0$

Let $W_f^* = \; -c, \quad (c \text{ is constant})$

$$\therefore \; \frac{dP_i}{dz_i} = \; \frac{c \, \alpha_i}{P_L^*} \quad \text{and} \quad \frac{dP_m}{dz_m} = \; \frac{c \, \alpha_m}{P_L^*} \quad \text{where,} \quad \alpha_i = \frac{\mu \, L_i^*}{K_{P_i}}, \;\; \alpha_m = \frac{\mu \, L_m^*}{K_{P_m}}$$

Now from equation A.12, the inner product gives us the constants A'_n as:

$$A'_n = \frac{-\sqrt{2} \, P_0 \, \alpha_i \, J_1(\sqrt{\lambda}_n)}{h_i \, \lambda_n \, \xi_I \, \sinh(h_i \sqrt{\lambda}_n) \, J_1(\sqrt{\lambda}_n \, \xi_I)} \left(\frac{c}{P_0^*} \right) \tag{A.14}$$

Thus, using A.14, Eq. A.10 $\Rightarrow$

$$P_i(r, z_i) = P_0 \; + \; P_0 \sum_{n=1}^{\infty} \left(A_n \, \frac{\cosh[\, h_i \, \sqrt{\lambda}_n \, (z_i - 1) \,]}{\cosh(h_i \sqrt{\lambda}_n)} \cdot J_0(\sqrt{\lambda}_n \, r) \right) \tag{A.15}$$

where,

$$A_n = \alpha_i \left(\frac{c}{P_0^*}\right) F_n$$

$$F_n = \frac{-2\, J_1(\sqrt{\lambda}_n)}{h_i \lambda_n \xi_I^2 \, \tanh(h_i \sqrt{\lambda}_n) \left[J_1(\sqrt{\lambda}_n \, \xi_I)\right]^2}$$

Similarly, inner products from Eq. A.13 give us constants C_0', C_p' as:

$$C_0' = \frac{P_0 \, \alpha_m}{\sqrt{2}\, \xi_I} \left(\frac{c}{P_0^*}\right) \tag{A.16}$$

$$C_p' = \frac{\sqrt{2}\, P_0 \, \alpha_m \, J_1(\sqrt{\lambda}_p)}{h_m \, \lambda_p \, \xi_I \, \cosh(h_m \sqrt{\lambda}_p) \, J_0(\sqrt{\lambda}_p \, \xi_I)} \left(\frac{c}{P_0^*}\right) \tag{A.17}$$

Thus, using A.16 and A.17, Eq. A.11 $\Rightarrow$

$$P_m(r, z_m) = P_0(z_m + 1)C_0 \; + \; P_0 \sum_{p=1}^{\infty} \left(C_p \, \frac{\sinh[\, h_m \sqrt{\lambda}_p \, (z_m + 1)\,]}{\sinh(h_m \sqrt{\lambda}_p)} \cdot J_0(\sqrt{\lambda}_p \, r) \right) \tag{A.18}$$

where,

$$C_0 = \alpha_m \left(\frac{c}{P_0^*}\right) E_0$$

$$C_p = \alpha_m \left(\frac{c}{P_0^*}\right) E_p$$

$$E_0 = \frac{1}{{\xi_I}^2}$$

$$E_p = \frac{2 J_1(\sqrt{\lambda}_p)}{h_m \lambda_p \xi_I^2 \, \coth(h_m \sqrt{\lambda}_p) \left[J_0(\sqrt{\lambda}_p \, \xi_I)\right]^2}$$

Calculation of c:

Since, $P_i^* = P_m^*$ at $r^* = 0,\ z^* = 0$

$\therefore$ From Eqs. A.8 and A.9, we get:

$$\left(\frac{c}{P_0^*}\right) = \frac{1}{\alpha_m \sum_{p=0}^{\infty} E_p - \alpha_i \sum_{n=1}^{\infty} F_n} \tag{A.19}$$

Calculation of P_0:

From Eq. A.4, we have:

$$L_{P_{nj}} \left(P_L^* - P_0^*\right) 2\pi R^* \frac{\triangle R^*}{2} = 2\pi \int_0^{r_f^*} c\ r^* dr^*$$

$$\therefore\ P_0 = \frac{1}{\left[1 + \frac{1}{R \triangle R\, L_{P_{nj}}} \left(\frac{c}{P_0^*}\right)\right]} \tag{A.20}$$

Huang et al.'s (36) Second Approximation:

W_f^* is constant and only average pressure $(\bar{P}_i^*)$ matches in the fenestral hole i.e., $\bar{P}_i^* = \bar{P}_m^*$ at $0 < r^* \leq r_f^*$, $z^* = 0$, where $\bar{P}^* = \frac{2}{r_f^{*2}} \int_0^{r_f^*} P^*(r^*)\, r^* dr^*$

Here, only the calculation of c is different.

Since, $\bar{P}_i^* = \bar{P}_m^*$

$$\therefore \left(\frac{c}{P_0^*}\right) = \frac{1}{\alpha_m \left[\frac{1}{\xi_I^2} + 2\sum_{p=1}^{\infty} \frac{E_p\, J_1(\sqrt{\lambda}_p)}{\sqrt{\lambda}_p}\right] - 2\alpha_i \left[\sum_{n=1}^{\infty} \frac{F_n\, J_1(\sqrt{\lambda}_n)}{\sqrt{\lambda}_n}\right]} \tag{A.21}$$

Huang et al.'s (36) Third Approximation:

$W_f^*(r)$ fits a cubic polynomial that satisfies $dW_f^*/dr^* = 0$ at $r^* = 0$ and the pressure is continuous at $r = 0,\ 0.5\, r_f^*,\ 0.9\, r_f^*$ i.e.,

$$W_f^* = -(\, a_0 + c_0 r^2 + d_0 r^3) P_0^*$$

$$\therefore \frac{dP_i}{dz_i} = \alpha_i (\, a_0 + c_0 r^2 + d_0 r^3) P_0$$

$$\therefore \frac{dP_m}{dz_m} = \alpha_m (\, a_0 + c_0 r^2 + d_0 r^3) P_0$$

Now, constants A_n', C_0', C_p' can be obtained by taking inner products from Eqs. A.12 and A.13:

$$A_n' = \frac{\sqrt{2}\, P_0\, \alpha_i\, (a_0 I_{i_1}^n + c_0 I_{i_3}^n + d_0 I_{i_4}^n)}{h_i \sqrt{\lambda}_n\, \xi_I \sinh(h_i \sqrt{\lambda}_n)\, J_1(\sqrt{\lambda}_n\, \xi_I)} \tag{A.22}$$

$$C_0' = \frac{\sqrt{2}\, P_0\, \alpha_m\, (a_0 I_{m_1}^0 + c_0 I_{m_3}^0 + d_0 I_{m_4}^0)}{\xi_I} \tag{A.23}$$

$$C_p' = \frac{\sqrt{2}\, P_0\, \alpha_m\, (a_0 I_{m_1}^m + c_0 I_{m_3}^m + d_0 I_{m_4}^m)}{h_m \sqrt{\lambda}_p\, \xi_I \cosh(h_m \sqrt{\lambda}_p)\, J_0(\sqrt{\lambda}_p\, \xi_I)} \tag{A.24}$$

Thus, using Eqs. A.22, A.23 and A.24, we get:

$$A_n = -H_n (a_0 I_{i_1}^n + c_0 I_{i_3}^n + d_0 I_{i_4}^n) \tag{A.25}$$

$$C_0 = G_0 (a_0 I_{m_1}^0 + c_0 I_{m_3}^0 + d_0 I_{m_4}^0) \tag{A.26}$$

$$C_p = G_p (a_0 I_{m_1}^m + c_0 I_{m_3}^m + d_0 I_{m_4}^m) \tag{A.27}$$

where,

$$H_n = \frac{2\alpha_i}{h_i\sqrt{\lambda}_n\,\xi_I^2\,\tanh(h_i\sqrt{\lambda}_n)\,[J_1(\sqrt{\lambda}_n\,\xi_I)]^2} \qquad n = 1, 2, 3, ..., \infty$$

$$G_0 = \frac{2\alpha_m}{\xi_I^2}$$

$$G_p = \frac{2\alpha_m}{h_m\sqrt{\lambda}_p\,\xi_I^2\,\coth(h_m\sqrt{\lambda}_p)\,[J_0(\sqrt{\lambda}_p\,\xi_I)]^2} \qquad p = 1, 2, 3, ..., \infty$$

$$I_{i_k}^n = \int_0^1 r^k\,J_0(\sqrt{\lambda}_n\,r)dr \qquad k = 1, 3, 4$$

$$I_{m_k}^0 = \int_0^1 r^k dr \qquad k = 1, 3, 4$$

$$I_{m_k}^m = \int_0^1 r^k\,J_0(\sqrt{\lambda}_p\,r)dr \qquad k = 1, 3, 4$$

Thus, Eqs. A.25, A.26 and A.27 can be used in Eqs. A.8 and A.9 to get P_i and P_m

Calculation of a_0, c_0, d_0:

Using pressure continuity at $r = 0, 0.5, 0.9$, these three constants can be obtained from following simultaneous equations:

$$a_0 b_{11} + c_0 b_{13} + d_0 b_{14} = 1$$

$$a_0 b_{21} + c_0 b_{23} + d_0 b_{24} = 1$$

$$a_0 b_{31} + c_0 b_{33} + d_0 b_{34} = 1$$

where,

$$b_{1k} = Q_k(0) \qquad k = 1, 3, 4$$

$$b_{2k} = Q_k(0.5) \qquad k = 1, 3, 4$$

$$b_{3k} = Q_k(0.9) \qquad k = 1, 3, 4$$

And,

$$Q_k(r) = C_0 I^0_{m_k} + \sum_{n=1}^{\infty} H_n I^n_{i_k} J_0(\sqrt{\lambda}_n\, r) + \sum_{p=1}^{\infty} G_p I^m_{m_k} J_0(\sqrt{\lambda}_p\, r)$$

Calculation of P_0:

From equation A.4, we have:

$$L_{P_{nj}} \left(P^*_L - P^*_0\right) 2\pi R^* \frac{\triangle R^*}{2} = 2\pi P^*_0 \int_0^{r^*_f} \left(a_0 + c_0 r^2 + d_0 r^3\right) r^* dr^*$$

$$\therefore\ P_0 = \frac{1}{\left[1 + \dfrac{2}{R \triangle R\, L_{P_{nj}}} \left(\dfrac{a_0}{2} + \dfrac{c_0}{4} + \dfrac{d_0}{5}\right)\right]} \tag{A.28}$$

A.3 Determination of Darcy permeability of the SI:

The lesion-free SI of healthy/normal artery wall mainly consists of randomly oriented PG and collagen fibers (24). Huang et al. (35) treated this intima layer as an extracellular matrix of heterogeneous fibers and estimated it's Darcy permeability (K_{P_i}) by separately considering the contributions from PG and collagen fibers.

Carman-Kozeny expression (15, 16, 17) gives the Darcy permeability of randomly oriented fibers of radius a with a void volume fraction of ϵ as:

$$K_P = \frac{a^2\,\epsilon^3}{4\,G\,(1-\epsilon^2)} \tag{A.29}$$

where G is the Kozeny constant. The Kozeny constant for uncharged, randomly oriented cylindrical fibers is (29):

$$G = \frac{2}{3}G_r + \frac{1}{3}G_p$$

where G_r and G_p represent, respectively, the Kozeny constant's for the two cases in which flow is perpendicular and parallel to the cylinderical fibers.

$$G_r = \frac{2\,\epsilon^3}{(1-\epsilon)\left[\,ln\left(\frac{1}{1-\epsilon}\right) - \frac{1-(1-\epsilon)^2}{1+(1-\epsilon)^2}\right]} \tag{A.30a}$$

$$G_p = \frac{2\,\epsilon^3}{(1-\epsilon)\left[\,2\,ln\left(\frac{1}{1-\epsilon}\right) - 3 + 4(1-\epsilon) - (1-\epsilon)^2\right]} \tag{A.30b}$$

Since the observed proteoglycan constituents (24) have non-uniform thicknesses, in order to use Eq. A.29, Huang et al. (35) defined an effective radius of the entire PG matrix (a^*) as:

$$a^* = \left(\frac{\alpha\,r_M^2 + r_{CF}^2}{\alpha+1}\right)^{1/2}$$

where, $r_M = \left(\beta\, r_G^2 + r_{CP}^2\right)^{1/2}$

The geometric parameters α, β, δ and the radii r_M, r_{CF}, r_G, r_{CP} are defined in the caption of Fig. A.1. The volume fraction of PG fibers with an effective radius r^* is (35):

$$1 - \epsilon = \left(\frac{r^*}{\xi_I}\right)^2 \left(\frac{\alpha + 1}{\alpha}\right) N$$

where N is the total monomer number in the volume ($\pi\, \xi_I^2 \times$ average mononer length) and can be approximated (35) as $\left(3\left(\frac{\xi_I}{\delta}\right)^2\right)$. Thus by calculating a^* and ϵ, one can compute K_P of PG matrix using Eq. A.29.

As explained by Huang et al. (35), the Darcy permeability of collagen fibers can be obtained by using Tsay and Weinbaum's theory for the hydrodynamic interaction between fibers arranged in a 2-D periodic array as:

$$\frac{K_{P_{(PG)}}}{K_{P_{(CG)}}} = \left(\frac{r_{CG}^*}{a^*}\right)^{0.377} \left(\frac{\delta_{PG0} - 2a^*}{\delta_{CG0} - 2r_{CG}^*}\right)^{2.377} \tag{A.31}$$

The overall Darcy permeability of the SI region (K_{P_i}) is estimated as (49):

$$\frac{1}{K_{P_i}} = \frac{1}{K_{P_{(PG)}}} + \frac{1}{K_{P_{(CG)}}} \tag{A.32}$$

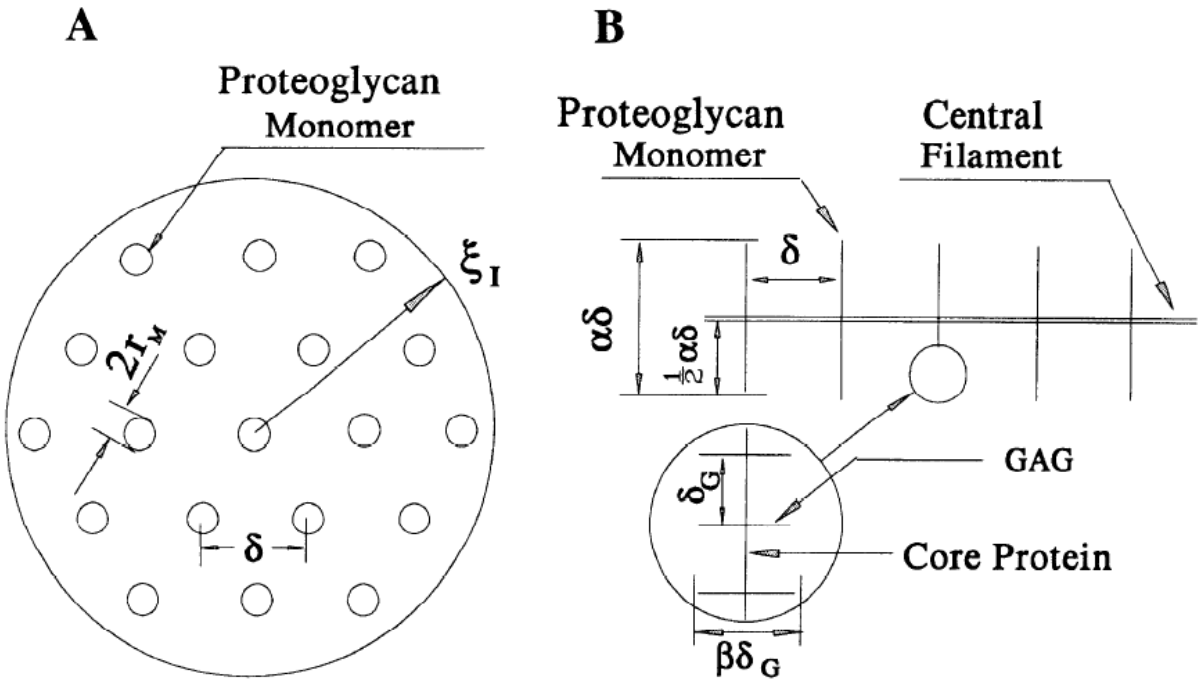

Figure A.1: Simplified proteoglycan matrix model from Huang et al. (36). (A) is the top view of the region, δ is the average spacing between PG fibers, r_M is the monomer radius. (B) is the structure of proteoglycan aggregate. r_{CF} is the radius of central filament ($\sim$ 2 nm), r_{CP} is the radius of core protein ($\sim$ 2 nm) and r_G is the radius of glycosaminoglycans, GAG ($\sim$ 0.6 nm). α is the length ratio of the total monomers to the central filament and β is the length ratio of the GAG to core protein. α =10 and β =5 (36). See (35) for more details.

A.4 Calculation of L_{P_m}:

Experimental measurements in table 2.1 give us the L_{P_t} and the $L_{P_{I+m}}$. Equation 2.16c relates L_{P_m} and L_{P_I}, which are unknowns and are obtained as part of the solution as discussed below. At steady state, incompressibility implies that water flow across each arterial layer is the same and thus one can average the solutions (Eqs. A.8 & A.9) for the pressure field at any z and require the resulting mean velocity to be independent of z i.e.,

$$\bar{W}_i^* = L_{P_I}(\bar{P}_i^* - \bar{P}_m^*)|_{z^*=0} = L_{P_m}\bar{P}_m^*|_{z^*=0} \tag{A.33}$$

Using Eqs. A.8 & A.9 and solving we get:

$$\frac{L_{P_m}}{L_{P_I}} = \frac{1}{C_0}\left[1 + \frac{2}{\xi_I^2}\sum_{n=1}^{\infty}\frac{A_n\, J_1(\sqrt{\lambda}_n\, \xi_I)}{\sqrt{\lambda}_n}\right] - 1 \tag{A.34}$$

Our model presumes that, due to its high density, an increasing transmural pressure does not compress the media; thus L_{P_m} is independent of transmural pressure. However, Eq. A.34 shows that the effective L_P of the IEL (due to intima compression) depends on the intimal thickness, which can vary with increasing pressure. Thus, we evaluate L_{P_m} at fixed intimal compaction, i.e. none ($L_i^* = {L_{i_0}}^*$), by comparing the calculated $L_{P_{I+m}}$ with its measured value in deendothelialized artery and maintaining this value of L_{P_m} for all intimal compressions, as done in (36). That is, to find L_{P_m}, we guess a value of L_{P_m} and calculate L_{P_I} by Eq. (A.34) at ($L_i^* = {L_{i_0}}^*$) and using Eq. (2.16c) verify if their inverse add up to the average experimental value until both values converge. The converged results for different data sets are given in table 2.4.

A.5 Additional results from filtration model: Chapter 2

A.5.1 Effect of SI compression on K_{P_i}

The thickness dependent Darcy permeability of the SI region is obtained using Eqs. A.29-A.32 and Eqs. 2.14 & 2.15. Fig. A.2 shows its variation with intimal thickness. As shown in Fig. A.2,

K_{P_i} decreases rapidly with a decrease in intima thickness. It's value at $L_i^* = 0.2\, L_{i_0}^*$ is one order of magnitude smaller than that at $L_i^* = L_{i_0}^*$.

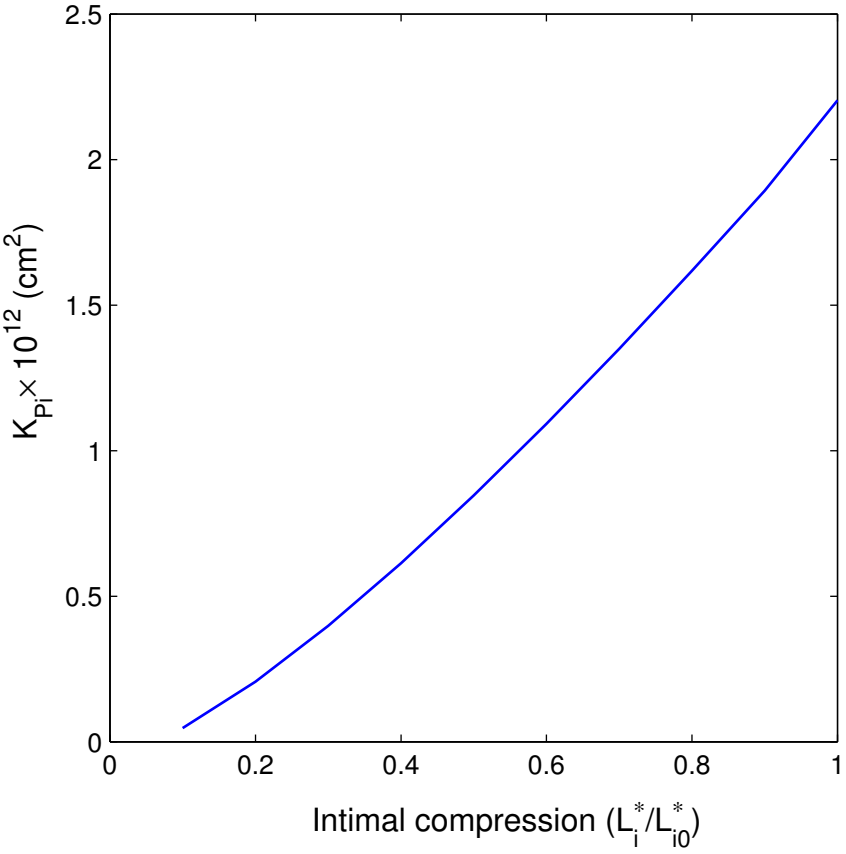

Figure A.2: Darcy permeability of SI as a function of intimal compression (L_i^*/L_{i0}^*). $L_{i0}^* = 500$ nm.

A.5.2 2-D pressure distribution in GX, SI and media

Figures A.3-A.5 show pressure distribution (non-dimensional) in the GX, SI and media region obtained by numerically solving Eqs. 3.2 - 2.11 and using Nguyen's (62) L_P data. In the GX region, as Fig. A.3 shows, the pressure is almost constant and equal to the lumen pressure (thus, non-dimensional pressure ~ 1), except near the junctional region $(r : 15 - 15.0125)$, where a small decrease in pressure is observed. Because the thickness of the SI region (L_i^*) is much smaller than the thickness of the media (L_m^*) and the radius of periodic wall unit (ξ_I), the pressure in the SI

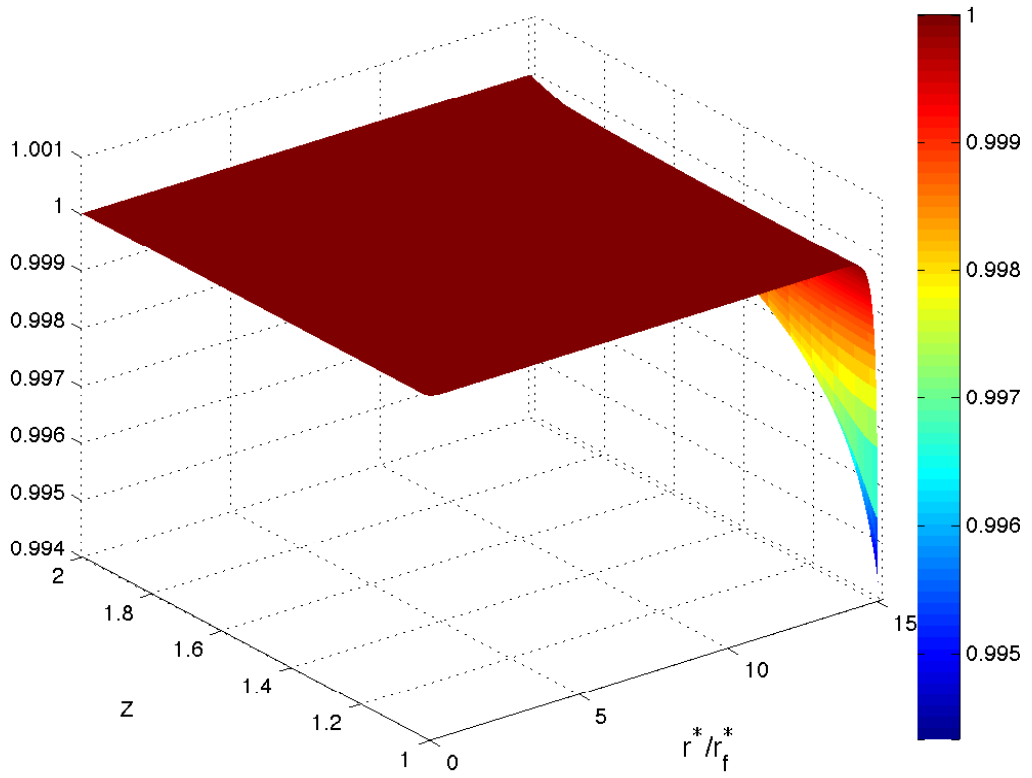

Figure A.3: Pressure distribution in the GX region as function of non-dimensional r and z distance. Note that normal junction is from $r^*/r_f^* = 15 - 15.0125$. $L_i^* = 500$ nm. L_{P_e} and L_{P_m} are from Nguyen's data (62), given in tables 2.5 and 2.4 respectively.

region (shown in Fig. A.4), as expected, varies only in radial direction, except in the close vicinity of the fesnstra and junctional region. This suggests that the velocity profiles in the SI would be nearly one-dimensional (radial only). In the media region, as shown in Fig. A.5, the maxima in the pressure that results in fenestral region disappear within a distance of $0.03L_m^*$ from the lower surface of the IEL $(z = 0)$. Figure A.5 shows that there is no significant radial pressure gradients in the media and thus it results in a nearly one-dimensional flow in the z-direction, in contrast to nearly radial flow in the SI region.

A.5.3 $L_{P_{m+I}}$ of intact vessel

Huang et al. (36) suggested that the hydraulic conductivity of an artery wall with denuded endothelium and thus representing contributions from the IEL and the media should be independent

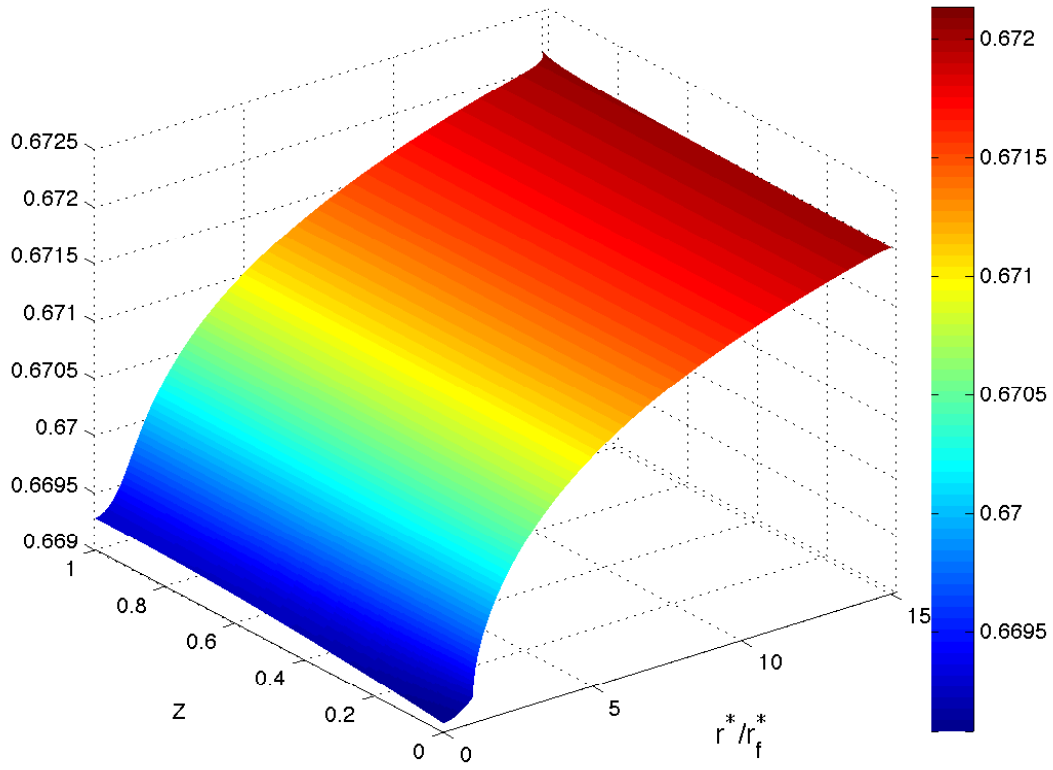

Figure A.4: Pressure distribution in the SI region as function of non-dimensional r and z distance. Note that normal junction is from $r^*/r_f^* = 15 - 15.0125$ and fenestral hole is at $0 < r^*/r_f^* \leq 1$. $L_i^* = 500$ nm. L_{P_e} and L_{P_m} are from Nguyen's data (62), given in tables 2.5 and 2.4 respectively

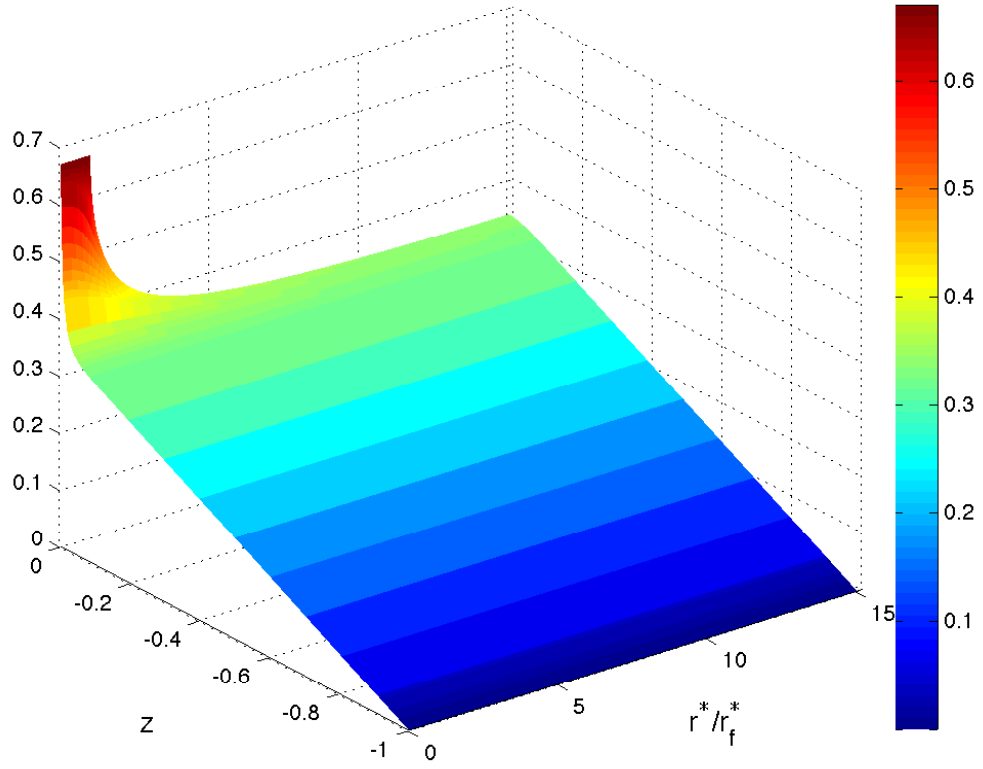

Figure A.5: Pressure distribution in the SI region as function of non-dimensional r and z distance. Note that fenestral hole is at $0 < r^*/r_f^* \leq 1$. $L_i^* = 500$ nm. L_{P_e} and L_{P_m} are from Nguyen's data (62), given in tables 2.5 and 2.4 respectively

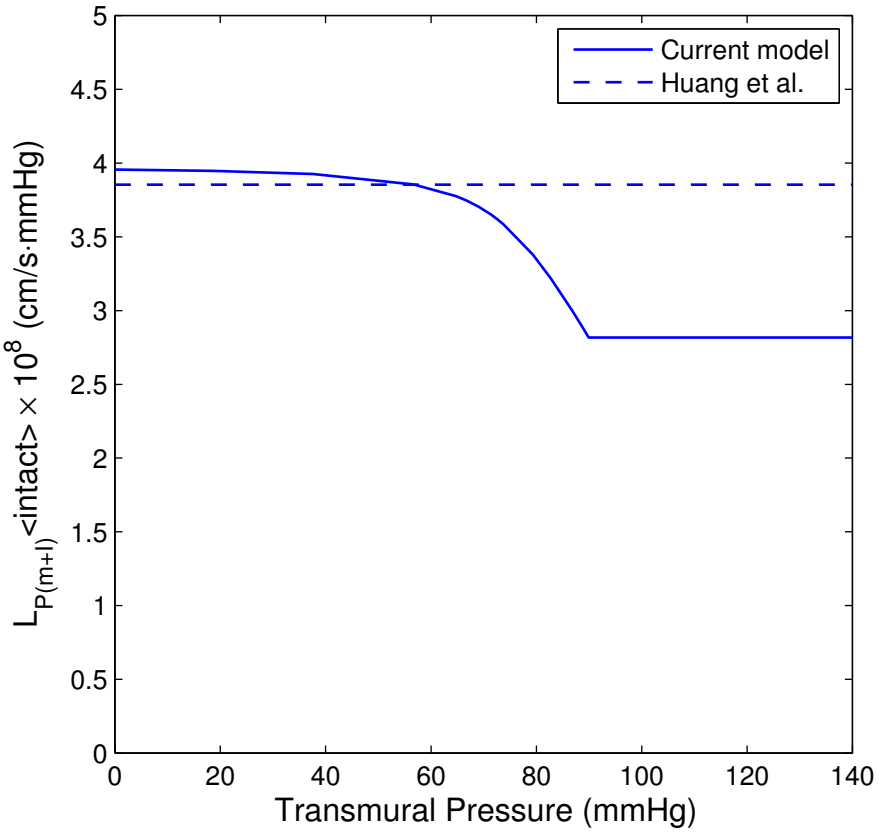

Figure A.6: The hydraulic conductivity of the media plus IEL of an intact vessel wall obtained using current model and comparison with Huang et al.'s (36) predictions. L_{P_e} and L_{P_m} are from Nguyen's data (62), given in tables 2.5 and 2.4 respectively

of pressure since there is no possibility of SI compression and the subsequent fenestra blockage. However, with an intact endothelium, the L_P of the IEL and media region is governed by the pressure distribution inside the SI region. Since pressure inside the SI region vary significantly upon pressure loadings (due to intima compression), the $L_{P_{m+I}}$ of an intact vessel may not be constant as assumed by Huang et al. (36). We can estimate this quantity by employing incompressibility of flow as:

$$L_{P_{m+I}}\,\bar{P}_i|_{z_i=0}\,\pi\xi_I^2 = \frac{2\pi K_{P_i}}{\mu\, L_i^*}\int_0^1 \frac{dP_i}{dz_i}\Big|_{z_i=0} r dr \tag{A.35}$$

where,

$$\bar{P}_i|_{z_i=0} = \frac{2}{\xi_I^2}\int_0^{\xi_I} P_i\big|_{z_i=0}\, r dr$$

Figure A.6 shows model predictions for the $L_{P_{m+I}}$ of intact artery wall obtained using Eq. A.35 and compares these predictions with Huang et al.'s assumption of constant $L_{P_{m+I}}$. Clearly, at lower transmural pressures, both the predictions suggest a constant $L_{P_{m+I}}$ for an intact artery wall. However, at higher pressures (beyond $\sim$ 60 mmHg), the $L_{P_{m+I}}$ decreases significantly until the SI reaches a critical compression limit after which $L_{P_{m+I}}$ stays constant. This result suggest that Huang et al.'s (36) assumption is valid at lower pressures, however as per Eq. 2.16a, an error in estimating $L_{P_{m+I}}$ at higher pressures can over-predict the L_P of the vessel wall (L_{P_t}). This explains the mismatch between the current and Huang et al.'s (36) method of predicting the L_{P_t} as discussed in section 2.2.5.

A.5.4 Effect of increasing AQPs on SI compression

Figure A.7 predicts how the thickness (non-dimensional) of the SI regions varies upon pressure loadings and the effect of increasing the number of AQPs, or transcellular pathways, on the level of intima compression. As shown in Fig. A.7 for each curve, there is a linear decrease in the intima thickness at lower pressures, after which it becomes non-linear until the intima reaches the critical compression limit, beyond which our model doesn't allow any further compression. Figure 2.12 suggests that, at a given transmural pressure, increasing the number of functioning AQPs reduces the force per unit area on the endothelium, which should decrease the level of intima compression. The predictions shown in Fig. A.7 confirm this hypothesis where we find higher intima thicknesses, or less compression, with more AQPs on the endothelium. Figure A.7 also suggests that, if there are more AQPs on the endothelium, the SI would attain full compression at much higher transmural pressure compared to the case with less number of AQPs on the EC.

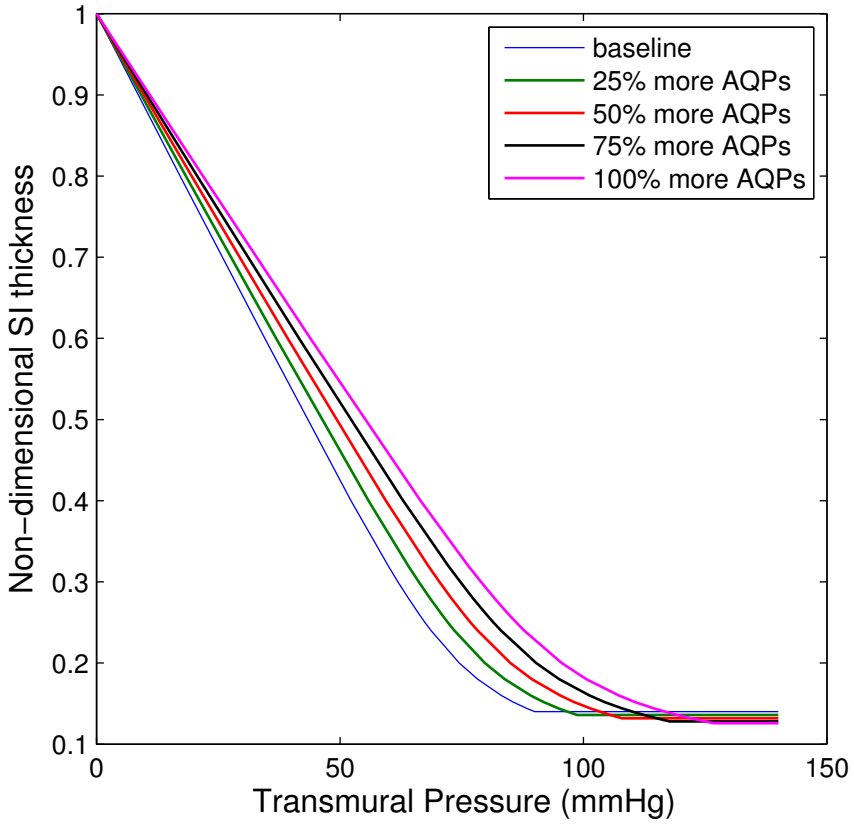

Figure A.7: Effect of increasing the number of AQPs on thickness of the SI region. Baseline results assume that AQPs contribute 40% to L_{P_e} (Eq. 2.22 gives corresponding $L_{P_{EC}}$ and $L_{P_{nj}}$); $L_{P_{nj}}$ (and thus k =27.9 mmHg) is fixed in all cases and $L_{P_{EC}}$ is varied based on assumed fraction

Appendix B.

B.1 Effect of SI compression on f_i, γ_i & D_i:

The variation of mass-transfer related SI parameters (γ_i, f_i and D_i) with intima compression is estimated using Eqs. 3.26-3.28 and plotted in Figs. B.1(a)-(c). The void fraction (ϵ) at a given intima compression required in these equations is estimated as discussed in our previous study (Ch. 2). As Fig. B.1 shows, all three parameters (γ_i, f_i and D_i) decrease with intima compression or a reduction in the SI thickness. In particular, the volume fraction available for albumin (γ_i) exhibits a rapid decrease (21% and 42% decrease at $L_i^* = 0.2L_{i0}^*$ and $L_i^* = 0.1L_{i0}^*$, respectively) with intima compression. For the same level of compression, f_i decreases by 6% and 20%, respectively. The resulting change in these transport properties significantly affects the transport of albumin through the SI and thus through the vessel wall, as discussed in Chapter 3.

B.2 2-D concentration of albumin in GX, SI and media:

Figures B.2 - B.4 show the 2-D non-dimensional concentration distribution of albumin in the GX, SI and media region, respectively, as a function of r and z. The concentration distribution in each region is obtained as a long-time solution of an unsteady problem (Eq. 3.24) with appropriate boundary conditions. As Fig. B.2 shows, the non-dimensional albumin concentration in the GX is almost constant, equal to 0.61 (volume fraction of albumin in the GX), with a small increase appearing near the junctional region (r = 15.0 - 15.0125). This increase in concentration results from the greater resistance offered by the junction to albumin's transport (governed by the osmotic reflection coefficient σ_{nj}) compared to that offered to water (solvent) flow. This phenomena is termed as "concentration polarization" effect and is observed when a solute is flowing through a porous medium. In the SI region, surprisingly, we find a uniform increase in albumin's con-

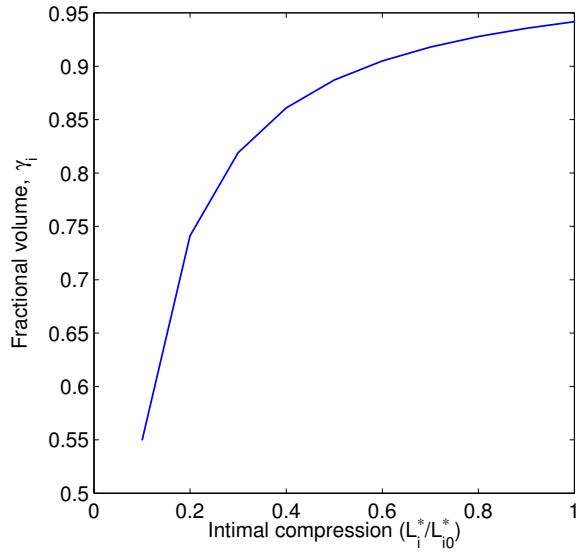

(a)

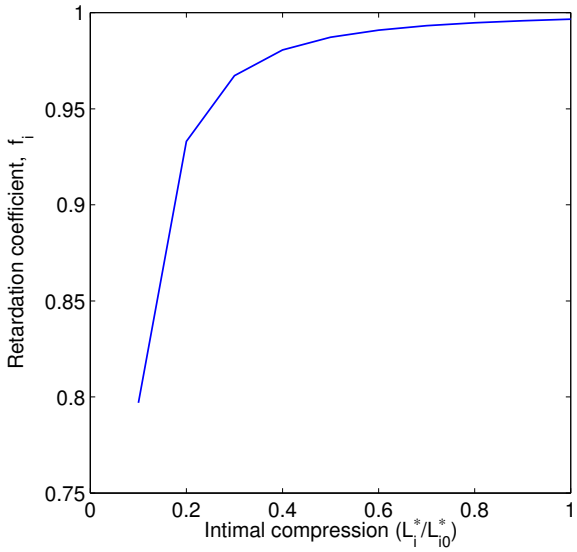

(b)

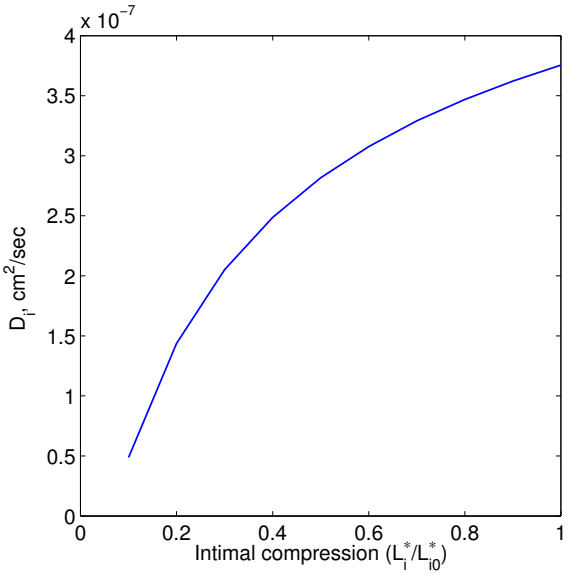

(c)

Figure B.1: The fractional volume for albumin (a), the retardation coefficient of albumin (b) and the effective diffusivity of albumin (c) in the SI as a function of intima compression (L_i^*/L_{i0}^*), L_{i0}^*= 500 nm

centration in the direction of flow i.e., from the junction towards the fenestra. Moreover, since the thickness of the SI region (L_i^*) is much smaller the radius of periodic wall unit (ξ_i^*) and the thickness of the media region (L_m^*), we do not find any variation in albumin's concentration in the z-direction, compared to the variation seen in radial direction. Note that the concentration in the SI at steady state is grater than one (or grater than lumen concentration in dimensional form), which is a result of the filtration of albumin taking place in the dense media region. The media concentration, shown in Fig. B.4, exhibits a strong z - dependence and negligible r- dependence, which is in contrast with the concentration distribution in the SI region, shown in Fig. B.3. The small maximum in concentration, near the fenestral hole, disappear within a distance of $0.03L_m^*$ from the lower surface of the IEL (z = 0) and the concentration uniformly reduces to the available volume fraction for albumin in the media region (i.e., γ_m = 0.08).

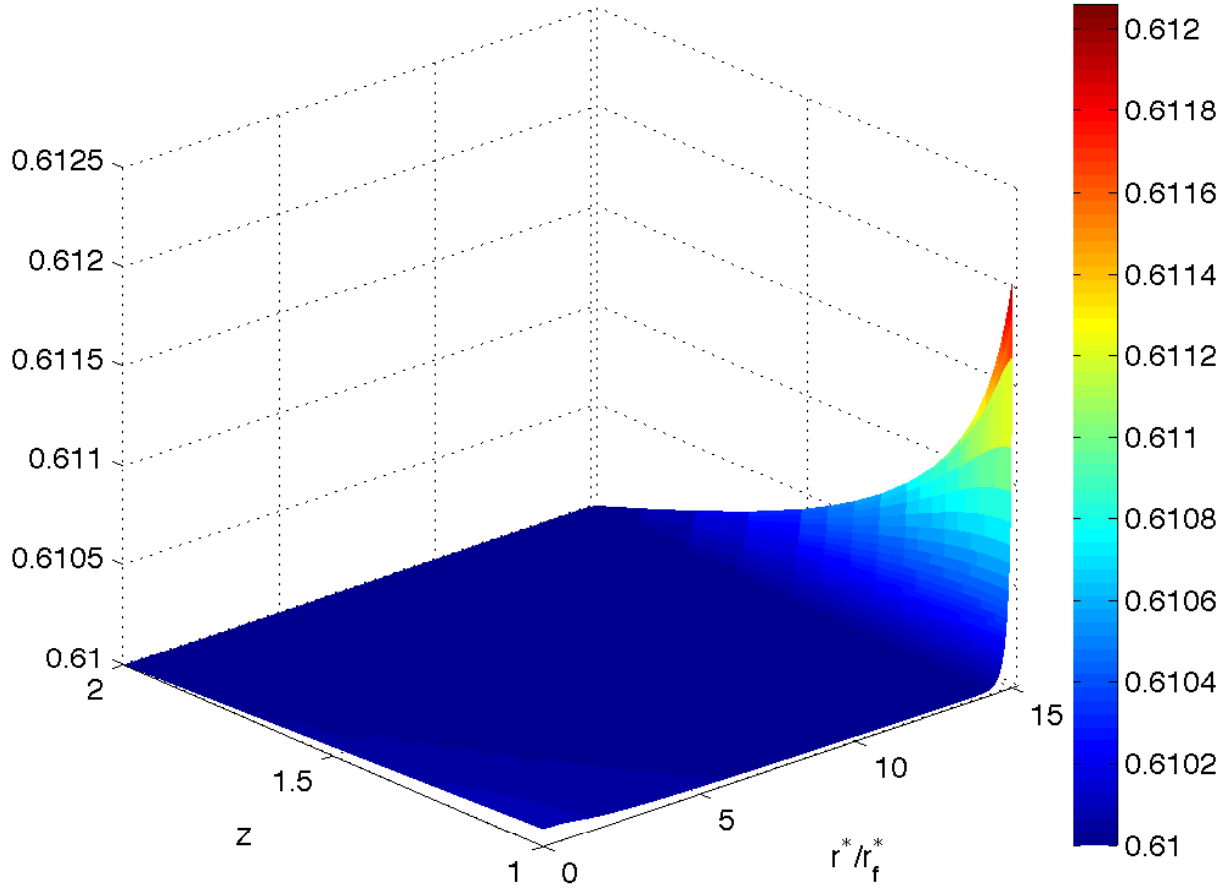

Figure B.2: Non-dimensional albumin concentration distribution in the GX region as function of r and z distance. Note that normal junction is from r^*/r_f^*= 15 -15.0125. P_L^*= 60 mmHg. L_{P_e} and L_{P_m} are from Nguyen's data (62).

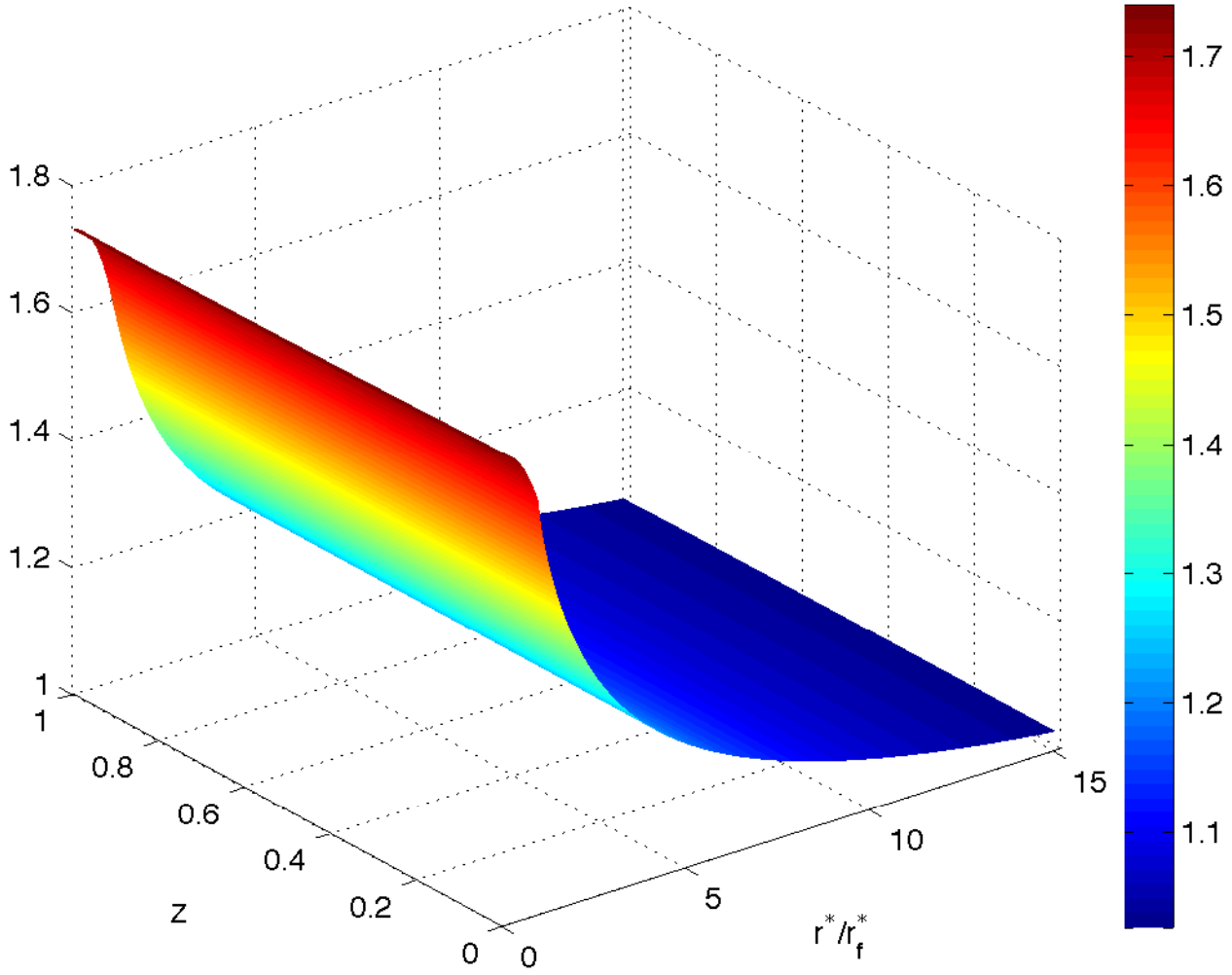

Figure B.3: Non-dimensional albumin concentration distribution in the SI region as function of r and z distance. Note that normal junction is from r^*/r_f^*= 15 -15.0125 and fenestral hole is at $0 < r^*/r_f^* \leq 1$. P_L^*= 60 mmHg. L_{P_e} and L_{P_m} are from Nguyen's data (62).

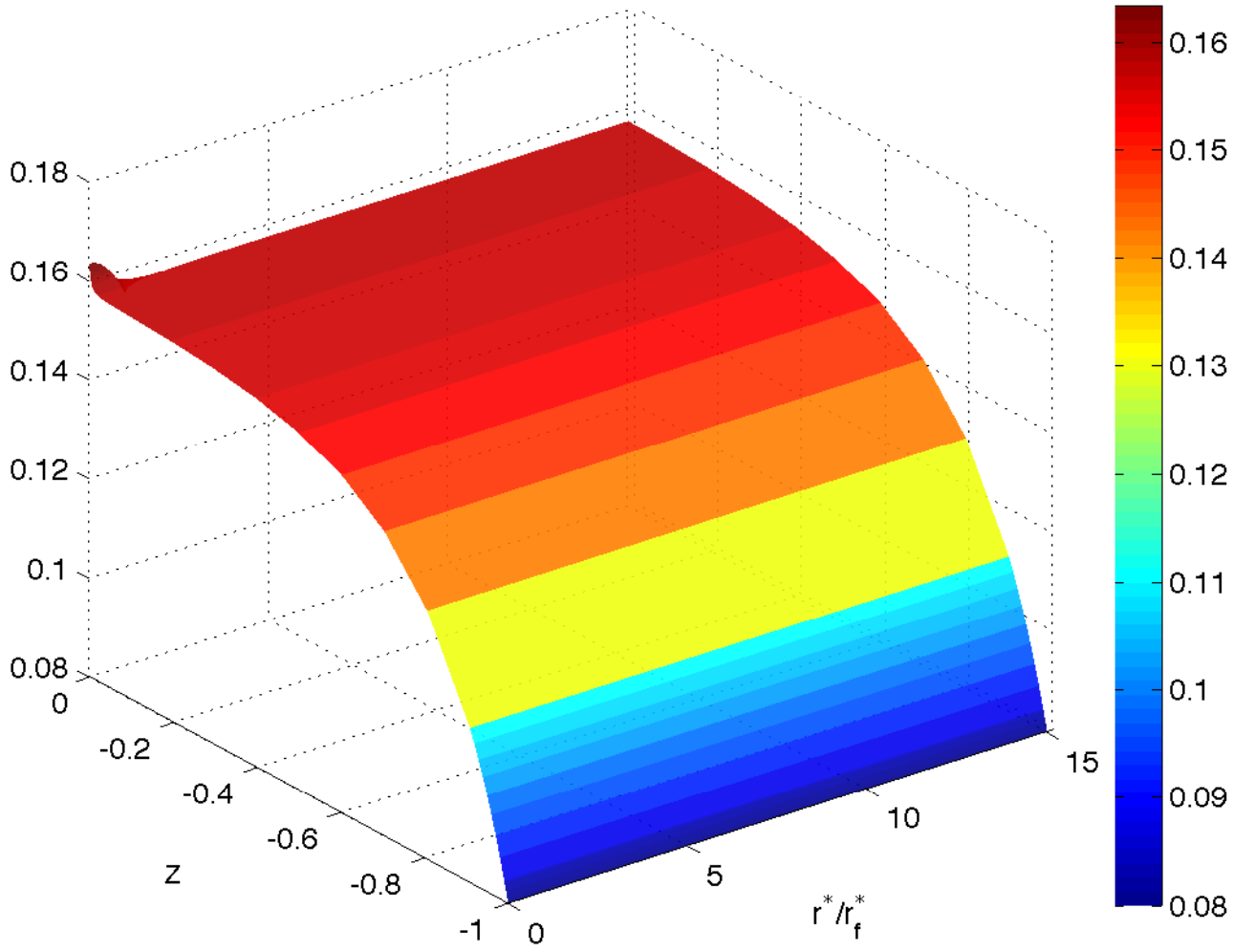

Figure B.4: Non-dimensional albumin concentration distribution in the media region as function of r and z distance. Note that fenestral hole is at $0 < r^*/r_f^* \leq 1$. P_L^*= 60 mmHg. L_{P_e} and L_{P_m} are from Nguyen's data (62).

Appendix C.

C.1 Additional results from Chapter 4

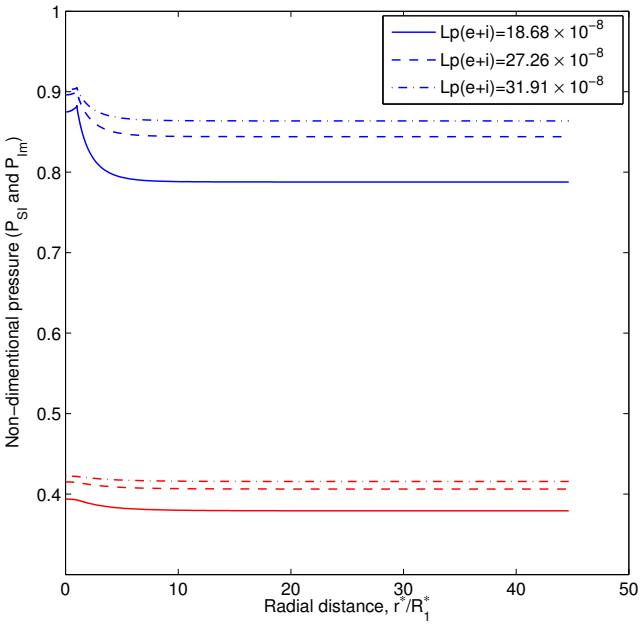

(a) ΔP^*= 60 mmHg

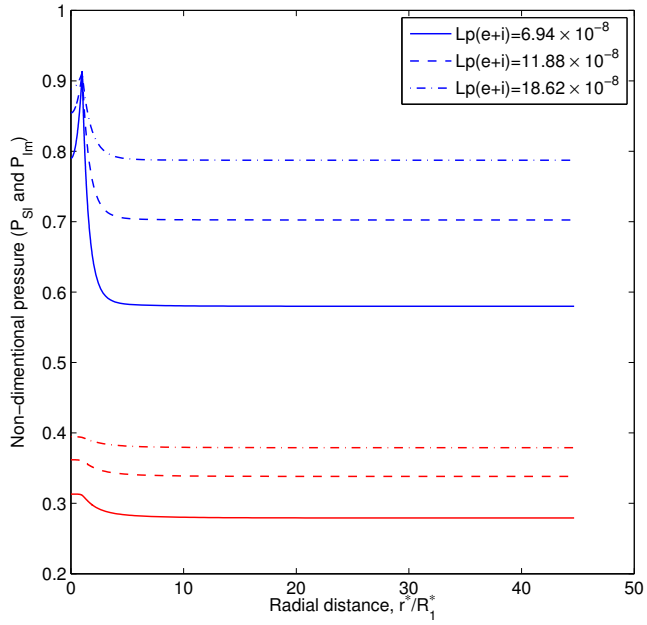

(b) ΔP^*= 80 mmHg

Figure C.1: Non-dimensional pressure in the SI at $z = 0$ (P_{SI} - upper blue curves) and at the interface of IEL and media (P_{IM} - lower red curves) as a function of radial distance r from the center of the leaky cell and with increasing endothelial AQP1 expression. Pressure is normalized by the transmural pressure drop (a) ΔP^*= 60 mmHg (b) ΔP^*= 100 mmHg

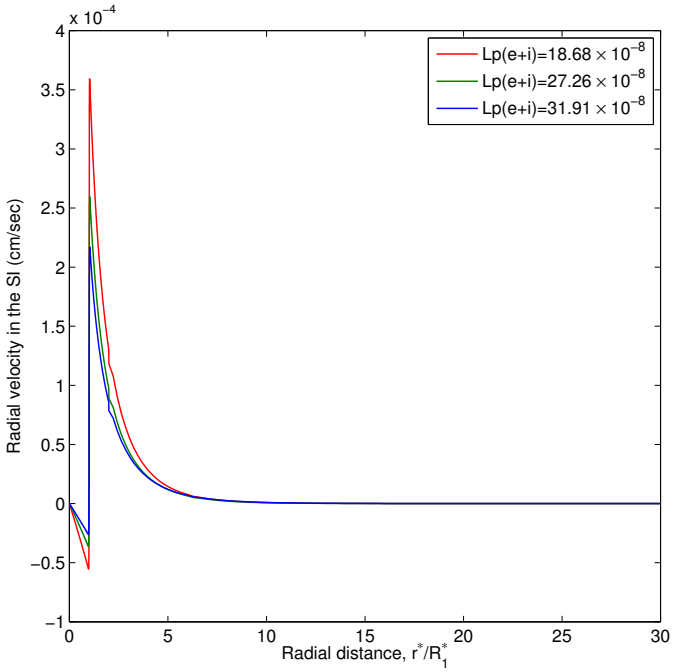

(a) ΔP^*= 60 mmHg

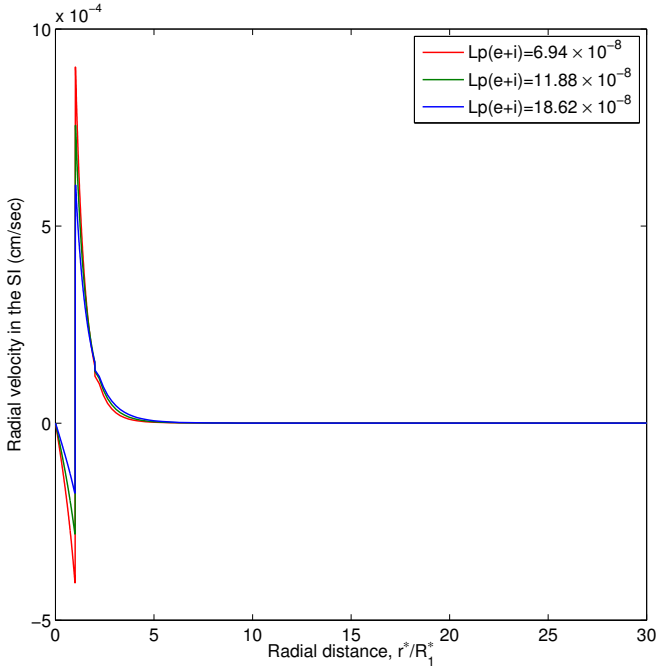

(b) ΔP^*= 100 mmHg

Figure C.2: Radial velocity in the SI (U_i) as a function of radial distance r from the center of the leaky cell and its variation with increasing endothelial AQP1 expression at (a) ΔP^*= 60 mmHg (b) ΔP^*= 100 mmHg. $L_{P_{e+i}}$ values are as described in Fig. 4.2

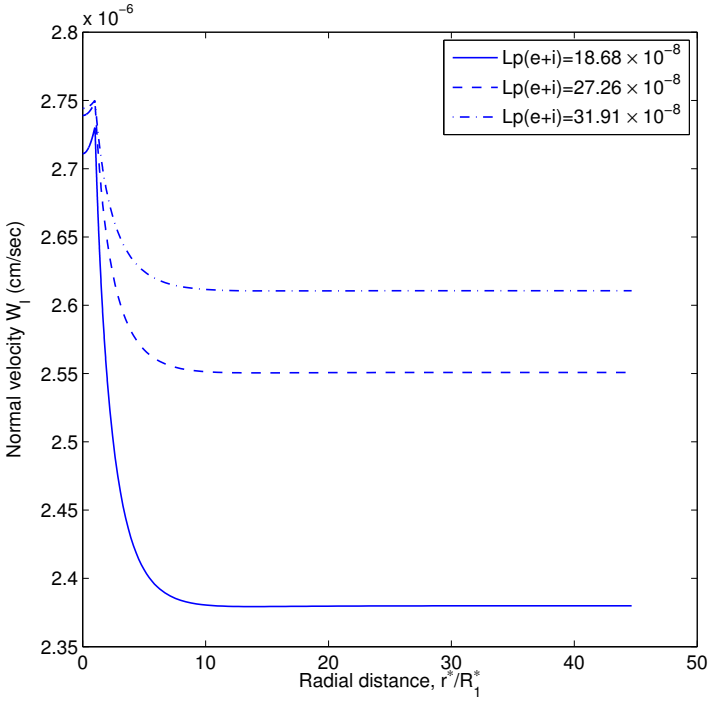

(a) ΔP^*= 60 mmHg

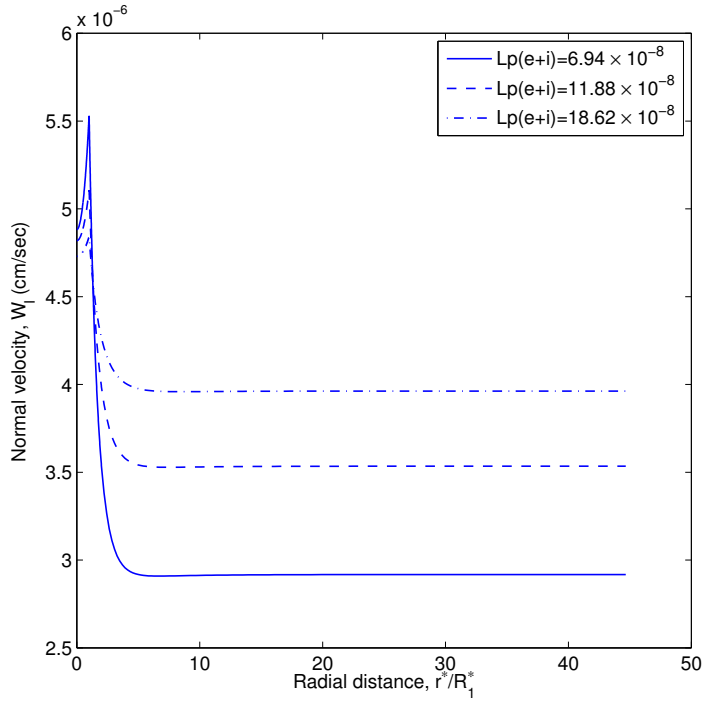

(b) ΔP^*= 100 mmHg

Figure C.3: Normal velocity across the IEL (W_I) as a function of radial distance r from the center of the leaky cell and its variation with increasing endothelial AQP1 expression at (a) ΔP^*= 60 mmHg (b) ΔP^*= 100 mmHg. $L_{P_{e+i}}$ values are as described in Fig. 4.2

Bibliography

[1] R.H. Adamson, J.F. Lenz, X. Zhang, G.N. Adamson, S. Weinbaum, and F.E. Curry. Oncotic pressures opposing filtration across non-fenestrated rat microvessels. *The Journal of physiology*, 557(3):889–907, 2004.

[2] A. L. Baldwin and L. M. Wilson. Endothelium increases medial hydraulic conductance of aorta, possibly by release of EDRF. *American Journal of Physiology-Heart and Circulatory Physiology*, 264(1):H26–H32, 1993.

[3] A.L. Baldwin, L.M. Wilson, and B.R. Simon. Effect of pressure on aortic hydraulic conductance. *Arteriosclerosis, Thrombosis, and Vascular Biology*, 12(2):163–171, 1992.

[4] L.M. Cancel, A. Fitting, and J.M. Tarbell. In vitro study of LDL transport under pressurized (convective) conditions. *American Journal of Physiology-Heart and Circulatory Physiology*, 293(1):H126–H132, 2007.

[5] C.G. Caro, J.M. Fitz-Gerald, and R.C. Schroter. Atheroma and arterial wall shear observation, correlation and proposal of a shear dependent mass transfer mechanism for atherogenesis. *Proceedings of the Royal Society of London. Series B. Biological Sciences*, 177(1046): 109–133, 1971.

[6] F.S.A. Cavalcante, S. Ito, K. Brewer, H. Sakai, A.M. Alencar, M.P. Almeida, J.S. Andrade Jr, A. Majumdar, E.P. Ingenito, and B. Suki. Mechanical interactions between collagen and proteoglycans: implications for the stability of lung tissue. *Journal of Applied Physiology*, 98(2):672–679, 2005.

[7] D.L. Chan, E.A. Rozanski, L.M. Freeman, and J.E. Rush. Colloid osmotic pressure in health and disease. *Compendium*, 2001.

[8] Y.L. Chen, K.M. Jan, H.S. Lin, and S. Chien. Ultrastructural studies on macromolecular permeability in relation to endothelial cell turnover. *Atherosclerosis*, 118(1):89–104, 1995.

[9] Y.L. Chen, K.M. Jan, H.S. Lin, and S. Chien. Relationship between endothelial cell turnover and permeability to horseradish peroxidase. *Atherosclerosis*, 133(1):7–14, 1997.

[10] S. Chien. Roles of flow mechanics in vascular cell biology in health and disease. *Introduction to Bioengineering, Edited by Y. C. Fung, World Scientific Publishing Co*, pages 1–12, 2001.

[11] S. Chien, S.J. Lin, S. Weinbaum, MM Lee, and K.M. Jan. The role of arterial endothelial cell mitosis in macromolecular permeability. *Advances in experimental medicine and biology*, 242:59, 1988.

[12] A. Cho, L. Mitchell, D. Koopmans, and B.L. Langille. Effects of changes in blood flow rate on cell death and cell proliferation in carotid arteries of immature rabbits. *Circulation research*, 81(3):328–337, 1997.

[13] PT Chuang, HJ Cheng, SJ Lin, KM Jan, MM Lee, and S. Chien. Macromolecular transport across arterial and venous endothelium in rats. studies with evans blue-albumin and horseradish peroxidase. *Arteriosclerosis, Thrombosis, and Vascular Biology*, 10(2):188–197, 1990.

[14] P.A. Curmi, L. Juan, and A. Tedgui. Effect of transmural pressure on low density lipoprotein and albumin transport and distribution across the intact arterial wall. *Circulation research*, 66(6):1692–1702, 1990.

[15] F. E. Curry. *Mechanics and thermodynamics of transcapillary exchange. In: Handbook of Physiology. The Cardiovascular system. Microcirculation*, volume IV, Chapter 8. American Physiology Society, Bethesda, MD, 1984.

[16] F. E. Curry. Determinants of capillary permeability: a review of mechanisms based on single capillary studies in the frog. *Circulation research*, 59(4):367, 1986.

[17] F.E. Curry and C.C. Michel. A fiber matrix model of capillary permeability. *Microvascular research*, 20(1):96, 1980.

[18] M. Dabagh, P. Jalali, and J.M. Tarbell. The transport of LDL across the deformable arterial wall: the effect of endothelial cell turnover and intimal deformation under hypertension. *American Journal of Physiology-Heart and Circulatory Physiology*, 297(3):H983–H996, 2009.

[19] E.R. Damiano and T.M. Stace. A mechano-electrochemical model of radial deformation of the capillary glycocalyx. *Biophysical journal*, 82(3):1153–1175, 2002.

[20] ER Damiano, DS Long, and ML Smith. Estimation of viscosity profiles using velocimetry data from parallel flows of linearly viscous fluids: application to microvascular haemodynamics. *Journal of Fluid Mechanics*, 512(1):1–19, 2004.

[21] L. DeMaio, Y.S. Chang, T.W. Gardner, J.M. Tarbell, and D.A. Antonetti. Shear stress regulates occludin content and phosphorylation. *American Journal of Physiology-Heart and Circulatory Physiology*, 281(1):H105–H113, 2001.

[22] S. Dimmeler, J. Haendeler, V. Rippmann, M. Nehls, and A.M. Zeiher. Shear stress inhibits apoptosis of human endothelial cells. *FEBS letters*, 399(1-2):71–74, 1996.

[23] J. Feng and S. Weinbaum. Flow through an orifice in a fibrous medium with application to fenestral pores in biological tissue. *Chemical engineering science*, 56(18):5255–5268, 2001.

[24] J. S. Frank and A. M. Fogelman. Ultrastructure of the intima in WHHL and cholesterol-fed rabbit aortas prepared by ultra-rapid freezing and freeze-etching. *Journal of lipid research*, 30(7):967–978, 1989.

[25] D. L. Fry. Acute vascular endothelial changes associated with increased blood velocity gradients. *Circulation Research*, 22(2):165–197, 1968.

[26] D.L. Fry. Mathematical models of arterial transmural transport. *American Journal of Physiology-Heart and Circulatory Physiology*, 248(2):H240–H263, 1985.

[27] DL Fry. Mass transport, atherogenesis, and risk. *Arteriosclerosis, Thrombosis, and Vascular Biology*, 7(1):88–100, 1987.

[28] A.R. Gourlay. Hopscotch: A fast second-order partial differential equation solver. *IMA Journal of Applied Mathematics*, 6(4):375–390, 1970.

[29] J. Happel and H. Brenner. *Low Reynolds number hydrodynamics: with special applications to particulate media*, volume 1. Springer, 1983.

[30] L. Hodgson and J.M. Tarbell. Solute transport to the endothelial intercellular cleft: the effect of wall shear stress. *Annals of biomedical engineering*, 30(7):936–945, 2002.

[31] J. P. Holman. *Heat Transfer*. McGraw-Hill, New York, 6^{th} edition, 1986.

[32] X. Hu and S. Weinbaum. A new view of starling's hypothesis at the microstructural level. *Microvascular research*, 58(3):281–304, 1999.

[33] X. Hu, RH Adamson, B. Liu, FE Curry, and S. Weinbaum. Starling forces that oppose filtration after tissue oncotic pressure is increased. *American Journal of Physiology-Heart and Circulatory Physiology*, 279(4):H1724–H1736, 2000.

[34] AL Huang, K.M. Jan, and S. Chien. Role of intercellular junctions in the passage of horseradish peroxidase across aortic endothelium. *Laboratory investigation; a journal of technical methods and pathology*, 67(2):201, 1992.

[35] Y. Huang, D. Rumschitzki, S. Chien, and S. Weinbaum. A fiber matrix model for the growth of macromolecular leakage spots in the arterial intima. *Journal of biomechanical engineering*, 116:430, 1994.

[36] Y. Huang, D. Rumschitzki, S. Chien, and S. Weinbaum. A fiber matrix model for the filtration through fenestral pores in a compressible arterial intima. *American Journal of Physiology-Heart and Circulatory Physiology*, 272(4):H2023–H2039, 1997.

[37] Y. Huang, K.M. Jan, D. Rumschitzki, and S. Weinbaum. Structural changes in rat aortic intima due to transmural pressure. *Journal of biomechanical engineering*, 120:476, 1998.

[38] Z. J. Huang and J. M. Tarbell. Numerical simulation of mass transfer in porous media of blood vessel walls. *American Journal of Physiology-Heart and Circulatory Physiology*, 273 (1):H464–H477, 1997.

[39] H. Jo, RO Dull, TM Hollis, and JM Tarbell. Endothelial albumin permeability is shear dependent, time dependent, and reversible. *American Journal of Physiology-Heart and Circulatory Physiology*, 260(6):H1992–H1996, 1991.

[40] M. Johnson and J.M. Tarbell. A biphasic, anisotropic model of the aortic wall. *Journal of biomechanical engineering*, 123:52, 2001.

[41] S. D. Joshi, K-M. Jan, and D. S. Rumschitzki. Mathematical modeling of effect of aquaporin-1 on aortic intima compression. To be submitted, 2012.

[42] G. Karner and K. Perktold. Effect of endothelial injury and increased blood pressure on albumin accumulation in the arterial wall: a numerical study. *Journal of Biomechanics*, 33 (6):709–715, 2000.

[43] O. Kedem and A. Katchalsky. Thermodynamic analysis of the permeability of biological membranes to non-electrolytes. *Biochimica et Biophysica Acta*, 27:229–246, 1958.

[44] M. Khakpour and K. Vafai. Critical assessment of arterial transport models. *International Journal of Heat and Mass Transfer*, 51(3-4):807–822, 2008.

[45] W.S. Kim and J.M. Tarbell. Macromolecular transport through the deformable porous media of an artery wall. *Journal of biomechanical engineering*, 116:156, 1994.

[46] M. Klanchar and JM Tarbell. Modeling water flow through arterial tissue. *Bulletin of mathematical biology*, 49(6):651–669, 1987.

[47] M.W. Lark, TK Yeo, H. Mar, S. Lara, I. Hellström, KE Hellström, and T.N. Wight. Arterial chondroitin sulfate proteoglycan: localization with a monoclonal antibody. *Journal of Histochemistry & Cytochemistry*, 36(10):1211, 1988.

[48] MJ Lever, JM Tarbell, and CG Caro. The effect of luminal flow in rabbit carotid artery on transmural fluid transport. *Experimental physiology*, 77(4):553–563, 1992.

[49] JR Levick. Flow through interstitium and other fibrous matrices. *Experimental Physiology*, 72(4):409–437, 1987.

[50] S.J. Lin, K.M. Jan, G. Schuessler, S. Weinbaum, and S. Chien. Enhanced macromolecular permeability of aortic endothelial cells in association with mitosis. *Atherosclerosis*, 73(2-3): 223–232, 1988.

[51] S.J. Lin, K.M. Jan, S. Weinbaum, and S. Chien. Transendothelial transport of low density lipoprotein in association with cell mitosis in rat aorta. *Arteriosclerosis, Thrombosis, and Vascular Biology*, 9(2):230–236, 1989.

[52] S.J. Lin, KM Jan, and S. Chien. Role of dying endothelial cells in transendothelial macromolecular transport. *Arteriosclerosis, Thrombosis, and Vascular Biology*, 10(5):703–709, 1990.

[53] X. Liu, Y. Fan, and X. Deng. Effect of the endothelial glycocalyx layer on arterial LDL transport under normal and high pressure. *Journal of Theoretical Biology*, 2011.

[54] S.V. Lopez-Quintero, R. Amaya, M. Pahakis, and J.M. Tarbell. The endothelial glycocalyx mediates shear-induced changes in hydraulic conductivity. *American Journal of Physiology-Heart and Circulatory Physiology*, 296(5):H1451–H1456, 2009.

[55] A. J. Lusis. Atherosclerosis. *Nature*, 407:233–241, 2000.

[56] RI Macey. Transport of water and urea in red blood cells. *American Journal of Physiology-Cell Physiology*, 246(3):C195–C203, 1984.

[57] J. N. McDonald and J. R. Levick. Effect of extravascular plasma protein on pressure-flow relations across synovium in anaesthetized rabbits. *The Journal of physiology*, 465(1):539–559, 1993.

[58] K. Murata, K. Mitsuoka, T. Hirai, T. Walz, P. Agre, J.B. Heymann, A. Engel, and Y. Fujiyoshi. Structural determinants of water permeation through aquaporin-1. *Nature*, 407 (6804):599–605, 2000.

[59] R. M. Nerem. Vascular fluid mechanics, the arterial wall, and atherosclerosis. *Journal of biomechanical engineering*, 114:274, 1992.

[60] R. M. Nerem. Atherosclerosis and the role of wall shear stress. *In Flow-dependent regulation of vascular function edited by Bevan, J.A. and Kaley, G. and Rubanyi, G.M., Oxford Univ. Press, New York*, 1995.

[61] M.K. Nguyen and I. Kurtz. Quantitative interrelationship between gibbs-donnan equilibrium, osmolality of body fluid compartments, and plasma water sodium concentration. *Journal of applied physiology*, 100(4):1293–1300, 2006.

[62] T.H. Nguyen. *Aquaporin-1 contribution to rat aortic endothelial hydraulic conductivity and how chronic transmural pressure affects it*. PhD thesis, City University of New York, 2008.

[63] S. Nielsen, B. L. Smith, E. I. Christensen, and P. Agre. Distribution of the aquaporin CHIP in secretory and resorptive epithelia and capillary endothelia. *Proceedings of the National Academy of Sciences*, 90(15):7275, 1993.

[64] C.M. Niemietz and S.D. Tyerman. New potent inhibitors of aquaporins: silver and gold compounds inhibit aquaporins of plant and human origin. *FEBS letters*, 531(3):443–447, 2002.

[65] A. G. Ogston, B. N. Preston, and J. D. Wells. On the transport of compact particles through solutions of chain-polymers. *Proceedings of the Royal Society of London. A. Mathematical and Physical Sciences*, 333(1594):297–316, 1973.

[66] R.F. Potter and M.R. Roach. Are enlarged fenestrations in the internal elastic lamina of the rabbit thoracic aorta associated with poststenotic dilatation? *Canadian journal of physiology and pharmacology*, 61(1):101, 1983.

[67] G.M. Preston, T.P. Carroll, W.B. Guggino, and P. Agre. Appearance of water channels in xenopus oocytes expressing red cell chip28 protein. *Science*, 256(5055):385–387, 1992.

[68] C.B. Raval. *Increasing aortic endothelial cell aquaporin-1 expression upregulates endothelial hydraulic conductivity in monolayers and in whole vessels ex vivo*. PhD thesis, City University of New York, 2012.

[69] W. Rosamond and K. Flegal. Heart disease and stroke statistics-2007 update: A report from the american heart association statistic committee and stroke statistics subcommittee. *Circulation*, 115:e69–e171, 2007.

[70] B.I. Rosengren, O. Carlsson, D. Venturoli, O. Al Rayyes, and B. Rippe. Transvascular passage of macromolecules into the peritoneal cavity of normo-and hypothermic rats in vivo: Active or passive transport? *Journal of vascular research*, 41(2):123–130, 2004.

[71] R. Ross. The pathogenesis of atherosclerosisan update. *New England Journal of Medicine*, 314(8):488–500, 1986.

[72] R. Ross. The pathogenesis of atherosclerosis: a perspective for the 1990s. *Nature*, 362:801, 1993.

[73] S. Russell. *Energy depletion causes endothelial hyperpermeability in hyperglycemia*. PhD thesis, City University of New York, 2009.

[74] D.C. Schwenke and T.E. Carew. Initiation of atherosclerotic lesions in cholesterol-fed rabbits II. selective retention of LDL vs. selective increases in LDL permeability in susceptible sites of arteries. *Arteriosclerosis, Thrombosis, and Vascular Biology*, 9(6):908–918, 1989.

[75] TW Secomb, R. Hsu, and AR Pries. Motion of red blood cells in a capillary with an endothelial surface layer: effect of flow velocity. *American Journal of Physiology-Heart and Circulatory Physiology*, 281(2):H629–H636, 2001.

[76] A. Selzer. Changing aspects of the natural history of valvular aortic stenosis. *New England Journal of Medicine*, 317(2):91–98, 1987.

[77] K. Shigematsu, H. Yasuhara, H. Shigematsu, and T. Muto. Direct and indirect effects of pulsatile shear stress on the smooth muscle cell. *International angiology: a journal of the International Union of Angiology*, 19(1):39, 2000.

[78] Y. Shou, K. Jan, and D.S. Rumschitzki. Transport in rat vessel walls. I. hydraulic conductivities of the aorta, pulmonary artery, and inferior vena cava with intact and denuded endothelia. *American Journal of Physiology-Heart and Circulatory Physiology*, 291(6): H2758–H2771, 2006.

[79] Y. Shou, K. Jan, and D.S. Rumschitzki. Transport in rat vessel walls II. Macromolecular leakage and focal spot size growth in rat arteries and veins. *American Journal of Physiology-Heart and Circulatory Physiology*, 292(6):H2881–H2890, 2007.

[80] H.W. Sill, Y.S. Chang, J.R. Artman, JA Frangos, TM Hollis, and JM Tarbell. Shear stress increases hydraulic conductivity of cultured endothelial monolayers. *American Journal of Physiology-Heart and Circulatory Physiology*, 268(2):H535–H543, 1995.

[81] N. Simionescu, E. Vasile, F. Lupu, G. Popescu, and M. Simionescu. Prelesional events in atherogenesis. accumulation of extracellular cholesterol-rich liposomes in the arterial intima and cardiac valves of the hyperlipidemic rabbit. *The American journal of pathology*, 123 (1):109, 1986.

[82] FH Sims, X. Chen, and JB Gavin. The importance of a substantial elastic lamina subjacent to the endothelium in limiting the progression of atherosclerotic changes. *Histopathology*, 23(4):307–317, 1993.

[83] M. L. Smith, D. S. Long, E. R. Damiano, and K. Ley. Near-wall μ-PIV reveals a hydrodynamically relevant endothelial surface layer in venules *in vivo*. *Biophysical Journal*, 85(1): 637 – 645, 2003.

[84] J.M. Squire, M. Chew, G. Nneji, C. Neal, J. Barry, and C. Michel. Quasi-periodic substructure in the microvessel endothelial glycocalyx: a possible explanation for molecular filtering? *Journal of structural biology*, 136(3):239–255, 2001.

[85] E.H. Starling. On the absorption of fluids from the connective tissue spaces. *The Journal of physiology*, 19(4):312–326, 1896.

[86] D. Steinberg. Lipoproteins and atherosclerosis. a look back and a look ahead. *Arteriosclerosis*, 3(4):283, 1983.

[87] D. Steinberg. Role of oxidized LDL and antioxidants in atherosclerosis. *Advances in experimental medicine and biology*, 369:39, 1995.

[88] D. Steinberg, S. Parthasarathy, T. E. Carew, J. C. Khoo, and J. L. Witztum. Beyond cholesterol. modifications of low-density lipoprotein that increase its atherogenicity. *The New England journal of medicine*, 320(14):915–924, 1989.

[89] M.B. Stemerman, E.M. Morrel, K.R. Burke, C.K. Colton, K.A. Smith, and R.S. Lees. Local variation in arterial wall permeability to low density lipoprotein in normal rabbit aorta. *Arteriosclerosis, Thrombosis, and Vascular Biology*, 6(1):64–69, 1986.

[90] AV Sterpetti, A. Cucina, L.S. D'Angelo, B. Cardillo, A. Cavallaro, et al. Response of arterial smooth muscle cells to laminar flow. *The Journal of cardiovascular surgery*, 33(5): 619, 1992.

[91] A.P. Stevens, V. Hlady, and R.O. Dull. Fluorescence correlation spectroscopy can probe albumin dynamics inside lung endothelial glycocalyx. *American Journal of Physiology-Lung Cellular and Molecular Physiology*, 293(2):L328–L335, 2007.

[92] M. Sugihara-Seki, T. Akinaga, and T. Itano. Flow across microvessel walls through the endothelial surface glycocalyx and the interendothelial cleft. *Journal of Fluid Mechanics*, 601:229–252, 2008.

[93] N. Sun, N.B. Wood, A.D. Hughes, S.A.M. Thom, and X.Y. Xu. Effects of transmural pressure and wall shear stress on LDL accumulation in the arterial wall: a numerical study using a multilayered model. *American Journal of Physiology-Heart and Circulatory Physiology*, 292(6):H3148–H3157, 2007.

[94] Y. Sun. *The focal spread of macromolecular tracers in vessel walls: Frequency and effect of intima compaction and blood pressure*. PhD thesis, City University of New York, 2008.

[95] S. Tada and J.M. Tarbell. Interstitial flow through the internal elastic lamina affects shear stress on arterial smooth muscle cells. *American Journal of Physiology-Heart and Circulatory Physiology*, 278(5):H1589–H1597, 2000.

[96] S. Tada and J.M. Tarbell. Fenestral pore size in the internal elastic lamina affects transmural flow distribution in the artery wall. *Annals of Biomedical Engineering*, 29(6):456–466, 2001.

[97] J.M. Tarbell. Mass transport in arteries and the localization of atherosclerosis. *Annual review of biomedical engineering*, 5(1):79–118, 2003.

[98] J.M. Tarbell. Shear stress and the endothelial transport barrier. *Cardiovascular research*, 87 (2):320, 2010.

[99] J.M. Tarbell and MY Pahakis. Mechanotransduction and the glycocalyx. *Journal of internal medicine*, 259(4):339–350, 2006.

[100] A. Tedgui and M. J. Lever. Filtration through damaged and undamaged rabbit thoracic aorta. *American Journal of Physiology-Heart and Circulatory Physiology*, 247(5):H784–H791, 1984.

[101] A. Tedgui and M. J. Lever. Effect of pressure and intimal damage on ^{131}I-albumin and [^{14}C] sucrose spaces in aorta. *American Journal of Physiology-Heart and Circulatory Physiology*, 253(6):H1530–H1539, 1987.

[102] J.R. Thiagarajah and AS Verkman. Aquaporin deletion in mice reduces corneal water permeability and delays restoration of transparency after swelling. *Journal of Biological Chemistry*, 277(21):19139–19144, 2002.

[103] J.D. Toussaint. *Aquaporin-1 and pressure-driven water transport across aortic endothelia. Aquaporin-1 expression, distribution and regulation*. PhD thesis, City University of New York, 2009.

[104] GA Truskey. Quantitative analysis of protein transport in the arterial wall. *In Structure and function of the circulation, edited by Schwartz CJ, Werthessen J. T., and Wolf S., Plenum Press, New York*, pages 287–355, 1981.

[105] GA Truskey, WL Roberts, RA Herrmann, and RA Malinauskas. Measurement of endothelial permeability to 125I-low density lipoproteins in rabbit arteries by use of en face preparations. *Circulation research*, 71(4):883–897, 1992.

[106] R.Y. Tsay and S. Weinbaum. Viscous flow in a channel with periodic cross-bridging fibres: exact solutions and Brinkman approximation. *Journal of Fluid Mechanics*, 226(1):125–148, 1991.

[107] G. Tzeghai, P. Ganatos, R. Pfeffer, S. Weinbaum, and A. Nir. A theoretical model to study the effect of convection and leaky junctions on macromolecule transport in artery walls. *Journal of theoretical biology*, 121(2):141–162, 1986.

[108] H. Ueba, M. Kawakami, and T. Yaginuma. Shear stress as an inhibitor of vascular smooth muscle cell proliferation: role of transforming growth factor-β1 and tissue-type plasminogen activator. *Arteriosclerosis, thrombosis, and vascular biology*, 17(8):1512–1516, 1997.

[109] B.M. van den Berg, J.A.E. Spaan, T.M. Rolf, and H. Vink. Atherogenic region and diet diminish glycocalyx dimension and increase intima-to-media ratios at murine carotid artery bifurcation. *American Journal of Physiology-Heart and Circulatory Physiology*, 290(2): H915–H920, 2006.

[110] C.B. Vargas, F.F. Vargas, J.G. Pribyl, and P.L. Blackshear. Hydraulic conductivity of the endothelial and outer layers of the rabbit aorta. *American Journal of Physiology-Heart and Circulatory Physiology*, 236(1):H53–H60, 1979.

[111] PE Vincent, SJ Sherwin, and PD Weinberg. Viscous flow over outflow slits covered by an anisotropic brinkman medium: A model of flow above interendothelial cell clefts. *Physics of Fluids*, 20:063106, 2008.

[112] P.E. Vincent, S.J. Sherwin, and P.D. Weinberg. The effect of a spatially heterogeneous transmural water flux on concentration polarization of low density lipoprotein in arteries. *Biophysical journal*, 96(8):3102–3115, 2009.

[113] PE Vincent, SJ Sherwin, and PD Weinberg. The effect of the endothelial glycocalyx layer on concentration polarisation of low density lipoprotein in arteries. *Journal of theoretical biology*, 265(1):1–17, 2010.

[114] H. Vink and B.R. Duling. Identification of distinct luminal domains for macromolecules, erythrocytes, and leukocytes within mammalian capillaries. *Circulation research*, 79(3): 581–589, 1996.

[115] J. Voigtlaender, B. Heindl, and B.F. Becker. Transmembrane water influx via aquaporin-1 is inhibited by barbiturates and propofol in red blood cells. *Naunyn-Schmiedeberg's archives of pharmacology*, 366(3):209–217, 2002.

[116] W. A. Wakeham, N. H. Salpadoru, and C. G. Caro. Diffusion coefficients for protein molecules in blood serum. *Atherosclerosis*, 25(2-3):225–235, 1976.

[117] DM Wang and JM Tarbell. Modeling interstitial flow in an artery wall allows estimation of wall shear stress on smooth muscle cells. *Journal of biomechanical engineering*, 117: 358–363, 1995.

[118] S. Weinbaum. 1997 whitaker distinguished lecture: Models to solve mysteries in biomechanics at the cellular level; a new view of fiber matrix layers. *Annals of biomedical engineering*, 26(4):627–643, 1998.

[119] S. Weinbaum, G. Tzeghai, P. Ganatos, R. Pfeffer, and S. Chien. Effect of cell turnover and leaky junctions on arterial macromolecular transport. *American Journal of Physiology-Heart and Circulatory Physiology*, 248(6):H945–H960, 1985.

[120] S. Weinbaum, P. Ganatos, R. Pfeffer, GB Wen, M. Lee, and S. Chien. On the time-dependent diffusion of macromolecules through transient open junctions and their subendothelial spread I. Short-time model for cleft exit region. *Journal of theoretical biology*, 135(1):1–30, 1988.

[121] S. Weinbaum, X. Zhang, Y. Han, H. Vink, and S.C. Cowin. Mechanotransduction and flow across the endothelial glycocalyx. *Proceedings of the National Academy of Sciences*, 100 (13):7988–95, 2003.

[122] S. Weinbaum, J.M. Tarbell, and E.R. Damiano. The structure and function of the endothelial glycocalyx layer. *Annu. Rev. Biomed. Eng.*, 9:121–167, 2007.

[123] GB Wen, S. Weinbaum, P. Ganatos, R. Pfeffer, and S. Chien. On the time dependent diffusion of macromolecules through transient open junctions and their subendothelial spread II. Long time model for interaction between leakage sites. *Journal of theoretical biology*, 135 (2):219–253, 1988.

[124] O. Wiklund, T.E. Carew, and D. Steinberg. Role of the low density lipoprotein receptor in penetration of low density lipoprotein into rabbit aortic wall. *Arteriosclerosis, Thrombosis, and Vascular Biology*, 5(2):135–141, 1985.

[125] H. Wolinsky and S. Glagov. Structural basis for the static mechanical properties of the aortic media. *Circulation Research*, 14(5):400–413, 1964.

[126] Y. Xue. *The transcellular pathway is a significant contributor to water flow through vascular endothelia*. PhD thesis, City University of New York, 2011.

[127] B. Yang, J.K. Kim, and AS Verkman. Comparative efficacy of hgcl2 with candidate aquaporin-1 inhibitors dmso, gold, tea+ and acetazolamide. *FEBS letters*, 580(28-29):6679–6684, 2006.

[128] Y. Yin, KH Lim, S. Weinbaum, S. Chien, and DS Rumschitzki. A model for the initiation and growth of extracellular lipid liposomes in arterial intima. *American Journal of Physiology-Heart and Circulatory Physiology*, 272(2):H1033–H1046, 1997.

[129] F. Yuan, S. Chien, and S. Weinbaum. A new view of convective-diffusive transport processes in the arterial intima. *Journal of biomechanical engineering*, 113:314, 1991.

[130] Z. Zeng, Y. Yin, K.M. Jan, and D.S. Rumschitzki. Macromolecular transport in heart valves II. Theoretical models. *American Journal of Physiology-Heart and Circulatory Physiology*, 292(6):H2671–H2686, 2007.

[131] Z. Zeng, K.M. Jan, and D.S. Rumschitzki. A theory for water and macromolecular transport in the pulmonary artery with a detailed comparison to the aorta. *American Journal of Physiology-Heart and Circulatory Physiology*, 302(8):H1683–H1699, 2012.

[132] X. Zhang, R.H. Adamson, F.R.E. Curry, and S. Weinbaum. A 1-D model to explore the effects of tissue loading and tissue concentration gradients in the revised starling principle. *American Journal of Physiology-Heart and Circulatory Physiology*, 291(6):H2950–H2964, 2006.

[133] X. Zhang, F.R. Curry, and S. Weinbaum. Mechanism of osmotic flow in a periodic fiber array. *American Journal of Physiology-Heart and Circulatory Physiology*, 290(2):H844–H852, 2006.